INVESTIGATION OF LATERAL STRESS RELIEF ON THE STABILITY OF $\phi = 0°$ SLOPES USING LABORATORY, FRACTURE MECHANICS, AND FINITE ELMENT METHOD APPROACHES

by

Walter G. Kutschke, PE

BS, State University of New York at Buffalo, 1993

MS, State University of New York at Buffalo, 1995

Submitted to the Graduate Faculty of

Swanson School of Engineering in partial fulfillment

of the requirements for the degree of

Doctor of Philosophy

University of Pittsburgh

2011

UNIVERSITY OF PITTSBURGH

SWANSON SCHOOL OF ENGINEERING

This dissertation was presented

by

Walter G. Kutschke, PE

It was defended on

March 31, 2011

and approved by

Anthony Iannacchione, PhD, PE, PG, Associate Professor
Civil and Environmental Engineering Department

Jeen-Shang Lin, PhD, PE, Associate Professor
Civil and Environmental Engineering Department

Patrick Smolinski, PhD, Associate Professor
Mechanical Engineering and Materials Science Department

Julie M. Vandenbossche, PhD, PE, Assistant Professor
Civil and Environmental Engineering Department

Dissertation Director: Luis E. Vallejo, PhD, Professor
Civil and Environmental Engineering Department

INVESTIGATION OF LATERAL STRESS RELIEF ON THE STABILITY OF $\phi = 0°$ SLOPES USING LABORATORY, FRACTURE MECHANICS, AND FINITE ELMENT METHOD APPROACHES

Walter G. Kutschke, PhD, PE

University of Pittsburgh, 2011

Total stress analyses of purely cohesive cut slopes utilize the undrained shear strength for slope stability analyses. These slopes can have an in-situ lateral earth pressure that is greater than the vertical pressure. Excavations into these materials results in expansion of the slope face due to release of confining pressure. When strains exceed that which can be internally absorbed through elastic deformation, failure planes or cracks may develop at the toe of the slope. However, conventional limit equilibrium methods of slope stability analysis do not account for the in-situ stress conditions or the development of shear zones or cracks that occur from lateral stress relief. Progressive failure of the slope may occur if internal lateral stresses are large enough to cause stress concentrations in front of the advancing toe cracks. Finite element methods using substitution methods reveal two distinct shear cracks at the toe of slope consisting of a horizontal and an inclined failure plane while a tension zone develops in the backslope region. The formation and extension of the shear cracks are strongly dependent on k_o and they can extend to approximately ¼ of the slope height due to initial lateral stress relief. Classical limit equilibrium solutions regarding the critical slope height have been revised to account for lateral stress relief. Analyses indicate good agreement with published case histories and they reveal how the shear zones propagate to create progressive slope failure in stiff clay slopes under total stress analyses.

TABLE OF CONTENTS

PREFACE xviii

1.0 INTRODUCTION 1

1.1 SLOPE STABILITY ANALYSES OF $\phi = 0°$ SLOPES 1

1.2 LIMIT EQUILIBRIUM SLOPE STABILITY ANALYSES 4

1.2.1 Vertical Slope with Plane Failure Surface 5

1.2.2 Vertical Slope with Circular Failure Surface 10

1.2.3 Vertical Slope with Plane Failure Surface and Tension Cracking 16

1.2.4 Inclined Slopes with Circular Failure Surface 18

1.3 CLAY SLOPE FAILURES THAT WILL BE USED FOR THIS STUDY 22

1.3.1 Oxford Clay Slope 22

1.3.2 Conemaugh Clay Slope 24

1.4 RESEARCH OBJECTIVES 26

2.0 FRACTURE MECHANICS 28

2.1 FRACTURE MECHANICS THEORIES 29

2.1.1 LEFM Applied to Stiff Clay 30

2.2 LINEAR ELASTIC FRACTURE MECHANICS 31

2.2.2 Tangential Stress 36

2.2.2.1 Open Cracks – Mode I 38

2.2.2.2 Open Cracks – Mode II 38

2.2.2.3 Open Cracks – Mixed Mode 38
2.2.2.4 Closed Cracks 42
2.2.3 Shear Stress 42
2.2.3.1 Open Cracks – Mode I 44
2.2.3.2 Open Cracks – Mode II 46
2.2.3.3 Open Cracks – Mixed Mode 46
2.2.3.4 Closed Cracks 47
2.2.4 LEFM Summary 48
3.0 LABORATORY PROGRAM 49
3.1 LABORATORY TEST PROGRAM OVERVIEW 50
3.2 SHEAR MODELS 52
3.2.1 Clay on Clay Test Results 53
3.2.2 Clayey Sand on Clay Test Results 56
3.2.3 Evaluation of Findings 59
3.3 SIMULATED VERTICAL SLOPE MODEL 60
3.3.1 Simulated Vertical Slope Test Results 61
3.3.2 Evaluation of Findings 64
4.0 FINITE ELEMENT METHODS 65
4.1 REVIEW OF FINITE ELEMENT THEORY 65
4.1.1 Stress-Strain Relationships 71
4.1.2 Numerical Integration 73
4.1.3 Incremental Analyses for Geotechnical Applications 76
4.1.4 Mesh Optimization 77
4.2 FINITE ELEMENT METHOD APPLIED TO GEOTECHNICAL FRACTURE MECHANICS PROBLEMS 83

4.3 SUMMARY FOR GEOTECHNICAL FRACTURE MECHANICS APPLICATIONS 85

5.0 EVALUATION OF LABORATORY PROGRAM RESULTS USING FINITE ELEMENT METHOD AND FRACTURE MECHANICS APPROACHES 86

5.1 DEVELOPMENT OF THE LABORATORY PROGRAM FINITE ELEMENT METHOD MODELS 86

5.1.1 Values of Parameters used for the FEM Analyses 88

5.1.2 FEM Slip Elements 90

5.1.3 Failure Plane Development and / or Crack Propagation 91

5.1.4 Coalesce of Micro-Cracks 92

5.2 SHEAR MODEL 94

5.2.1 Clay on Clay Shear Model Results 96

5.2.2 Clayey Sand on Clay Shear Model Results 108

5.3 HOMOGENEOUS VERTICAL SLOPE MODEL 121

5.3.1 Vertical Slope Model Results 123

5.4 SUMMARY OF FINDINGS 133

6.0 EVALAUTION OF THEORETICAL $\phi = 0°$ SLOPES USING FINITE ELEMENT METHODS 136

6.1 INTRODUCTION OF FINITE ELEMENT MODELS 136

6.1.1 Initial FEM Analyses 138

6.1.2 Evaluation of FEM Stress Conditions 142

6.2 CLAY SLOPE ON CLAY BASE 145

6.2.1 Sequence of Crack Propagation due to Lateral Stress Relief 147

6.3 CLAY SLOPE ON CLAY BASE WITH OPEN TOE CRACK 153

6.3.1 FEM Modeling of an Open Toe Crack 154

6.3.2 FEM Analyses for Slope with an Open Toe Crack 156

6.4 CLAY SLOPE ON SAND BASE 162

6.4.1 FEM Analyses for Clay Slope on Sand Base 162
6.5 SUMMARY OF FEM 168
7.0 MODIFICATION OF LIMIT EQUILIBRIUM STABILITY ANALYSES 170
7.1 VERTICAL SLOPES 170
7.2 INCLINED SLOPES 176
8.0 EVALUATION OF CASE HISTORIES USING FINITE ELEMENT METHODS 183
8.1 OXFORD CLAY SLOPE 183
8.1.1 Site Characterization 184
8.1.2 Finite Element Model 189
8.1.2.1 Finite Element Slip Element. 193
8.1.3 Finite Element Model Results 195
8.2 CONEMAUGH SLOPE 208
8.2.1 Geologic Conditions 208
8.2.2 Conemaugh Slope Geometry 210
8.2.3 Project Instrumentation 210
8.2.4 Site Characterization for Finite Element Analyses 217
8.2.4.1 Residual Soil. 217
8.2.4.2 Bedrock 218
8.2.5 Finite Element Model 223
8.2.6 Evaluation of Model Results 226
8.3 SUMMARY 235
9.0 CONCLUSIONS 237
APPENDIX A DERIVATION OF STABILITY NUMBER 240
APPENDIX B FINITE ELEMENT MESH OPTIMIZATION 244
APPENDIX C CLAYEY SAND ON CLAY SHEAR MODEL MOHR-COULOMB GRAPHS 248

APPENDIX D FEM MODELS FOR EVALUATION OF $\phi = 0°$ SLOPES 255

APPENDIX E FEM MODELS FOR EVALUATION OF $\phi = 0°$ VERTICAL SLOPES WITH AN OPEN TOE CRACK 290

APPENDIX F FEM MODELS FOR EVALUATION OF $\phi = 0°$ VERTICAL SLOPES ON A SAND BASE 298

BIBLIOGRAPHY 305

LIST OF TABLES

Table 1.1 Failures in Excavated Natural Slopes Involving Theoretically Stable Slopes for $\phi = 0°$ Analysis Conditions 4

Table 2.1 Typical Toughness (K_{IC}) Values 30

Table 2.2 Theoretical Angle of Crack Propagation 48

Table 3.1 PSDSA Test Results for Clay on Clay 55

Table 3.2 PSDSA Test Results for Clayey Sand on Clay 58

Table 3.3 PSDSA Test Results for Simulated Vertical Slope 63

Table 4.1 Node Points and Weightings for Four Node Quadrilateral 74

Table 5.1 Elastic – Plastic Constitutive Model Parameters 87

Table 5.2 Geotechnical Parameters and Values Used for the Laboratory FEM Models 89

Table 6.1 Geotechnical Parameters and Values Used for the FEM Models 137

Table 6.2 FEM Model Critical Slope Height Parameters 139

Table 6.3 Summary of Finite Element Results for Clay Slope on Clay Base 146

Table 6.4 Depth of Initial Tension Crack for Vertical Clay Slope on Clay Base without and with an Open Toe Crack 161

Table 7.1 FEM Results for Clay Slope on Clay Base due to Initial LSR 173

Table 7.2 Revised Critical Height Values for a Vertical Slope 175

Table 7.3 Toe Crack Height, Distance from Crest to Toe Crack, and Depth of Tension Crack Normalized to Total Slope Height 179

Table 7.4 Revised Critical Height Values for ¼H:1V Slope 182

Table 8.1 Geotechnical Parameters and Values Used for the Oxford Slope FEM Model .. 192

Table 8.2 Geotechnical Parameters and Values for the Conemaugh Slope FEM Model ... 218

Table 8.3 Claystone Geotechnical Parameters and Values for the Conemaugh Slope FEM Model ... 221

Table 8.4 Sandstone Geotechnical Parameters and Values for the Sandstone Slope FEM Model ... 222

LIST OF FIGURES

Figure 1.1 $\phi = 0°$ Strength Envelope 2

Figure 1.2 Vertical Slope with Plane Failure Surface 6

Figure 1.3 Vertical Slope with Circular Failure Surface 10

Figure 1.4 Vertical Slope with Plane Failure Surface and Tension Crack 16

Figure 1.5 Inclined Slope with Circular Failure Surface 19

Figure 1.6 Stability Factor vs Slope Angle for Toe Circles and $\phi = 0°$ Slopes 21

Figure 1.7 Clay Slope Failure 25

Figure 2.1 Three Modes of Crack Development 32

Figure 2.2 Typical Crack Mode Conditions for a Slope 33

Figure 2.3 LEFM Reference Model 34

Figure 2.4 $K_I \sin(\theta) + K_{II}(3\cos(\theta) - 1)$ vs. θ for Various Values of K_I and K_{II} 40

Figure 2.5 Tensile Stress Open Crack Propagation under Mixed Mode Loading Conditions 41

Figure 2.6 Mohr-Coulomb Shear Strength Graph for a Typical Geotechnical Material 45

Figure 2.7 Open Crack Propagation from Shear Stress Loading under Mixed Mode Conditions 47

Figure 3.1 Laboratory Loading Conditions Reference Model 49

Figure 3.2 Plane Stress Direct Shear Apparatus 51

Figure 3.3 PSDSA Test for Clay on Clay 54

Figure 3.4 Shear Stress vs Shear Displacement for Clay on Clay 55

Figure 3.5 PSDSA Test for Clayey Sand on Clay 57

Figure 3.6 Shear Stress vs Shear Displacement for Clayey Sand on Clay 58

Figure 3.7 Mode II Loading Condition 59

Figure 3.8 Simulated Vertical Slope Model 60

Figure 3.9 Simulated Vertical Cut Slope 62

Figure 3.10 Stress vs Shear Displacement for Simulated Vertical Clay Slope 63

Figure 4.1 Standard two dimensional elements 66

Figure 4.2 Typical Four Node, Two Dimensional Element 68

Figure 4.3 Gauss Numerical Integration over a Typical Rectangular Element 75

Figure 4.4 FEM Model used for Mesh Concentration Study 79

Figure 4.5 Comparison of Vertical Stress for Different FEM Element Concentrations, x = 20-m from Slope Face (Left) 81

Figure 4.6 Comparison of Vertical Stress for Different FEM Element Concentrations, x = 20-m from Slope Face (Right) 82

Figure 4.7 LEFM Reference Model 84

Figure 5.1 Typical Slip Surface Element 90

Figure 5.2 Mohr-Coulomb Failure Criterion Envelope for a $\phi = 0°$ Material 92

Figure 5.3 Successive Development of a Shear Zone 93

Figure 5.4 Clay on Clay FEM Shear Model 94

Figure 5.5 FEM Boundary Conditions 95

Figure 5.6 Shear Stress Contours (4 kPa) Indicating Shear Failure Zones for Clay on Clay FEM Shear Model with $\nu = 0.10$ and No Cohesion Reduction along Crack 98

Figure 5.7 Shear Stress Contours (4 kPa) Indicating Shear Failure Zones for Clay on Clay FEM Shear Model with $\nu = 0.10$ and 25% Cohesion Reduction along Crack 99

Figure 5.8 Shear Stress Contours (4 kPa) Indicating Shear Failure Zones for Clay on Clay FEM Shear Model with $\nu = 0.10$ and 50% Cohesion Reduction along Crack ... 100

Figure 5.9 Shear Stress Contours (4 kPa) Indicating Shear Failure Zones for Clay on Clay FEM Shear Model with $\nu = 0.45$ and No Cohesion Reduction along Crack 101

Figure 5.10 Shear Stress Contours (4 kPa) Indicating Shear Failure Zones for Clay on Clay FEM Shear Model with $\nu = 0.45$ and 25% Cohesion Reduction along Crack ... 102

Figure 5.11 Shear Stress Contours (4 kPa) Indicating Shear Failure Zones for Clay on Clay FEM Shear Model with $\nu = 0.45$ and 50% Cohesion Reduction along Crack ... 103

Figure 5.12 Shear Stress for Clay with $\nu = 0.10$ and Cohesive Strength Reduction along Slip Element ... 105

Figure 5.13 Shear Stress for Clay with $\nu = 0.45$ and Variable Cohesive Strength Reduction along Slip Element ... 107

Figure 5.14 Clayey Sand on Clay FEM Shear Model ... 108

Figure 5.15 Clayey Sand on Clay FEM Shear Model Analyses with $\nu = 0.10$, No Pre-Existing Crack and Shear Stress Contours (4 kPa) Indicating Shear Failure Zones for the Clay ... 111

Figure 5.16 Clayey Sand on Clay FEM Shear Model Analyses with $\nu = 0.10$, Pre-Existing Crack with a 25% Cohesive Strength Reduction, and Shear Stress Contours (4 kPa) Indicating Shear Failure Zones Clay ... 112

Figure 5.17 Clayey Sand on Clay FEM Shear Model Analyses with $\nu = 0.10$, Pre-Existing Crack with a 50% Cohesive Strength Reduction, and Shear Stress Contours (4 kPa) Indicating Shear Failure Zones for the Clay ... 113

Figure 5.18 Clayey Sand on Clay FEM Shear Model Analyses with $\nu = 0.45$, No Pre-Existing Crack and Shear Stress Contours (4 kPa) Indicating Shear Failure Zones for the Clay ... 114

Figure 5.19 Clayey Sand on Clay FEM Shear Model Analyses with $\nu = 0.45$, Pre-Existing Crack with a 25% Cohesive Strength Reduction, and Shear Stress Contours (4 kPa) Indicating Shear Failure Zones for the Clay ... 115

Figure 5.20 Clayey Sand on Clay FEM Shear Model Analyses with $\nu = 0.45$, Pre-Existing Crack with a 50% Cohesive Strength Reduction, and Shear Stress Contours (4 kPa) Indicating Shear Failure Zones for the Clay ... 116

Figure 5.21 FEM Shear and Normal Stresses for the Clayey Sand Layer Obtained Directly Above the Clayey Sand-Clay Interface with $\nu = 0.10$ for the Clay with No Slip Element Strength Reduction. ... 118

Figure 5.22 FEM Shear and Normal Stresses for the Clayey Sand Layer Obtained Directly Above the Clayey Sand-Clay Interface with $\nu = 0.45$ for the Clay with No Slip Element Strength Reduction. ... 120

Figure 5.23 FEM Vertical Slope Model ... 122

Figure 5.24 Homogeneous Vertical Slope FEM Model Boundary Conditions 123

Figure 5.25 Vertical Slope FEM Model Analyses with ν = 0.10, No Pre-Existing Toe Crack and Negative X-Stress Contours (10-kPa) Indicating Tension Zones 125

Figure 5.26 Vertical Slope FEM Model Analyses with ν = 0.10, Pre-Existing Toe Crack with a 25% Cohesive Strength Reduction, and Negative X-Stress Contours (10-kPa) Indicating Tension Zones 126

Figure 5.27 Vertical Slope FEM Model Analyses with ν = 0.10, Pre-Existing Toe Crack with a 50% Cohesive Strength Reduction, and Negative X-Stress Contours (10-kPa) Indicating Tension Zones 127

Figure 5.28 Vertical Slope FEM Model Analyses with ν = 0.45, No Pre-Existing Toe Crack and Negative X-Stress Contours (10-kPa) Indicating Tension Zones 128

Figure 5.29 Vertical Slope FEM Model Analyses with ν = 0.45, Pre-Existing Toe Crack with a 25% Cohesive Strength Reduction, and Negative X-Stress Contours (10-kPa) Indicating Tension Zones 129

Figure 5.30 Vertical Slope FEM Model Analyses with ν = 0.45, Pre-Existing Toe Crack with a 50% Cohesive Strength Reduction, and Negative X-Stress Contours (10-kPa) Indicating Tension Zones 130

Figure 5.31 Shear Stress along a Horizontal Plane from the Tip of the Slip Element for ν = 0.10 and a 25% Cohesive Strength Reduction along the Slip Element. 132

Figure 6.1 Typical FEM Model Used to Establish Initial Stress Conditions for a Clay Slope on Clay Base 139

Figure 6.2 Horizontal Movement of the Slope Face from LSR Neglecting Shear Zones 140

Figure 6.3 Impact of k_o from Lateral Stress Relief on a Vertical Slope without Consideration for Shear Zones 141

Figure 6.4 Total Stress for a Theoretical Element with k_o = 3.0 143

Figure 6.5 Progressive Failure Propagation for a Vertical Slope with k_o = 3.0 148

Figure 6.6 Progressive Horizontal Movement along a Vertical Slope Face Predicted by FEM 150

Figure 6.7 Progressive Horizontal Movement along a ¼H:1V Slope Face Predicted by FEM 151

Figure 6.8 Progressive Horizontal Movement along a ½H:1V Slope Face Predicted by FEM 152

Figure 6.9 PennDOT Design Detail to Minimize Continued Development of a Toe Crack 153

Figure 6.10 Typical FEM Model developed for a Vertical Excavation with *Crack* = 0.25 ... 155

Figure 6.11 Initial Horizontal Movement due to LSR along a Vertical Slope Face with an Open Toe Crack and Neglecting the Development of Shear Zones 157

Figure 6.12 Variation of the Lateral Earth Pressure Coefficient for a Vertical Slope subjected to LSR with an Initial k_o = 1.0 158

Figure 6.13 Variation of the Lateral Earth Pressure Coefficient for a Vertical Slope subjected to LSR with an Initial k_o = 2.0 159

Figure 6.14 Variation of the Lateral Earth Pressure Coefficient for a Vertical Slope subjected to LSR with an Initial k_o = 3.0 160

Figure 6.15 Typical FEM Model Used to Establish Initial Stress Conditions for a Clay Slope on Sand Base. 163

Figure 6.16 Horizontal Slope Face Movement from LSR Neglecting Shear Zones 163

Figure 6.17 Comparison of Horizontal Slope Face Movement due to LSR between Vertical Clay Slopes on Sand and Clay Bases Neglecting Shear Zones 165

Figure 6.18 Variation of Lateral Earth Pressure along Top of Slope from LSR for a Vertical Clay Slope on Sand Base 166

Figure 6.19 Differential Horizontal Movement due to LSR along the Interface between the Upper Clay and Lower Sand 167

Figure 6.20 Failure Planes Created by Lateral Stress Relief 169

Figure 7.1 Vertical Slope with Plane Failure Surface, Tension and Toe Crack 171

Figure 7.2 N_s as a Function of k_o 174

Figure 7.3 Inclined Slope with Plane Failure Surface and Tension Crack 176

Figure 7.4 Variation of Lateral Earth Pressure due to LSR along the Top of Slope 180

Figure 7.5 N_s as a Function of k_o for Inclined Slopes 181

Figure 8.1 Variation of Undrained Shear Strength with Depth for the Oxford Clay 187

Figure 8.2 Variation of Modulus of Elasticity with Depth for the Oxford Clay 188

Figure 8.3 Oxford Clay Slope FEM Model 190

Figure 8.4 FEM In-Situ Horizontal and Vertical Earth Pressures Prior to Excavation..... 193
Figure 8.5 FEM Stage 1 Analysis – Mesh Deformation after Removal of Callow 196
Figure 8.6 FEM Stage 2 Analysis – Mesh Deformation after First Cut..... 196
Figure 8.7 FEM Stage 3 Analysis – Mesh Deformation after Second Cut 197
Figure 8.8 FEM Stage 4 Analysis – Mesh Deformation after Third Cut 197
Figure 8.9 FEM Stage 5 Analysis – Mesh Deformation after Fourth Cut 198
Figure 8.10 Individual Slope Face Movements After Each Cut 198
Figure 8.11 Differential Movement between LOC and Kellaways Sand..... 200
Figure 8.12 Lateral Earth Pressure in Backslope Region after each Successive Cut..... 201
Figure 8.13 Vertical Movement Along Top of MOC Cut After Each Cut 203
Figure 8.14 Variation of Lateral Earth Pressure at Mid-Height of MOC 204
Figure 8.15 Variation of Lateral Earth Pressure at Mid-Height of LOC 205
Figure 8.16 Shear Stress Contours (200 kPa) at the 3rd Excavation Stage..... 207
Figure 8.17 Shear Stress Contours (200 kPa) at the 4th Excavation Stage..... 207
Figure 8.18 Aerial View of Conemaugh Slope During Construction 209
Figure 8.19 Cross Section View of Conemaugh Slope Prior to Slope Failure 211
Figure 8.20 As-Built Conemaugh Slope Cross Section 211
Figure 8.21 Inclinometer Locations along Conemaugh Slope 212
Figure 8.22 Inclinometer Plot for I-2 214
Figure 8.23 Conemaugh Slope Time Rate of Movement at El. 289.5± 215
Figure 8.24 Conemaugh Clay Slope Failure 216
Figure 8.25 Non-Linear Mohr Envelope for Claystone 221
Figure 8.26 Non-Linear Mohr Envelope for Sandstone..... 222
Figure 8.27 Initial FEM Model Indicating Construction Stage Conditions 223
Figure 8.28 Initial Vertical Stress Contours (100 kPa) Prior to Excavation 225

Figure 8.29 FEM Initial Horizontal and Vertical Earth Pressures Along the Inclinometer Prior to Excavation 225

Figure 8.30 Shear Stress Contours (50-kPa) for Stage 1 Excavation with No Pre-Existing Crack 227

Figure 8.31 Shear Stress Contours (50-kPa) for Stage 2 Excavation with No Pre-Existing Crack 227

Figure 8.32 Shear Stress Contours (50-kPa) for Stage 3 Excavation with No Pre-Existing Crack 228

Figure 8.33 Shear Stresses Near Clay – Claystone Interface 229

Figure 8.34 FEM Slope Face Movements at Each Excavation Stage 230

Figure 8.35 FEM Slope Face Movements at Excavation Stage 3 230

Figure 8.36 Lateral Earth Pressure at Base of 1st Stage along a Horizontal Plane from Slope Face to Inclinometer 232

Figure 8.37 Lateral Earth Pressure at Base of 2nd Stage along a Horizontal Plane from Slope Face to Inclinometer 233

Figure 8.38 Lateral Earth Pressure at Base of 3rd Stage along a Horizontal Plane from Slope Face to Inclinometer 234

PREFACE

This work would not have been possible if not for the help and support of my family, and especially my wife, Teresa Kutschke. She has made many sacrifices without complaint so that I could complete this work. Her support and encouragement has helped me more than she will ever know. I have spent many hours away from her and my four children, Mary, Michael, Peter and Laura, completing this work. I thank them for their understanding when I could not always be there; this work is dedicated to you.

I also wish to thank my advisor, Professor Luis Vallejo, for his wisdom and patience. I enjoyed our Thursday meetings and discussions. I also extend my gratitude to the members of my doctoral committee: Assistant Professor Julie M. Vandenbossche, PE; Associate Professor Anthony Iannacchione, PE, PG; Associate Professor Jeen-Shang Lin, PE; and Associate Professor Patrick Smolinski. I thank all of them for their efforts and support.

1.0 INTRODUCTION

Excavation into a stiff cohesive material will result in outward movement of the new slope face due to lateral stress relief. Expansion of the slope face can create a discontinuity at the toe of the slope as well as a tension crack at the surface of the backslope. However, conventional limit equilibrium methods of slope stability analysis only consider the equilibrium of a soil mass tending to move down slope under the influence of gravity without regard for the in-situ stress conditions or the development of shear zones that occur from lateral stress relief. There is very little known about how these two discontinuities form as well as how they interact to produce the final failure of the slope. Research presented herein provides insight into the propagation of these shear zones that lead to the progressive failure of clay slopes due to lateral stress relief.

1.1 SLOPE STABILITY ANALYSES OF $\phi = 0°$ SLOPES

Terzaghi (1950) indicated that the cause of landslides can be divided into external and internal failure modes. External failure modes are those that produce an increase in shear stress under unaltered shear resistance of the slope material. Examples of external failure modes include steepening or heightening of a slope by excavation. Internal failure modes are those that produce slope failure without any change in surface conditions. These failures are caused by a reduction in the shearing resistance of the slope material.

Skempton and Sowa (1963) indicated that the undrained strength of saturated clay is independent of the changes in total stress acting on clay, provided that the water content remained constant and that there were no micro-structural alterations caused by the stress changes. Under these conditions, the clay would behave as a $\phi = 0°$ material with respect to changes in total stress (Skempton and Sowa, 1963). Undrained shear strength is mobilized when failure occurs before any significant dissipation of shear induced pore water pressure; that is, the undrained shear strength of saturated clay is not affected by changes in confining pressure as long as the water content does not change (Terzaghi, Peck and Mesri, 1996).

Analyses performed for this research consider purely cohesive slopes and utilize the undrained shear strength (c_u) of the soil analyzed in terms of total stress. Under this situation, c_u is equal to the cohesive value of the Mohr-Coulomb envelope, which is a horizontal line as noted on Figure 1.1. These conditions are prevalent immediately after unloading of saturated clay with very low permeability and represents an end-of-construction condition design check (EM 1110-2-1913).

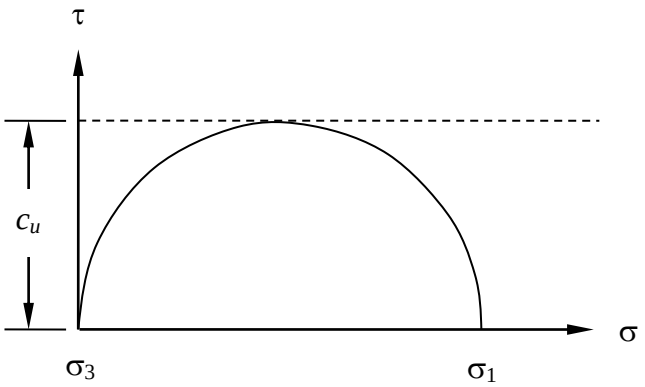

Figure 1.1. $\phi = 0°$ Strength Envelope.

Duncan (1996) notes that the $\phi = 0°$ condition is applicable to impermeable soils under multi-stage loading conditions, which includes rapid drawdown, stage construction, and any other condition where a period of consolidation under one set of loads is followed by a change in load under undrained conditions. Terzaghi (1943), and Terzaghi and Peck (1967) note that combinations of shearing rates and drainage boundary conditions that could lead to undrained failure are theoretically possible in any soil, including soft to stiff clays and silts as well as fissured clays and shales. Terzaghi and Peck (1967) also note that the $\phi = 0°$ condition is also applicable to lightly overconsolidated clays. For example, undrained failure could be induced in stiff clay from a deep and rapid excavation (Terzaghi, Peck, and Mesri, 1996).

Slope stability analysis using limit equilibrium methods and mass procedures have been developed based on the $\phi = 0°$ condition (Culmann, 1866; Fellenius, 1927; Taylor, 1937; Terzaghi, 1943; Gibson and Morgenstern, 1962; Janbu, 1968; and Hunter and Schuster, 1968). Design codes developed for the professional engineering community often require $\phi = 0°$ analysis as part of design requirements for civil infrastructure projects (AASHTO, 2007; AREMA, 2007; EM 1110-2-1913; USDA Technical Release 60). However, as noted in Table 1.1, the literature contains examples of external failure modes in which the $\phi = 0°$ analysis theoretically applied and predicted a stable excavation, yet failure occurred during or immediately after construction.

Table 1.1. Failures in Excavated Natural Slopes Involving Theoretically Stable Slopes for $\phi = 0°$ Analysis Conditions.

Slide	Height of Slope (m)	Time from End of Construction to Failure	Reference
Bradwell Slip	14.8	5 days	Skempton and LaRochelle (1965)
South Saskatchewan River Dam Canal	12.2 to18.3	During Construction	Peterson, et al (1957)
Wothorpe - B	6.1	During Construction	Chandler (1972, 1974)
New Cross	23	3 years	Skempton (1977)
Isle of Sheppey – A	12	6 years	James (1970)
Isle of Sheppey – B	10	8 years	James (1970)
Oxford Slope	25	During Construction	Burland, et al (1977)
Conemaugh Slope	16.1	8 months	Kutschke, et al (2007)

It should be noted that drained shear strength parameters utilizing effective stress for stability analyses generally represent a long term condition. These analyses consider that the maximum resistance to shear in the soil is a function the difference between the total normal stress and the pore pressure. The propagation of shear zones due to lateral stress relief utilizing effective stress analyses requires a separate analysis since shear strength is dependent on normal stress and this analysis is left for others.

1.2 LIMIT EQUILIBRIUM SLOPE STABILITY ANALYSES

Limit equilibrium stability analyses either consider a *mass* or *method of slices* procedure to determine the factor of safety. As the name implies, the mass procedure considers the mass of soil above the surface of sliding to act as a unit. This analysis is useful when the slope is a homogeneous soil mass. Conversely, the method of slices procedure divides the mass of soil

above the surface of sliding into a number of vertical parallel slices and the stability of each slice is calculated. This analysis is useful when the slope is non-homogeneous and pore water pressures are considered.

The mass procedure is applicable to total stress analyses and they represent the classical closed form solutions in slope stability analyses. Research presented herein has an emphasis on vertical slopes, although inclined slopes are considered for completeness. The following sections present the derivation of these classical equations. As is readily evident, these classical solutions do not consider lateral stress relief.

1.2.1 Vertical Slope with Plane Failure Surface

Culmann (1866), a German structural engineer, was a pioneer of graphical methods in engineering. Although much of his life was dedicated to railroad bridges, Culmann (1866) developed perhaps the first slope stability solution to determine the critical depth that an excavation into a cohesive deposit may stand without lateral support utilizing mass procedure concepts. The analysis is based on the assumption that slope failure occurs along a plane when the average shearing stress tending to cause failure is greater than the shear strength of the soil. Consider a cohesive slope of unit thickness with a vertical height (H), slope face angle (β), and a trial failure plane defined by $\overline{ac}$, as shown on Figure 1.2.

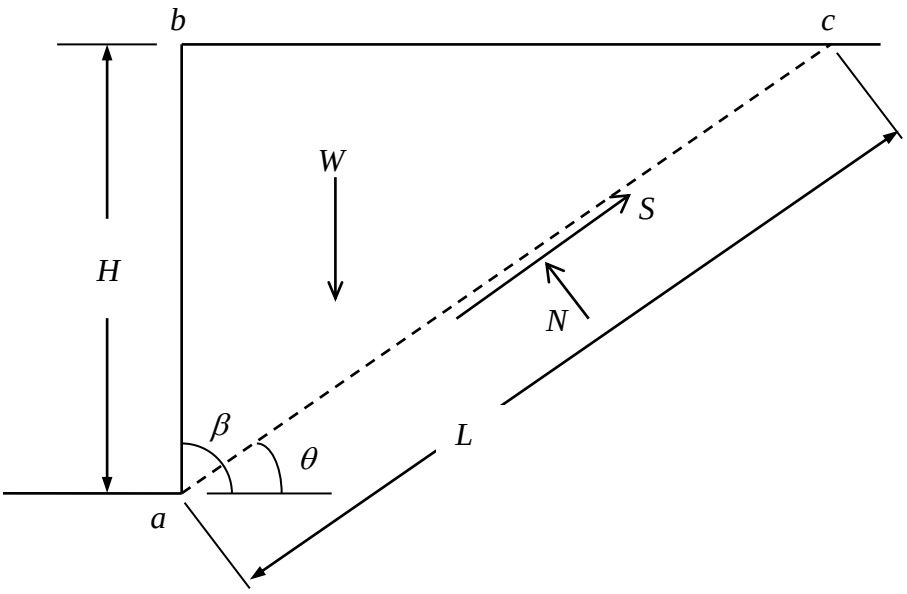

Figure 1.2. Vertical Slope with Plane Failure Surface.

The length of the failure surface (L) is defined as:

$$L = \frac{H}{\sin\theta} \tag{1-1}$$

where θ is the angle of the failure plane with respect to the horizontal. The mass of the soil above the failure plane (W) is defined by the soil unit weight (γ) multiplied by the wedge area $\overline{abc}$, and is expressed as:

$$W = 0.5\gamma H\left[\sin(\beta-\theta)\right]L \tag{1-2}$$

Substituting Equation 1-1 into Equation 1-2 and reducing the expression results in the following:

$$W = 0.5\gamma H\left[\sin(\beta-\theta)\right]\frac{H}{\sin\theta} \tag{1-3}$$

$$W = 0.5\gamma H^2 \frac{\sin(\beta - \theta)}{\sin\theta} \quad \text{1-4}$$

Equation 1-4 presents the mathematical expression of the mass of soil above a failure plane defined by variables H, β, θ, and γ.

The normal force (N) and the shear force (S) acting along the failure plane $\overline{ac}$ is expressed as:

$$N = W\cos\theta \quad \text{1-5}$$

$$S = W\sin\theta \quad \text{1-6}$$

The Mohr-Coulomb failure criterion states that:

$$\tau = c + \sigma_n \tan\phi \quad \text{1-7}$$

where τ = shear stress, c = cohesion, and σ_n = normal stress. Substituting Equations 1-5 and 1-6 into the Mohr-Coulomb failure criterion and expressing in terms of force per unit width results in:

$$W\sin\theta = cL + W\cos\theta\tan\phi \quad \text{1-8}$$

Simplifying Equation 1-8 to account for a total stress analysis with ϕ = 0°, results in the following:

$$W\sin\theta = cL \quad \text{1-9}$$

Next, substitute Equation 1-9 into Equation 1-4 and simplify:

$$\left[0.5\gamma H^2 \frac{\sin(\beta-\theta)}{\sin\theta}\right]\sin\theta = c\left(\frac{H}{\sin\theta}\right) \quad \text{1-10}$$

$$c = 0.5\gamma H \sin(\beta-\theta)\sin\theta \quad \text{1-11}$$

The angle of the critical failure plane (θ_f) is obtained by differentiating Equation 1-11 with respect to θ, and recognizing that the terms γ, H and c are constants, results in:

$$\frac{d}{d\theta}\left[\sin(\beta-\theta)\sin\theta\right] = 0 \quad \text{1-12}$$

$$-\cos(\beta-\theta)\sin\theta + \sin(\beta-\theta)\cos\theta = 0 \quad \text{1-13}$$

$$\cos(\beta-\theta)\sin\theta = \sin(\beta-\theta)\cos\theta \quad \text{1-14}$$

$$\frac{\sin\theta}{\cos\theta} = \frac{\sin(\beta-\theta)}{\cos(\beta-\theta)} \quad \text{1-15}$$

$$\tan\theta = \tan(\beta-\theta) \quad \text{1-16}$$

$$\theta_f = \frac{\beta}{2} \quad \text{1-17}$$

Let β = 90° and set $c_f = \frac{c}{FOS}$ where the factor of safety (FOS) = 1.0 to represent the average mobilized cohesive strength at failure. Next substitute Equation 1-17 into Equation 1-11:

$$c_f = 0.5\gamma H \sin(\beta-\theta)\sin\theta \quad \text{1-18}$$

$$c_f = 0.5\gamma H \sin\left(\beta - \frac{\beta}{2}\right)\sin\frac{\beta}{2} \quad \text{1-19}$$

$$c_f = 0.5\gamma H \sin 45^\circ \sin 45^\circ \quad \text{1-20}$$

$$c_f = 0.5\gamma H(0.5) \quad \text{1-21}$$

$$H_{Critical} = \frac{4c_f}{\gamma} \quad \text{1-22}$$

Equation 1-22 represents the classical solution for the critical height ($H_{Critical}$) of a vertical slope considering a $\phi = 0°$ analysis and a plane failure surface.

After extensive investigation of slope failures in the 1920's, a Swedish geotechnical commission recommended that the actual surface of sliding may be better approximated by a circular slip surface. Two pioneers in slope stability analyses that developed the first stability theories using circular failure surfaces were Fellenius (1927, 1936) and Taylor (1937). Fellenius (1927) developed his procedure based on method of slices, commonly referred to as the Ordinary Method of Slices, and was carried out by graphical trial procedure. Conversely, Taylor (1937) based his analysis on a mass procedure, commonly referred to as the friction-circle method. Taylor (1948) notes that these two methods show close agreement, however, the mathematical solution developed by Taylor (1937) is more precise and thorough.

1.2.2 Vertical Slope with Circular Failure Surface

Taylor (1937) published some of the first stability charts using a mass procedure known as the friction-circle method. His analysis considered moment equilibrium and a circular failure surface, unlike Culmann's Method which considered force equilibrium and a plane failure surface. However, the same assumption is still applicable, that being that slope failure occurs when the average shearing stress tending to cause failure is greater than the shear strength of the soil. It should also be noted that for a vertical slope where c_u is constant with depth, the critical failure surface will be a toe circle with the slip surface passing through the toe of slope, as shown on Figure 1.3 (Fellenius, 1927; Taylor, 1937, 1948; Terzaghi, 1943; Terzaghi and Peck, 1967).

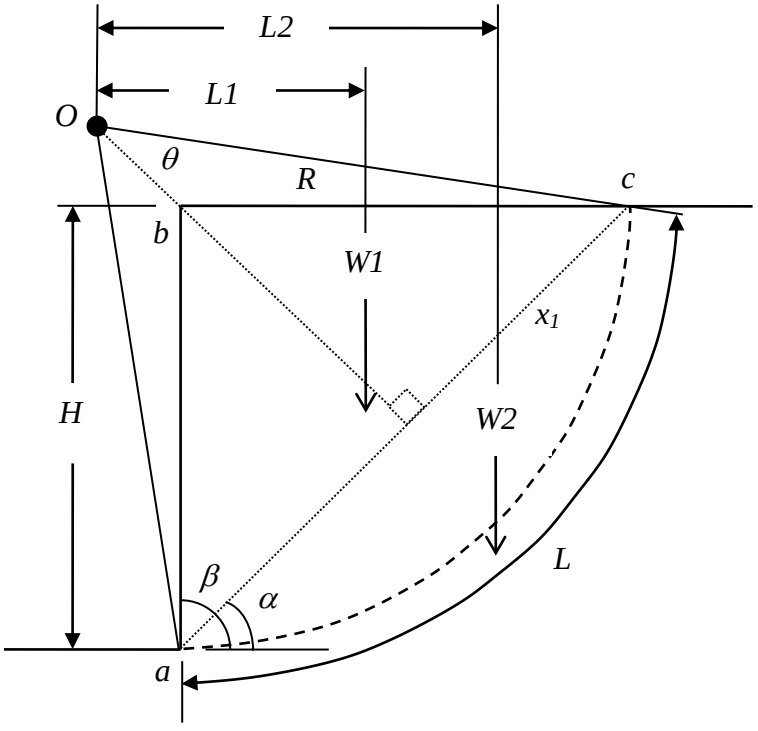

Figure 1.3. Vertical Slope with Circular Failure Surface.

The following derivation has been modified from Taylor's (1937) original work to account for a $\phi = 0°$ analysis. Consider a cohesive slope of unit thickness with a vertical height (H), slope face angle (β), and a trial failure plane defined by $\overline{ac}$, as shown on Figure 1.3. Moment equilibrium requires calculating driving and resisting moments. We shall first consider the resisting moment ($M_{RESISTING}$) about Point O by developing an expression for the radius (R) in terms of α, θ, and H:

$$\sin\theta = \frac{x_1}{R} \tag{1-23}$$

$$\sin\alpha = \frac{H}{2x_1} \tag{1-24}$$

Rearranging in terms of x_1 and combining Equation 1-23 and 1-24 results in:

$$R = \frac{H}{2\sin\theta\sin\alpha} \tag{1-25}$$

Next, solve for the length of the failure surface (L) in terms of α, θ, and H:

$$L = 2\theta R = 2\theta\left(\frac{\pi}{180}\right)R \tag{1-26}$$

and substitute Equation 1-25 into Equation 1-26.

$$L = \theta\left(\frac{\pi}{180}\right)\frac{H}{\sin\theta\sin\alpha} \tag{1-27}$$

The resisting moment is the cohesive strength multiplied by Equation 1-25 and Equation 1-27, which results in the following expression:

$$M_{RESISTING} = c(L)R = c\left[\frac{\theta\left(\frac{\pi}{180}\right)H}{\sin\theta\sin\alpha}\right]\frac{H}{2\sin\theta\sin\alpha} \qquad 1\text{-}28$$

Equation 1-28 can be simplified to:

$$M_{RESISTING} = \frac{c\left(\pi/180\right)H^2}{2\sin^2\theta\sin^2\alpha} \qquad 1\text{-}29$$

The next step is to calculate the driving moments. This will be accomplished in two parts; the first part is the wedge area created by $\overline{abc}$, and the second part by the circular segment area created by arc $\overline{ac}$. First, consider the wedge created by $\overline{abc}$ and solve for the soil mass (*W1*) in terms of *H* and α.

$$W1 = (\gamma_{sat})\left[\frac{1}{2}(H_C)\left(\frac{H}{\tan\alpha}\right)\right] = \frac{\gamma_{sat}H^2}{2\tan\alpha} \qquad 1\text{-}30$$

Next, solve for the moment arm *L1* in terms of θ, α, and *H*.

$$L1 = R\cos(90+\theta-\alpha) + \frac{1}{3}\left(\frac{H}{\tan\alpha}\right) \qquad 1\text{-}31$$

Substitute Equation 1-25 into Equation 1-21 to obtain:

$$L1 = \frac{H}{2\sin\theta\sin\alpha}\cos(90+\theta-\alpha) + \frac{1}{3}\left(\frac{H}{\tan\alpha}\right) \qquad 1\text{-}32$$

The driving moment ($M_{DRIVING\text{-}\Delta abc}$) created by wedge $\overline{abc}$ is (W1) x (L1), or:

$$M_{DRIVING-\Delta abc} = \left(\frac{\gamma_{sat} H^2}{2\tan\alpha}\right)\left[\frac{H}{2\sin\theta\sin\alpha}\cos(90+\theta-\alpha)+\frac{1}{3}\left(\frac{H}{\tan\alpha}\right)\right] \qquad 1\text{-}33$$

which simplifies to:

$$M_{DRIVING-\Delta abc} = (\gamma H^3)\left(\frac{\cos(90+\theta-\alpha)}{4\sin\theta\sin\alpha\tan\alpha}+\frac{1}{6\tan^2\alpha}\right) \qquad 1\text{-}34$$

Next, consider the area of the circular segment defined by arc $\overline{ac}$. Using the common mathematical formula for the area of a circular segment, which is $\frac{R^2}{2}\left[2\theta\left(\frac{\pi}{180}\right)-\sin 2\theta\right]$, the mass of *W2* is readily calculated as:

$$W2 = \gamma\left\{\frac{R^2}{2}\left[2\theta\left(\frac{\pi}{180}\right)-\sin 2\theta\right]\right\} \qquad 1\text{-}35$$

Next, consider the centroid of a circle segment, which is commonly defined as $\frac{4R\sin^3\theta}{3(2\theta-\sin 2\theta)}$.

The moment arm *L2* is readily calculated as:

$$L2 = \frac{4R\sin^3\theta}{3(2\theta-\sin 2\theta)}\sin\alpha \qquad 1\text{-}36$$

The driving moment ($M_{DRIVING\text{-arc abc}}$) created by arc $\overline{ac}$ is (W2) x (L2), or:

$$M_{DRIVING(arc-abc)} = \frac{\gamma R^2}{2}\left[2\theta\left(\frac{\pi}{180}\right)-\sin 2\theta\right]\left[\frac{4R\sin^3\theta}{3(2\theta-\sin 2\theta)}\sin\alpha\right] \qquad 1\text{-}37$$

$$M_{DRIVING(arc-abc)} = \frac{2}{3}\gamma R^3\left(\sin\alpha \sin^3\theta\right) \tag{1-38}$$

$$M_{DRIVING(arc-abc)} = \frac{2}{3}\gamma\left(\frac{H}{2\sin\theta\sin\alpha}\right)^3\left(\sin\alpha \sin^3\theta\right) \tag{1-39}$$

$$M_{DRIVING(arc-abc)} = \frac{1}{12}\gamma\left(H\right)^3\left(\frac{1}{\sin^2\alpha}\right) \tag{1-40}$$

The last step is to establish limit equilibrium by setting the resisting moments equal to the driving moments, which results in the following expression:

$$\frac{cH^2}{2\sin^2\theta\sin^2\alpha} = \gamma H^3\left[\frac{\cos(90+\theta-\alpha)}{4\sin\theta\sin\alpha\tan\alpha} + \frac{1}{6\tan^2\alpha}\right] + \frac{1}{12}\gamma H^3\left(\frac{1}{\sin^2\alpha}\right) \tag{1-41}$$

Solving for H:

$$H = \frac{c}{\gamma}\left[\frac{\left(\frac{\theta\left(\pi/180\right)}{2\sin^2\theta\sin^2\alpha}\right)}{\left(\frac{\cos(90+\theta-\alpha)}{4\sin\theta\sin\alpha\tan\alpha} + \frac{1}{6\tan^2\alpha} + \frac{1}{12\sin^2\alpha}\right)}\right] \tag{1-42}$$

Equation 1-42 may be represented by:

$$H = \left(\frac{c}{\gamma}\right) f(\alpha,\theta) \tag{1-43}$$

The critical height is determined by differentiating Equation 1-43 with respect to θ and α as follows:

$$\frac{d}{d\alpha} f(\alpha,\theta) = 0 \text{ and } \frac{d}{d\theta} f(\alpha,\theta) = 0 \qquad 1\text{-}44$$

Differentiating Equation 1-44 results in two rather cumbersome expressions and their solution is presented in Appendix A. In summary, the solution to Equation 1-44 resulted in $\alpha = 47.6°$ and $\theta = 15.1°$ (Taylor, 1937). Substituting these values into Equation 1-42, resulted in the following (Taylor, 1937):

$$H_{Critical} = 3.83\frac{c}{\gamma} \qquad 1\text{-}45$$

Equation 1-45 represents the critical height of a vertical slope considering a circular failure surface. Recall that Equation 1-22 presented the critical height considering a plane failure. The difference between these two equations is less than 5% and Terzaghi (1943) notes that these estimates are accurate enough that the curvature of the sliding surface through a vertical bank can be disregarded.

Taylor (1948) recognized the possibility of cracking at the top of the slope introduces uncertainty in stability analyses. The presence of water and / or ice in the zone of cracking further exacerbates the situation. Taylor (1937, 1948) notes that the scarcity of knowledge in this area could, at the present time, only be overcome by the use of a generous factor of safety or a reduced value of the average cohesion.

1.2.3 Vertical Slope with Plane Failure Surface and Tension Cracking

Karl Terzaghi spent his early professional life in search of a rational approach to earthwork engineering problems. His efforts were rewarded with the publication of his famous book on soil mechanics in 1925 (Terzaghi, 1925) and he has since been recognized as the Father of Soil Mechanics. Of his many accomplishments, Terzaghi (1943) developed an expression which addressed the influence of tension cracks on the stability of vertical slopes and assumed a plane failure surface. Terzaghi (1943) utilized force limit equilibrium and the assumption that slope failure occurred when the average shearing stress tending to cause failure was greater than the shear strength of the soil. Consider a cohesive slope of unit thickness with a vertical height (H), slope face angle (β), tension crack depth (z), and a trial failure plane defined by $\overline{ad}$, as shown on Figure 1.4.

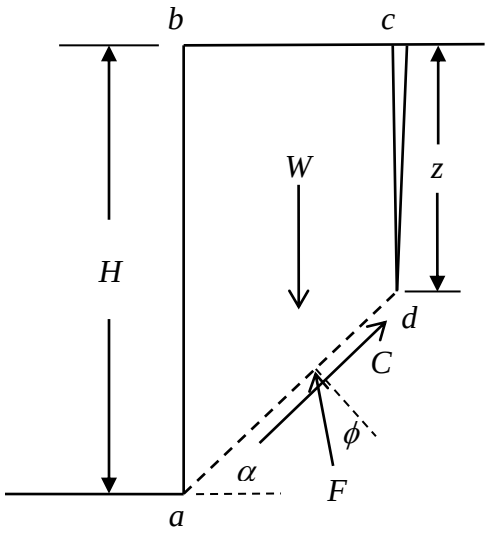

Figure 1.4. Vertical Slope with Plane Failure Surface and Tension Crack.

The mass of soil (W) defined by block $\overline{abcd}$ is expressed as:

$$W = \frac{\gamma\left(H^2 - z^2\right)}{2\tan\alpha} \tag{1-46}$$

and the sliding resistance (C) is given by:

$$C = \frac{c_f}{\sin\alpha}\left(H - z\right) \tag{1-47}$$

At limit equilibrium, the sum of the forces on the sliding plane must equal 0. Therefore, combining Equation 1-46 and Equation 1-47 results in:

$$\frac{\gamma\left(H^2 - z^2\right)}{2\tan\alpha}\sin\alpha - \frac{c}{\sin\alpha}\left(H - z\right) = 0 \tag{1-48}$$

Manipulating Equation 1-48 produces:

$$\left(H^2 - z^2\right)\sin 2\alpha - \frac{4c_f}{\gamma}\left(H - z\right) = 0 \tag{1-49}$$

The angle of the critical failure plane ($\alpha_{CRITICAL}$) is obtained by differentiating Equation 1-49 with respect to α, which is as follows:

$$\frac{d}{d\alpha}\left[\left(H^2 - z^2\right)\sin 2\alpha - \frac{4c_f}{\gamma}\left(H - z\right)\right] = 0 \tag{1-50}$$

$$\left(H^2 - z^2\right)\left(2\cos 2\alpha_{CRITICAL}\right) = 0 \tag{1-51}$$

$$\cos 2\alpha_{CRITICAL} = 0 \tag{1-52}$$

The solution to Equation 1-52 results in $\alpha_{CRITICAL} = 45°$.

Based on laboratory testing using gelatin samples, Terzaghi (1943) made the assumption that $z = H/2$ and substituting this value into Equation 1-49, along with letting $H = H_{CRITICAL}$, $\alpha_{CRITICAL} = 45°$, and $c = c_f$, the critical height for a vertical excavation considering a plane failure surface and tension crack is represented by (Terzaghi, 1943):

$$H_{CRITICAL} = \frac{2.67 c_f}{\gamma} \qquad 1\text{-}53$$

Equation 1-53 is a 33% reduction in slope height when compared to Equation 1-22. This underscores the significance that the tension zone can have on slope stability. However, Terzaghi's (1943) assumption was based on limited gelatin tests and did not consider the influence of lateral stress relief. Additionally and to date, literature review has not encountered any research that would validate $z = H/2$.

1.2.4 Inclined Slopes with Circular Failure Surface

When a slope failure occurs in such a way that the sliding surface intersects the toe of slope, the failure circle is referred to as a toe circle. If the slope angle is greater than 53°, the critical circle is always a toe circle (Fellenius, 1927, 1936; Taylor, 1937, 1948; Terzaghi, 1943; Terzaghi and Peck, 1967). Moreover, Terzaghi and Peck (1967) note that if $\theta \geq 53°$, the entire sliding surface is located above the level of the toe and the danger of a base failure does not exist.

Terzaghi and Peck (1967) note that mass procedures using moment equilibrium and a circular failure surface are applicable for total stress analyses. The undrained strength is not dependent on normal stress and a very simple, but theoretically accurate method for analysis of

circular slip surface can be employed (Terzaghi, 1943). Consider a cohesive slope of unit thickness with a vertical height (H), slope face angle (β), tension crack depth (z), and a trial failure plane defined by $\overline{ad}$, as shown on Figure 1.5. Moment equilibrium requires calculating driving and resisting moments. The driving moment per unit width about O ($M_{O(Driving)}$) tending to cause slope instability is:

$$M_{O(Driving)} = W \times L \qquad 1\text{-}54$$

where W = the mass of the soil above the failure surface and L = moment arm.

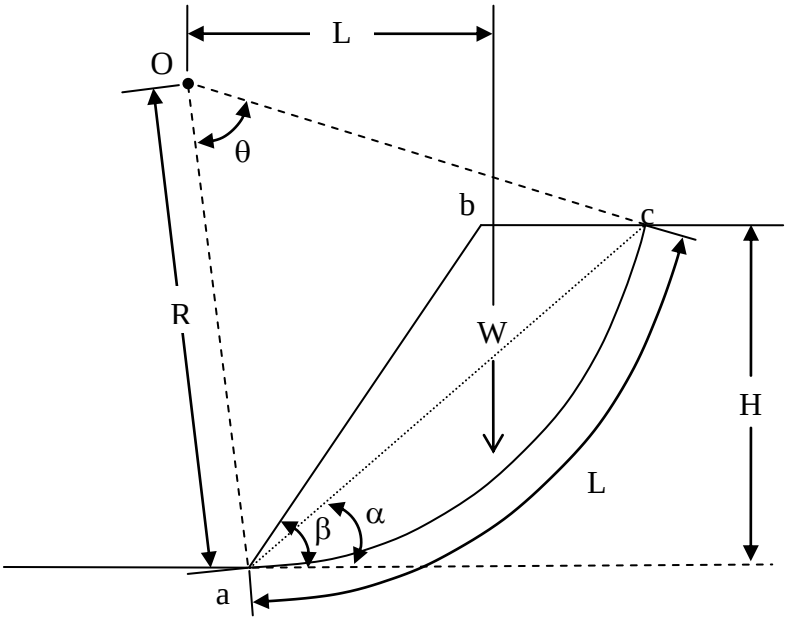

Figure 1.5. Inclined Slope with Circular Failure Surface.

The resistance to sliding is derived from the average cohesion acting along the failure surface. The resisting moment ($M_{O(Resisting)}$) per unit width is expressed as:

$$M_{O(Resisting)} = c_u\,(AC)(1)(R) = c_u\,R\,\theta \qquad 1\text{-}55$$

At limit equilibrium, $M_{O(Driving)} = M_{O(Resisting)}$, or combining Equation 1-54 and Equation 1-55 results in the following:

$$W L = c_u R \theta \tag{1-56}$$

As demonstrated under Section 1.2.2, the variables W, L, and R can be expressed in terms of H, θ, α. As such, Equation 1-56 can be rearranged to the following expression (Terzaghi, 1943):

$$c_u = \gamma H \left[\frac{1}{f(\alpha, \beta, \theta)} \right] \tag{1-57}$$

The slope failure occurs along a toe circle for which c_u is a maximum. Since the angle of the slope (β) is constant, the position of the critical slip surface is determined by the following expressions (Terzaghi, 1943):

$$\frac{d}{d\alpha} c_u = 0 \text{ and } \frac{d}{d\theta} c_u = 0 \tag{1-58}$$

The solution to these equations will result in critical values of α and θ that are substituted into Equation 1-57 to determine the cohesion required to prevent a critical toe circle for a slope with an angle of β. Terzaghi (1943) expressed Equation 1-57 using the stability factor, N_s, which is as follows:

$$H_c = \left(\frac{c_u}{\gamma} \right) N_s \tag{1-59}$$

where $N_s = f(\alpha, \beta, \theta)$. Terzaghi (1943) developed values of N_s for various slope angles, which has been redrawn as Figure 1.6. The stability factor varies linearly from 3.85 at β = 90° to 5.52

at $\beta = 53°$. For completeness, Figure 1.6 also presents N_s values for $\beta < 53°$ considering toe failures.

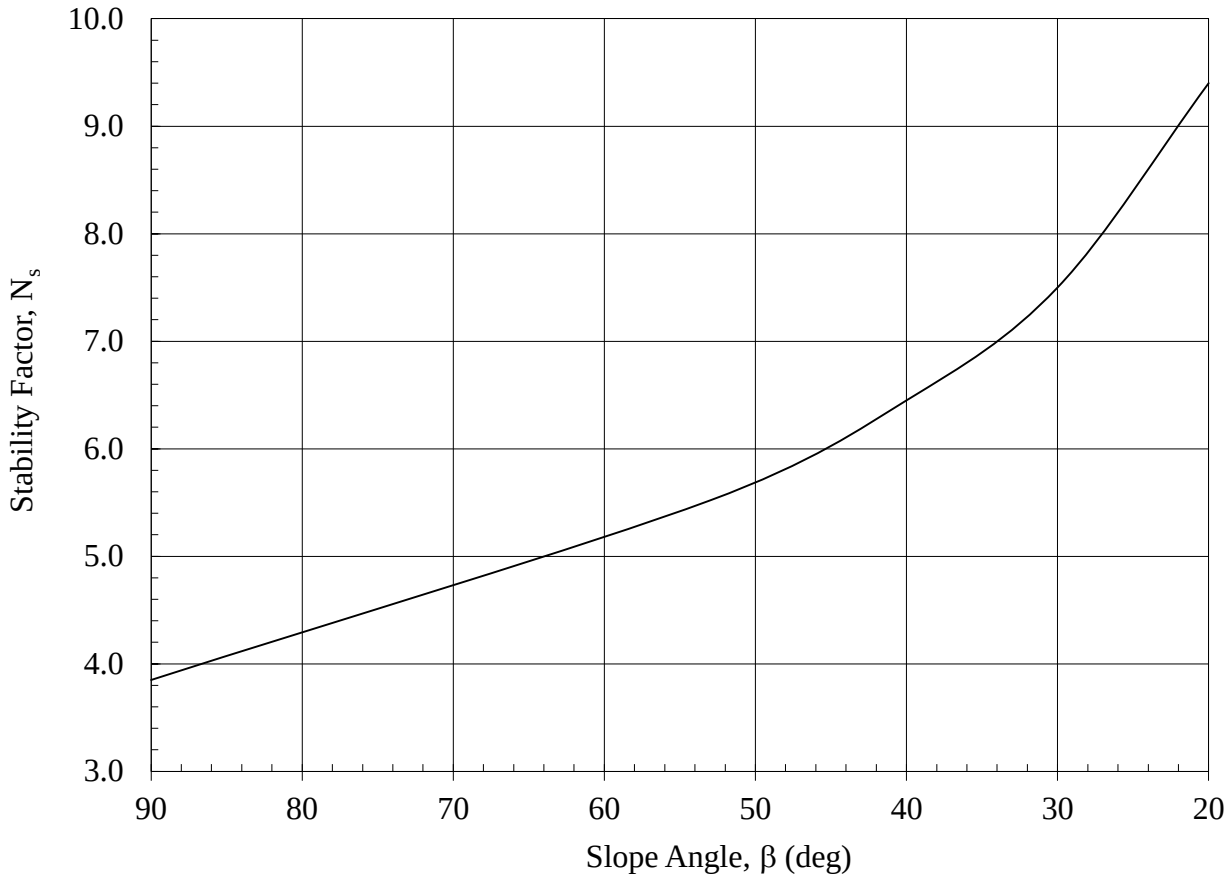

Figure 1.6. Stability Factor vs Slope Angle for Toe Circles and $\phi = 0°$ Slopes.

1.3 CLAY SLOPE FAILURES THAT WILL BE USED FOR THIS STUDY

Research presented herein considered two case histories that involved clay slope failures related to lateral stress relief. The first case history involved a 29 meter deep excavation in Oxford Clay in which a horizontal shear band developed at the base of the excavation and tension cracks were observed in the backslope region. The second case history involved a 30 meter deep excavation in Conemaugh Clay in which an inclined shear band developed at the toe of slope and extended into the backslope region resulting in a catastrophic slope failure.

1.3.1 Oxford Clay Slope

Burland, Longworth, and Moore (1977) studied a 25-m deep excavation that occurred in stiff Oxford Clay. Their work was part of a long-term research study that was carried out from 1969 to 1971 at the London Brick Company's Saxon pit near Petersborough, England. The Oxford Clay was excavated with a slope face of 72°, or approximately 1/3H:1V (horizontal:vertical). The main purpose of their study was to measure the magnitude and extent of ground movement and to examine the relative influence of material properties and geological factors on deformation behavior. The measurements performed by Burland, et al (1977) provide direct field evidence that lateral stress relief occurred during excavation and generated a progressive shear band at the base of the excavation.

Instrumentation was installed both at the surface and at depth to measure movement of the ground surrounding the excavation. Instrumentation consisted of piezometers, precise surveying, photogrammetry, horizontal extensometers, inclinometers, and vertical extensometers. Burland, et al (1977) indicated that the measurements all indicated a mechanism of behavior in which the

ground within a region of about 1 to 1.5 times the depth away from the face appeared to move as a block, sliding on a horizontal shear band formed by bedding planes near the base of the excavation. The magnitude and rate of the horizontal movement of the surface points was dependent on their relative position to the face, the distance the face advanced in a given cut, and the time period between cuts. Measurable movements extended back from the top of the face for a distance of about 2.5 times the depth of the excavation. Burland, et al (1977) indicated that at distances greater than 30-m the vertical movements were approximately the same as the horizontal movements, whereas closer to the face the horizontal movement dominated.

Site characterization indicated a relatively constant unit weight with depth of 19.9 kN/m^3 and a complicated shear strength profile in which c_u increased with depth from 50 to 1200 kN/m^2. Using Equation 1-59, an assessment of the theoretical stability is as follows:

$$H_c = \left(\frac{c_u}{\gamma}\right) N_s = \left(\frac{c_u}{19.9}\right)(4.66)$$

The slope was 25-m high excavation, therefore:

$$25 = \left(\frac{c_u}{19.9}\right)(4.66)$$

and c_u = 106 kN/m^2. The shear strength profile of the slope was such that only the extreme upper reaches exhibited a c_u < 106 kN/m^2 while the vast majority exhibited a c_u > 106 kN/m^2. As is readily evident, Equation 1-59 does not consider the impact of lateral stress relief which can have a significant impact on slope stability.

1.3.2 Conemaugh Clay Slope

The author was personally involved with this project and details are presented in Kutschke, et al (2007). This cut slope was part of a larger project that involved creating a new 8.7 km rail bed alignment at acceptable grades through the relatively mountainous terrain of southwestern Pennsylvania. One aspect of the project design required the use of inclinometers to monitor slope movement and observation wells to monitor groundwater elevations for this 29 meter deep excavation. The inclinometers all indicated the development of slope movements occurring at distinct zones during construction of the slope. Because these movements stabilized following the completion of the excavation, they have been attributed to lateral stress relief coupled with vibrations from blasting operations. However, approximately eight months after excavation, a slide involving approximately 6,200 m^3 occurred. The slide occurred in front of and down slope of the inclinometers (i.e., I-2 and I-3) noted in Figure 1.7. The main scarp and flank daylighted in front of the inclinometer casing and not pass through the casing. As such, the inclinometer did not notice any pre-slide movement as the failure plane extended from the toe of slope and daylighted in the backslope region. The height of the slope from toe to scarp was 16.1-m. The author firmly believes that lateral stress relief contributed to this slope failure.

Figure 1.7. Clay Slope Failure.

Site characterization indicated a relatively constant unit weight with depth of 20.4 kN/m^3 and a c_u 86.1 kN/m^2. The slope was excavated at approximately 45° (1H:1V) with a 26.6° (2H:1V) backslope. Recognizing Equation 1-59 is for a level backslope condition, it is conservative to consider a full height slope of 45° as follows:

$$H_c = \left(\frac{c_u}{\gamma}\right) N_s = \left(\frac{86.1}{20.4}\right)(6.1) = 25.7$$

Equation 1-59 indicates that the theoretical critical slope height should be at least 25.7-m. However, the slope failure occurred with a critical slope height of 16.1-m, much less than theoretical. As is readily evident, Equation 1-59 does not consider the impact of lateral stress relief which can have a significant impact on slope stability.

1.4 RESEARCH OBJECTIVES

Unsupported excavation into a clay stratum can result in lateral stress relief that would produce an outward movement of the slope face. The outward movement can result in a toe crack and a tension zone in the backslope. Classical solutions regarding stability of a clay slope do not address the toe crack as well as its interaction with the tension zone that can result in slope failure. This research will analyze stiff clay and shale cut-slopes using laboratory, finite element, and fracture mechanics approaches to understand the formation and propagation of discontinuities that result in eventual slope failure. In particular, the objectives of this study are as follows:

- The mechanics of formation and propagation of cracks developed during the excavation of vertical and inclined slopes in a stiff $\phi = 0$ soil will be analyzed. These cracks develop at the toe of slope. The formation of these cracks will be analyzed using Finite Element Methods. The direction of propagation of these cracks will be analyzed using Fracture Mechanics theory. The theoretical analyses will be substantiated using: (a) laboratory tests on slopes with similar geometry and loads as slopes in the field, and (b) the failure modes experienced by two clay slopes in the field (Conemaugh Clay Slope in Pennsylvania and Oxford Clay Slope in England).

- For the direction of crack propagation under Mixed-Mode type of loading, the maximum tangential stress and the maximum shear stress criteria will be used. The first criterion assumes that cracks propagate in a direction normal to the maximum gravity induced tensile stress in the intact material surrounding the tip of the cracks. The maximum shear strength criterion assumes the crack propagates in the direction of its own plane.

- Numerical methods permit solutions to many challenging geotechnical problems. In this study, finite element method models of the field and laboratory models of the slopes will be used to understand not only how cracks form in the slopes due to lateral stress relief, but also to understand how these cracks propagate.

As outlined above, this research will utilize laboratory, fracture mechanics, and finite element method approaches to understand the impact that lateral stress relief has on slope stability of stiff purely cohesive clay slopes. Classical solutions regarding stability of a clay slope do not address the toe crack as well as its interaction with the tension zone that can result in slope failure. The ultimate objective of this research is to develop a solution regarding the stability of slopes with vertical and inclined slope faces that develop cracks as a result of a lateral stress relief.

2.0 FRACTURE MECHANICS

Fracture mechanics is the field of study concerned with the propagation of cracks in materials. The purpose of fracture mechanics is to analyze the stability of existing cracks; how the crack originated in the material is another matter. Griffith (1921), an English aeronautical engineer, is credited with being the first one to develop the field of fracture mechanics. His work focused on explaining the failure of brittle materials that occurred during World War I. Griffith (1921) quantitatively related the flaw size to the fracture stress using the First Law of Thermodynamics to formulate a fracture theory based on a simple energy balance. He theorized that brittle fracture happened as a result of a struggle between strain energy release and surface energy required to create new fracture surfaces. Griffith (1921) predicted that for a given crack length there is a unique critical stress above which a crack grows and below which a crack remains in equilibrium.

The work of Griffith (1921) was largely ignored until Irwin (1957) took it up during World War II at the U.S. Naval Research Laboratory. Irwin (1956) developed the energy release rate concept, which was related to the Griffith (1921) theory, but was in a more useful form for solving engineering problems. Shortly thereafter, several of Irwin's colleagues brought to his attention a paper by Westergaard (1939) in which Westergaard developed a technique for analyzing stresses and displacements ahead of a sharp crack (Anderson, 1995). Irwin (1957) found that the stress field around a micro-crack in a linear elastic material could be uniquely

defined by a stress intensity factor, K, which was related to the energy release rate. As such, Irwin (1957) developed a modified form of Griffith's approach in which K replaced strain energy release rate, and the material property fracture toughness (K_{IC}) replaced surface energy. When the stresses near the crack tip exceed the material fracture toughness, the crack will grow and this condition is expressed as (Irwin, 1957):

$$K \geq K_{IC} \qquad 2\text{-}1$$

All analyses that base K as the similitude parameter are generally referred to as Linear Elastic Fracture Mechanics (Broek, 1986); this parameter will be discussed further in subsequent sections.

2.1 FRACTURE MECHANICS THEORIES

The field of fracture mechanics can be divided into linear elastic fracture mechanics (LEFM) and elastic-plastic fracture mechanics (EPFM). LEFM requires that plastic straining in the crack tip region is limited and is applicable to linear-elastic material (Hellen, 2001). The stress field near the crack tip is calculated using the theory of elasticity. LEFM is valid only when the inelastic deformation is small compared to the size of the crack, often termed small-scale yielding. If large zones of plastic deformation develop before the crack grows, then Elastic Plastic Fracture Mechanics (EPFM) must be used. EPFM conditions exist for a crack region which contains a considerable amount of plastic straining and the material behaves in a ductile manner (Hellen, 2001). EPFM is applicable with high toughness materials and has considerable influence in the aerospace, shipbuilding, and off-shore oil industry (Broek, 1989; SSC-345, 1990). Table 2.1

presents typical toughness (K_{IC}) values for ready reference and comparison purposes (Barsom and Rolfe, 1987; and Wang, et al, 2007).

Table 2.1. Typical Toughness (K_{IC}) Values.

Material	K_{IC} $MPa\text{-}m^{1/2}$
Aluminum Alloy	17 - 44
High-Strength Steel	50 - 154
Titanium Alloy	77 - 116
Shale	0.6
Silty Clay	0.04

2.1.1 LEFM Applied to Stiff Clay

The introduction of fracture mechanics to geotechnical engineering applications is generally created to Bishop (1967), Bjerrum (1967), and Skempton and Hutchinson (1969), where they considered fracture mechanics concepts to help explain progressive failure of stiff clay deposits. Since then, fracture mechanics has been applied to geotechnical engineering applications mostly involving theoretical applications and limited small scale laboratory testing (Aliabadi, 1999; Chudnovsky, et al, 1988; Covarrubias, 1969; Fang, et al, 1989; Lee, et al, 1988; Morris, et al, 1992; Palmer and Rice, 1973; Saada, et al, 1985; Rice, 1968; Rudnicki and Rice, 1975; and Vallejo, 1985, 1987, 1988, 1989, 1994).

The proper application of LEFM principles to geotechnical applications requires an understanding of stress-strain behavior of the material; that is LEFM is applicable to brittle materials such as those involving stiff clays and rocks (Aliabadi, 1999; Chudnovsky, et al, 1988; Covarrubias, 1969; Fang, et al, 1989; Lee, et al, 1988; Morris, et al, 1992; Saada, et al, 1985;

Vallejo, 1985, 1987, 1988, 1989, 1994). Bishop, et al (1975), Marsland (1972), and Wang, et al (2007) indicated that stiff clays exhibit a stress-strain relationship that very closely approximates that of a linear elastic material, and therefore LEFM principles apply (Irwin, 1957).

Duncan and Chang (1970) indicated that the stress-strain behavior of any type of soil depends on a number of factors such as density, water content, structure, drainage conditions, strain conditions, stress history, and shear stress conditions. With regard to water content, Vallejo (1988) noted that this parameter was significant in determining whether clay behaves as a brittle or ductile material. Vallejo (1988) reported that kaolinite clay samples with moisture contents greater than 20% by weight behaved and failed like a ductile material whereas samples with moisture content less than 20% behaved and failed like a brittle material. Wang, et al (2007) also noted that there is an optimum moisture content for K_{IC}, which for his study resulted in a substantial reduction to K_{IC} for water contents greater than 18%. This result is in general conformance with the findings of Vallejo (1988).

In summary, LEFM is applicable to stiff brittle clays (Aliabadi, 1999; Chudnovsky, et al, 1988; Lee, et al, 1988; Saada, et al, 1985; Vallejo, 1985, 1987, 1988, 1989, 1994; and Wang, et al., 2007).

2.2 LINEAR ELASTIC FRACTURE MECHANICS

LEFM concepts may be applied to materials which exhibit inelastic deformations around the crack tip, provided that such deformations are confined to the immediate vicinity of the tip (Xie, 1993). However, when the zone is small compared to the overall structure such as a crack in a

slope, the actual evolution of stresses will still be governed by LEFM (Aliabadi, 1999). LEFM is based on the assumption that crack propagation can be studied thorough the superposition of three independent load applications, as shown in Figure 2.1 (Irwin, 1957):

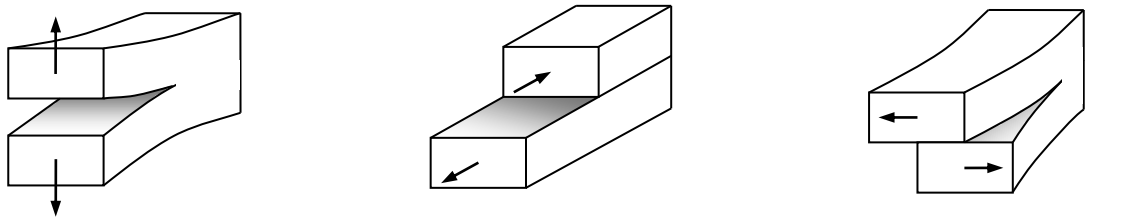

Mode I - Tensile Crack Mode II - Shear Crack Mode III - Tearing Crack

Figure 2.1. Three Modes of Crack Development.

The concept of LEFM may be applied to those materials which obey Hooke's law so that stress is proportional to strain. Figure 2.2 displays typical cases of cracks in an earth slope subjected to Mode I and Mode II conditions (Aliabadi, 1999).

Ingraffea and Heuze (1980) summarized the three theories for mixed-mode fracture initiation, namely: the maximum tensile stress theory, the minimum strain energy density theory, and the maximum energy release rate theory. Cursory details regarding these three theories are as follows:

- Maximum tensile stress theory (Erdogan and Sih, 1963) – This theory is dependent on the circumferential tensile stress near the crack tip. Fracture initiates from the crack tip in a direction normal to the maximum tensile stress.

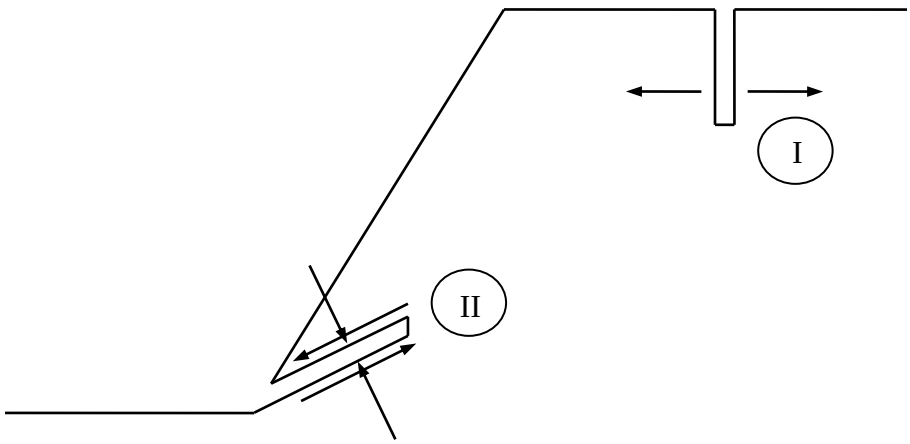

Figure 2.2. Typical Crack Mode Conditions for a Slope.

- Minimum strain energy density theory (Sih, 1974) – This theory considers that fracture initiation is dependent on the near tip strain energy density. Fracture propagation will occur in the direction of the minimum strain energy density function. The critical intensity of this potential field governs the onset of crack propagation.

- Maximum energy release rate theory (Hussain, et al, 1974) – This theory differs in a number of ways from the first two theories since it does not depend on a measurement of a near-tip field variable but rather on a global energy change. Fracture initiates from the crack tip in the direction in which the energy release rate is maximized and the crack propagates if the maximized energy release rate equals its critical intensity.

This research utilized the maximum tangential stress criterion developed by Erdogan and Sih (1963). This theory requires knowledge of stress conditions near the crack tip (obtainable through numerical modeling) and is particularly well suited for geotechnical applications since soil has limited tensile resistance. According to this criteria, and referring to Figure 2.3, the tangential stress

(σ_θ), the radial stress (σ_r), and the shear stress ($\tau_{r\theta}$) in the material located in the vicinity of a crack subjected to a mixed mode type of loading can be obtained from the following relationships (Broek, 1986; and Chao and Liu, 1997):

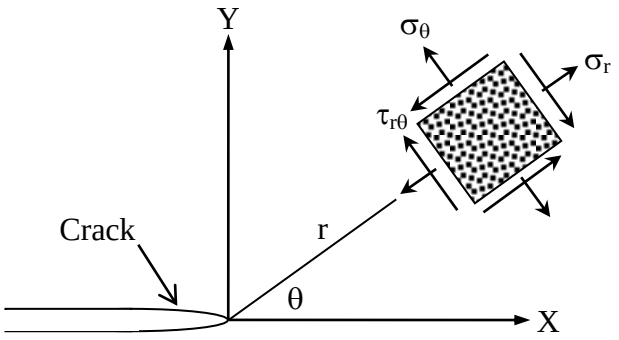

Figure 2.3. LEFM Reference Model.

$$\sigma_\theta = \frac{1}{\sqrt{2\pi r}} \cos\frac{\theta}{2}\left(K_I \cos^2\frac{\theta}{2} - \frac{3}{2} K_{II} \sin\theta \right) \qquad 2\text{-}2$$

$$\sigma_r = \frac{1}{\sqrt{2\pi r}} \cos\frac{\theta}{2}\left[K_I\left(1+\sin^2\frac{\theta}{2}\right) + \frac{3}{2} K_{II} \sin\theta - 2K_{II} \tan\frac{\theta}{2} \right] \qquad 2\text{-}3$$

$$\tau_{r\theta} = \frac{1}{2\sqrt{2\pi r}} \cos\frac{\theta}{2}\left[K_I \sin\theta + K_{II}\left(3\cos\theta - 1\right) \right] \qquad 2\text{-}4$$

where r is the radius between the tip of the crack and a point in the clay surrounding the crack where the stresses are being measured, θ is the angle that the radius makes with the axis of the crack, and K_I and K_{II} are the stress intensity factors for Mode I and Mode II type of loading.

2.2.1 Stress Intensity Factor

A fundamental concept of LEFM is that the stress field ahead of a crack can be characterized in terms of a single parameter known as the stress intensity factor, *K*. This parameter is related to both the nominal stress level (σ) applied to the element and the size of an existing open crack (c). In all cases, the general forms of the stress-intensity factors are given by Equation 2-5 and Equation 2-6 (Barsom and Rolfe, 1987; Broek, 1989; Anderson, 1995; and Liu and Mahadevan, 2006):

$$K_I = (\sigma)\sqrt{(c)}\, f(g) \tag{2-5}$$

$$K_{II} = (\tau)\sqrt{(c)}\, f(g) \tag{2-6}$$

where $f(g)$ is a function dependent on geometry and crack characteristics. Several closed-form solutions of stress intensity factors for loading with simple configurations have been derived and are readily available in the literature (Sih, 1973; Broek, 1989; Boresi, et al, 1993; Anderson, 1995; Liu and Mahadevan, 2006). As an example, Equation 2-7 presents the solution for K_I for a single edge crack in an infinite sheet and is applicable to Mode I loading conditions (Boresi, et al, 1993).

$$K_I = 1.12(\sigma)\sqrt{\pi(c)} \tag{2-7}$$

One of the significant aspects of the stress intensity factor is that it relates the local stress field ahead of a crack to the nominal stress applied to the element away from the crack (Barsom and Rolfe, 1987).

2.2.2 Tangential Stress

Erdogan and Sih (1963) hypothesized that crack propagation in a brittle material will occur in a radial direction from the tip and propagate in a direction in which σ_θ reaches its maximum value. The direction of crack propagation is normal to the direction of maximum σ_θ, and is found by:

$$\frac{d\sigma_\theta}{d\theta} = 0 \text{ and } \frac{d^2\sigma_\theta}{d\theta^2} < 0 \text{ at } \theta = \alpha \qquad 2\text{-}8$$

where α is the value reached by θ when crack propagation occurs. Differentiating Equation 2-2 results in the following expression:

$$\frac{d\sigma_\theta}{d\theta} = -\sin\left(\frac{\theta}{2}\right)\left[\frac{K_I \cos^2\left(\frac{\theta}{2}\right) - \frac{3}{2}K_{II}\sin\theta}{2}\right] - \cos\left(\frac{\theta}{2}\right)\left[\frac{3}{2}K_{II}\cos\theta + K_I\cos\left(\frac{\theta}{2}\right)\sin\left(\frac{\theta}{2}\right)\right] = 0 \qquad 2\text{-}9$$

Rearranging and simplifying Equation 2-9 results in the following:

$$\frac{-K_I\sin\left(\frac{\theta}{2}\right)\cos^2\left(\frac{\theta}{2}\right)}{2} + \frac{3K_{II}\sin\theta\sin\left(\frac{\theta}{2}\right)}{4} - \frac{3}{2}K_{II}\cos\theta\cos\left(\frac{\theta}{2}\right) - K_I\cos^2\left(\frac{\theta}{2}\right)\sin\left(\frac{\theta}{2}\right) = 0 \qquad 2\text{-}10$$

$$-\frac{3}{2}K_I\sin\left(\frac{\theta}{2}\right)\cos^2\left(\frac{\theta}{2}\right) + \frac{3}{4}K_{II}\sin\theta\sin\left(\frac{\theta}{2}\right) - \frac{3}{2}K_{II}\cos\theta\cos\left(\frac{\theta}{2}\right) = 0 \qquad 2\text{-}11$$

Equation 2-11 may be further simplified by applying the two-angle cosine trigonometric identity, $\cos(\theta \pm \phi) = \cos\theta\cos\phi \mp \sin\theta\sin\phi$, and letting $\theta = \theta$ and $\phi = \theta/2$. This results in the following:

$$-\frac{3}{2}K_I \sin\left(\frac{\theta}{2}\right)\cos^2\left(\frac{\theta}{2}\right)+\frac{3}{4}K_{II}\left[\cos\left(\frac{\theta}{2}\right)-\cos\theta\cos\left(\frac{\theta}{2}\right)\right]-\frac{3}{2}K_{II}\cos\theta\cos\left(\frac{\theta}{2}\right)=0 \qquad 2\text{-}12$$

Continued mathematical manipulation of Equation 2-12 resulted in the following expressions:

$$-\frac{3}{2}K_I \sin\left(\frac{\theta}{2}\right)\cos^2\left(\frac{\theta}{2}\right)+\frac{3}{4}K_{II}\cos\left(\frac{\theta}{2}\right)-\frac{3}{4}K_{II}\cos\theta\cos\left(\frac{\theta}{2}\right)-\frac{6}{4}K_{II}\cos\theta\cos\left(\frac{\theta}{2}\right)=0 \qquad 2\text{-}13$$

$$-\frac{3}{2}K_I \sin\left(\frac{\theta}{2}\right)\cos^2\left(\frac{\theta}{2}\right)+\frac{3}{4}K_{II}\cos\left(\frac{\theta}{2}\right)-\frac{9}{4}K_{II}\cos\theta\cos\left(\frac{\theta}{2}\right)=0 \qquad 2\text{-}14$$

$$-\frac{3}{2}K_I \sin\left(\frac{\theta}{2}\right)\cos\left(\frac{\theta}{2}\right)+\frac{3}{4}K_{II}-\frac{9}{4}K_{II}\cos\theta=0 \qquad 2\text{-}15$$

$$-\frac{3}{2}K_I \sin\left(\frac{\theta}{2}\right)\cos\left(\frac{\theta}{2}\right)+\frac{K_{II}(3-9\cos\theta)}{4}=0 \qquad 2\text{-}16$$

$$-6K_I \sin\left(\frac{\theta}{2}\right)\cos\left(\frac{\theta}{2}\right)+K_{II}(3-9\cos\theta)=0 \qquad 2\text{-}17$$

$$2K_I \sin\left(\frac{\theta}{2}\right)\cos\left(\frac{\theta}{2}\right)-K_{II}(3-9\cos\theta)=0 \qquad 2\text{-}18$$

Recognizing that $\sin 2\theta = 2\sin\theta\cos\theta$, Equation 2-18 can be reduced to the following:

$$K_I \sin\theta+K_{II}(9\cos\theta-3)=0 \qquad 2\text{-}19$$

Equation 2-19 applies to an open crack and this solution has been widely published in the literature (Broek, 1989; Vallejo, 1994; Anderson, 1995; and Aliabadi, 1999). This expression may be used to predict crack propagation for either open or closed cracks by using the appropriate stress intensity factor (Aliabadi, 1999).

2.2.2.1 Open Cracks – Mode I. Aliabadi (1999) noted that crack propagation can occur due to tensile stresses either directly under Mode I loading or induced tensile stresses under Mode II loading. If loading occurs under pure Mode I conditions, then $K_I \neq 0$ and $K_{II} = 0$ and Equation 2-19 reduces to the following expression (Aliabadi, 1999):

$$K_I \sin\theta = 0 \qquad 2\text{-}20$$

where θ = 0° and also satisfies the second requirement, namely $\frac{d^2\sigma_\theta}{d\theta^2} < 0$ (Aliabadi, 1999). Under this loading condition, crack propagation occurs along the pre-existing open crack plane. This solution is analogous to a tension crack propagating vertically downward, as noted on Figure 2.2 and is intuitively correct.

2.2.2.2 Open Cracks – Mode II. If loading occurred under pure Mode II conditions, then $K_I = 0$ and $K_{II} \neq 0$ and Equation 2-18 reduces to the following expression:

$$K_{II}\left(3\cos\theta - 1\right) = 0 \qquad 2\text{-}21$$

where θ = 70.5°, which also satisfies $\frac{d^2\sigma_\theta}{d\theta^2} < 0$ (Vallejo, 1994; and Aliabadi, 1999). This solution has been validated by Vallejo (1994) using controlled laboratory experiments.

2.2.2.3 Open Cracks – Mixed Mode. If loading occurs under mixed mode loading conditions in which $K_I \neq 0$ and $K_{II} \neq 0$, Equation 2-19 contains three unknowns, namely: K_I, K_{II}, and θ. The stress intensity factors are dependent on loading conditions, geometry, and crack characteristics and as such, a general solution for mixed mode loading is not possible. However, Figure 2.4 presents a graphical representation of Equation 2-19 utilizing arbitrarily assigned stress intensity

factors and Figure 2.5 presents the graphical solution for Equation 2-19 where the stress intensity factors have been normalized. Review of these figures indicates that under:

- Pure Mode I conditions, $K_I \neq 0$ and $K_{II} = 0$ and $\theta = 0°$, which was noted above;
- Pure Mode II conditions, $K_I = 0$ and $K_{II} \neq 0$, and $\theta = 70.5°$, which was also noted above; and
- Mixed mode conditions when $K_I = 1$ and $K_{II} = 1$, the theoretical angle of crack propagation is, $\theta = 90°$, that is, tensile stresses will cause the crack to propagate normal to the existing crack plane.

Review of Figure 2.5 also indicated that unless the specimen undergoes pure Mode I loading conditions, the angle of crack propagation due to tensile stresses will generally be greater than 70.5°.

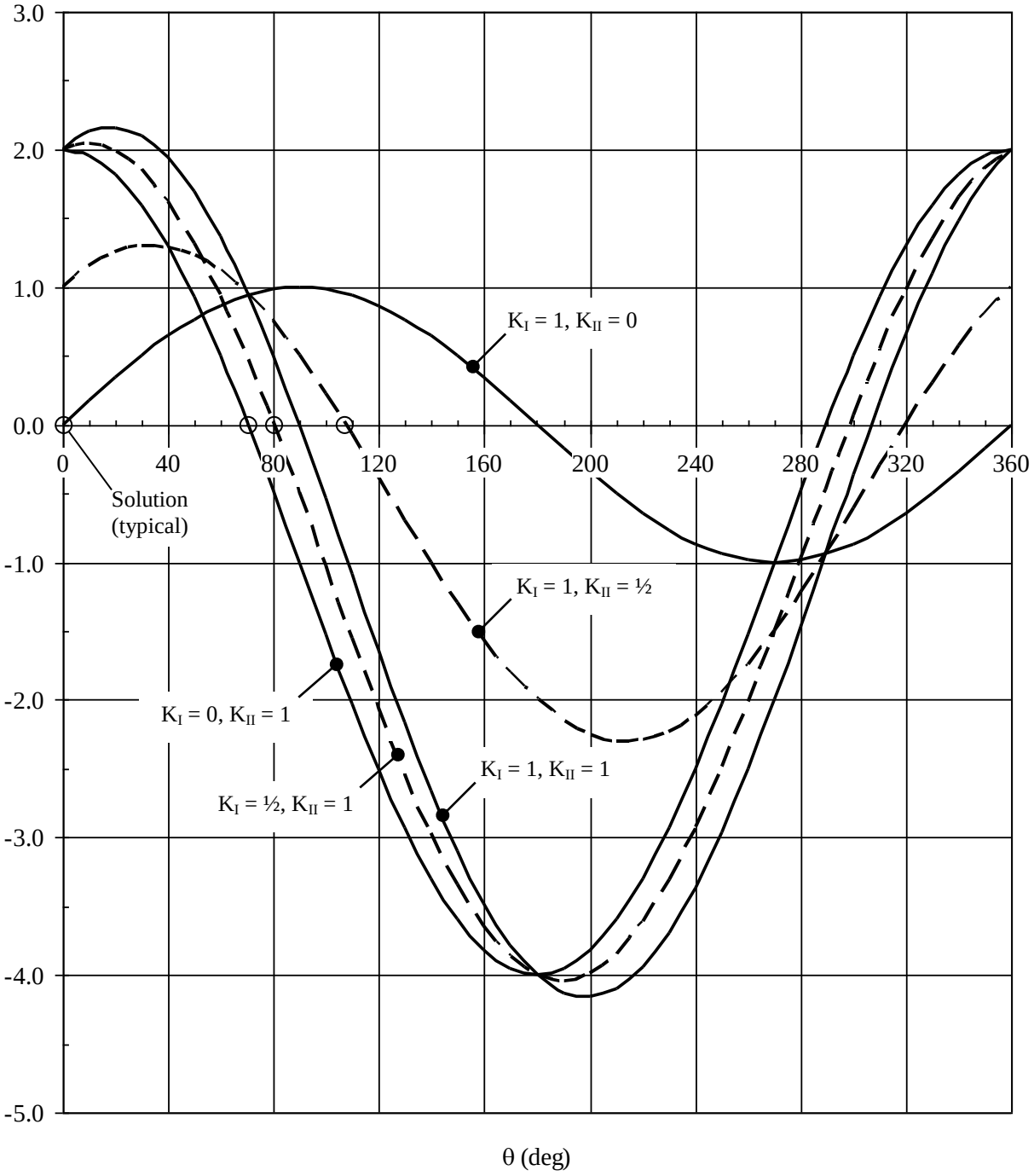

Figure 2.4. $K_I \sin\theta + K_{II}(3\cos\theta - 1)$ vs. θ for Various Values of K_I and K_{II}.

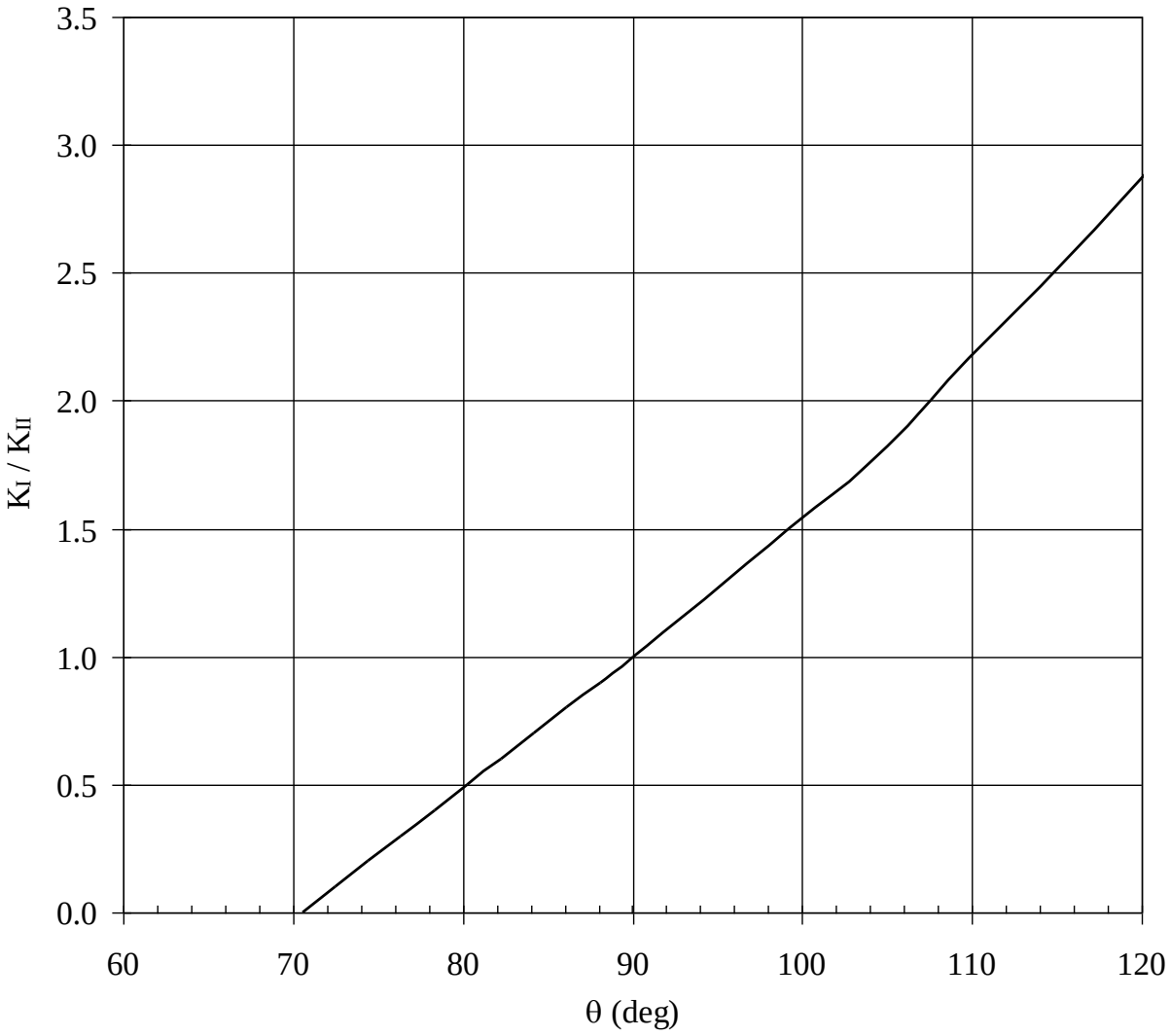

Figure 2.5. Tensile Stress Open Crack Propagation under Mixed Mode Loading Conditions.

2.2.2.4 Closed Cracks. The stress intensity factor for a closed crack will result in $K_I = 0$ (Broek, 1986; and Aliabadi, 1999). As such, Equation 2-18 reduced to the following expression:

$$K_{II}\left(3\cos\theta - 1\right) = 0 \qquad 2\text{-}22$$

where θ = 70.5°. This result is similar to the one described for an open crack under Mode II loading conditions. The original crack remains compressed while the part that propagates is open and in a tensile stress field. Therefore, a closed crack will propagate at θ = 70.5° (Vallejo, 1994; Aliabadi, 1999).

2.2.3 Shear Stress

Shear propagation develops in a plane that is critical from the viewpoint of shear strength. By similar analogy to Erdogan and Sih (1963), this research hypothesizes that crack propagation in brittle material will occur in a direction parallel to that where $\tau_{r\theta}$ reaches its maximum value, which is expressed as:

$$\frac{d\tau_{r\theta}}{d\theta} = 0 \text{ and } \frac{d^2\tau_{r\theta}}{d\theta^2} < 0 \text{ at } \theta = \alpha \qquad 2\text{-}23$$

where α is the value reached by θ when crack propagation occurs. However, it must be noted that the use of LEFM concepts with regard to shear failure and ultimate propagation is a controversial issue as Aliabadi (1999) notes that propagation is accompanied by considerable energy dissipation due to friction. Whittaker, et al (1992) note that if the crack is closed and the crack surfaces are not friction free, then Equations 2-2 to 2-4 are no longer valid since they were derived assuming that the crack surfaces are stress-free. However, Aliabadi (1999) also noted that several researchers have successfully modeled this phenomenon using fracture mechanics

(Horri and Nemat-Nasser, 1985; Reches and Lockner, 1994; and Dyskin and Germanovich, 1995) and as such, the use of LEFM concepts for shear failure cannot be dismissed and is further explored by this research.

Applying Equation 2-23 by differentiating Equation 2-4 resulted in the following expression:

$$\frac{d\tau_{r\theta}}{d\theta} = \cos\left(\frac{\theta}{2}\right)\left(K_I \cos\theta - 3K_{II} \sin\theta\right) - \frac{1}{2}\sin\left(\frac{\theta}{2}\right)\left[K_I \sin\theta + K_{II}\left(3\cos\theta - 1\right)\right] = 0 \qquad 2\text{-}24$$

Rearranging and manipulating Equation 2-24 produced the following expressions:

$$K_I \cos\theta\cos\left(\frac{\theta}{2}\right) - 3K_{II} \sin\theta\cos\left(\frac{\theta}{2}\right) - \frac{K_I}{2}\sin\theta\sin\left(\frac{\theta}{2}\right) - K_{II}\left[\frac{3}{2}\cos\theta\sin\left(\frac{\theta}{2}\right)\right] + \frac{K_{II}}{2}\sin\left(\frac{\theta}{2}\right) = 0 \qquad 2\text{-}25$$

$$K_I\left[\cos\theta\cos\left(\frac{\theta}{2}\right) - \frac{1}{2}\sin\theta\sin\left(\frac{\theta}{2}\right)\right] + K_{II}\left[\frac{1}{2}\sin\left(\frac{\theta}{2}\right) - 3\sin\theta\cos\left(\frac{\theta}{2}\right) - \frac{3}{2}\cos\theta\sin\left(\frac{\theta}{2}\right)\right] = 0 \qquad 2\text{-}26$$

$$K_I\left[2\cos\theta\cos\left(\frac{\theta}{2}\right) - \sin\theta\sin\left(\frac{\theta}{2}\right)\right] + K_{II}\left[\sin\left(\frac{\theta}{2}\right) - 6\sin\theta\cos\left(\frac{\theta}{2}\right) - 3\cos\theta\sin\left(\frac{\theta}{2}\right)\right] = 0 \qquad 2\text{-}27$$

Equation 2-27 can is simplified by applying the following two trigonometry identities:

$$\cos(u)\cos(v) = \tfrac{1}{2}\left[\cos(u-v) + \cos(u+v)\right]$$

$$\sin(u)\sin(v) = \tfrac{1}{2}\left[\cos(u-v) - \cos(u+v)\right]$$

and let $u = \theta$ and $v = \theta/2$.

$$K_I\left[\left(\cos\frac{\theta}{2} + \cos\frac{3\theta}{2}\right) - \frac{1}{2}\left(\cos\frac{\theta}{2} - \cos\frac{3\theta}{2}\right)\right] + K_{II}\left[\sin\frac{\theta}{2} - 3\sin\frac{3\theta}{2} - 3\sin\frac{\theta}{2} - \frac{3}{2}\sin\frac{3\theta}{2} + \frac{3}{2}\sin\frac{\theta}{2}\right] = 0 \qquad 2\text{-}28$$

$$K_I\left[\left(\frac{1}{2}\cos\frac{\theta}{2}+\frac{3}{2}\cos\frac{3\theta}{2}\right)\right]-K_{II}\left[\frac{9}{2}\sin\frac{3\theta}{2}+\frac{1}{2}\sin\frac{\theta}{2}\right]=0 \quad \text{2-29}$$

$$K_I\left(\cos\frac{\theta}{2}+3\cos\frac{3\theta}{2}\right)-K_{II}\left(9\sin\frac{3\theta}{2}+\sin\frac{\theta}{2}\right)=0 \quad \text{2-30}$$

Equation 2-30 applies to an open crack, but this expression may also be used to predict crack propagation for either open or closed cracks by using the appropriate stress intensity factor.

2.2.3.1 Open Cracks – Mode I. Typically, a geotechnical material with an open crack will undergo tensile failure before shear failure since tensile strength (and therefore tensile failure) is often the governing failure mode for geotechnical materials under Mode I loading conditions, as noted by Figure 2.6. However, if shear loading occurs under pure Mode I conditions, then $K_I \neq 0$ and $K_{II} = 0$ and Equation 2-30 reduces to the following expression:

$$\cos\frac{\theta}{2}+3\cos\frac{3\theta}{2}=0 \quad \text{2-31}$$

The solution to Equation 2-31 results in θ = 70.5°, 180° and 289.5°. However, these values must also satisfy $\frac{d^2\tau_{r\theta}}{d\theta^2}<0$, which is expressed as:

$$-K_I\left(sin\frac{\theta}{2}+9\sin\frac{3\theta}{2}\right)-K_{II}\left(cos\frac{\theta}{2}\right)-27K_{II}\left(cos\frac{3\theta}{2}\right)<0 \quad \text{2-32}$$

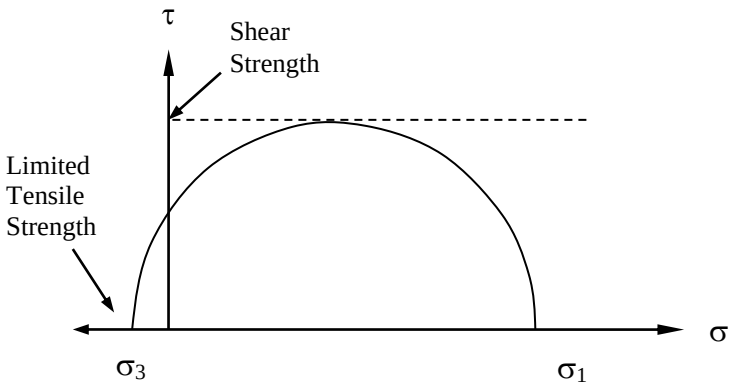

Figure 2.6. Mohr-Coulomb Shear Strength Graph for a Typical Geotechnical Material.

Recognizing that $K_{II} = 0$, Equation 2-32 may be reduced to the following expression:

$$-K_I\left(sin\frac{\theta}{2} + 9\sin\frac{3\theta}{2}\right) < 0 \qquad 2\text{-}33$$

Applying the solutions of θ = 70.5°, 180° and 289.5°, Equation 2-33 is satisfied when θ = 70.5° and 289.5°. This result indicates that an open crack will propagate ±70.5° from the pre-existing crack plane under Mode I induced shear stress if the shear strength of the material is less than the tensile strength. It should be noted that although there is very little published literature regarding Mode II crack propagation, Li, et al (2000) reported crack propagation of θ = 60°, for a pure frozen silty sand and helps conform the above analysis.

2.2.3.2 Open Cracks – Mode II. If shear loading occurs under pure Mode II conditions, then $K_I = 0$ and $K_{II} \neq 0$ and Equation 2-30 reduces to the following expression:

$$9\sin\frac{3\theta}{2} + \sin\frac{\theta}{2} = 0 \qquad 2\text{-}34$$

The solution to Equation 2-34 results in θ = 0°, 123.8° and 236.3°. However, these values must also satisfy $\frac{d^2\tau_{r\theta}}{d\theta^2} < 0$, which is shown as Equation 2-32. Recognizing that $K_I = 0$, Equation 2-32 may be reduced to the following:

$$-\left(cos\frac{\theta}{2}\right) - 27\left(cos\frac{3\theta}{2}\right) < 0 \qquad 2\text{-}35$$

Applying the solutions of θ = 0°, 123.8°, and 236.3°, Equation 2-39 is satisfied when θ = 0° and 236.3°, although based on observation the solution of θ = 236.3° is dismissed. This result indicates that an open crack will propagate along the pre-existing crack plane when subjected to pure Mode II conditions.

2.2.3.3 Open Cracks – Mixed Mode. If loading occurs under mixed mode loading conditions in which $K_I \neq 0$ and $K_{II} \neq 0$, Equation 2-30 contains three unknowns, namely: K_I, K_{II}, and θ. Figure 2.7 presents the graphical solution for Equation 2-30 where the stress intensity factors have been normalized. Review of this figure indicates that under:

- Pure Mode I conditions, $K_I \neq 0$ and $K_{II} = 0$ and θ → 70.5°, which was noted above;
- Pure Mode II conditions, $K_I = 0$ and $K_{II} \neq 0$, and θ = 0°, which was also noted above; and
- Mixed mode conditions when $K_I \neq 0$ and $K_{II} \neq 0$, the theoretical angle of crack propagation will vary from θ = 0° to 70.5° as Mode I conditions become more dominate.

2.2.3.4 Closed Cracks. For a closed crack, $K_I = 0$ (Broek, 1986) and Equation 2-30 reduces to the following expression:

$$9\sin\frac{3\theta}{2} + \sin\frac{\theta}{2} = 0 \qquad 2\text{-}36$$

This condition resulted in the identical expression to Equation 2-34, with θ = 0°, and indicates that a closed crack will propagate along the pre-existing crack plane.

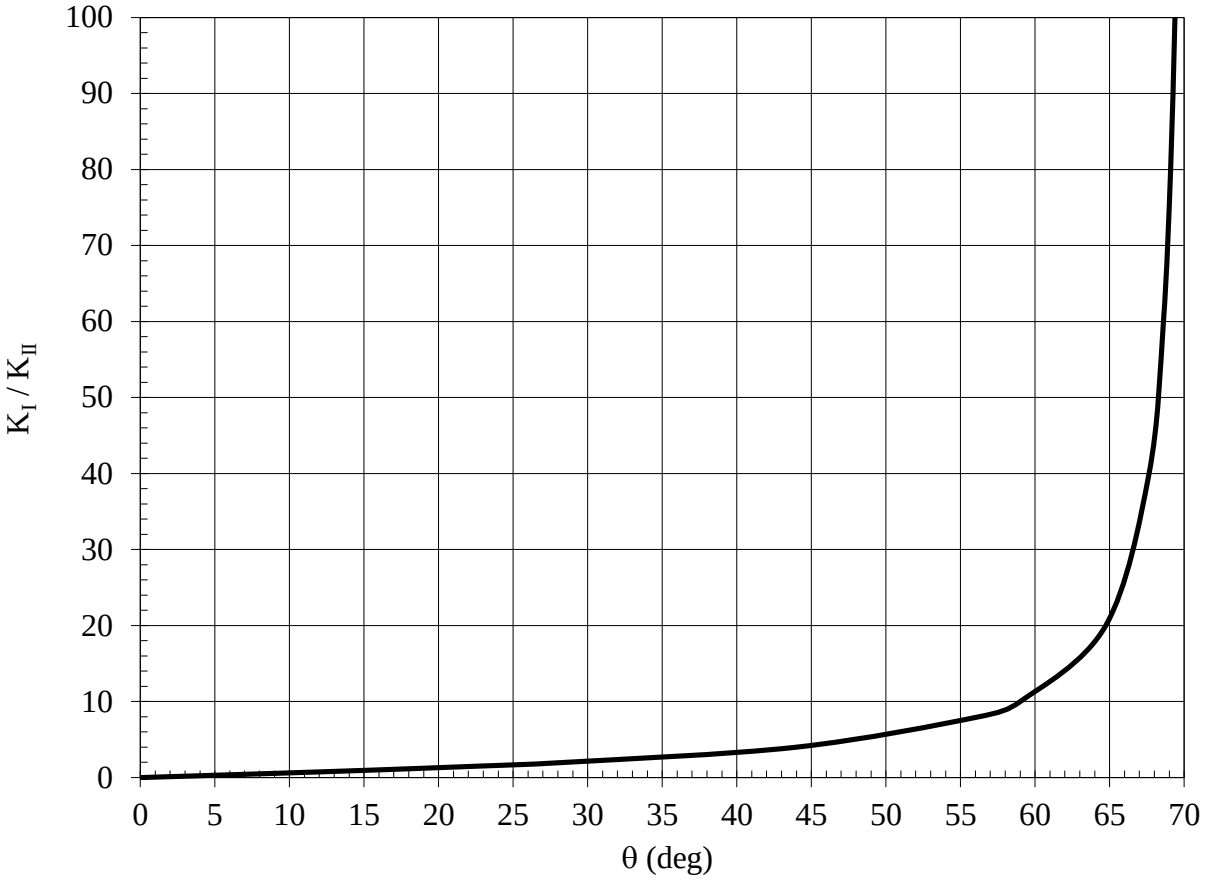

Figure 2.7. Open Crack Propagation from Shear Stress Loading under Mixed Mode Conditions.

2.2.4 LEFM Summary

LEFM considers that crack propagation can be studied thorough the superposition of three independent load applications, as noted on Figure 2.1. This research utilizes the maximum tangential stress theory developed by Erdogan and Sih (1963) as well as advances the concept of crack propagation from shear stress utilizing a similar analogy; that is crack propagation would also occur under maximum shear stress. Table 2.2 summarizes the findings of these two concepts.

Table 2.2. Theoretical Angle of Crack Propagation.

Loading Condition	σ_θ		$\tau_{r\theta}$	
	Open Crack	Closed Crack	Open Crack	Closed Crack
Mode I	0°	N/A	±70.5°	N/A
Mode II	70.5°	70.5°	0°	0°
Mixed Mode	> 70.5°	N/A	0° - 70.5°	N/A

The controlling mode of failure will be governed by the loading conditions and the materials shear strength characteristics. For example, tension cracks near the crest of a slope undergo σ_θ Mode I loading conditions, which indicates that the cracks would tend to propagate vertically, or $\theta = 0°$ with the crack plane.

3.0 LABORATORY PROGRAM

A laboratory testing program to study crack propagation in cohesive soils was conducted in the soil mechanics laboratory at the University of Pittsburgh, Pittsburgh, PA. Testing involved constructing prismatic soil samples for plane stress direct shear testing. The purpose of the laboratory testing program was to observe and record the propagation of the failure plane when soil models were subjected to shear loading as well as simulated lateral stress loading conditions.

The first model investigated crack propagation subjected to shear loading conditions; that is $\tau_{r\theta}$ loading conditions noted in Figure 3.1. These models are termed shear models for this study and fracture mechanics principles indicated that a closed crack would propagate along the

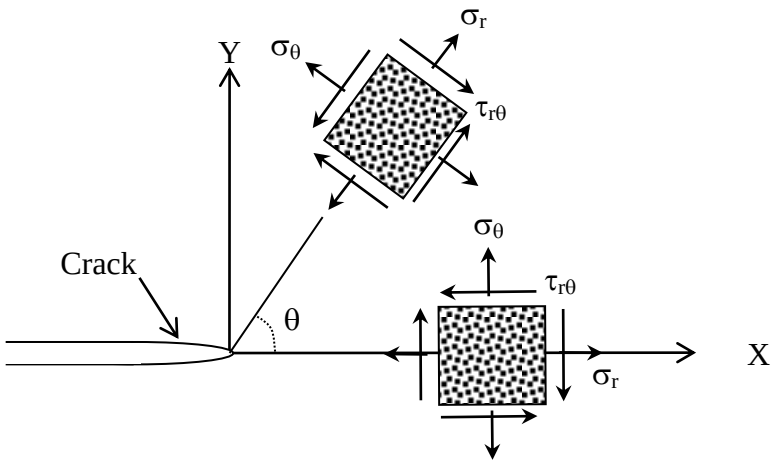

Figure 3.1. Laboratory Loading Conditions Reference Model.

pre-existing crack plane at θ = 0°, or along the X-Axis at noted in Figure 3.1. The second model investigated crack propagation subjected to a simulated lateral stress, which is a σ_θ loading condition noted in Figure 3.1. This model is termed the homogeneous vertical slope model for this study and fracture mechanics principles indicated that a closed crack would propagate along an axis inclined from the pre-existing crack plane at θ = 70.5°.

3.1 LABORATORY TEST PROGRAM OVERVIEW

ASTM D3080 and AASHTO T236 provide an industry standard test methodology for direct shear testing of soils. The procedure involves placing a test specimen in a shear device, which consists of a moveable upper frame and fixed lower frame. Sample size is generally limited square or circular specimens with a minimum width or diameter of 50 mm, respectively. The frames are sufficiently rigid to prevent their distortion during shear. The test begins by applying a normal force to the soil sample and shear is applied by either controlled-displacement or controlled-stress test methods.

A disadvantage of the direct shear test apparatus is that the upper and lower frames do not permit observation of the developing failure plane. The propagation of the failure surface can not be recorded unless the test is stopped and the sample removed for inspection. However, stopping the test and inspecting the sample can introduce significant changes in the clay structure that could impact the development of the failure surface (Vallejo, 1987).

The plane stress direct shear apparatus (PSDSA) was developed at the University of Pittsburgh to permit observation and recording of the developing failure surface without removal of the sample

(Vallejo, 1987; 1991). A schematic of the PSDSA is shown as Figure 3.2. The device consists of an open shear box formed by two U-sections that enclose a prismatic soil sample. The upper U-section is movable and transmits the normal and shear load to the soil sample by rotation of a hand crank screw system. The magnitude of normal and shear loads transmitted to the soil sample are measured by proving rings. The movable upper U-section rests on a metallic plate that contains a ball-bearing system to minimize friction while the lower U-section is fixed to the metallic plate. Displacement of the upper U-section is measured by a dial gauge. The device creates a plane stress loading condition since loads on a prismatic soil sample are applied in two directions

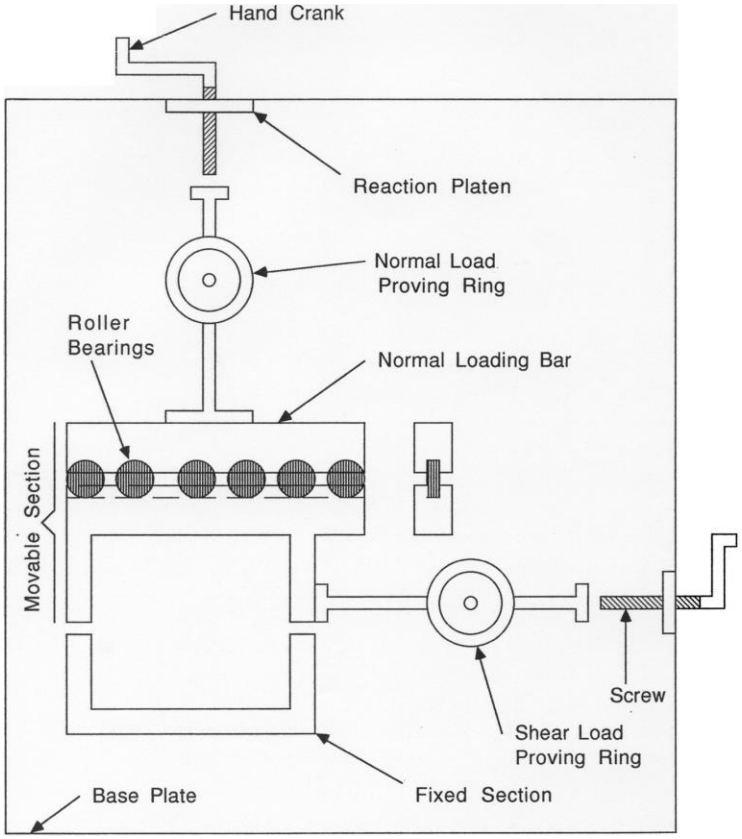

Figure 3.2. Plane Stress Direct Shear Apparatus.

(x- and y- direction) with a free face (z- direction) to permit visual observation of the developing failure surface. The PSDSA can accommodate soil samples measuring 12.7 cm in length, 11.4 cm in width, and 3.17 cm in thickness.

3.2 SHEAR MODELS

Two laboratory shear models were developed for PSDSA testing. Kaolinite clay and Ottawa sand were used to construct the models. Model details are as follows:

- Model 1, Clay on Clay – Model consisted of 90% clay and 10% sand mixture in the upper U-section, and 100% clay in the lower U-section.

- Model 2, Clayey Sand on Clay – Model consisted of 20% clay and 80% sand mixture in the upper U-section, and 100% clay in the lower U-section.

Kaolinite clay was chosen because it forms a homogeneous material and will minimize the adverse effects of micro-scale heterogeneities (Vallejo, 1987). Kaolinite used for this research exhibited a liquid limit = 58%, plastic limit = 28%, and plasticity index = 30%. The material classified as CH, in accordance with the Unified Soil Classification System (USCS). The Ottawa sand was a clean, uniform, sub-rounded quartz sand. The addition of kaolinite created plastic-type fines as well as non-plastic-type fines consisting of crushed quartz sand.

Clay-water and clay-sand-water mixtures were created by mixing with distilled water. Samples were then placed in an oedometer and consolidated under a normal pressure of 25.7 kPa for a period of 5 days. After unloading the oedometer, samples were then cut to size for testing

in the PSDSA. The water content of the samples were at or slightly above the plastic limit after removal from the oedometer. Cracks were artificially made in the samples by a process of inserting and removing a thin glass sheet that was 1-mm thick and 3-cm in width in a direction normal to the free face. This process of creating artificial cracks proved to be effective for Vallejo (1985, 1988), and Vallejo and Pramono (1984) in understanding crack propagation in brittle clays.

3.2.1 Clay on Clay Test Results

After the prepared soil sample was place in the PSDSA, a normal stress of 34.5 kPa was applied and the normal stress closed the crack. The sample was sheared using a controlled displacement rate of 1 mm per minute. The PSDSA test photographs for the clay on clay sample are shown as Figure 3.3. The crack began to propagate at 8.6 kPa, which was approximately 0.5% strain, and exhibited a peak shear stress of 14.1 kPa. At a shear displacement of 0.28 cm, or 2.2% strain, the crack propagated completely through the sample along a horizontal failure plane. A summary of the test data is presented as Table 3.1. Figure 3.4 presents a plot of shear stress against shear displacement. The shear stress plot indicates a peak and residual strength that is characteristic of a stiff, brittle clay with peak strain occurring around 2±% (Lambe and Whitman, 1969; Bowles, 1996; and Das, 1990).

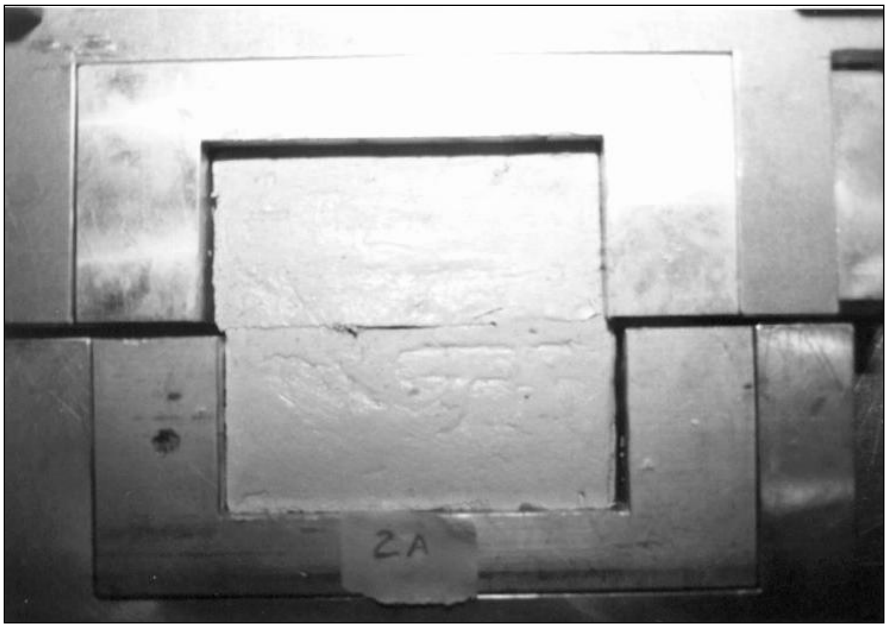

a) Shear displacement = 0.28 cm, crack propagates through sample.

b) Shear displacement = 0.65 cm, near conclusion of test.

Figure 3.3. PSDSA Test for Clay on Clay.

Table 3.1. PSDSA Test Results for Clay on Clay.

Top of Sample Composition	Bottom of Sample Composition	Shear Stress at which Crack Propagated (kPa)	Shear Stress at Failure (kPa)	Water Content for Top Sample (%)	Water Content for Bottom Sample (%)
90% Clay 10% Sand	100% Clay	8.6	14.1	30.0	33.2

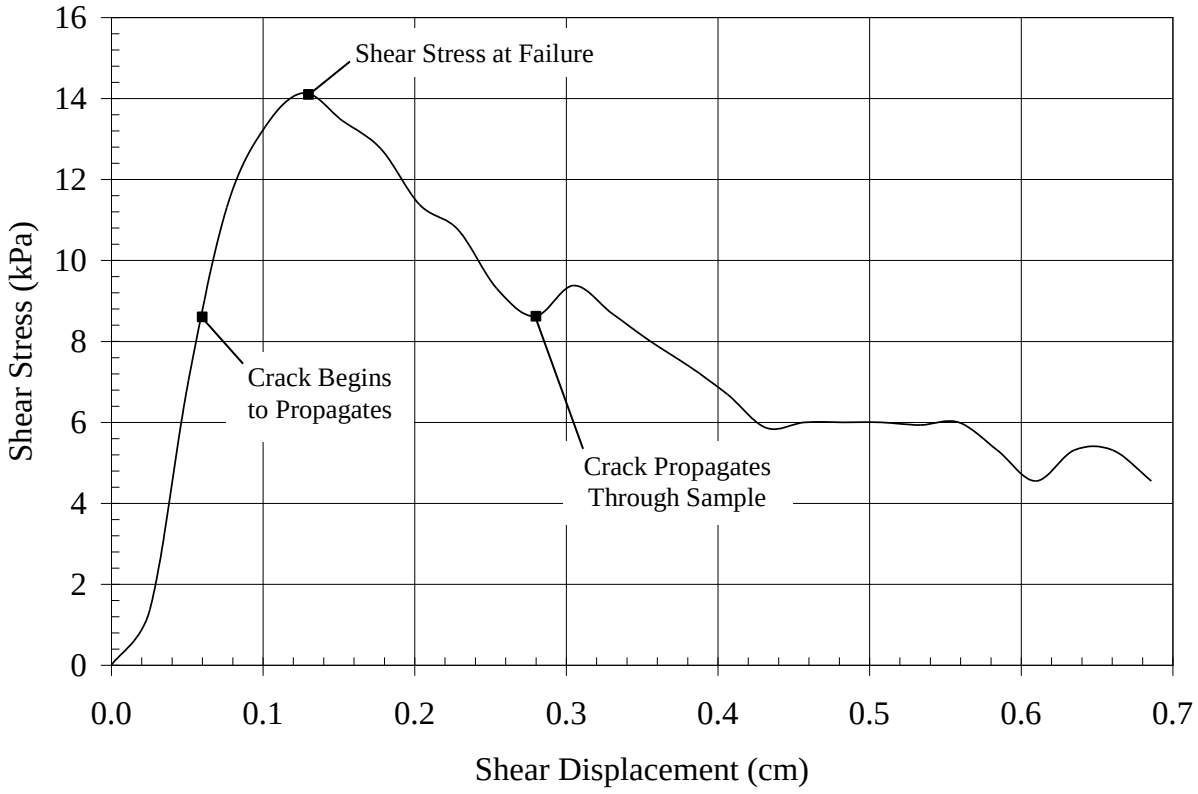

Figure 3.4. Shear Stress vs Shear Displacement for Clay on Clay.

3.2.2 Clayey Sand on Clay Test Results

As with the clay on clay test arrangement, the clayey sand on clay test also applied a normal stress of 34.5 kPa, which closed the crack. The sample was sheared at a controlled displacement rate of 1 mm per minute. Figure 3.5 presents the PSDSA test photographs for the clayey sand on clay sample. Review of these figures indicated that the failure plane propagated horizontally, just below the interface in the lower clay stratum. The water content of the upper sample was 8.4% whereas the lower sample was 32.9%, suggesting that failure occurred in the more ductile clay material rather than the brittle clayey sand mixture.

Crack propagation for the clayey sand on clay sample began to propagate at a much higher shear stress of 28.9 kPa, or 2.0±% strain, as compared to the clay on clay sample which began propagation at 0.5% strain. The sample exhibited a peak shear stress of 30.1 kPa. Table 3.2 presents a summary of the test data and Figure 3.6 presents a plot of shear stress against shear displacement. The shear stress plot indicated peak strength with a slight reduction to the residual strength. This type of plot is characteristic of lightly to normally consolidated clay. (Lambe and Whitman, 1969; Bowles, 1996; and Das, 1990).

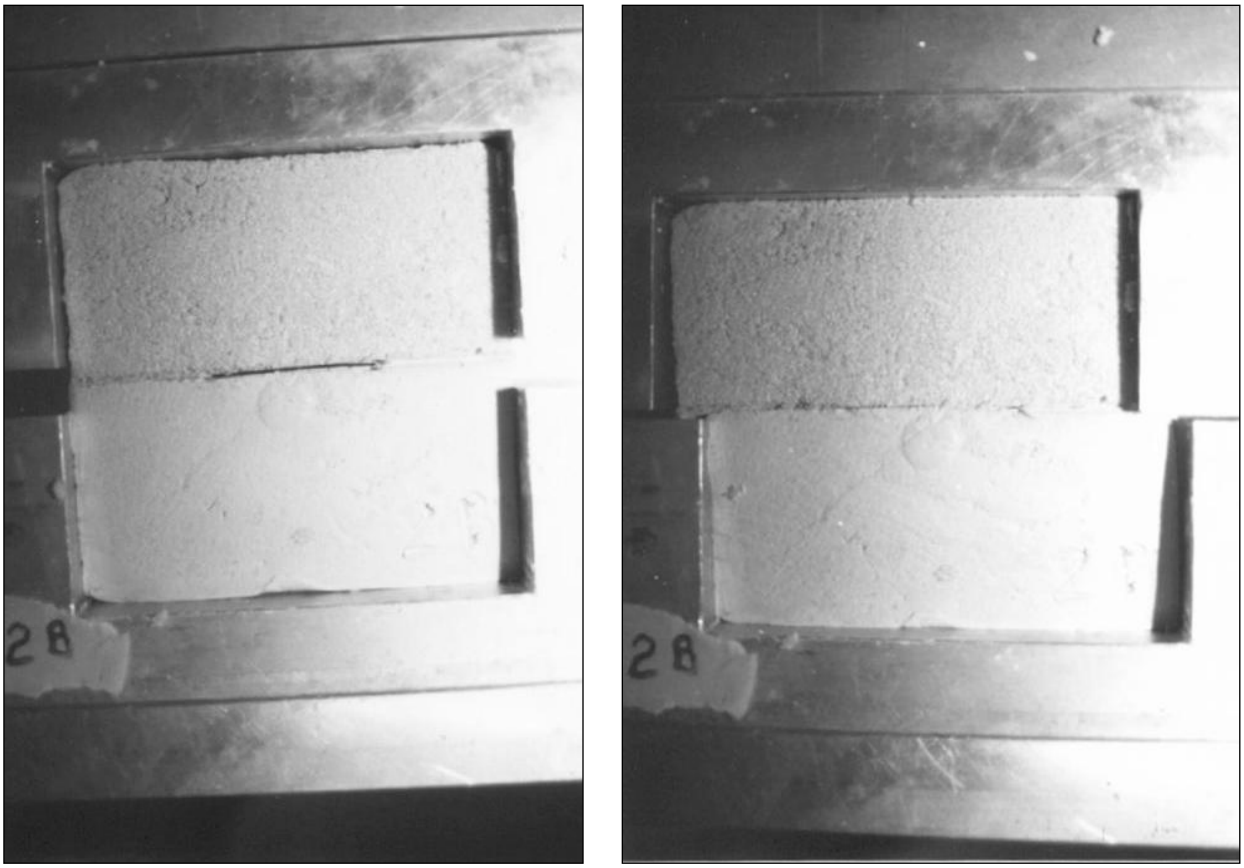

a) At Shear Displacement = 0, start of test. b) At Shear Displacement = 0.58 cm

Figure 3.5. PSDSA Test for Clayey Sand on Clay.

Table 3.2. PSDSA Test Results for Clayey Sand on Clay.

Top of Sample Composition	Bottom of Sample Composition	Shear Stress at which Crack Propagated (kPa)	Shear Stress at Failure (kPa)	Water Content for Top Sample (%)	Water Content for Bottom Sample (%)
20% Clay 80% Sand	100% Clay	28.9	30.1	8.4	32.9

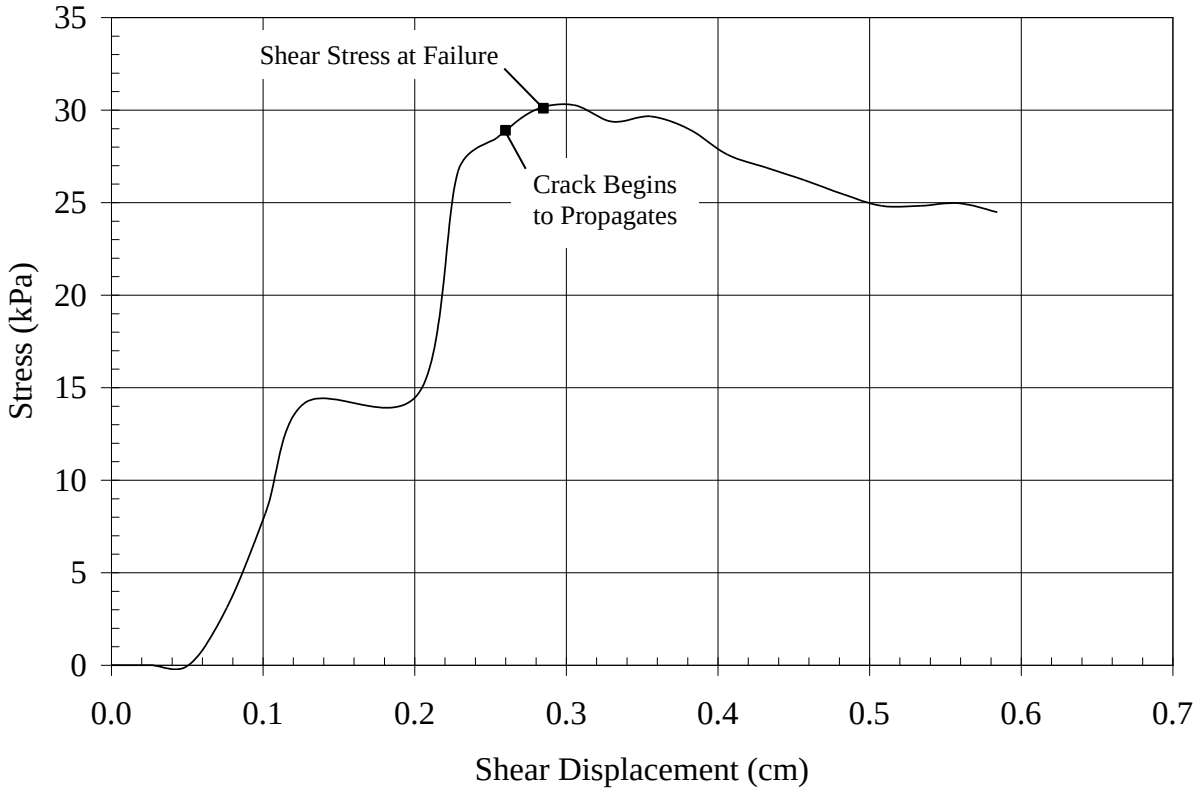

Figure 3.6. Shear Stress vs Shear Displacement for Clayey Sand on Clay.

3.2.3 Evaluation of Findings

Both samples considered a closed crack under direct shear loading, which resulted in a fracture mechanics $\tau_{r\theta}$ - Mode II loading condition as shown on Figure 3.7. An artificial crack was created in the samples and the crack was closed by a normal stress. The closed crack resulted in

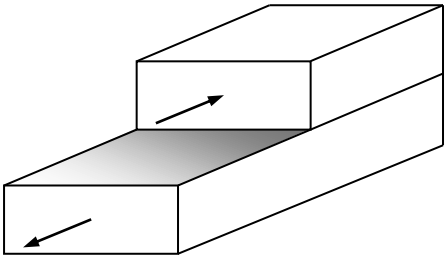

Mode II - Shear Crack

Figure 3.7. Mode II Loading Condition.

$K_I = 0$. In accordance with Table 2.2, fracture mechanics indicates that a closed crack under $\tau_{r\theta}$ - Mode II conditions will propagate along the pre-existing crack plane. Both the clay on clay and clayey sand on clay resulted in a failure plane that propagated in a near horizontal fashion along the existing crack plane.

The closed crack began to propagate before the samples reached the peak shear stress and the crack fully propagated before the sample reached an apparent residual shear stress value, as observed in the shear stress vs. shear displacement figures. This suggests that pre-existing cracks in cohesive materials propagate before achieving peak shear strengths. Excessive strain can also result in full crack propagate before reaching residual shear strength.

3.3 SIMULATED VERTICAL SLOPE MODEL

A simulated vertical slope with an artificial crack inserted at the toe of slope was tested in the PSDSA. The clay model simulated a vertical cut in a horizontal clay deposit. The lateral earth pressure applied by the PSDSA created an idealized fracture mechanics loading condition in which the governing mode of failure was tangential stress (σ_θ), as noted on Figure 3.1. The laboratory model consisted of a homogeneous prismatic clay sample prepared by consolidating kaolinite clay in an oedometer. Samples were cut from the larger consolidated sample and a toe crack was created by inserting and removing a thin glass sheet. Figure 3.8 presents the general model dimensions. The applied normal stress (σ_n) simulates gravity stress acting on the slope and the lateral stress (σ_l) simulates the lateral earth pressure.

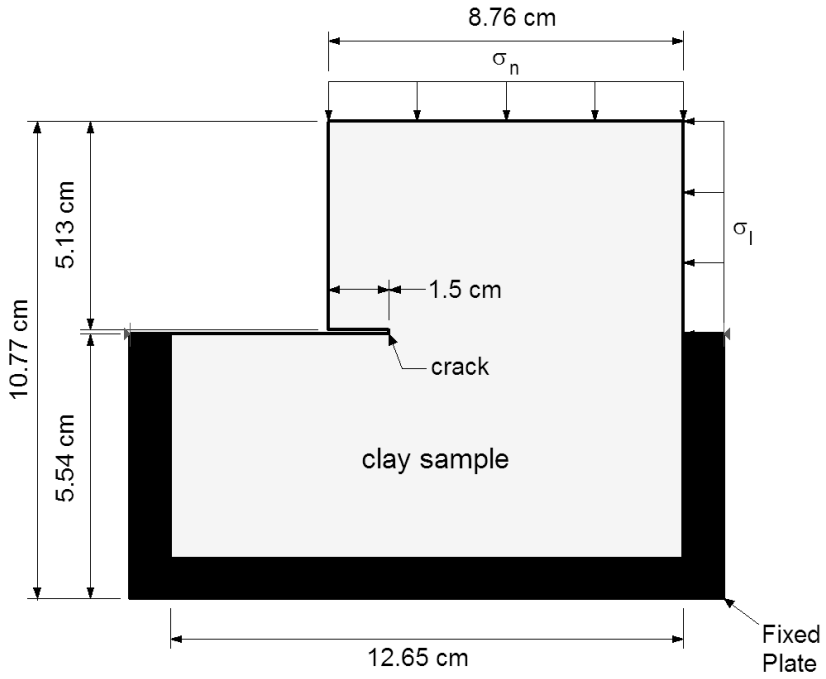

Figure 3.8. Simulated Vertical Slope Model.

3.3.1 Simulated Vertical Slope Test Results

A normal stress of 40 kPa was applied to the sample, which closed the toe crack. The normal stress was kept constant during the experiment. Lateral stress was gradually increased until the toe crack began to propagate, which occurred at 512 kPa. The toe crack propagated in the model in the form of a secondary crack that extend from the top of the pre-existing crack and deviated from the original horizontal direction. Figure 3.9 presents the clay model before and after the test. Table 3.3 presents a summary of the test data and Figure 3.10 presents a plot of shear stress against shear displacement.

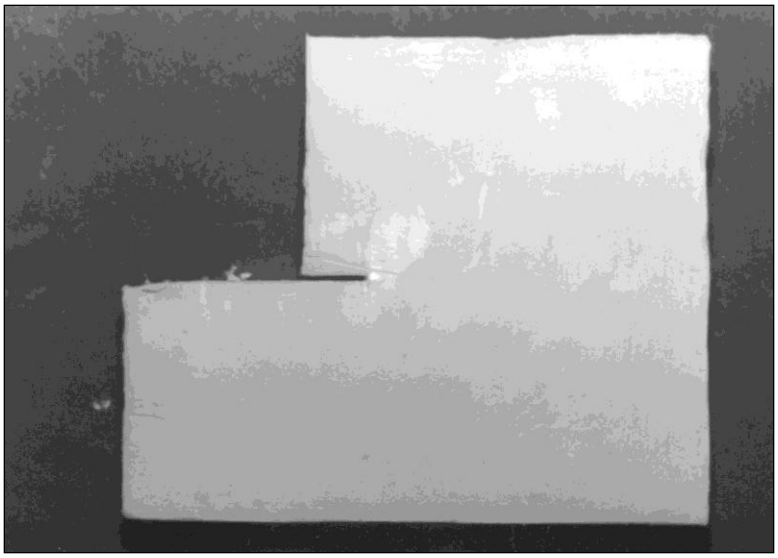

a) Model before test with open toe crack.

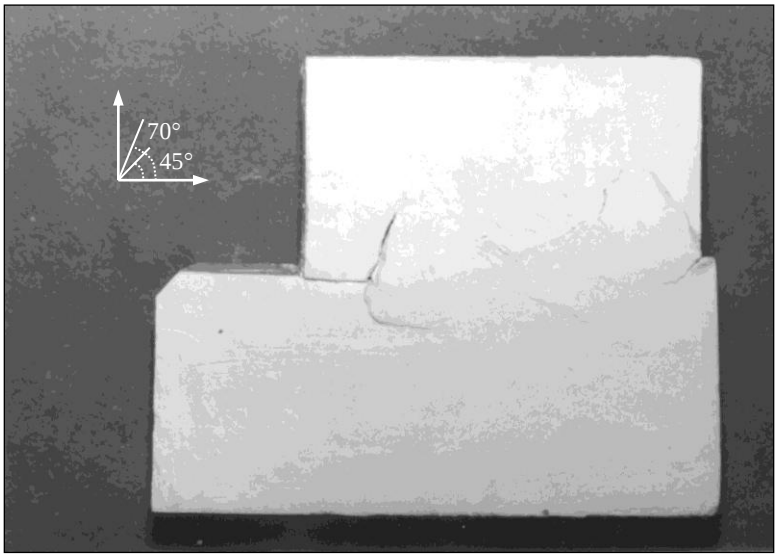

b) Model after test with closed toe crack and inclined crack propagation.

Figure 3.9. Simulated Vertical Cut Slope.

Table 3.3. PSDSA Test Results for Simulated Vertical Slope.

Sample Composition	Lateral Stress at which Crack Propagated (kPa)	Shear Stress at which Crack Propagated (kPa)	Normal Stress Maintained on Sample (kPa)	Sample Water Content (%)
100% Clay	512	300	40	27%

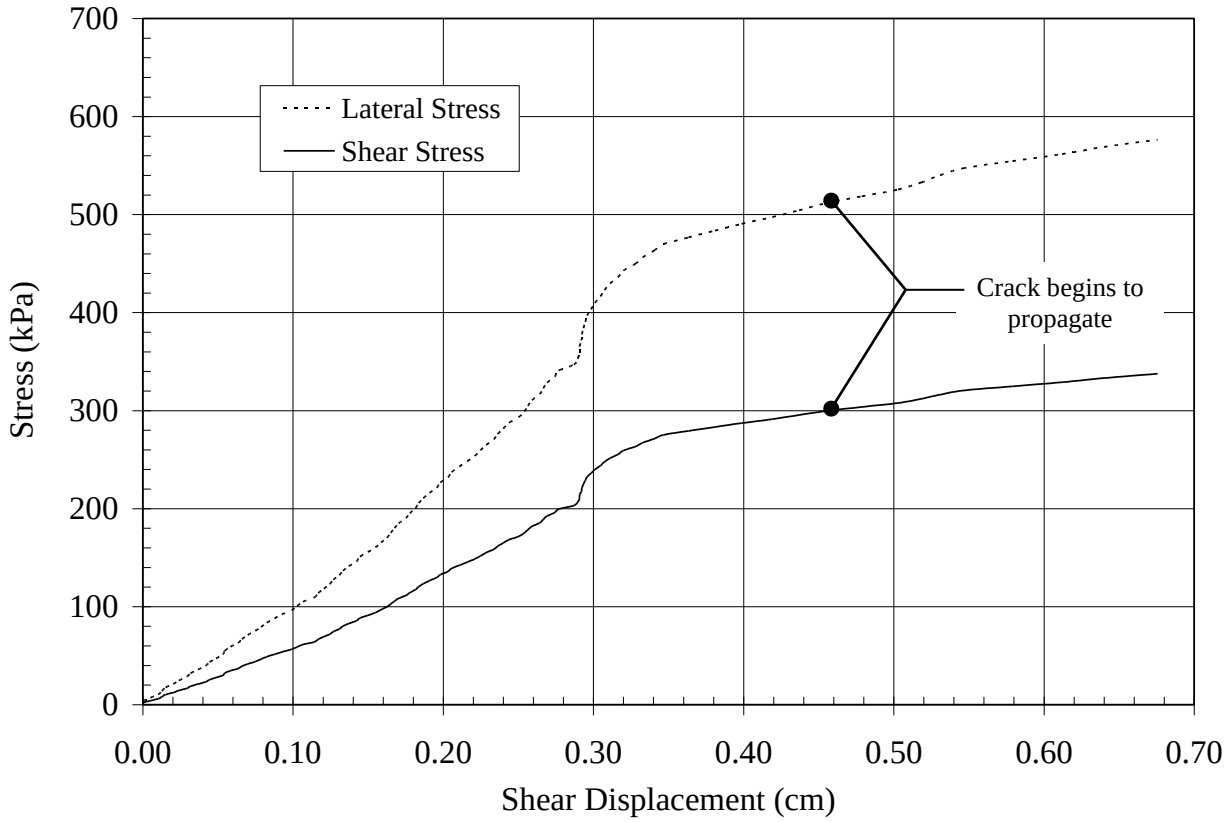

Figure 3.10. Stress vs Shear Displacement for Simulated Vertical Clay Slope.

3.3.2 Evaluation of Findings

The simulated vertical slope model was subjected to lateral stresses (i.e., σ_θ) under Mode II loading conditions. An artificial crack was created and the crack was closed by a normal stress. A closed crack resulted in $K_I = 0$. In accordance with Table 2.2, fracture mechanics indicates that a closed crack subjected to σ_θ - Mode II conditions will propagate at an angle of 70.5° from the pre-existing crack. The simulated vertical slope model exhibited crack propagation at an angle of 70°, as predicted by fracture mechanics. This finding is contrary to the assumptions of Bjerrum (1967), and Palmer and Rice (1973) in which they indicate that a closed crack at the base of a slope will propagate in a direction that follows the plane of the original crack.

The closed crack began to propagate before the sample reached the peak shear stress, as observed in the stress vs. shear displacement figures. A similar finding with the shear models was also observed. This suggests that a pre-existing crack in a stiff cohesive material will propagate before achieving peak shear strengths.

4.0 FINITE ELEMENT METHODS

Clough (1960) was a structural engineering professor for the University of California at Berkeley and he is considered one the founders of the Finite Element Method (FEM). Although renowned for his pioneering work in the field of earthquake engineering, Clough (1960) first termed "finite element" for a plane stress analysis that he presented at a conference in Pittsburgh, PA. Since then, a large amount of research has been devoted to FEM and it was first introduced to the geotechnical engineering community by Clough and Woodward (1967) at the first Berkeley Conference on the stability and performance of slopes and embankments. The most significant aspect of their paper was the use of non-linear stress-strain relationships for the analysis of an embankment dam (Duncan, 1996).

4.1 REVIEW OF FINITE ELEMENT THEORY

Advanced numerical methods permit solutions to many challenging geotechnical problems. Two well know numerical methods that are used in the professional engineering community are the finite difference method and the finite element method. The finite difference method approximates solutions to differential equations by replacing derivative expressions with approximately equivalent difference quotients. The finite difference method envisions the solution region as an array of grid points whereas the finite element method envisions the

solution region as many small, interconnected sub-regions or elements. FEM is particularly suitable for evaluating accurate fracture mechanic parameters in arbitrarily shaped two and three dimensional problems (Hellen, 2001) and is the method used for this research.

The basic premise of the FEM is that a solution region can be analytically modeled or approximated by replacing it with an assembly of discrete elements. This reduces the problem to a finite number of unknowns. Each unknown variable is expressed in terms of an assumed approximating function that is defined at specified points called nodes. Nodes usually are situated on the element boundaries where adjacent elements are connected to create a mesh. An element may also have interior nodes. The behavior of the field variable within the element is completely defined by the field variable and the interpolation functions. The solution and degree of approximation depend not only on the size and number of the elements, but also on the selected interpolation functions (Huebner, et al, 2008). Figure 4.1 depicts a typical triangular and rectangular two dimensional element (Bathe, 1982).

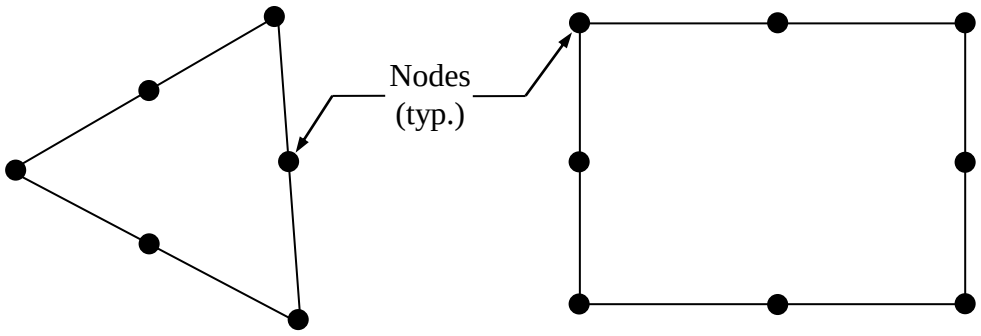

Figure 4.1. Standard two dimensional elements.

Displacements are fundamental variables and at any point within an element, they are related to the displacements at the nodes by making certain assumptions. Strains are calculated from the displacements and stresses are calculated using stress-strain relationships. Displacements at any point within the element are related to the displacements of the nodes through shape functions. The best overall elements for two dimensional meshes are isoparametric elements (Ingraffea and Heuze, 1980; Griffiths and Lane, 1999; Griffiths, 2000; and Hellen, 2001). The basis of the isoparametric finite element formulation is the interpolation of the element coordinates and element displacements using the same interpolation functions, which are defined in a natural coordinate system (Bathe, 1982). Considering a general two dimensional isoparametric element, the coordinate interpolations are (Bathe, 1982):

$$x = \sum_{i=1}^{q} h_i x_i \quad \text{and} \quad y = \sum_{i=1}^{q} h_i y_i \qquad \text{4-1}$$

where x and y are the coordinates at any point of the element (local coordinates), and x_i and y_i, i = 1, …. , q are the coordinates of the q element nodes (Bathe, 1982). The interpolation function h_i is defined in the natural coordinate system of the element. The interpolation function has variables r and s that vary from -1 to +1 and are the unknowns. Bathe (1982) indicates that the fundamental property of h_i is that its value in the natural coordinate system is unity at node i and is zero at all other nodes. The procedure for constructing element interpolation functions for two dimensional elements is relatively straightforward. For example, consider the four-node, two dimensional element noted in Figure 4.2, with parabolic interpolation in which interpolation polynomials that involve r^2 as the highest power of r; higher order interpolation could be derived in an analogous way. At Node 1, h_1 must equal 1 and therefore by inspection,

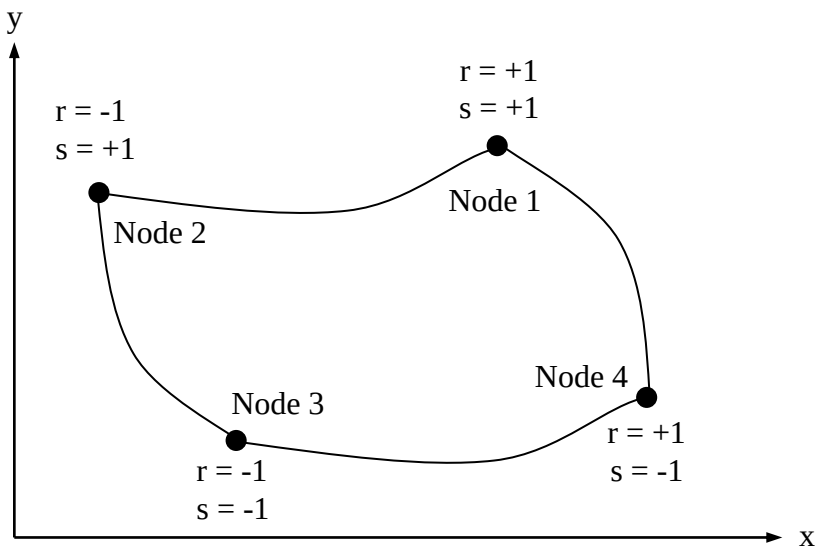

Figure 4.2. Typical Four Node, Two Dimensional Element.

$$h_1 = \frac{1}{4}(1+r)(1+s) \qquad 4\text{-}2$$

By similar analogy, the remaining interpolation functions for the four node, two dimensional element noted in Figure 4.2 are as follows (Bathe, 1982):

$$h_2 = \frac{1}{4}(1-r)(1+s) \qquad 4\text{-}3$$

$$h_3 = \frac{1}{4}(1-r)(1-s) \qquad 4\text{-}4$$

$$h_4 = \frac{1}{4}(1+r)(1-s) \qquad 4\text{-}5$$

Elements can have curved boundaries and another important advantage is the ease with which element displacements are constructed for isoparametric formulation (Bathe, 1982). The element displacements are interpolated the same way as geometry, namely,

$$u = \sum_{i=1}^{q} h_i u_i \text{ and } v = \sum_{i=1}^{q} h_i v_i \qquad 4\text{-}6$$

where u and v are the local element displacements at any point and u_i, v_i, $i = 1, \ldots, q$ are the corresponding element displacements at the node (Bathe, 1982).

The element stiffness matrix is evaluated by calculating the strain-displacement transformation matrix. With respect to the local coordinate system, element strains are obtained in terms of derivatives of element displacements. Since element displacements are defined by Equation 4-6 using natural coordinate system, we need to relate the x and y derivatives to the r and s derivatives. As such, Equation 4-1 is of the form,

$$x = f_1(r,s) \text{ and } y = f_2(r,s) \qquad 4\text{-}7$$

The inverse relationship is expressed as,

$$r = f_3(x,y) \text{ and } s = f_4(x,y) \qquad 4\text{-}8$$

The required derivatives are $\partial/\partial x$ and $\partial/\partial y$ and the Chain Rule is applied (Stein, 1987), which for $\partial/\partial x$ is as follows, with a similar analogy to $\partial/\partial y$,

$$\frac{\partial}{\partial x} = \frac{\partial}{\partial r}\frac{\partial r}{\partial x} + \frac{\partial}{\partial s}\frac{\partial s}{\partial x} \qquad 4\text{-}9$$

Calculating Equation 4-9 requires computing $\partial r / \partial x$ and $\partial s / \partial x$. However, this requires evaluating Equation 4-8, which can be difficult to establish (Bathe, 1982; Pande, et al, 1990). Using the chain rule, the required derivatives are evaluated using the following expression in matrix notation (Bathe, 1982; and Pande, et al, 1990):

$$\begin{bmatrix} \frac{\partial}{\partial r} \\ \frac{\partial}{\partial s} \end{bmatrix} = \begin{bmatrix} \frac{\partial x}{\partial r} & \frac{\partial y}{\partial r} \\ \frac{\partial x}{\partial s} & \frac{\partial y}{\partial s} \end{bmatrix} \begin{bmatrix} \frac{\partial}{\partial x} \\ \frac{\partial}{\partial y} \end{bmatrix} \tag{4-10}$$

Equation 4-10 is more commonly expressed in matrix notation as,

$$\frac{\partial}{\partial r} = J \frac{\partial}{\partial x} \tag{4-11}$$

where [J] is defined as the Jacobian operator which relates the natural coordinate derivatives to the local coordinate derivatives. Bathe (1982) also notes that the Jacobian operator can also be found using Equation 4-1,

$$\frac{\partial}{\partial x} = J^{-1} \frac{\partial}{\partial r} \tag{4-12}$$

This requires that the inverse of the Jacobian operator exist. Bathe (1982) notes that the inverse will exist, provided that there is a unique correspondence between the natural and local element coordinates. However, this requirement will not be satisfied if there is too much element distortion or the element folds back upon itself (Bathe, 1982). For [J] to be nonsingular, all interior angles must be smaller than 180 degrees (Bathe, 1982).

Equation 4-6, along with Equation 4-12, can be used to evaluate $\partial u/\partial x$, $\partial u/\partial y$, $\partial v/\partial y$, and $\partial v/\partial y$ and therefore are used to create the strain-displacement transformation matrix [*B*],

$$\varepsilon = B\hat{u} \tag{4-13}$$

where [$\hat{u}$] is the vector listing the element nodal point displacement of Equation 4-6 and [*J*] affects the element in [*B*]. The elements of [*B*] are a function of the natural coordinates r and s. The fundamental core of FEM is the element stiffness matrix, which is as follows for plain strain conditions (Bathe, 1982; Pande, et al, 1990; and SIGMA/W, 2007):

$$K = t\int_A [B]^T [C][B]dA \tag{4-14}$$

where *t* is the element thickness and [*C*] is the element property or constitutive matrix, which is further discussed in Section 4.1.1.

4.1.1 Stress-Strain Relationships

The constitutive matrix relates stresses to strains by considering the material properties of the element. Equation 4-15 displays the constitutive matrix for a linear elastic, plain strain problem (Bathe, 1982).

$$[C] = \frac{E(1-\nu^2)}{(1+\nu)(1-2\nu)}\begin{bmatrix} 1 & \frac{\nu}{1-\nu} & 0 \\ \frac{\nu}{1-\nu} & 1 & 0 \\ 0 & 0 & \frac{1-2\nu}{2(1-\nu)} \end{bmatrix} \tag{4-15}$$

Duncan's (1996) state-of-the-art treatise regarding FEM modeling for geotechnical engineering applications presented 20 linear-elastic, 19 multi-linear elastic, 21 hyperbolic elastic, and 17 elasto-plastic / elasto-visco-plastic FEM stress-strain models that were developed by others. These models were created to study various dam and embankment problems regarding incremental construction stress-strain and / or post-construction stress-strain. Selecting the appropriate soil stress-strain property depends on the type of relationship that is most suitable for the conditions analyzed. Duncan (1996) indicates that:

- The principle advantage of linear elastic analyses is simplicity; however their shortcoming is that it is not a good model for the actual stress-strain behavior of soils, except at low stress levels and small strains.

- Multi-linear elastic stress-strain analyses use two or more straight lines to model soil behavior. However, the models must be developed on a case-by-case basis to approximate the stress-strain curve of a particular soil. Because they model non-linear stress-strain behavior, Duncan (1996) indicates that they offer some potential for studying the development of local failures within and around slopes. Duncan (1996) indicates that it is possible to infer likely crack locations based on zones of tension computed in analyses.

- Elastoplastic stress-strain relationships are useful in cases where undrained conditions are analyzed in terms of effective stresses and the accuracy of the analyses depends on reasonable predictions of the changes in pore pressures caused by changes in total stress. Elastoplastic and elastoviscoplastic stress-strain relationships have the advantage that

they model more realistically the behavior of soils close to, at, and after failure. However, they have the limitation of being more complex.

- Hyperbolic stress-strain relationships can be used to model nonlinear behavior. Parameters used to develop the model have physical significant and can be evaluated using the triaxial tests. However, they have the limitation that they are inherently inelastic and do not model plastic deformation in a fully logical manner.

Wyllie and Mah (2006) indicate that linear elastic-perfectly plastic stress-strain relations are the most commonly used rock mass material models.

4.1.2 Numerical Integration

A global stiffness matrix is evaluated as a summation of the individual element stiffness matrices over all the elements in the mesh. Each element stiffness matrix is evaluated using numerical integration. To carry out numerical integration, the integral form of the element stiffness matrix,

$$K = t\int_A [B]^T [C][B]dA \qquad 4\text{-}16$$

is replaced with the following expression,

$$\sum_{j=1}^{n} [B_j]^T [C_j][B_j]\det|J_j|(W_{1j})(W_{2j}) \qquad 4\text{-}17$$

where j is the integration point, n is the total number of integration points, $\det|J_j|$ is the determinant of the Jacobian matrix, and W_{1j} and W_{2j} are the weighting factors which are chosen to obtain the maximum accuracy in the integration. An important numerical integration procedure in which both the positions of the sampling points and the weights have been

optimized is Gauss quadrature. This scheme requires *n* unequally spaced sampling points and integrated exactly a polynomial of order at most (2*n*-1) (Bathe, 1982). However, for larger *n* the solution becomes cumbersome and it is expedient to use Legendre polynomials, which is termed the Gauss-Legendre integration procedure. This procedure is commonly used in isoparametric finite element analysis (Bathe, 1982) and their values are readily available in the literature (Bathe, 1982, SIGMA/W, 2007). For ready reference, Table 4.1 presents the node locations and weightings for a four node quadrilateral, with node locations corresponding to the node locations identified in Figure 4.2 (SIGMA/W, 2007).

Table 4.1. Node Points and Weightings for Four Node Quadrilateral.

Node	*r*	*s*	W_1	W_2
1	+0.57735	+0.57735	1.0	1.0
2	-0.57735	+0.57735	1.0	1.0
3	-0.57735	-0.57735	1.0	1.0
4	+0.57735	-0.57735	1.0	1.0

A choice of different Gaussian quadrature rules exist for this integration, the order of which has considerable bearing on the final results. The "complete" rule for any two dimensional quadratic displacement element uses three strategically placed points in each spatial direction. The "reduced" integration rule is one order less. Under certain conditions, it is acceptable to use four-point integration for quadrilateral elements which have secondary nodes. This procedure is called reduced integration and is described in Bathe (1982), and Zienkiewicz and Taylor (1989). For example, reduced integration may yield more accurate results in nearly incompressible elasticity and in elements under flexure (Hellen, 2001). In addition, selective use of reduced integration can greatly reduce the required number of computations (SIGMA/W, 2007). Hellen

(2001) also notes that reduced integration is well known to be more accurate than the complete rule, which can exhibit an effect known as “locking” in many applications and particularly so in fracture related problems. Bathe (1982) confirms this and also notes that a great deal of research effort has been spent to evaluate the optimum integration order and scheme for isoparametric finite element analysis. The integration points are known as Gauss points and are also the locations where stresses are most accurately calculated in each element (Bathe, 1982). Figure 4.3 indicates the location of Gauss points for a typical rectangular element.

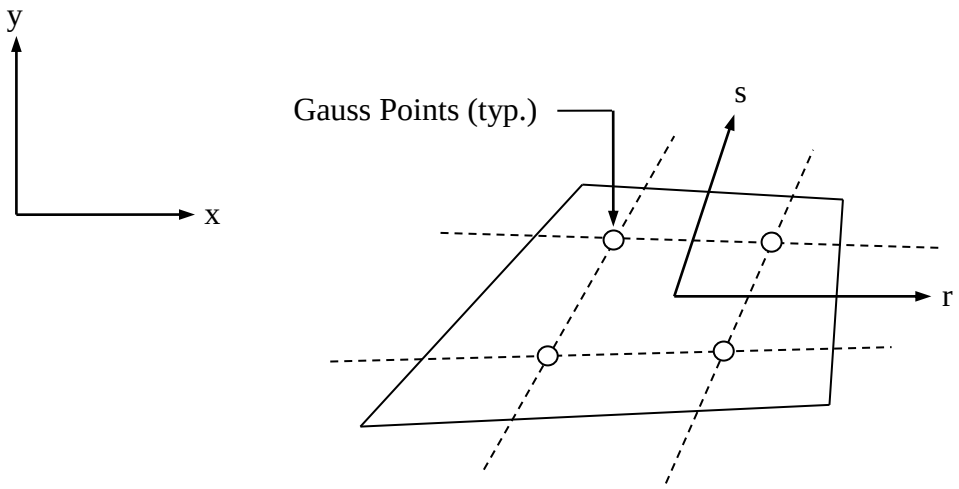

Figure 4.3. Gauss Numerical Integration over a Typical Rectangular Element.

It is also possible to use higher order (three-point and nine-point) integration with elements that have no secondary nodes. However, in this case, the benefits of using higher order integration are marginal, particularly for quadrilateral elements. Nine-point integration for quadrilateral elements involves substantially more computing than four point integration, and there is little to be gained from the additional computations (Hellen, 2001). As a general rule,

quadrilateral elements should have secondary nodes to achieve significant benefits from the nine point integration (SIGMA/W, 2007).

The situation is slightly different for triangular elements. Using one-point integration implies that the material properties and strains are constant within the element. This can lead to poor performance of the element, particularly if the element is in a region of large stress gradients (SIGMA/W, 2007). Using three point integration, even without using secondary nodes, can improve the performance since material properties and gradients within the elements are distributed in a more realistic manner. The use of three point integration in triangular elements with no secondary nodes is considered acceptable in a mesh that has predominantly quadrilateral elements (SIGMA/W, 2007). This approach is not recommended if the mesh consists primarily of triangular elements with no secondary nodes (SIGMA/W, 2007).

4.1.3 Incremental Analyses for Geotechnical Applications

Static geotechnical problems in FEM require the use of incremental analysis techniques (Duncan, 1996). Incremental analyses provide a convenient means of modeling two very important aspects in geotechnical engineering, namely changes in geometry and nonlinear stress-strain behavior. Geometry is changed by adding or removing elements to a mesh. However, prior to changing geometric conditions, initial stress conditions must first be established in the FEM. Initial stresses for finite element analyses are needed for the following reasons (Duncan, 1996):

- For incremental analyses, the changes in stress calculated during each increment are added to the stress at the beginning of the increment to evaluate the stress at the end. As such, to begin this process, it is necessary to know the initial stress;

- The stiffness of the soil depends on the stresses in the soil; and

- The forces that are applied to simulate excavation of the soils are calculated using the before excavation stresses on the boundary of the excavation. To calculate these forces, it is necessary to know the initial stresses.

A significant parameter used in incremental analyses is the at-rest horizontal earth pressure coefficient, k_o. Field and laboratory studies of heavy overconsolidated clays and shales show that they are characterized by large horizontal stresses and thus have a greater tendency to laterally rebound more than normally consolidated clays.

4.1.4 Mesh Optimization

FEM are based on the concept of subdividing a continuum into small pieces, describing the behavior of the individual pieces, and then reconnecting all the pieces to represent the behavior of the continuum as a whole. The process of subdividing the continuum into smaller pieces is known as meshing where the individual pieces are known as finite elements. An appropriate finite element mesh is problem-dependent and there are no hard and fast rules for how to create a mesh (SIGMA/W, 2007). Moreover, Griffiths (2009) indicates that there is no golden rule to mesh density; a mesh needs to be "refined enough" to give acceptable accuracy considering the reliability of the input data.

Bathe (1982) notes that the amount of stress discontinuities between elements are a measure of the “appropriateness” of the finite element idealization used. The overall objective in the design of a finite element mesh is that in an area where high solution accuracy is required, the stress discontinuities between elements should be small, whereas larger stress discontinuities can

be tolerated away from the area of interest. The actual amount of stress discontinuities that can be tolerated depends on the accuracy required in the analysis. Bathe (1982) notes that another consideration in the design of a finite element mesh layout is that the performance of the isoparametric elements is generally best when they are used without distortion.

The use of FEM for geotechnical fracture mechanic investigations does require careful consideration. Because of the singular nature of a crack tip, stress gradients occur which require graded element meshes to optimize overall accuracy. Thus, as the crack tip is approached, the elements should get smaller and smaller. However, practical mesh refinements do not need to be too severe provided that quadratic (or higher) displacement elements are used with reduced integration (Hellen, 2001). The best overall elements for two dimensional meshes are the isoparametric elements, particularly those with quadratic displacement and pseudo-linear stress variations, which appear as either six nodded triangles or eight-noded quadrilaterals (Hellen, 2001; Griffiths and Lane, 1999; Griffiths, 2000; and Ingraffea and Heuze, 1980).

Literature reviews of published slope stability FEM studies indicate that six to twelve elements with eight-node quadrilaterals using reduced integration represent an appropriate distribution over the slope height (Duncan and Dunlop, 1969; Dunlop and Duncan, 1970; Lee, Lo, and Lee, 1988; Griffiths and Lane, 1999; Griffiths, 2000; Khatri and Kumar, 2009). Duncan and Dunlop (1969) used a non-uniform mesh that consisted of eight quadrilateral elements over the slope height to study stress concentrations associated with a vertical cut made in stiff clay. Additionally, Lee, Lo and Lee (1988) used six, eight node quadrilateral elements equally spaced over the height of the slope to investigate tension crack effects. Based on the available literature, Figure 4.4 presents a straightforward FEM model that was developed to study the influence that mesh concentration has on vertical stress predictions.

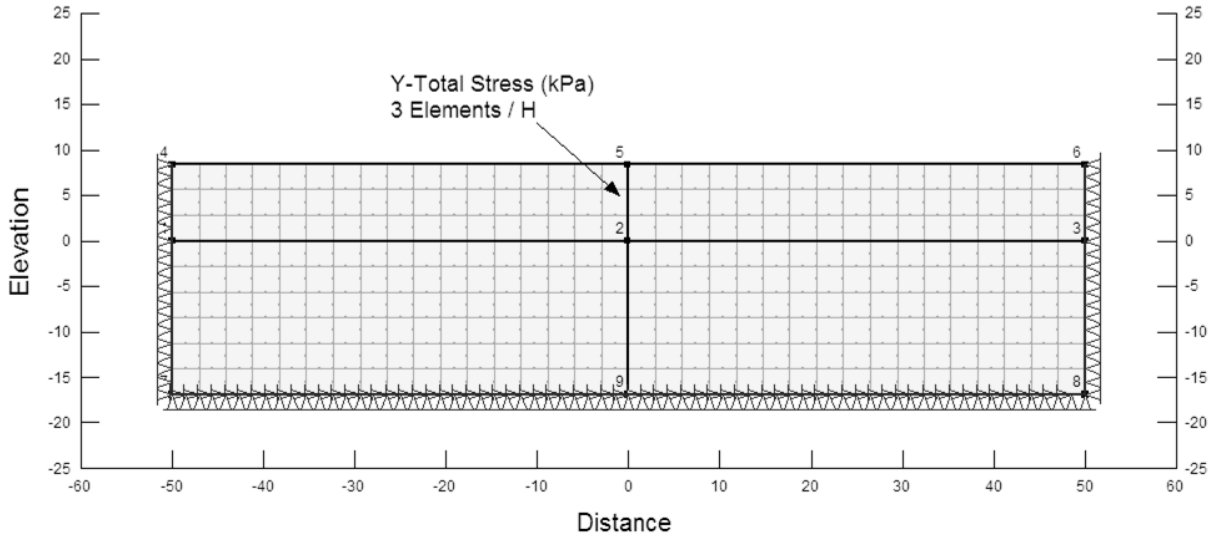

a) Model used to establish initial stress conditions.

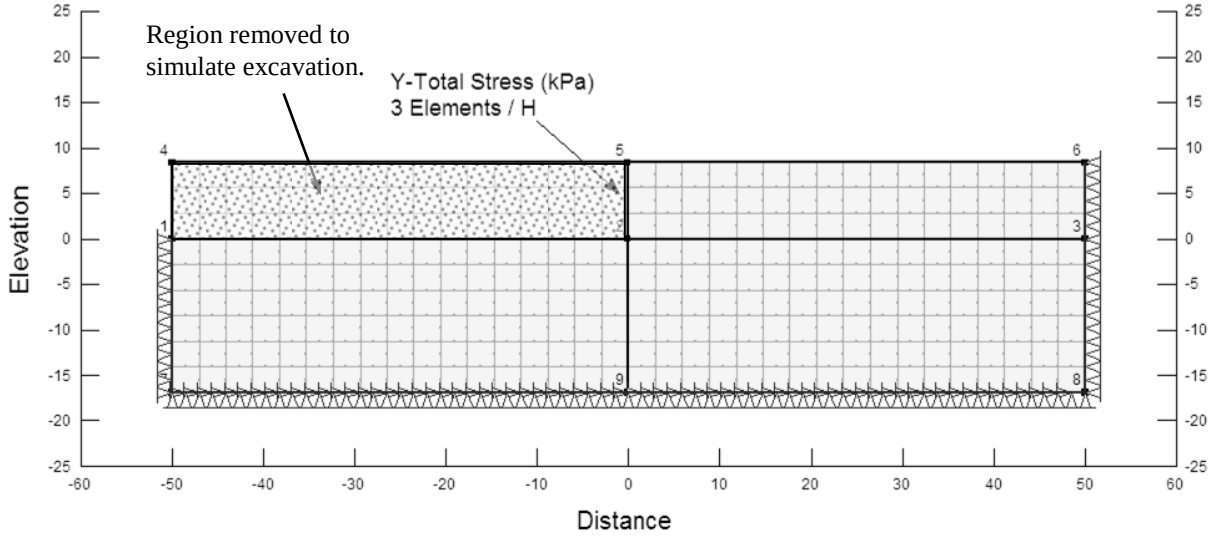

b) Model used to predict vertical stress conditions.

Figure 4.4. FEM Model used for Mesh Concentration Study.

The FEM model used a unit weight, γ, and an earth pressure coefficient, k_o, that were constant; thus the initial horizontal and vertical stresses increase linearly with depth. The model used eight-node quadrilateral elements with reduced integration. The initial mesh concentration consisted of 3 elements over the slope height, as noted on Figure 4.4. Initial stresses were calculated (Figure 4.4(a)) and elements were removed to simulate excavation (Figure 4.4(b)). Vertical stress values (σ) obtained from the FEM model at an arbitrary distance of 20 meters left and 20 meters right of the cut slope were compared to simple hand calculation values considering the following expression,

$$\sigma = (\gamma)(depth) = \left(20.42 \frac{kN}{m^3}\right)(depth)$$

The model was then re-meshed using an increased element concentration over the slope height. Appendix B contains the FEM output sheets and Figures 4.5 and 4.6 presents a graphical summary of the analyses. The datum is the base of the excavation at the toe of slope.

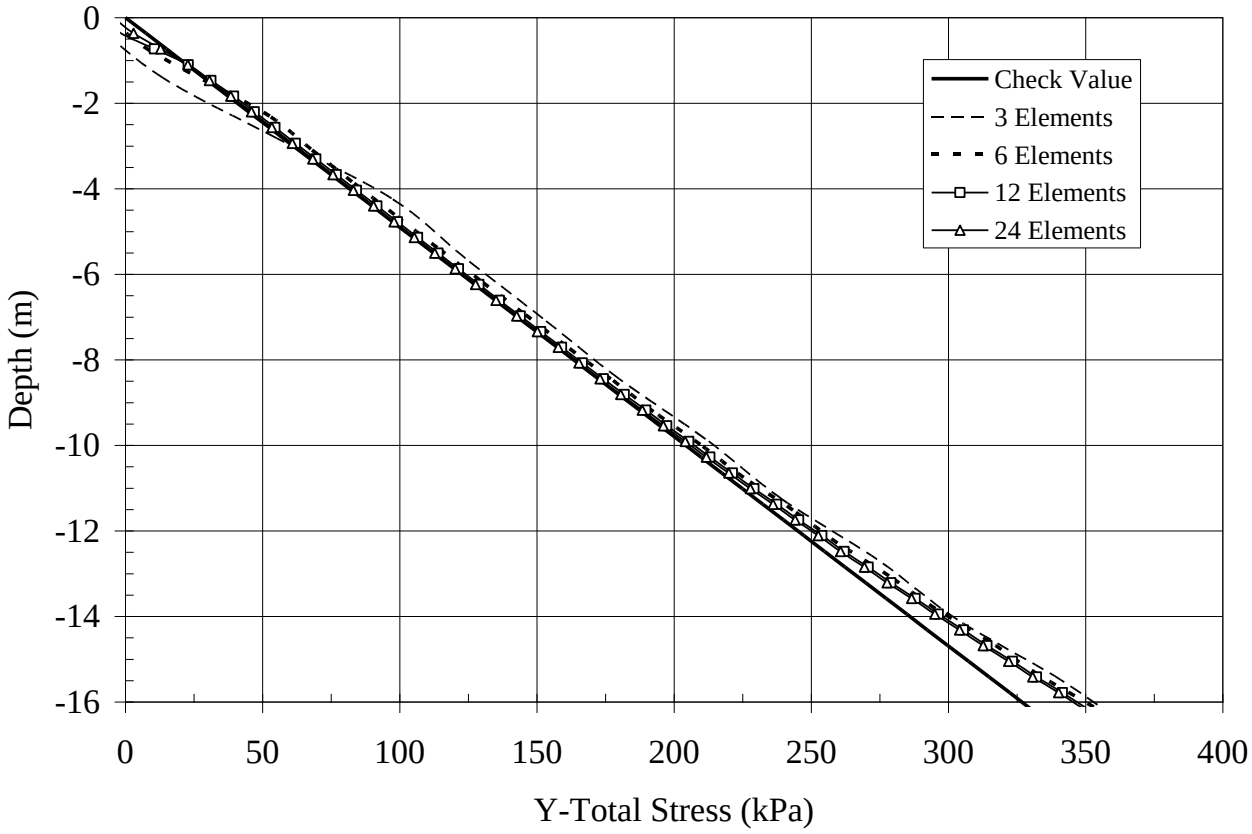

Figure 4.5. Comparison of Vertical Stress for Different FEM Element Concentrations, x = 20-m from Slope Face (Left).

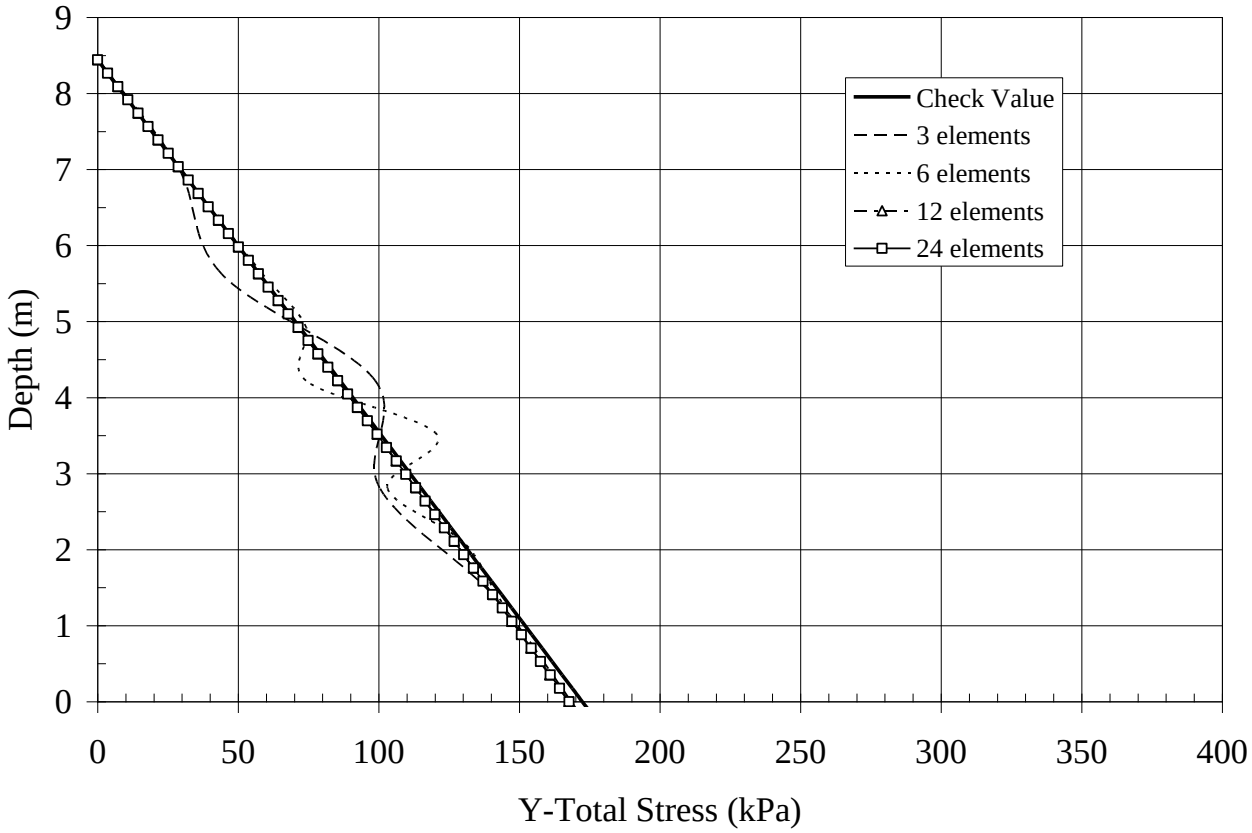

Figure 4.6. Comparison of Vertical Stress for Different FEM Element Concentrations, x = 20-m from Slope Face (Right).

Based on this study, the use of 3 and 6 elements over the slope height does not provide good agreement for a simple vertical stress profile. Concentrations greater than 12 elements over the slope height provide nearly identical results that are in good agreement with the hand calculation checks. Although this analysis is not comprehensive, it does demonstrate good agreement with Duncan and Dunlop (1969), Dunlop and Duncan (1970), Griffiths and Lane (1999), and Griffiths (2000), which used a similar mesh concentration consisting of 8 to 12 elements over the slope height to study stress gradients within the slope.

4.2 FINITE ELEMENT METHOD APPLIED TO GEOTECHNICAL FRACTURE MECHANICS PROBLEMS

The use of FEM to study geotechnical related fracture mechanics problems has been well documented (Hellen, 2001; Lee et al, 1988; Ingraffea and Heuze, 1980; Wyllie and Mah, 2006). Based on the results of finite element analysis, a procedure known as Substitution Methods can be used to calculate the main fracture parameters of LEFM (Hellen, 2001).

Substitution Methods for FEM fracture mechanic investigations consist of two methods, namely: displacement substitution and stress substitution. These analyses are conducted at the post-FEM analysis stage and use calculated displacements (at nodes) and stresses (at Gauss points). Referencing Figure 4.7, the Substitution Methods consider that for each point (r, θ), both (u, v) and (σ_θ, σ_r, and $\tau_{r\theta}$) are available and can be substituted in the LEFM equations. FEM analyses are conducted, and displacements and stresses are tabulated in the crack tip region. An advantage of the substitution method is that no special software coding is required to model node fracture through deformation (Hellen, 2001).

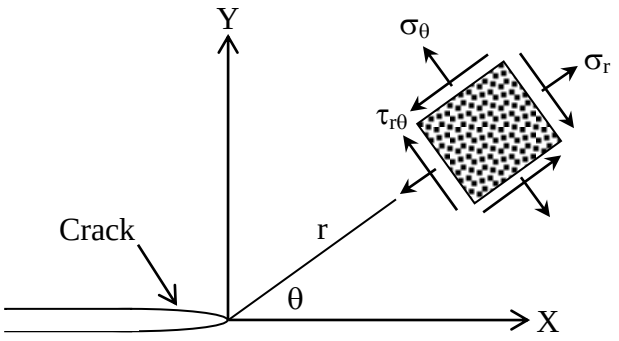

Figure 4.7. LEFM Reference Model.

Several finite element models have been used to study tension cracking in soils and they are based on substitution methods (Zienkiewicz, et al, 1968; Duncan and Dunlop, 1969; Dunlop and Duncan, 1970; Kawai, 1979; Naylor and Pande, 1981; and Lee, et al, 1988). These methods consider cracking of the soil medium by either imposition of zero tensile stresses or zero tensile stiffness on the cracked elements when their tensile strength has been exceeded. Lee et al (1988) conducted FEM analyses using a tensile strength criterion, whereby by computed principal tensile stresses were compared with an experimentally determined tensile strength to predict the onset of cracking of a stiff embankment on soft soil as well as an excavated clay slope.

Griffiths (2009) also indicates that for conventional slope stability analysis, the factor of safety can be obtained quite well using remarkably coarse meshes. However, for fracture mechanics problems where cracks may be opening up, the FEM model will require remeshing as the crack propagates and localized phenomena may govern the situation requiring a finer mesh (Griffiths, 2009).

4.3 SUMMARY FOR GEOTECHNICAL FRACTURE MECHANICS APPLICATIONS

The use of FEM for geotechnical fracture mechanic investigations requires careful consideration due to the singular nature of a crack tip. As the crack tip is approached, the elements should seemingly get smaller and smaller. However, practical mesh refinements do not need to be too severe provided that elements consist of isoparametric elements, particularly those with quadratic displacement and pseudo-linear stress variations, which appear as either six nodded triangles or eight-noded quadrilaterals. Where high solution accuracy is required, the stress discontinuities between elements should be small, however, the mesh concentration needs to consider the reliability of the input data. Mesh concentrations greater than 8 to 12 elements over a vertical slope height produce nearly identical vertical stress results. FEM analyses should use reduced integration, which has particular application to fracture related problems.

Substitution methods can be used with FEM analyses to study fracture mechanics; hence no special software is required. In particular, stress substitution method considers that for each point (r, θ), that the σ_θ, σ_r, and $\tau_{r\theta}$ are available and obtained at the Gauss points. Stress values can be tabulated and compared to failure criterion. Crack propagation will require re-meshing where cracks may open.

5.0 EVALUATION OF LABORATORY PROGRAM RESULTS USING FINITE ELEMENT METHOD AND FRACTURE MECHANICS APPROACHES

Three laboratory test models were created to study closed crack propagation under $\tau_{r\theta}$ and σ_{θ} loading conditions. The models consisted of two shear models and one vertical slope model with artificial cracks created in each model. The shear models consisted of clay on clay and sand on clay to create two different interfaces along the potential failure plane. The vertical slope model consisted of clay on clay with a pre-existing toe crack. Finite element models were developed in an effort to replicate the observed laboratory results and therefore validate the use of FEM for additional fracture mechanics studies.

5.1 DEVELOPMENT OF THE LABORATORY PROGRAM FINITE ELEMENT METHOD MODELS

The FEM models used a two dimensional mesh with isoparametric elements consisting of either six node triangles or eight-node quadrilaterals. The clay material utilized an elastic-plastic constitutive model which describes an elastic-perfectly plastic relationship. Stresses are directly proportional to strains until the yield point is reached; beyond yield, the stress-strain curve is perfectly horizontal. This constitutive model is most appropriate for clay slopes under undrained conditions, where both stress-strain relationships and the failure criteria are expressed in terms of total stresses (Dunlop and Duncan, 1970; Smith and Hobbs, 1974; Griffiths and Lane, 1999; and

Griffiths 2000). Table 5.1 indicates the six geotechnical parameters required to develop the elastic-plastic constitutive model.

Table 5.1. Elastic – Plastic Constitutive Model Parameters.

Model Parameters
E, Modulus of Elasticity
ν, Poisson's Ratio
c, Cohesion
ϕ, Friction Angle
ψ, Dilation Angle

Perhaps with the exception of the dilation angle (ψ), the parameters noted in Table 5.1 are relatively straightforward geotechnical material properties. The dilation angle affects the volume change of a soil during yield. It is well known that the volume change exhibited by a soil during yield is quite variable. Griffiths and Lane (1999), and Griffiths (2000) indicate that $\psi < 0$ for a medium dense material where the material would tend to exhibit some volume decrease during shear followed by a dilative phase in which $\psi > 0$, leading eventually to yield under constant volume conditions where $\psi = 0$. Griffiths (2000) notes that when $\psi = \phi$, then the plasticity flow rule is associated with frictional soil models predicting far greater dilation than is ever observed in reality. This will lead to increased failure load prediction, especially for confined problems such as bearing capacity (Griffiths, 1982). However, slope stability analyses are relatively unconfined and the choice of dilation angle is less important (Griffiths and Lane, 1999; and Griffiths, 2000). A value of $\psi = 0$, corresponding to a non-associated flow rule with zero volume change during yield enables slope stability analyses to give reliable factors of safety and

a reasonable indication of the location and shape of potential failure surfaces (Griffiths and Lane, 1999; and Griffiths, 2000). Additionally, it is well known that saturated, purely cohesive materials do not exhibit volume change when subjected to shear loading under undrained conditions (Craig, 1992; and Bowles, 1996).

5.1.1 Values of Parameters used for the FEM Analyses

The intent of the FEM analyses is to replicate the observed laboratory model results. FEM analyses for the laboratory shear models should indicate crack propagation along the existing failure plane due to shear failure. FEM analyses for the simulated vertical slope model should indicate crack propagation due to excessive tensile stress inclined from the existing toe crack. Aside from the concept that LEFM is based on materials which obey Hooke's law, the direction of crack propagation predicted by LEFM is independent of material properties. Crack propagation will occur when the material's shear strength or tensile strength has been exceeded; however the direction of crack propagation is independent of these parameters. With this in mind, FEM models considered standardized material properties for all models used in this research. The use of standardized material properties allowed comparison between models to observe propagation behavior under different load conditions.

The clay material properties used for the FEM models were derived from laboratory testing of a geologic stratum known locally as the Pittsburgh Red Bed (URS, 2005). It is important to note that the Pittsburgh Red Bed formation is highly variable and generalized data regarding this formation is not practical (Hamel and Flint, 1972; Hamel and Adams, 1981; Hamel, 1998; Kutschke, et al, 2007 and 2007; and Hamel, 2009). Shear strength properties depend on whether the stratum is weathered or unweathered (as opposed to colluvial or residual soils derived from

this formation) as well as dependent on composition, degree and types of fissures and fractures at both macro & micro levels (Hamel, 2009). The selected values used for the FEM laboratory FEM models are presented in Table 5.2. The parameter values for sand are representative of a medium dense sand material (AASHTO, 1996, 2007).

Table 5.2. Geotechnical Parameters and Values Used for the Laboratory FEM Models.

Geotechnical Parameter	Material and Parameter Values	
	Clay	Sand
E, Modulus of Elasticity	177,100 kPa	44,375 kPa
ν, Poisson's Ratio	0.10 and 0.45	0.35
c, Cohesion	86.2 kPa	0
ϕ, Friction Angle	0°	30°
ψ, Dilation Angle	0°	0°
γ, Unit Weight	20.42 kN/m^3	18 kN/m^3

Table 5.2 indicates that the clay analyses considered two different values for the Poisson's ratio. A ν = 0.45 is representative of a saturated clay (Kulhawy, et al, 1983; AASHTO, 1996, 2007; and Bowles, 1996). It is recognized that an ideal saturated clay exhibits a ν = 0.50, however, the use of 0.50 will result in numerical stability problems for FEM modeling. The reason for the numerical problems is that, and recalling the following term in Equation 4-15, $E/[(1+\nu)(1-2\nu)]$ which tends toward infinity as $(1-2\nu)$ tends towards zero when $\nu \rightarrow 0.50$. A value of ν = 0.10 is representative of an unsaturated, brittle clay (Bowles, 1996).

5.1.2 FEM Slip Elements

The laboratory shear model for the clay on clay condition considered a closed crack located along the plane of horizontal movement. It is well known that closed cracks within cohesive materials tend to exhibit reduced shear strength properties (Bjerrum, 1967; Duncan and Dunlop, 1969; Skempton, 1964; Skempton and LaRochelle, 1965; Burland, et al, 1977). A closed crack for these FEM models utilized a slip surface element, in particular a quadrilateral slip surface element. The slip surface element is modeled as a combination of four bar elements. Figure 5.1 presents a typical slip surface element with the long axis (x′) inclined with respect to the global axis (X), and nodes 1, 2, 3 and 4 labeled.

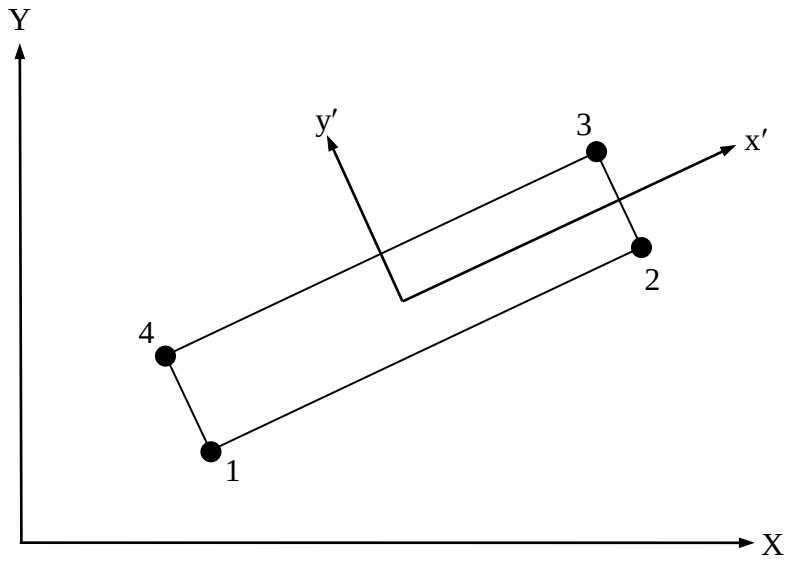

Figure 5.1. Typical Slip Surface Element.

The slip surface element considered two bar elements with normal stiffness (K_N) in the local, normal y′-direction 1-4 and 2-3, and two bar elements with tangential stiffness (K_T) in the local x′-direction 1-2 and 4-3. When formulating the element stiffness matrix [K], instead of evaluating the integral $\int [B]^T [C][B] dv$, the local stiffness matrix [K′] is first evaluated by assigning stiffness values K_T and K_N directly to the appropriate location in the matrix (SIGMA/W, 2007). [K′] is then rotated to the global coordinate system to obtain [K].

This constitutive model is in essence equivalent to a spring model where normal springs keep the opposing sides apart and tangential springs control lateral slip. When the mobilized shear resistance exceeds the available shear resistance, the tangential springs are removed and replaced with tangential nodal forces representing the available shear resistance. Stresses in the slip element are obtained from neighboring elements above and below from the Gauss points to the interface nodes. Then interpolation from the nodes to the slip element Gauss points using shape functions. The available shear resistance is controlled by the cohesion, and the friction angle and normal stress on the slip surface using shear strength properties that represent reduced or residual values. In the case of $\phi = 0°$, the available shear resistance is controlled by cohesion.

5.1.3 Failure Plane Development and / or Crack Propagation

Geotechnical failure resulting in the development of a failure plane or crack propagation is taken as the limiting shear stress on the potential failure surface as discussed by Duncan and Dunlop (1969), Griffiths and Lane (1999), and Griffiths (2000). That is, once the shear strength of the material is exceeded, either a failure plane develops or the crack propagates if the crack already exists. Figure 5.2 presents a typical Mohr-Coulomb failure criterion envelope for a $\phi = 0°$

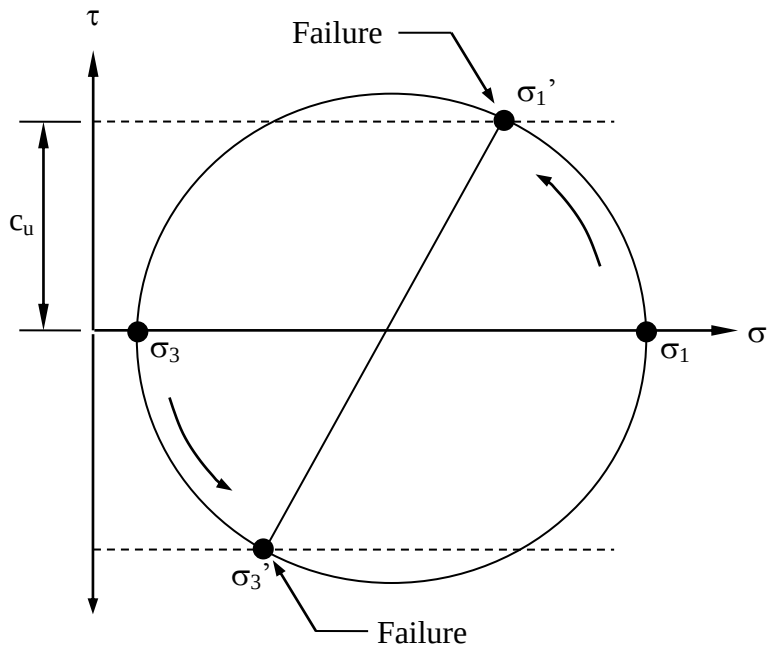

Figure 5.2. Mohr-Coulomb Failure Criterion Envelope for a $\phi = 0°$ Material.

material. The initial state of stress of an element may be given as σ_1 and σ_3 to represent the in-situ horizontal and vertical stress conditions for an overconsolidated material, respectively. Values of σ_1 and σ_3 will change as the soil element undergoes shear loading. Failure occurs when the stress conditions reach the undrained cohesive strength for a $\phi = 0°$ material.

5.1.4 Coalesce of Micro-Cracks

The development of a failure plane results from coalesce of micro-cracks. At low displacement levels, Skempton (1966) notes that stiff clay will develop Riedel slip discontinuities, which are generally inclined to the direction of shear. As shear displacement continues, a new set of discontinuities develop which are termed Thrust or P- discontinuities and these develop at a flatter angle than the Riedel slip discontinuities. Finally, at large shear displacement levels, the

Riedel and Thrust discontinuities coalesce and form an undulating, continuous sliding surface (Skempton, 1966). The successive stages in the development of a shear zone are shown in Figure 5.3. FEM analyses are used to idealize and predict the development and propagation of this final slip surface without consideration for the initial Riedel or Thrust discontinuities.

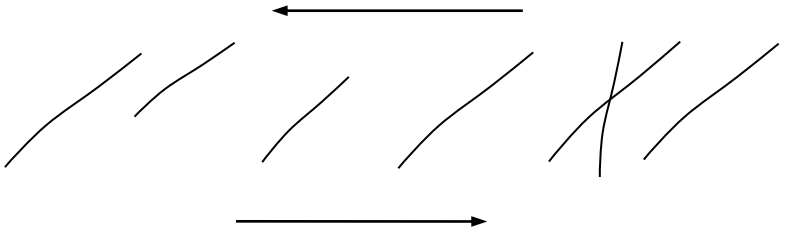

Stage 1 – Riedel slip discontinuities develop.

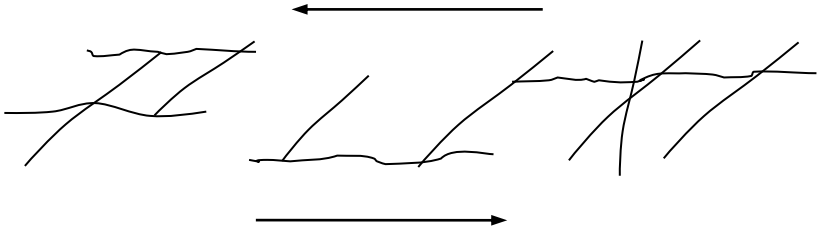

Stage 2 – Thrust discontinuities develop.

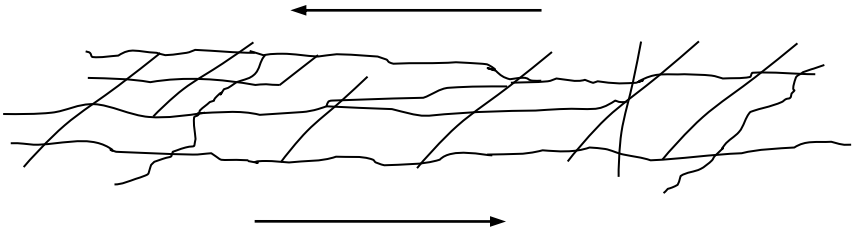

Stage 3 – Coalesce of microcracking.

Figure 5.3. Successive Development of a Shear Zone.

5.2 SHEAR MODEL

The shear model represented a fracture mechanics shear stress - closed crack condition. The FEM model has been scaled-up from the laboratory model (Duncan and Dunlop, 1969; Griffiths and Lane, 1999; Griffiths 2000; Khatri and Kumar, 2009). FEM analyses were performed in stages, with the first stage used to create the in-situ stress conditions (Duncan, 1996), which is shown as Figure 5.4. The model used fixed boundary conditions at the base with rollers along

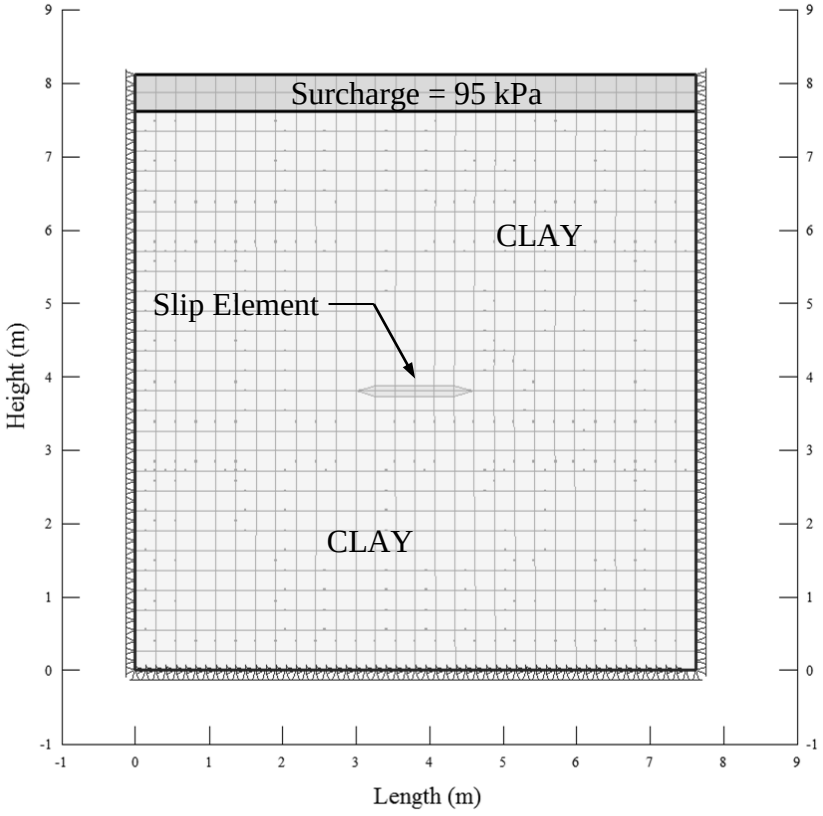

Figure 5.4. Clay on Clay FEM Shear Model.

the sides during the initial stages to establish the in-situ stress. After the initial stresses were established, the second stage applied a normal stress of 95 kPa in the form of a surcharge load, as noted in Figure 5.4. The normal stress created a downward displacement as the model deformed under load and y-displacements were fixed along the top boundary condition for subsequent stages. This procedure very closely mimicked the laboratory experiment procedure using the Plane Stress Direct Shear Apparatus. The FEM model then applied lateral displacement increments. Figure 5.5 indicates the FEM boundary conditions used during application of the lateral increments.

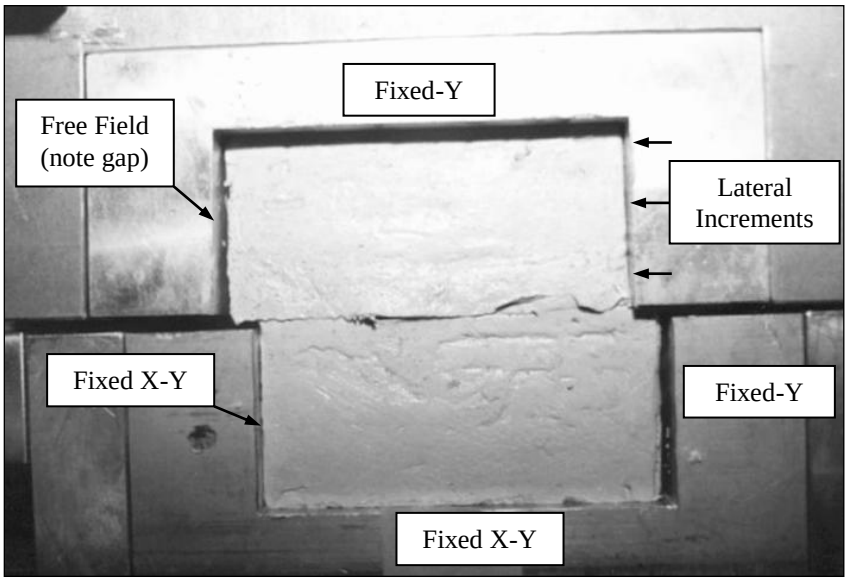

Figure 5.5. FEM Boundary Conditions.

5.2.1 Clay on Clay Shear Model Results

Analyses considered three different shear strength conditions along the slip surface element to represent a closed crack condition. The shear strengths for the slip elements were as follows: no cohesive strength reduction, an arbitrary reduction in the cohesive strength of 25%, and an arbitrary shear strength reduction in cohesive strength of 50%. The no cohesive strength reduction case served as a baseline analysis to understand how a reduction in cohesive strength influences crack propagation as well as the influence that a pre-existing crack has on failure propagation.

The results of the FEM analyses were drawn with 4 kPa shear strength contours at each load increment for shear stress values greater than the full cohesive strength, which was 86.2 kPa. This condition represents a zone of failure where a failure plane has developed and / or the crack propagates. The following figures present the results of the FEM analyses at various displacement increments (all figures magnified by 50 for clarity purposes):

- Figure 5.6 – Poisson's ratio = 0.1 representing a brittle clay with no cohesive strength reduction at the slip element.

- Figure 5.7 – Poisson's ratio = 0.1 representing a brittle clay with a 25% cohesive strength reduction at the slip element and full cohesive strength everywhere else.

- Figure 5.8 – Poisson's ratio = 0.1 representing a brittle clay with a 50% cohesive strength reduction at the slip element and full cohesive strength everywhere else.

- Figure 5.9 – Poisson's ratio = 0.45 representing a saturated clay with no cohesive strength reduction at the slip element.

- Figure 5.10 – Poisson's ratio = 0.45 representing a saturated clay with a 25% cohesive strength reduction at the slip element and full cohesive strength everywhere else.

- Figure 5.11 – Poisson's ratio = 0.45 representing a brittle clay with a 50% cohesive strength reduction at the slip element and full cohesive strength everywhere else.

Figures are presented in the subsequent pages.

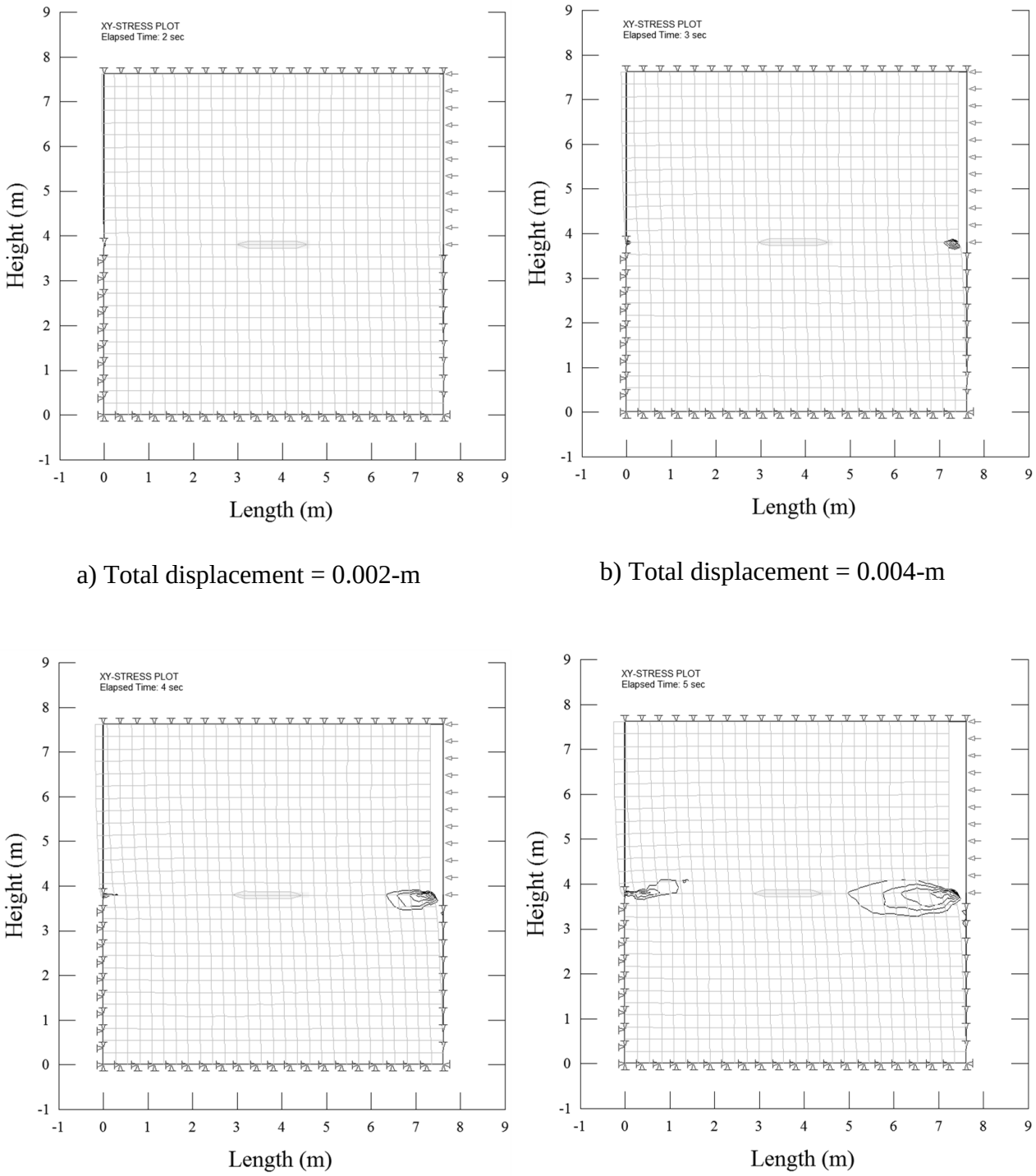

a) Total displacement = 0.002-m

b) Total displacement = 0.004-m

c) Total displacement = 0.006-m

d) Total displacement = 0.008-m

Figure 5.6. Shear Stress Contours (4 kPa) Indicating Shear Failure Zones for Clay on Clay FEM Shear Model with $\nu = 0.10$ and No Cohesion Reduction along Crack.

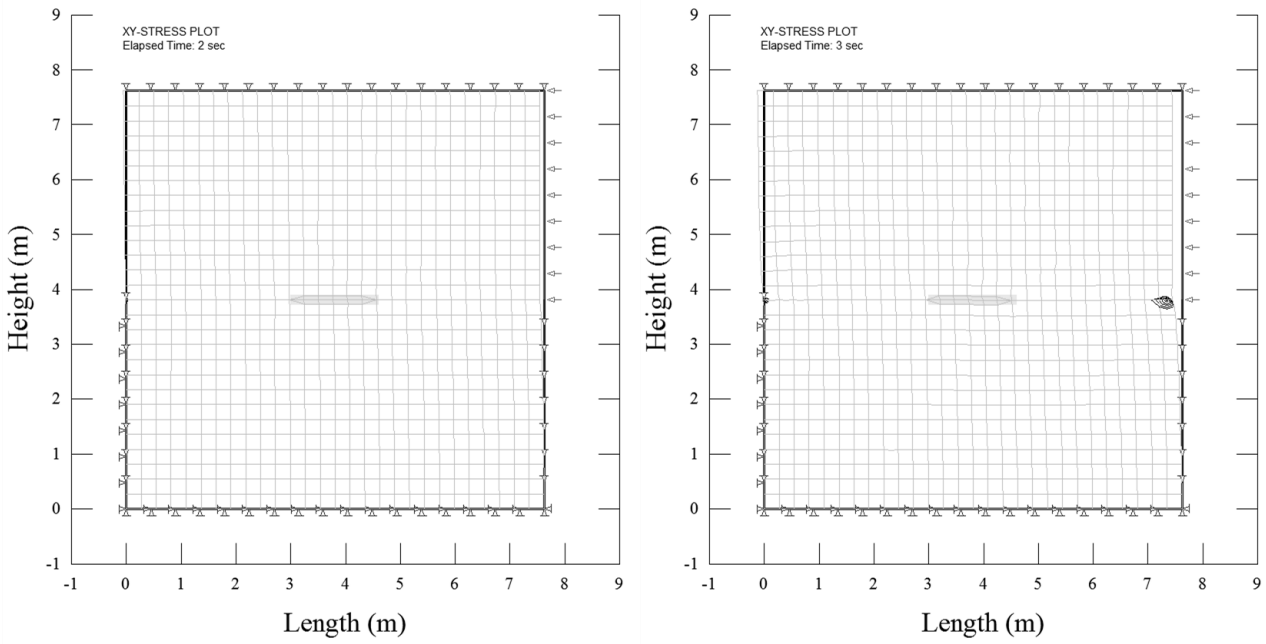

a) Total displacement = 0.002-m

b) Total displacement = 0.004-m

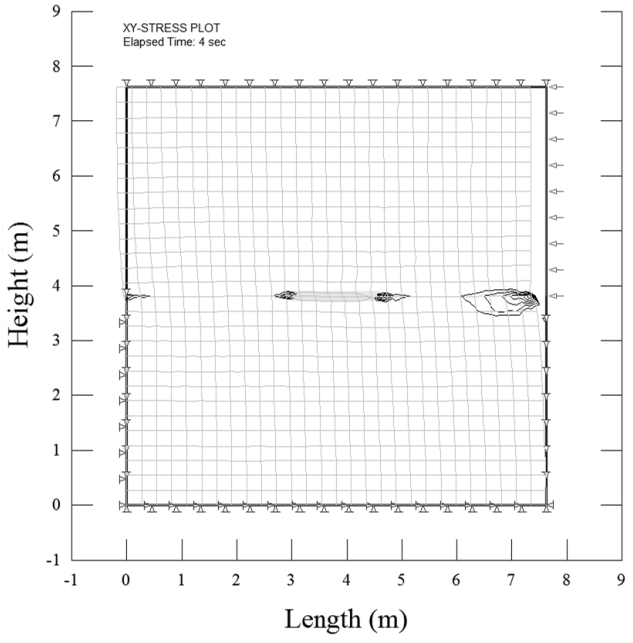

c) Total displacement = 0.006-m

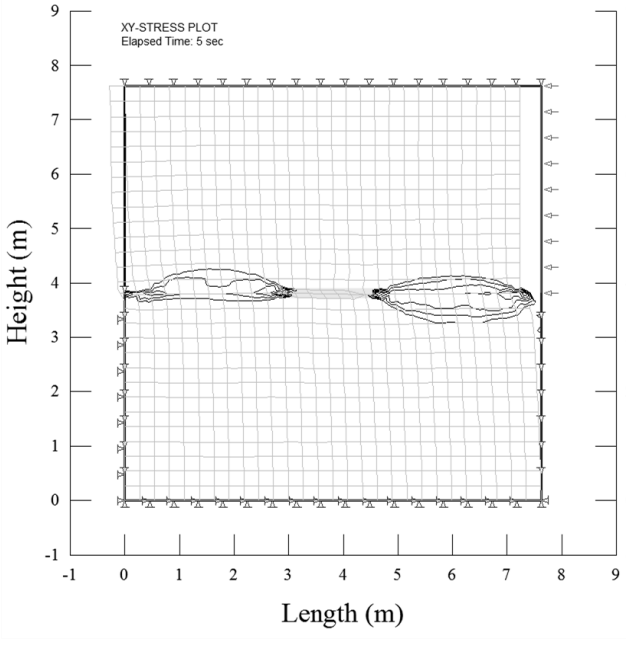

d) Total displacement = 0.008-m

Figure 5.7. Shear Stress Contours (4 kPa) Indicating Shear Failure Zones for Clay on Clay FEM Shear Model with $\nu = 0.10$ and 25% Cohesion Reduction along Crack.

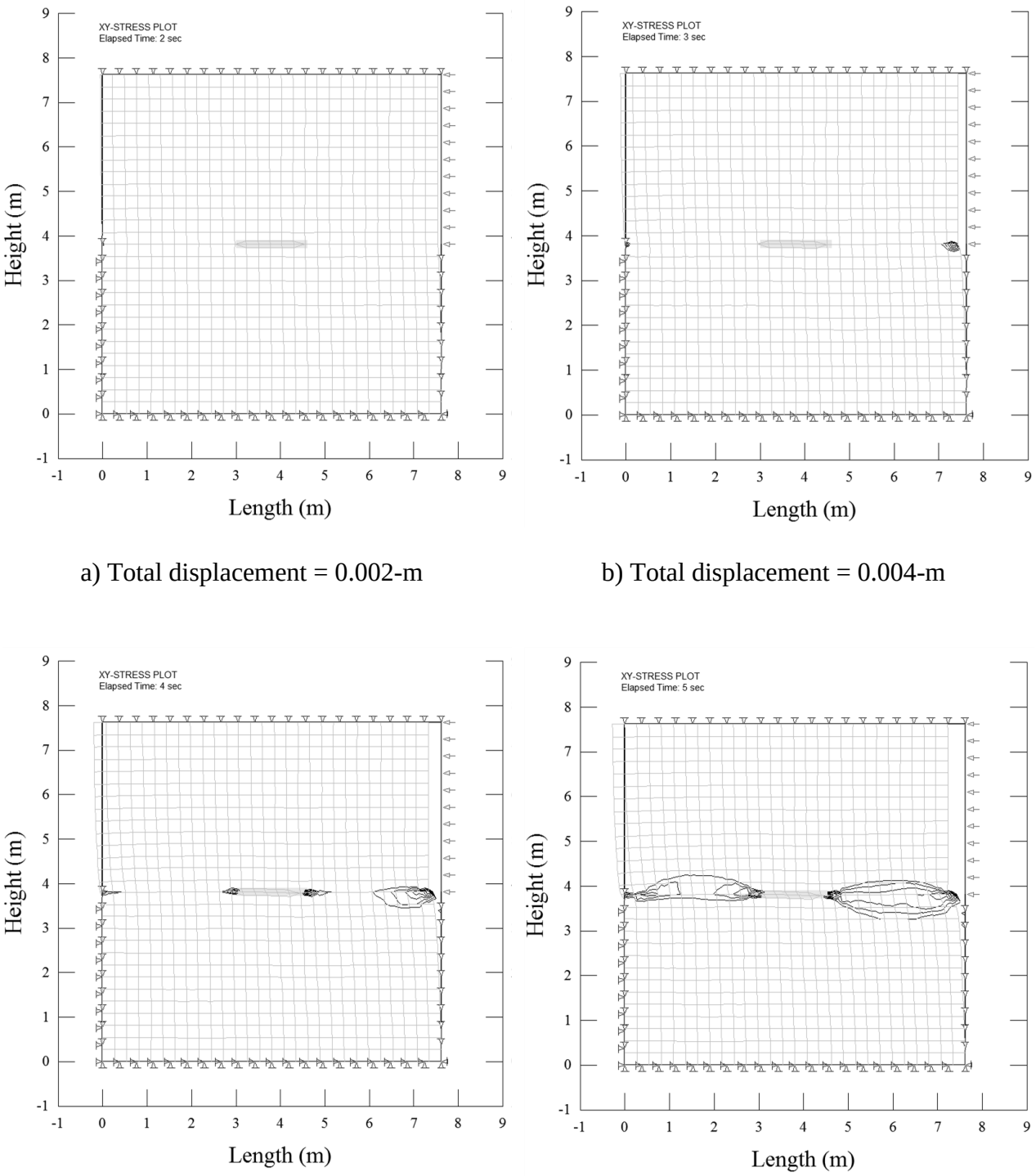

a) Total displacement = 0.002-m

b) Total displacement = 0.004-m

c) Total displacement = 0.006-m

d) Total displacement = 0.008-m

Figure 5.8. Shear Stress Contours (4 kPa) Indicating Shear Failure Zones for Clay on Clay FEM Shear Model with $\nu = 0.10$ and 50% Cohesion Reduction along Crack.

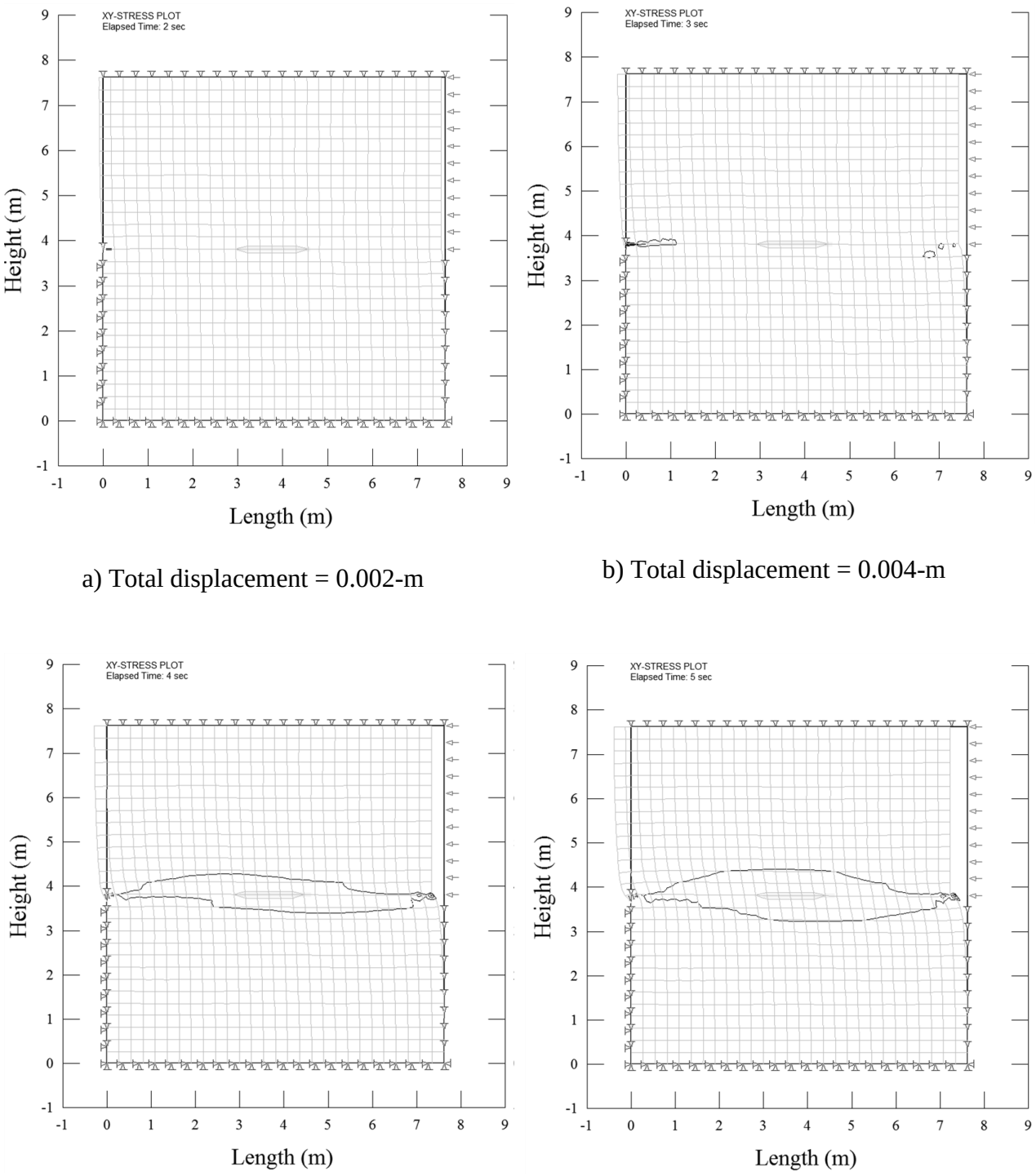

a) Total displacement = 0.002-m

b) Total displacement = 0.004-m

c) Total displacement = 0.006-m

d) Total displacement = 0.008-m

Figure 5.9. Shear Stress Contours (4 kPa) Indicating Shear Failure Zones for Clay on Clay FEM Shear Model with $\nu = 0.45$ and No Cohesion Reduction along Crack.

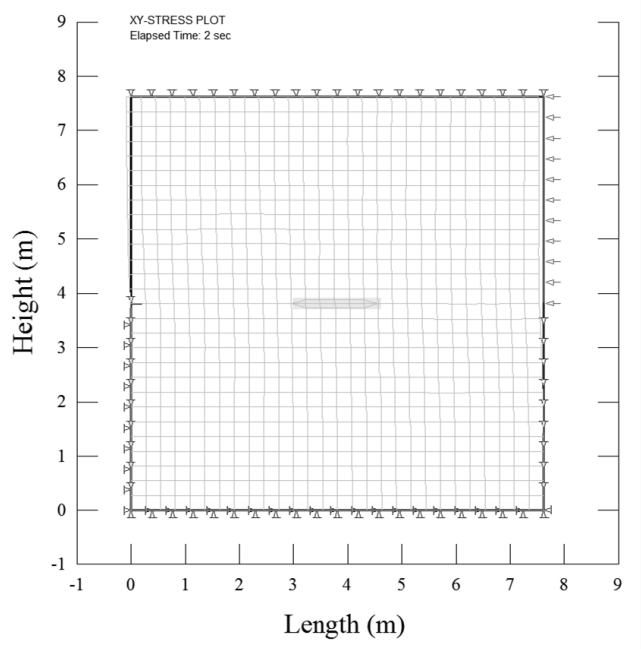

a) Total displacement = 0.002-m

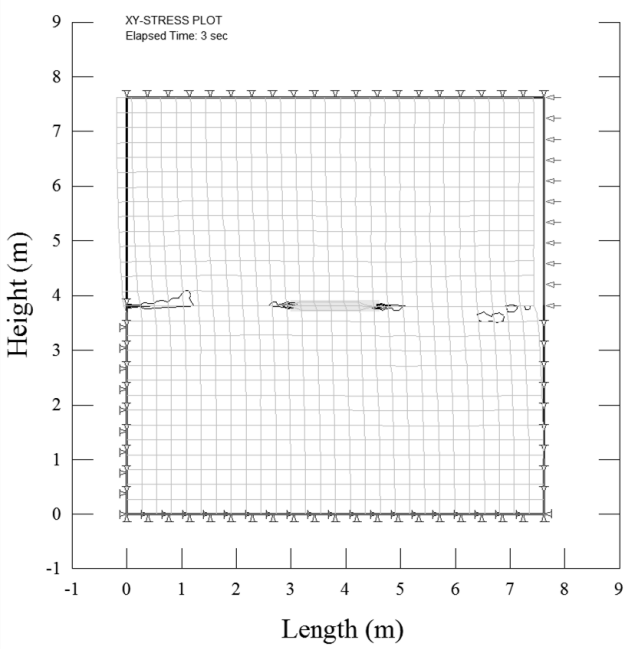

b) Total displacement = 0.004-m

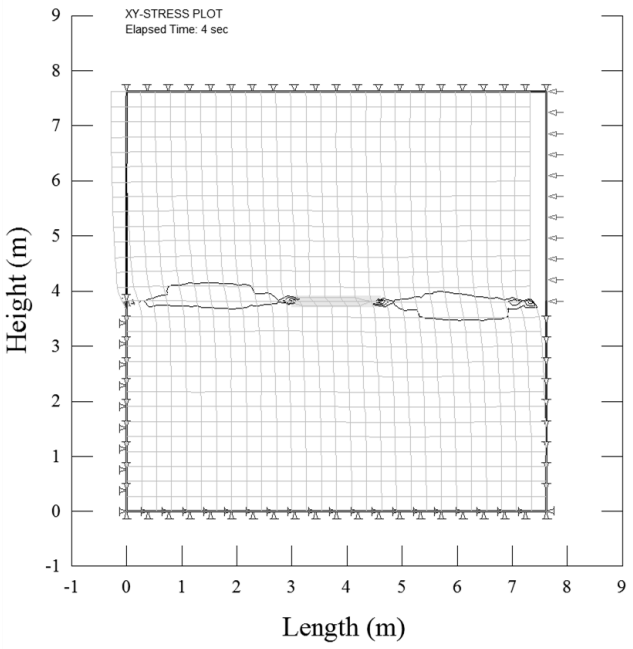

c) Total displacement = 0.006-m

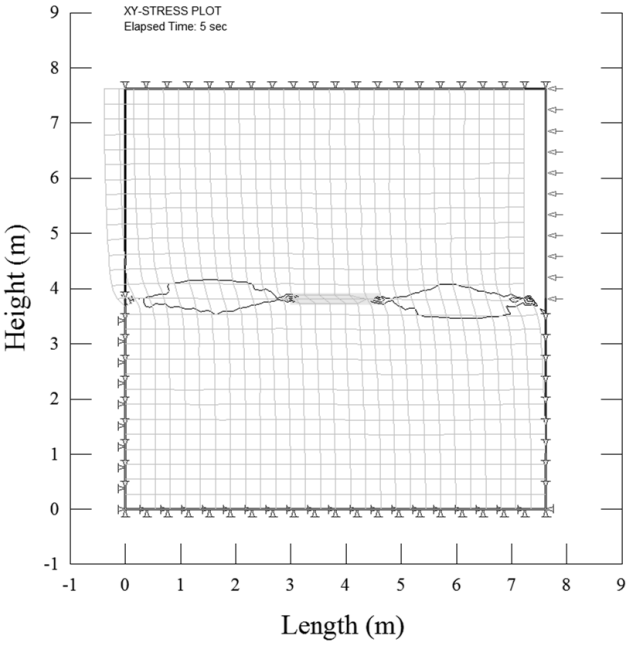

d) Total displacement = 0.008-m

Figure 5.10. Shear Stress Contours (4 kPa) Indicating Shear Failure Zones for Clay on Clay FEM Shear Model with ν = 0.45 and 25% Cohesion Reduction along Crack.

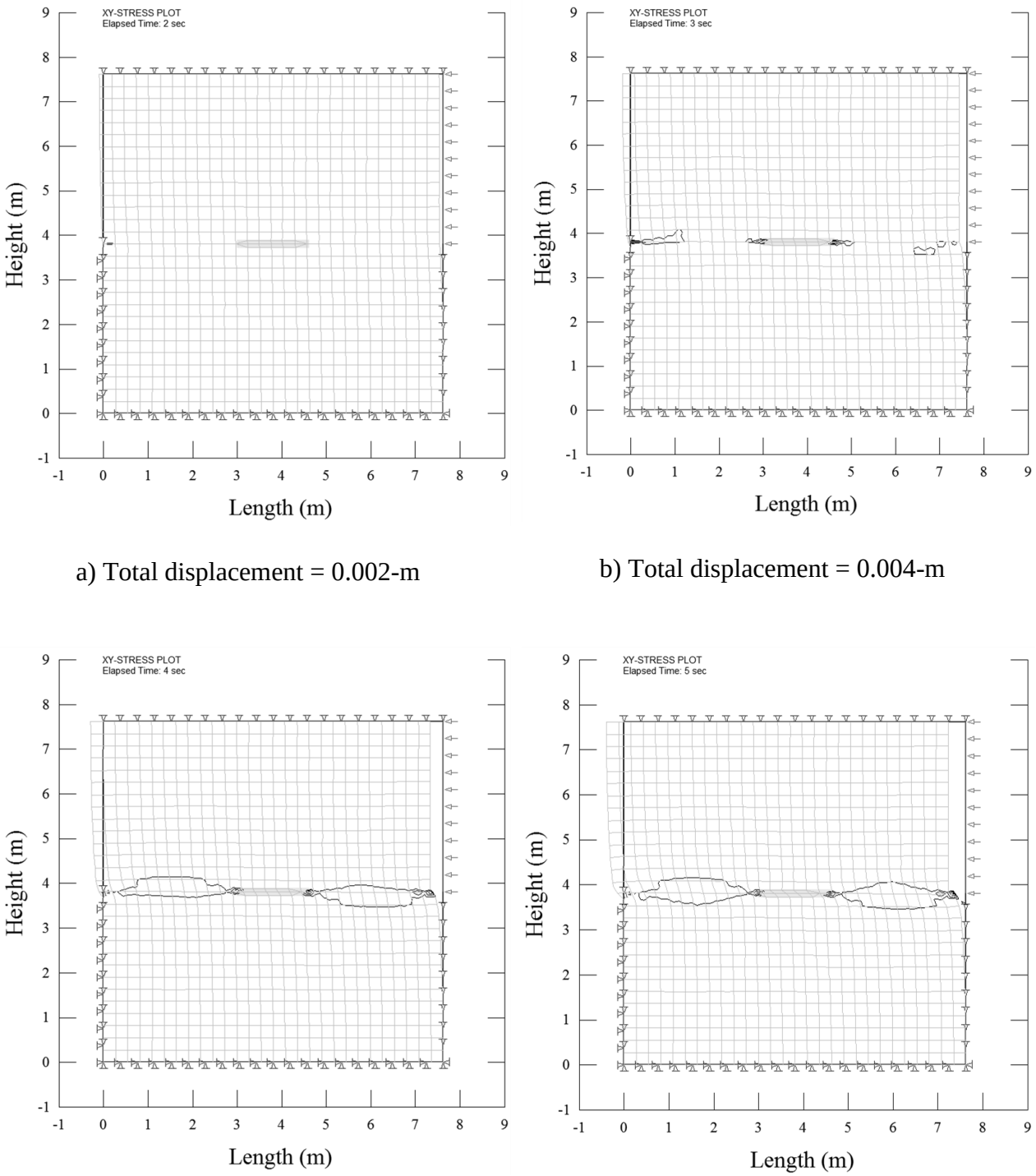

a) Total displacement = 0.002-m

b) Total displacement = 0.004-m

c) Total displacement = 0.006-m

d) Total displacement = 0.008-m

Figure 5.11. Shear Stress Contours (4 kPa) Indicating Shear Failure Zones for Clay on Clay FEM Shear Model with $\nu = 0.45$ and 50% Cohesion Reduction along Crack.

5.2.1.1 Discussion of Findings. The use of fracture mechanics principles is particularly applicable for this model since it is based on a $\phi = 0°$ condition for a purely cohesive material (Whittaker, 1992; and Aliabadi, 1999). Review of the failure stress contours presented in Figures 5.6 to 5.11 indicated that the failure plane propagated in a near horizontal plane. As is intuitively correct, the failure plane initiated at the displacement application end where the shear stress was the greatest. The failure plane then propagated to the slip element in a horizontal manner. The failure plane quickly propagated through the slip element and proceeded through the clay in a horizontal manner. The following findings are noted:

- The FEM analyses for $\nu = 0.10$ indicated that a reduction in cohesive strength along the slip element had negligible influence on failure plane propagation; that is, both the 25% cohesive reduction (Figure 5.7) and the 50% cohesive reduction (Figure 5.8) resulted in nearly identical rates of the failure plane propagation whereas the model with no cohesive reduction (Figure 5.6) did not exhibit the same rate of failure plane propagation under identical lateral displacement. Figure 5.12 presents the shear stresses obtained along the horizontal failure plane at 0.002-meter displacement. The shear stress increase was nearly identical at the ends of the sample for all cases, but stress concentrations are present approaching the slip element. This conclusion suggested that a slip element (or closed crack) with a reduced cohesive strength will promote failure plane propagation and rate of failure plane propagation is relatively independent from the magnitude of cohesive strength reduction for $\nu = 0.10$ materials.

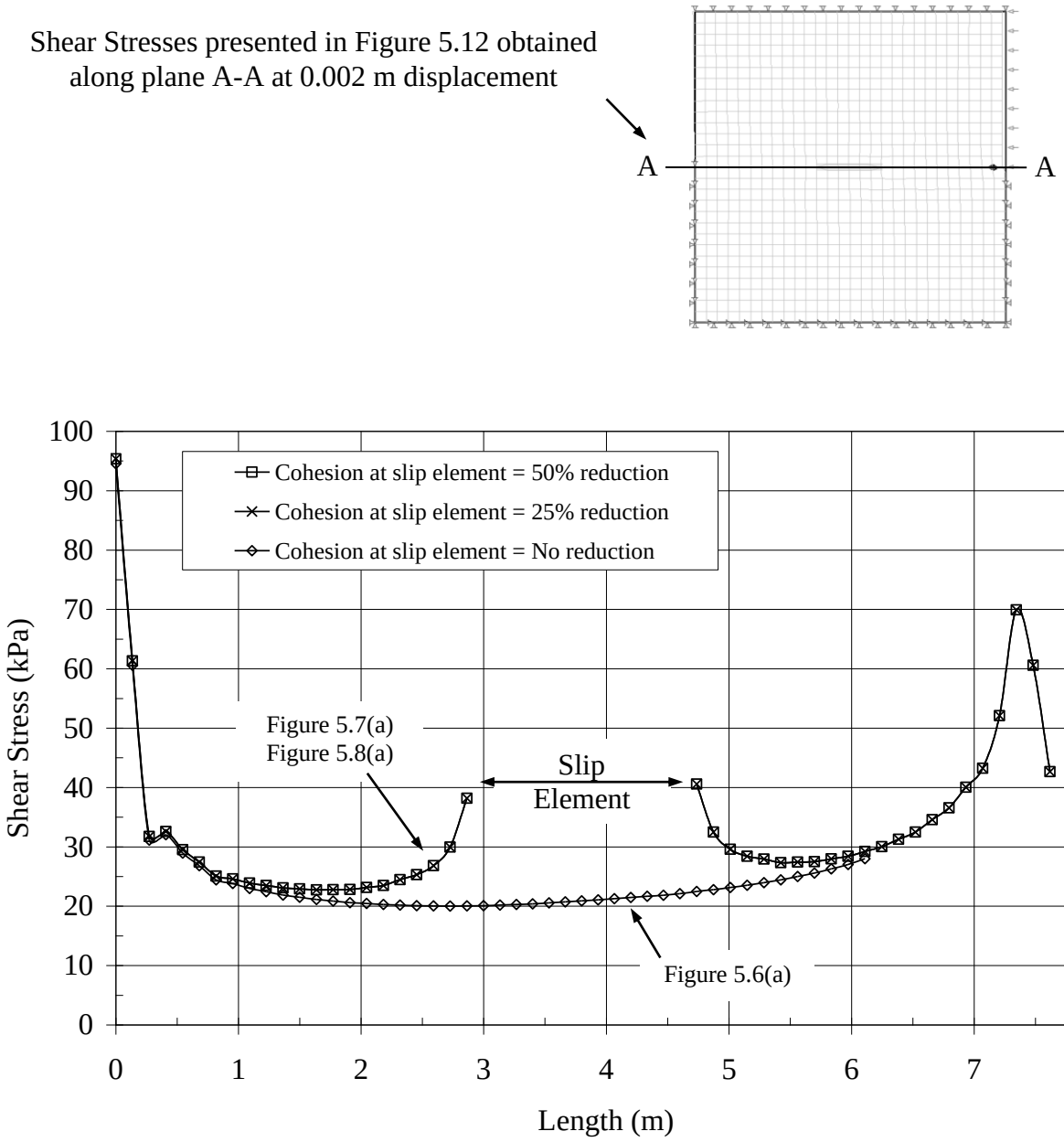

Figure 5.12. Shear Stress for Clay with ν = 0.10 and Cohesive Strength Reduction along Slip Element.

- The FEM analyses for $\nu = 0.45$ indicated that a reduction in cohesive strength along the slip element also had negligible influence on failure plane propagation; that is, no cohesive strength reduction (Figure 5.9), 25% cohesive reduction (Figure 5.10), 50% cohesive reduction (Figure 5.11) resulted in nearly identical rates of the failure plane propagation under identical lateral displacement. Figure 5.13 presents the shear stresses obtained along the horizontal failure plane at 0.002 meters displacement. However, comparing Figures 5.12 and 5.13, it is evident that the shear stresses are slightly higher for the $\nu = 0.45$ case under the same lateral displacement. The reason is as $\nu \rightarrow 0.50$, the volumetric strain tends toward zero and the material becomes incompressible with shearing occurring under constant volume for a total stress analysis. Since the material is confined, it becomes stiffer and consequently shear stress increased for the same displacement.

- The failure planes for $\nu = 0.10$ and 0.45 both propagated in a horizontal manner. Fracture mechanics predicted that a closed crack will propagate along the pre-existing crack plane when subjected to shear loading (Equation 2-40).

The FEM models replicated the laboratory test results with regard to failure plane propagation and fracture mechanics correctly predicted the direction of propagation for the clay on clay models.

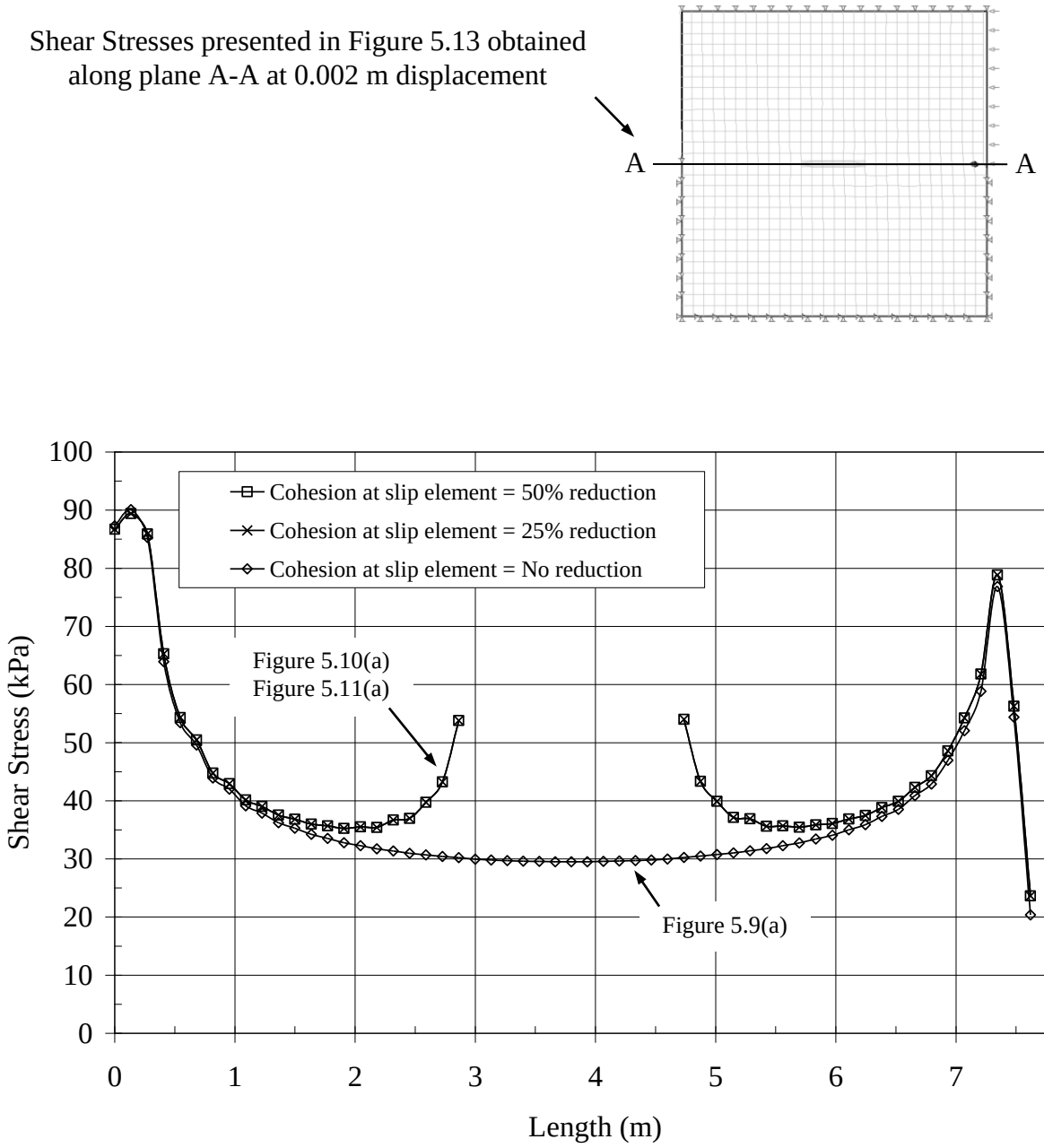

Figure 5.13. Shear Stress for Clay with ν = 0.45 and Variable Cohesive Strength Reduction along Slip Element.

5.2.2 Clayey Sand on Clay Shear Model Results

FEM analyses were conducted with clayey sand as the upper material and clay as the base material. As with the clay on clay model, the FEM analyses for the clayey sand on clay model also considered staged analyses. The first stage established the initial in-situ stress conditions. The laboratory model considered a closed crack and this has been idealized in the FEM analyses using a slip element at the sand-clay interface, as shown on Figure 5.14. The slip element was

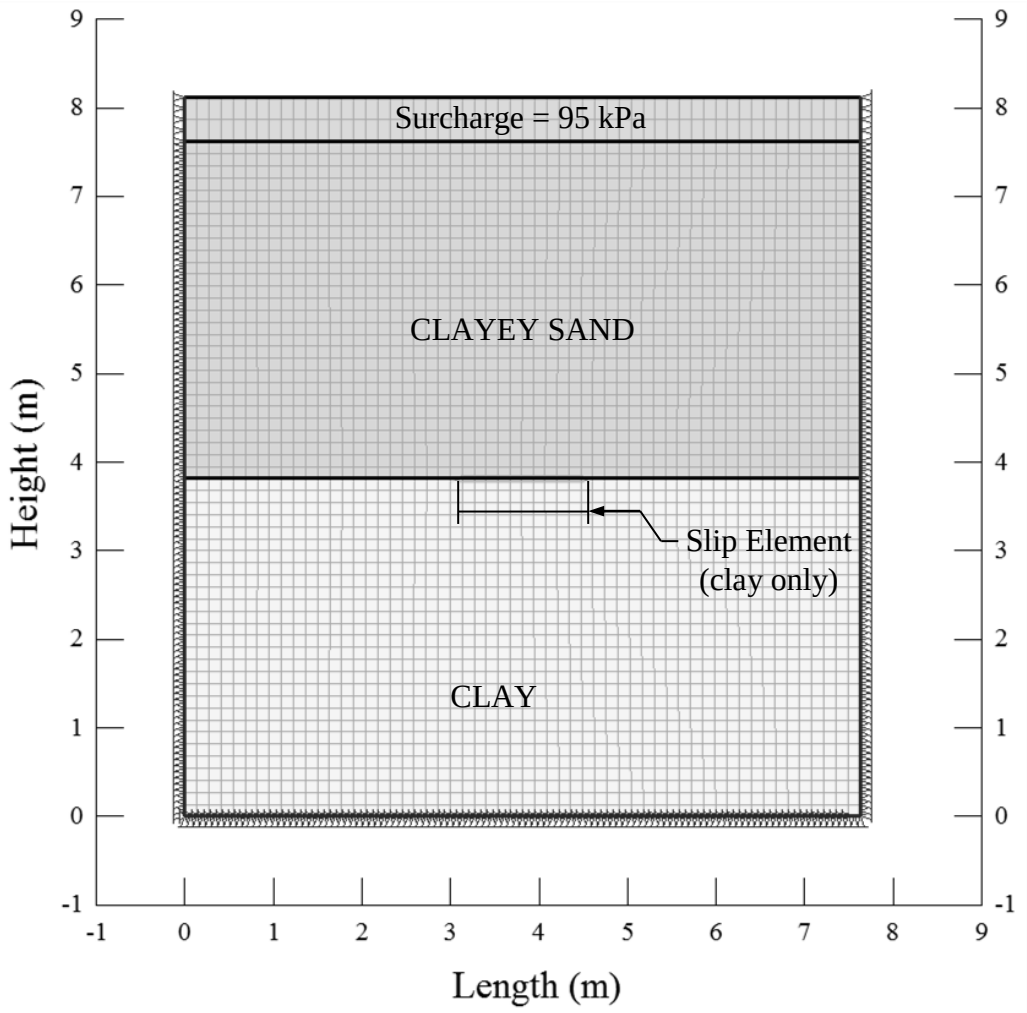

Figure 5.14. Clayey Sand on Clay FEM Shear Model.

situated in the lower clay and considered three different shear strength reductions in the analyses: 0%, 25%, and 50% reduction in shear strength properties of clay layer. The slip element did not apply to the clayey sand layer. Boundary conditions were similar to the clay on clay model. Lateral load was applied at 0.005-m increments. The results of the FEM analyses were drawn with 4 kPa shear strength contours at each load increment for shear stress values greater than the full cohesive strength of the lower clay section, which was 86.2 kPa. This condition represented a zone of failure in the clay material where a failure plane developed and / or the crack propagated. The following figures present the results of the FEM analyses at various displacement increments (all figures magnified by 50 for clarity purposes):

- Figure 5.15 – Poisson's ratio = 0.1 representing a brittle clay and no pre-existing.
- Figure 5.16 – Poisson's ratio = 0.1 representing a brittle clay with a 25% cohesive strength reduction at the slip element and full cohesive strength everywhere else (clay layer only).
- Figure 5.17 – Poisson's ratio = 0.1 representing a brittle clay with a 50% cohesive strength reduction at the slip element and full cohesive strength everywhere else (clay layer only).
- Figure 5.18 – Poisson's ratio = 0.45 representing a saturated clay and no-pre-existing crack.
- Figure 5.19 – Poisson's ratio = 0.45 representing a saturated clay with a 25% cohesive strength reduction at the slip element and full cohesive strength everywhere else (clay layer only).

- Figure 5.20 – Poisson's ratio = 0.45 representing a saturated clay with a 50% cohesive strength reduction at the slip element and full cohesive strength everywhere else (clay layer only).

Figures are presented in the subsequent pages.

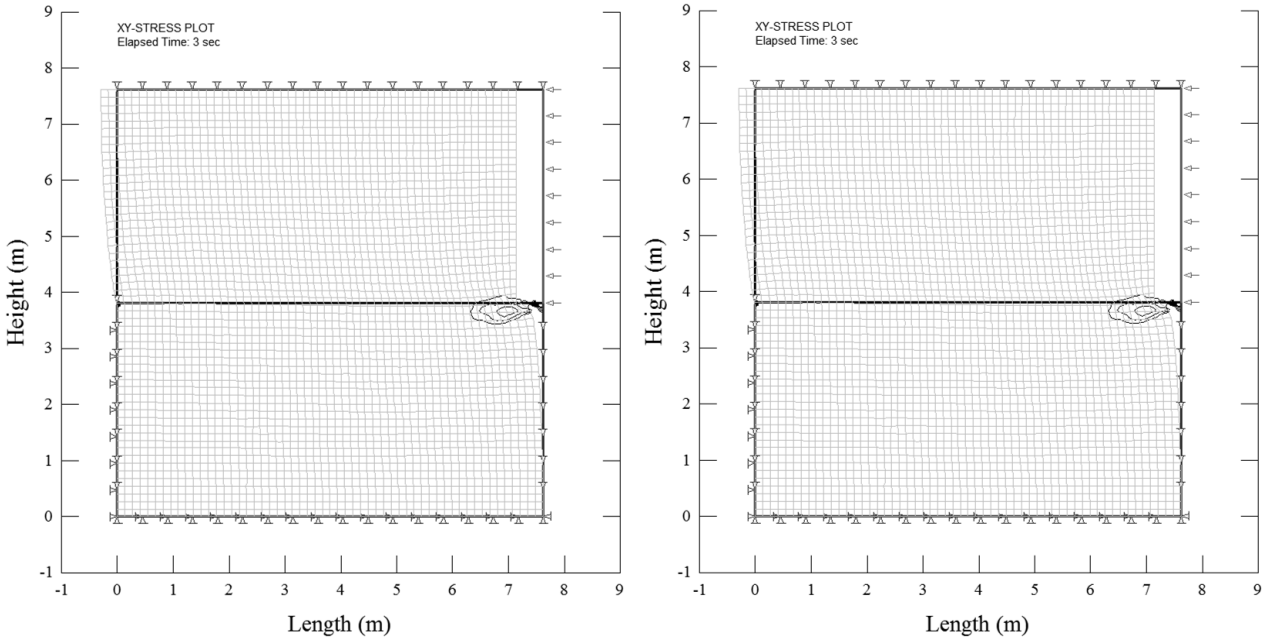

a) Total displacement = 0.005-m

b) Total displacement = 0.010-m

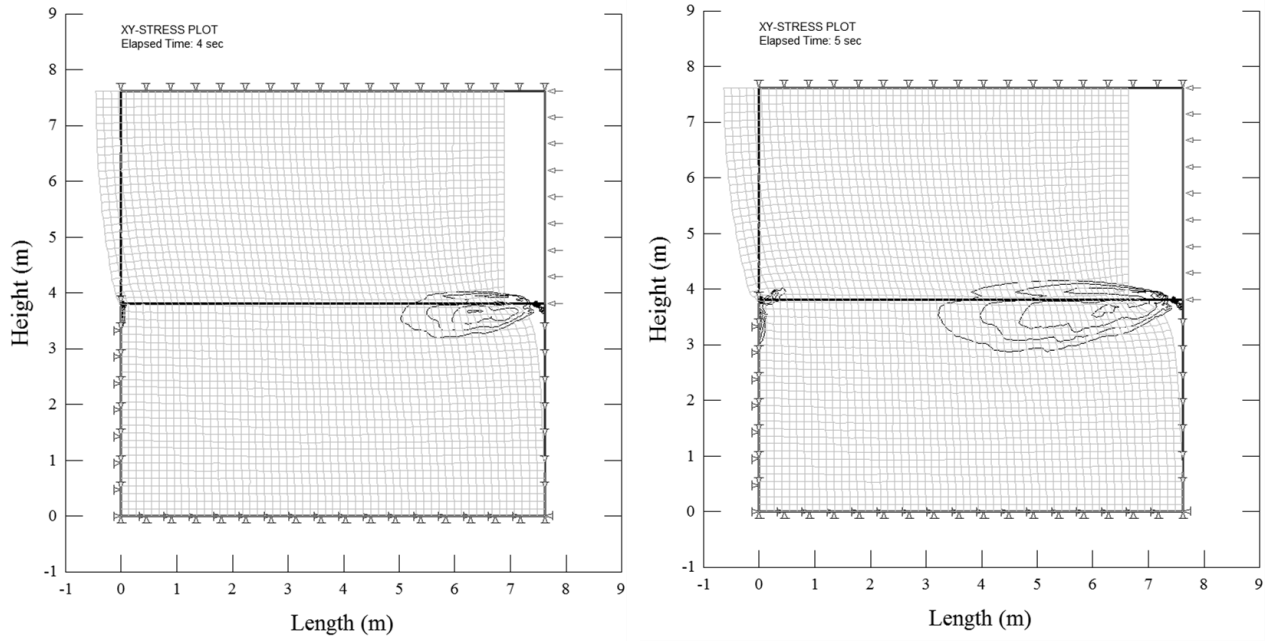

c) Total displacement = 0.015-m

d) Total displacement = 0.020-m

Figure 5.15. Clayey Sand on Clay FEM Shear Model Analyses with ν = 0.10, No Pre-Existing Crack and Shear Stress Contours (4 kPa) Indicating Shear Failure Zones for the Clay.

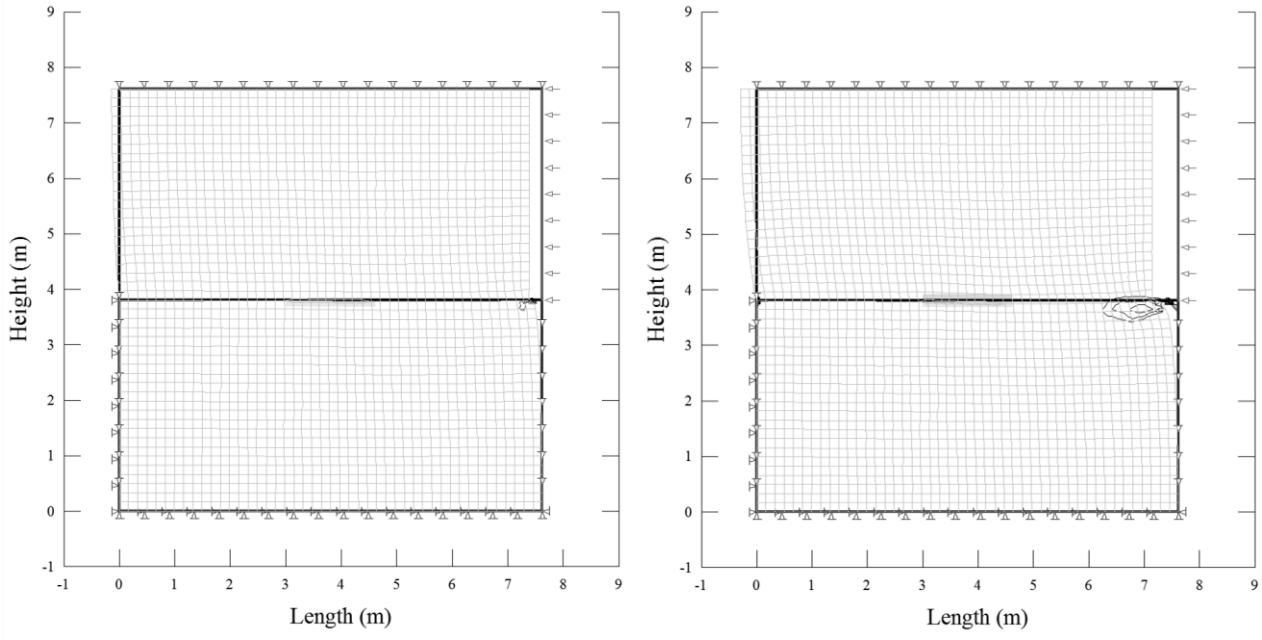

a) Total displacement = 0.005-m

b) Total displacement = 0.010-m

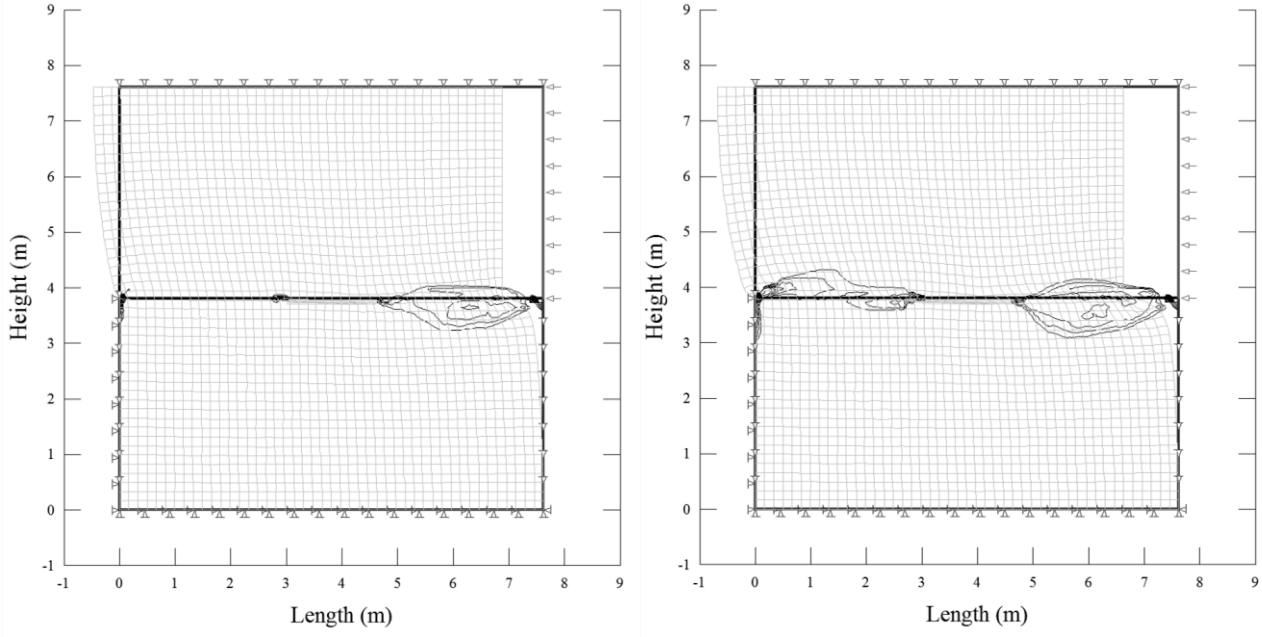

c) Total displacement = 0.015-m

d) Total displacement = 0.020-m

Figure 5.16. Clayey Sand on Clay FEM Shear Model Analyses with ν = 0.10, Pre-Existing Crack with a 25% Cohesive Strength Reduction, and Shear Stress Contours (4 kPa) Indicating Shear Failure Zones for the Clay.

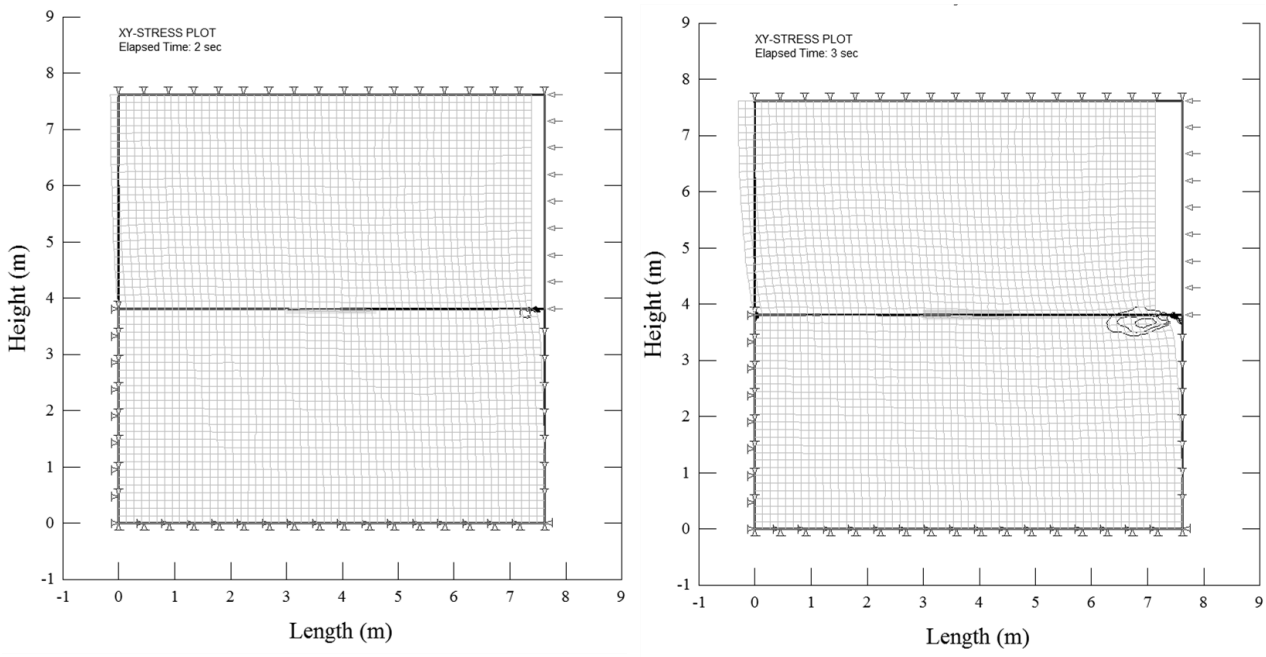

a) Total displacement = 0.005-m

b) Total displacement = 0.010-m

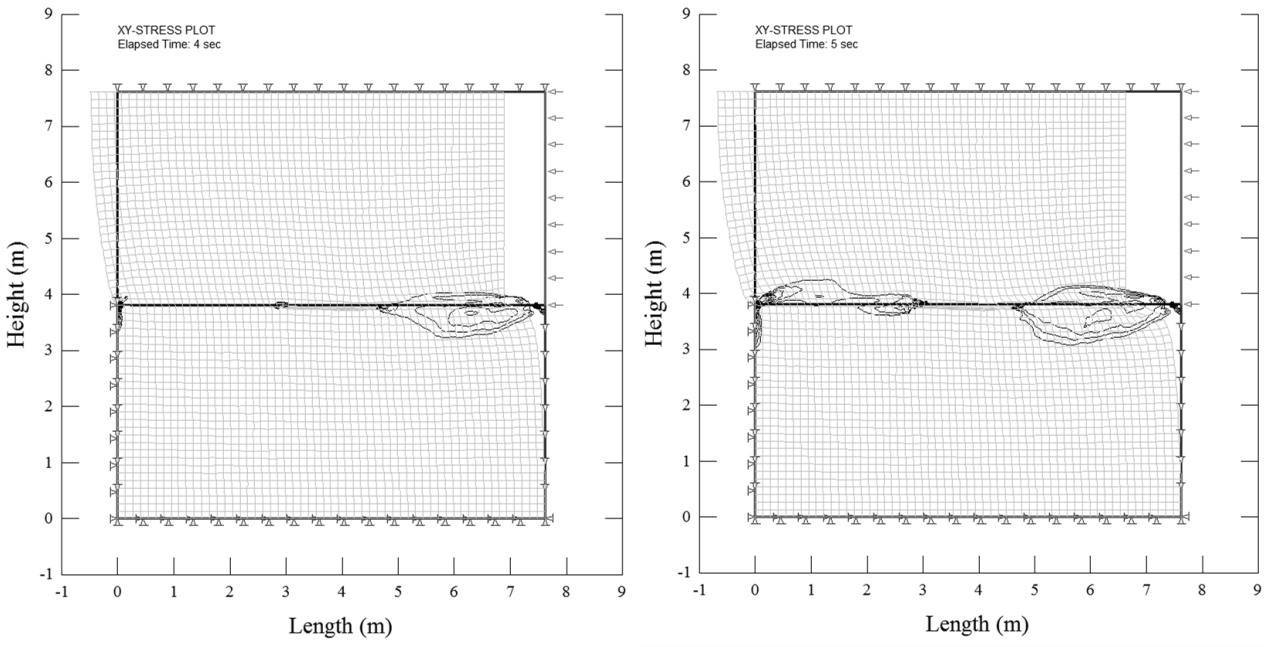

c) Total displacement = 0.015-m

d) Total displacement = 0.020-m

Figure 5.17. Clayey Sand on Clay FEM Shear Model Analyses with ν = 0.10, Pre-Existing Crack with a 50% Cohesive Strength Reduction, and Shear Stress Contours (4 kPa) Indicating Shear Failure Zones for the Clay.

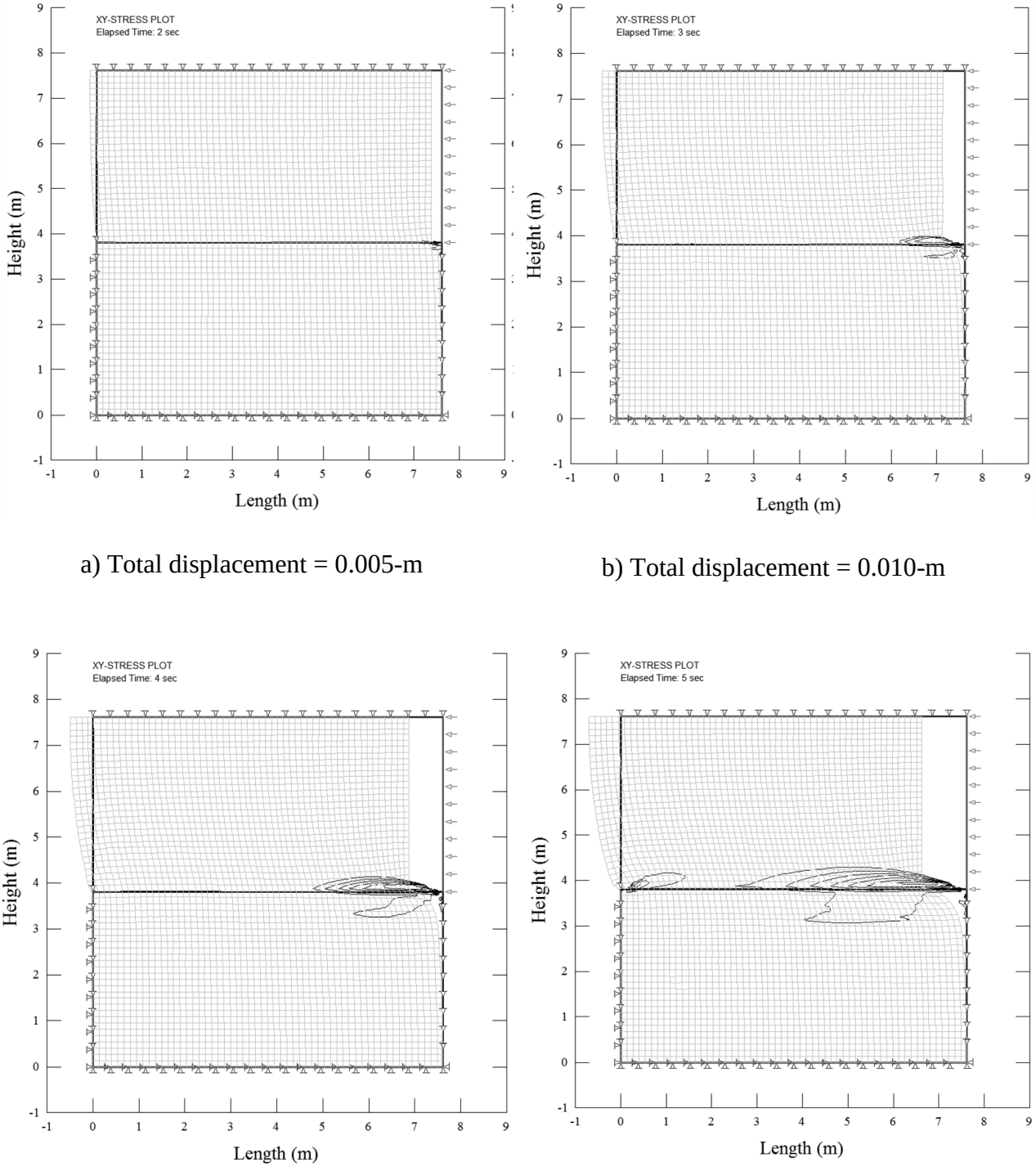

a) Total displacement = 0.005-m

b) Total displacement = 0.010-m

c) Total displacement = 0.015-m

d) Total displacement = 0.020-m

Figure 5.18. Clayey Sand on Clay FEM Shear Model Analyses with $\nu = 0.45$, No Pre-Existing Crack and Shear Stress Contours (4 kPa) Indicating Shear Failure Zones for the Clay.

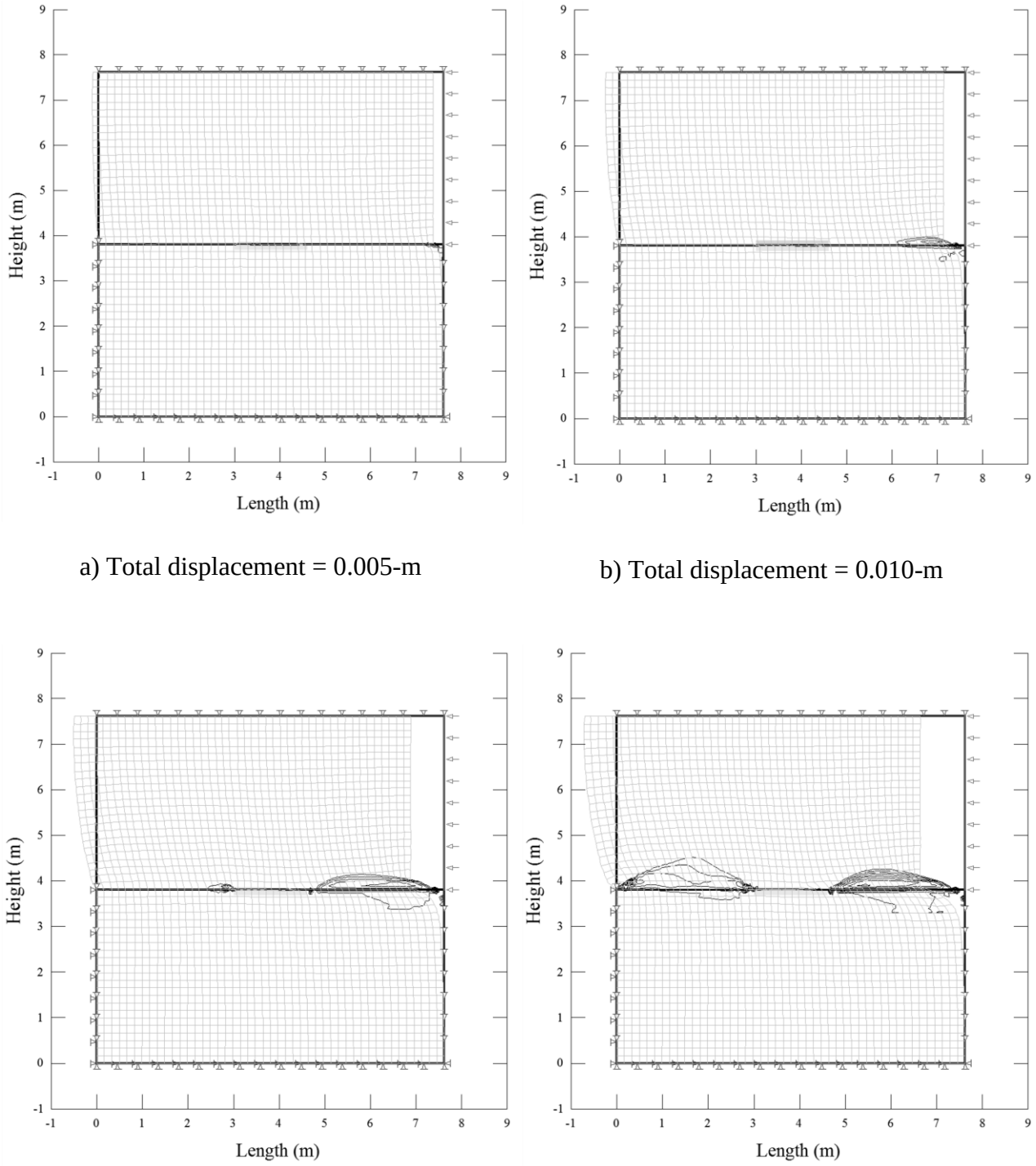

a) Total displacement = 0.005-m

b) Total displacement = 0.010-m

c) Total displacement = 0.015-m

d) Total displacement = 0.020-m

Figure 5.19. Clayey Sand on Clay FEM Shear Model Analyses with ν = 0.45, Pre-Existing Crack with a 25% Cohesive Strength Reduction, and Shear Stress Contours (4 kPa) Indicating Shear Failure Zones for the Clay.

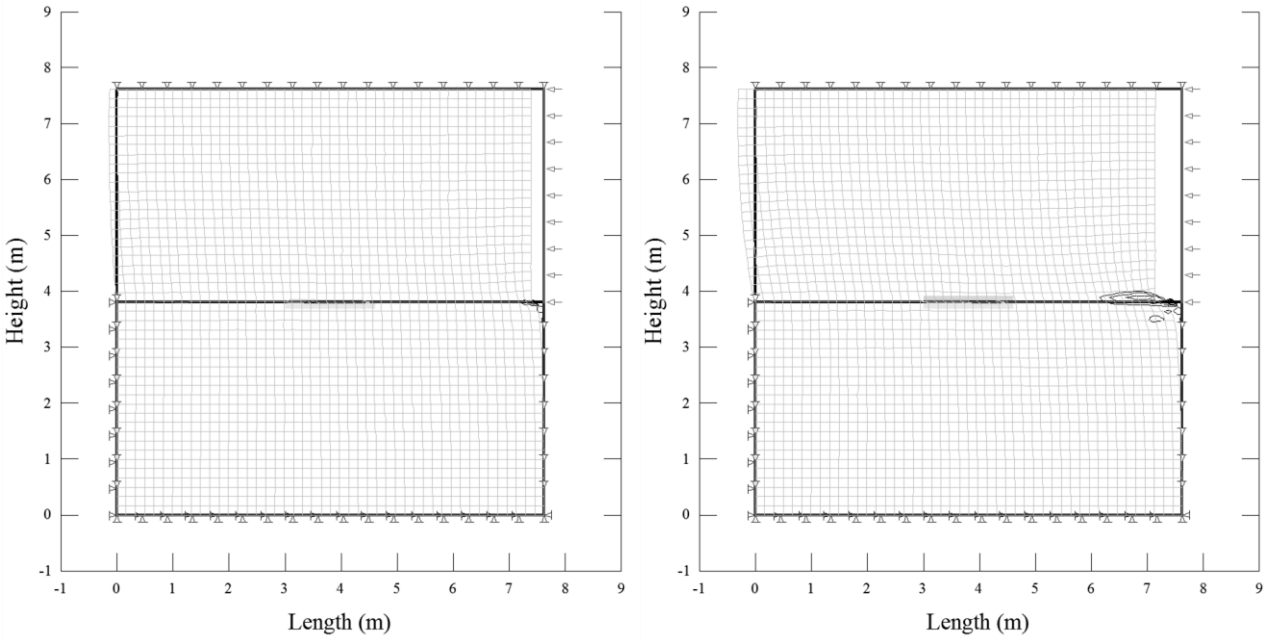

a) Total displacement = 0.005-m

b) Total displacement = 0.010-m

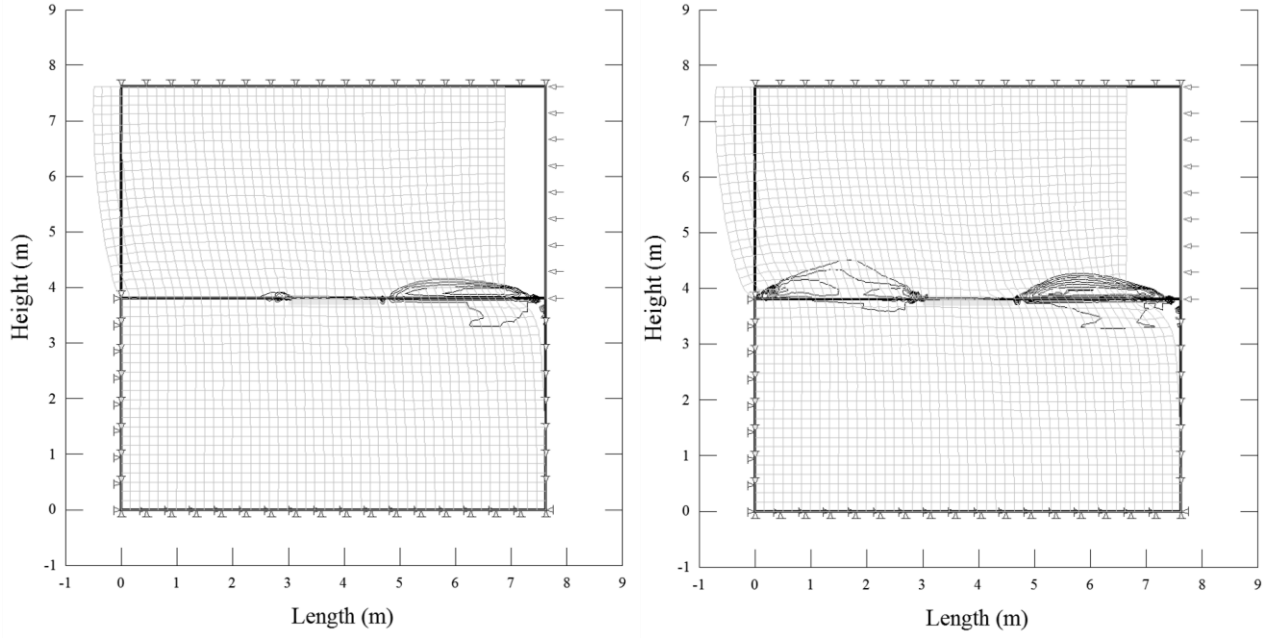

c) Total displacement = 0.015-m

d) Total displacement = 0.020-m

Figure 5.20. Clayey Sand on Clay FEM Shear Model Analyses with ν = 0.45, Pre-Existing Crack with a 50% Cohesive Strength Reduction, and Shear Stress Contours (4 kPa) Indicating Shear Failure Zones for the Clay.

5.2.2.1 Discussion of Findings. Review of Figures 5.15 through 5.20 indicated that the failure plane propagated in a near horizontal plane. As is intuitively correct, the failure planes initiated at the displacement application end where the shear stress was the largest. The failure plane then propagated to the slip element in a horizontal manner and quickly propagated across the model. The following findings are noted:

- The FEM analyses for $\nu = 0.10$ indicated that the reduction in cohesive strength along the slip element had negligible influence on failure plane propagation; that is, both the 25% cohesive reduction (Figure 5.16) and the 50% cohesive reduction (Figure 5.17) resulted in nearly identical rates of the failure plane propagation whereas the model with no cohesive reduction (Figure 5.15) did not exhibit the same rate of failure plane propagation under identical lateral displacement. As noted in Figure 5.15 through 5.17, the shear stress contours indicated shear stress values greater than the cohesive strength of the lower clay section with increasing displacement. However, these contours are not applicable to shear failure in the upper sand section because failure of this material is dependent on normal and shear stress. Figure 5.21 presents a typical Mohr-Coulomb failure envelope with shear stress against normal stress taken from the FEM model directly above the sand-clay interface. Refer to Appendix C for Mohr-Coulomb failure envelope graphs for all of the analyses. Figure 5.21 indicates that the failure plane did not propagate through the sand layer as no stress values were beyond the Mohr-Coulomb failure criteria for all analyses. Recall that examination of Figure 3.5 indicated that the laboratory model exhibited failure through the lower clay section and these FEM analyses indicated a similar condition.

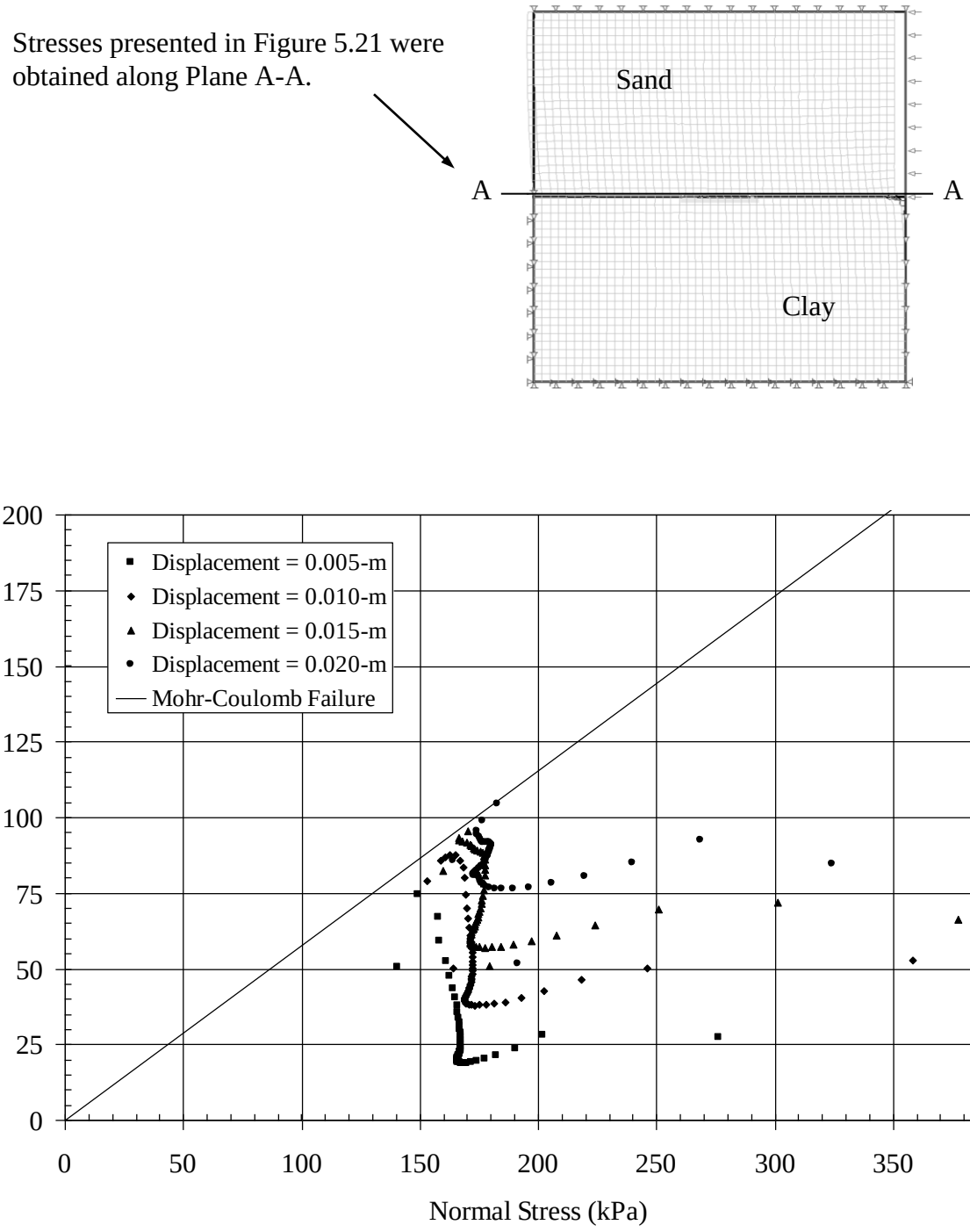

Figure 5.21. FEM Shear and Normal Stresses for the Clayey Sand Layer Obtained Directly Above the Clayey Sand-Clay Interface with $\nu = 0.10$ for the Clay with No Slip Element Strength Reduction.

- The FEM analyses for $\nu = 0.45$ indicated that the reduction in cohesive strength along the slip element also had negligible influence on failure plane propagation; that is, both the 25% cohesive reduction (Figure 5.19) and the 50% cohesive reduction (Figure 5.20) resulted in nearly identical rates of the failure plane propagation whereas the model with no cohesive reduction (Figure 5.18) did not exhibit the same rate of failure plane propagation under identical lateral displacement. As previously noted, the shear stress contours presented in Figure 5.18 through 5.20 are not necessarily applicable to shear failure in the upper clayey sand section. Figure 5.22 presents a typical Mohr-Coulomb failure envelope of shear stress against normal stress taken from the FEM model directly above the clayey sand-clay interface. The figure indicates that the failure plane did not propagate through the clayey sand layer as no stress values were beyond the Mohr-Coulomb failure criteria. Refer to Appendix C for Mohr-Coulomb failure envelope graphs for all of the analyses.

- FEM analyses indicated the significance of an existing crack. The FEM models with an existing crack exhibited a greater rate of shear plane propagation than the models without an existing crack.

- The failure planes for $\nu = 0.10$ and 0.45 both propagated in a horizontal manner. Fracture mechanics predicted that a closed crack will propagate along the pre-existing crack plane when subjected to shear loading (Equation 2-40).

As observed in the laboratory and FEM models, the failure plane propagated just below the clayey sand-clay interface in the clay stratum; the use of LEFM concepts is entirely valid. The FEM models replicated the laboratory test results with regard to failure plane propagation and

fracture mechanics correctly predicted the direction of propagation for the clayey sand on clay models.

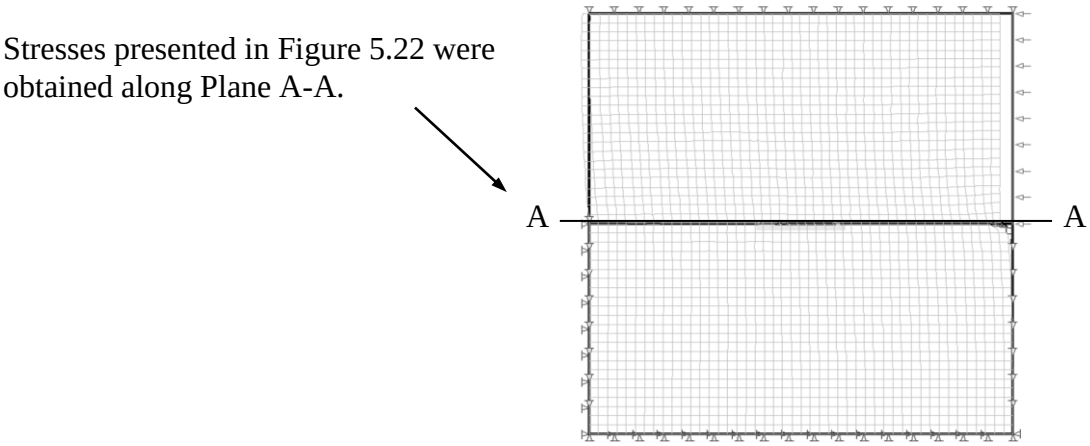

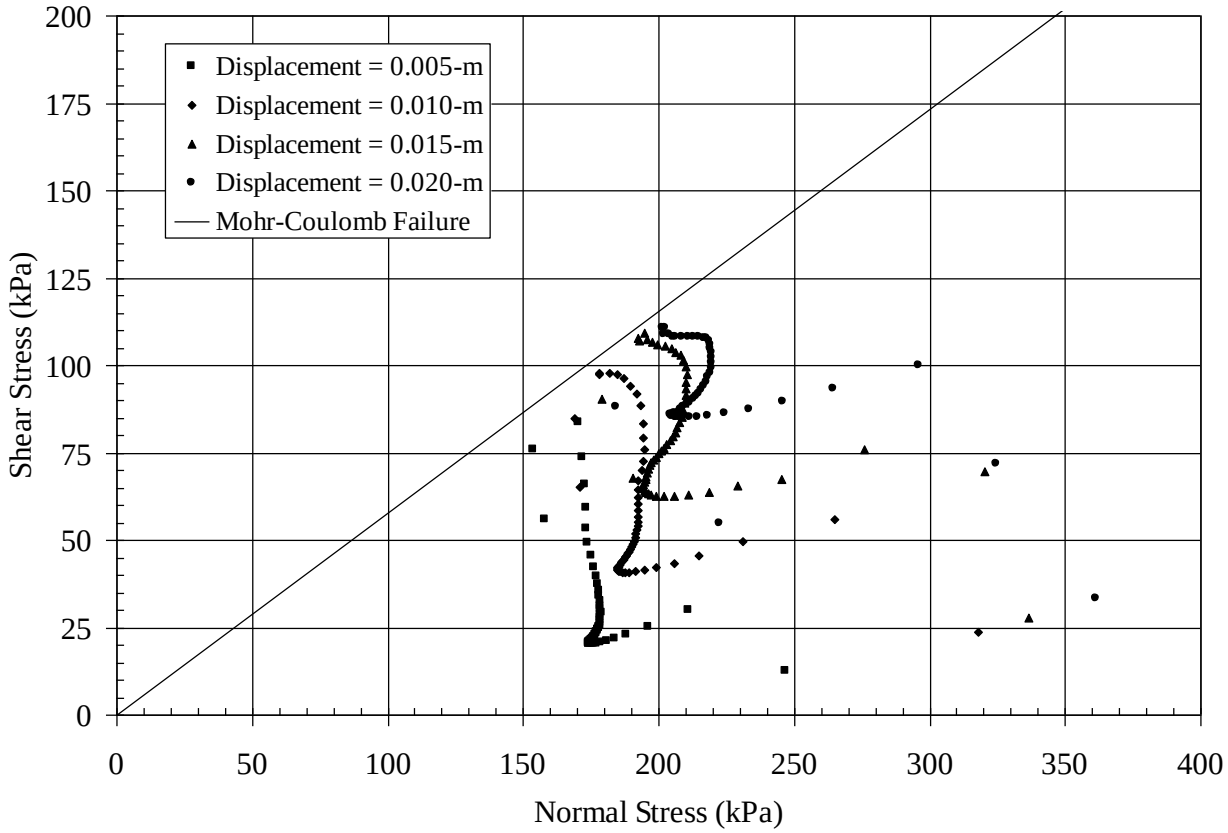

Figure 5.22. FEM Shear and Normal Stresses for the Sand Layer Obtained Directly Above the Clayey Sand-Clay Interface with $\nu = 0.45$ for the Clay with No Slip Element Strength Reduction.

5.3 HOMOGENEOUS VERTICAL SLOPE MODEL

The homogeneous vertical slope model represented a fracture mechanics tangential - closed crack condition. The FEM model has been scaled-up from the laboratory model (Duncan and Dunlop, 1969; Griffiths and Lane, 1999; Griffiths 2000; Khatri and Kumar, 2009). FEM analyses were performed in stages as follows:

- Stage 1 established the in-situ stress conditions. As shown on Figure 5.23(a), the FEM model used fixed boundary conditions at the base with rollers along the sides to permit vertical displacement.

- Stage II created the vertical slope by "turning-off" select elements, inserted the toe crack using a slip element, and applied the normal stress of 40 kPa at the top of slope in the form of a surcharge. The model used fixed boundary conditions at the base with rollers along the sides. Recall that the normal stress applied to the laboratory model closed the toe crack and the normal stress was kept constant during the experiment. The FEM model maintained a constant normal stress and employed a frictionless slip element at the surcharge – clay interface, as noted on Figure 5.23(b).

- Subsequent stages applied lateral stress increments to simulate the PSDSA experiment.

Figure 5.24 indicates the FEM boundary conditions used during application of the lateral increments. The FEM model very closed simulated the PSDSA experimental procedures.

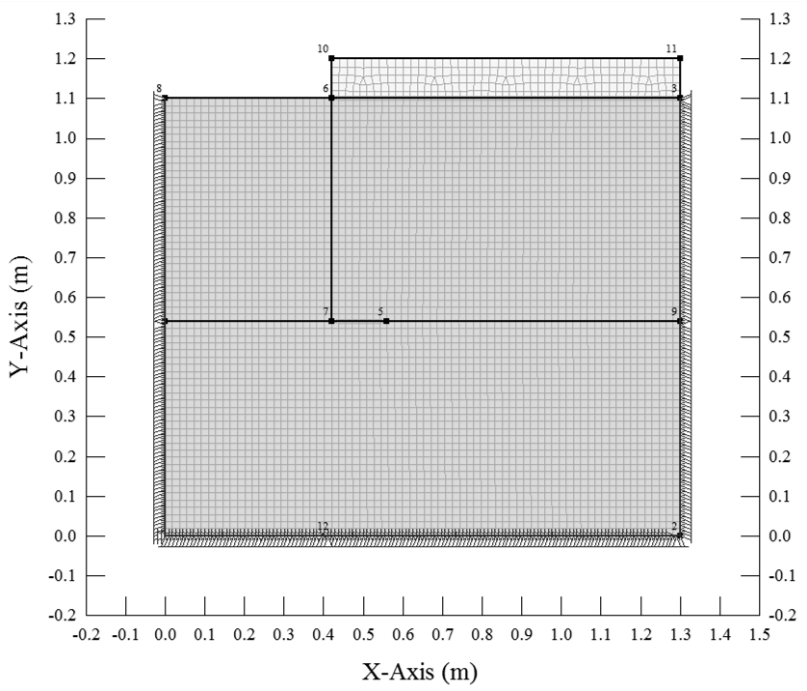

a) Stage I - FEM Model to Establish Initial Stresses.

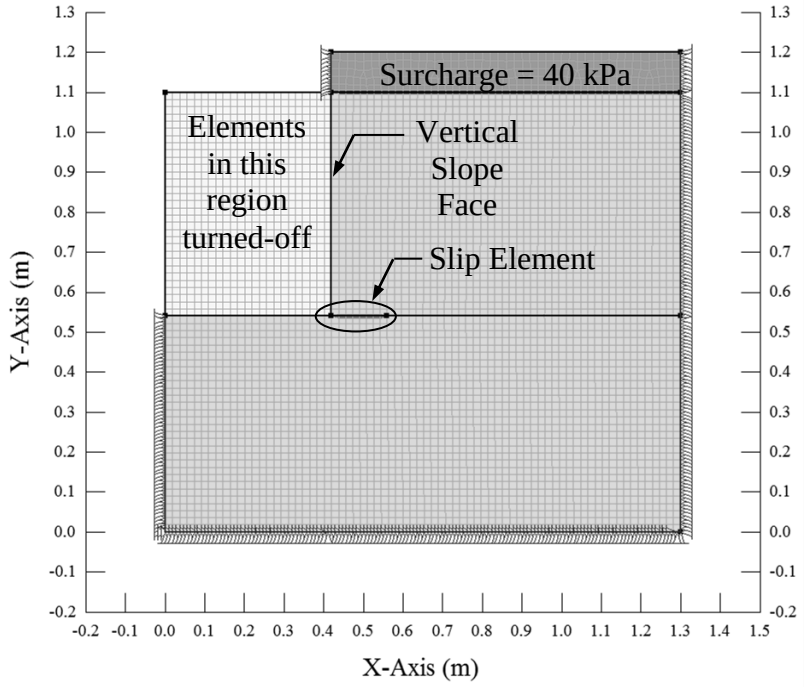

b) Stage II - Simulated Vertical Slope FEM Model with Surcharge.

Figure 5.23. FEM Vertical Slope Model.

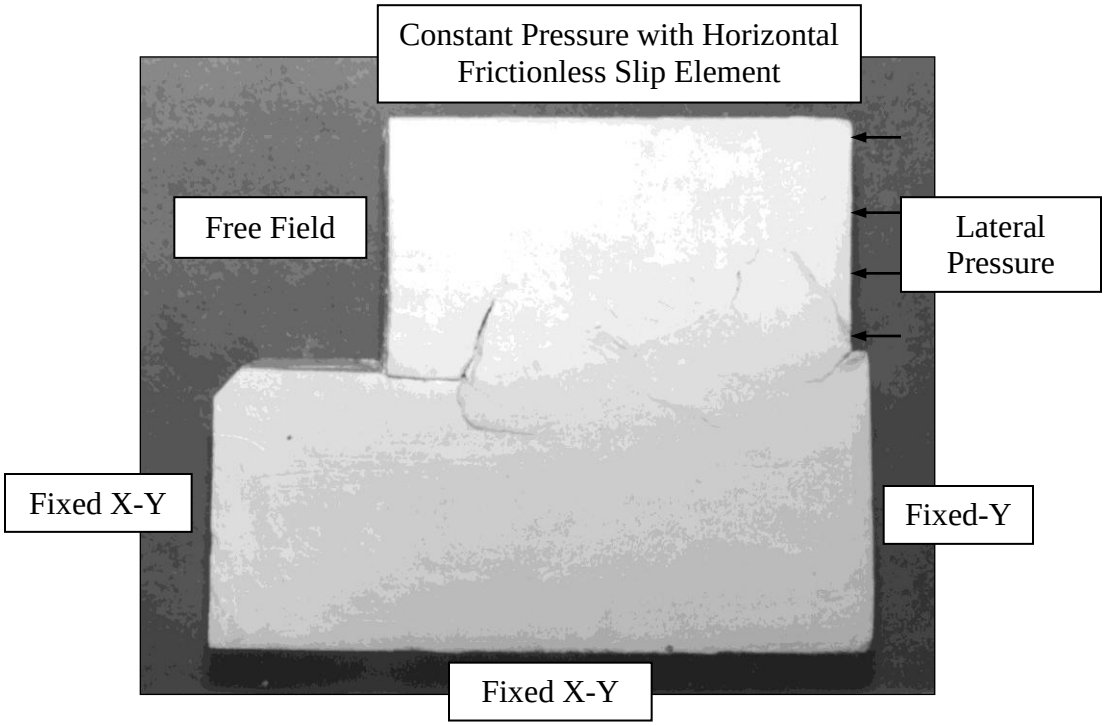

Figure 5.24. Homogeneous Vertical Slope FEM Model Boundary Conditions.

5.3.1 Vertical Slope Model Results

Analyses considered three different slip surface element shear strength conditions to represent a closed crack condition; no cohesive strength reduction, an arbitrary reduction in cohesive strength of 25%, and an arbitrary reduction in cohesive strength of 50%. The no cohesive strength reduction served as a baseline analysis to understand how a reduction in cohesive strength influenced crack propagation.

The results of the FEM analyses are drawn with lateral stress contours at -10 kPa intervals beginning at 0-kPa, indicating a tension zone. The following figures present the results of the FEM analyses at various lateral stress increments:

- Figure 5.25 – Poisson's ratio = 0.1 representing a brittle clay with no cohesive strength reduction along the slip element.

- Figure 5.26 – Poisson's ratio = 0.1 representing a brittle clay with a 25% cohesive strength reduction along the slip element and full cohesive strength everywhere else.

- Figure 5.27 – Poisson's ratio = 0.1 representing a brittle clay with a 50% cohesive strength reduction along the slip element and full cohesive strength everywhere else.

- Figure 5.28 – Poisson's ratio = 0.45 representing a brittle clay with no cohesive strength reduction along the slip element.

- Figure 5.29 – Poisson's ratio = 0.45 representing a brittle clay with a 25% cohesive strength reduction along the slip element and full cohesive strength everywhere else.

- Figure 5.30 – Poisson's ratio = 0.45 representing a brittle clay with a 50% cohesive strength reduction along the slip element and full cohesive strength everywhere else.

Figures are presented in the subsequent pages.

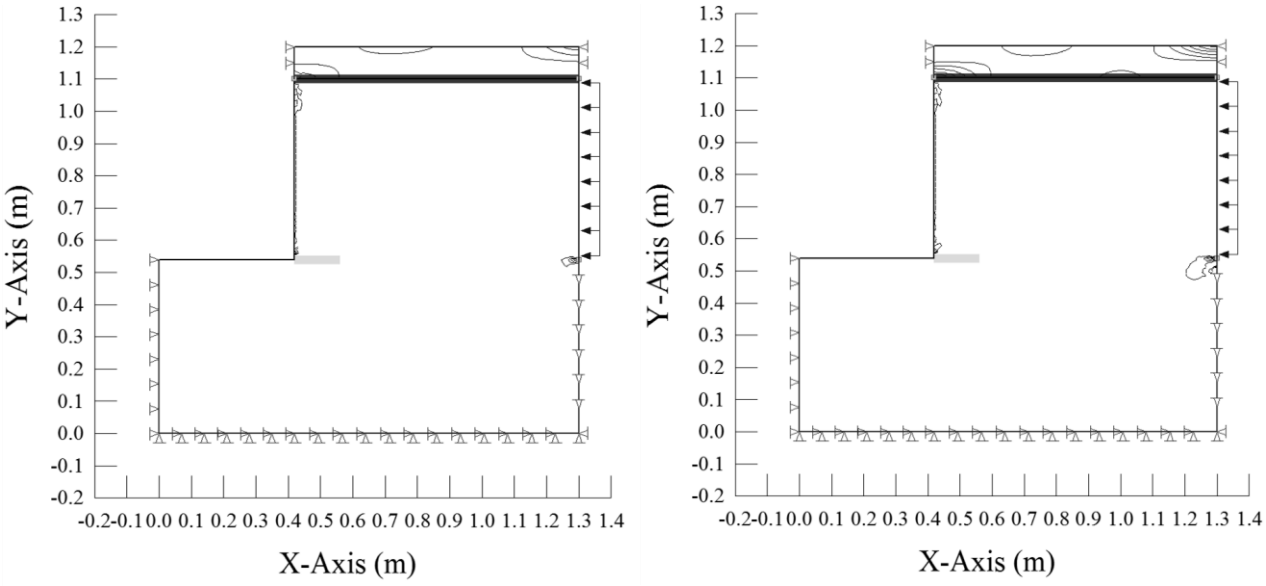

a) Lateral stress = 40-kPa

b) Lateral stress = 80-kPa

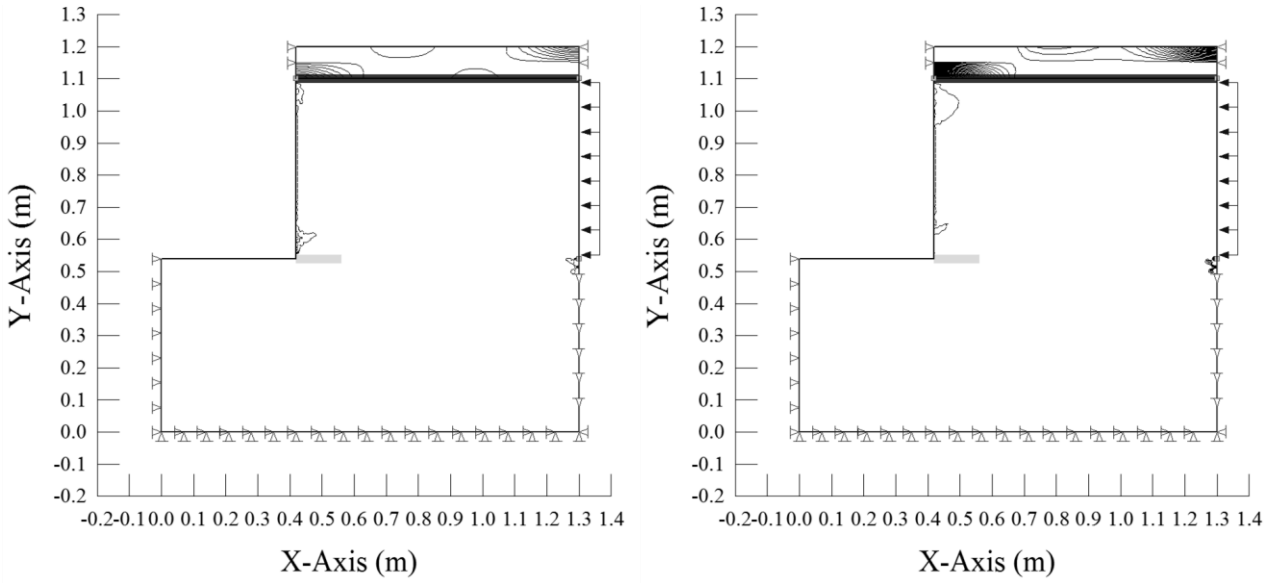

c) Lateral stress = 120-kPa

d) Lateral stress = 160-kPa

Figure 5.25. Vertical Slope FEM Model Analyses with ν = 0.10, No Pre-Existing Toe Crack and Negative X-Stress Contours (10-kPa) Indicating Tension Zones.

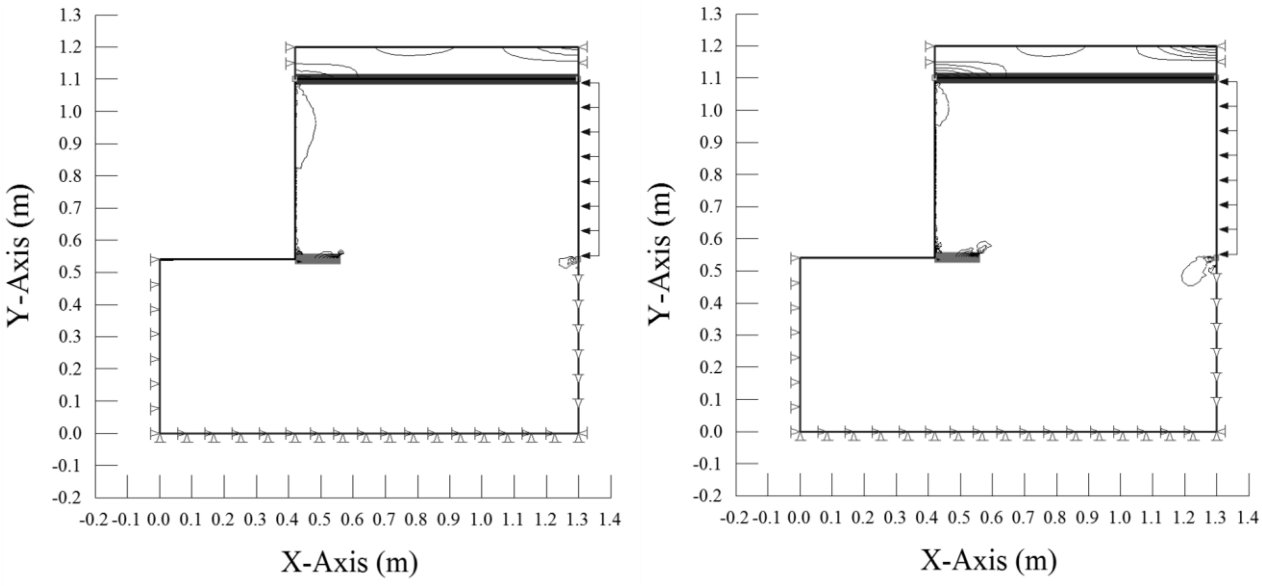

a) Lateral stress = 40-kPa

b) Lateral stress = 80-kPa

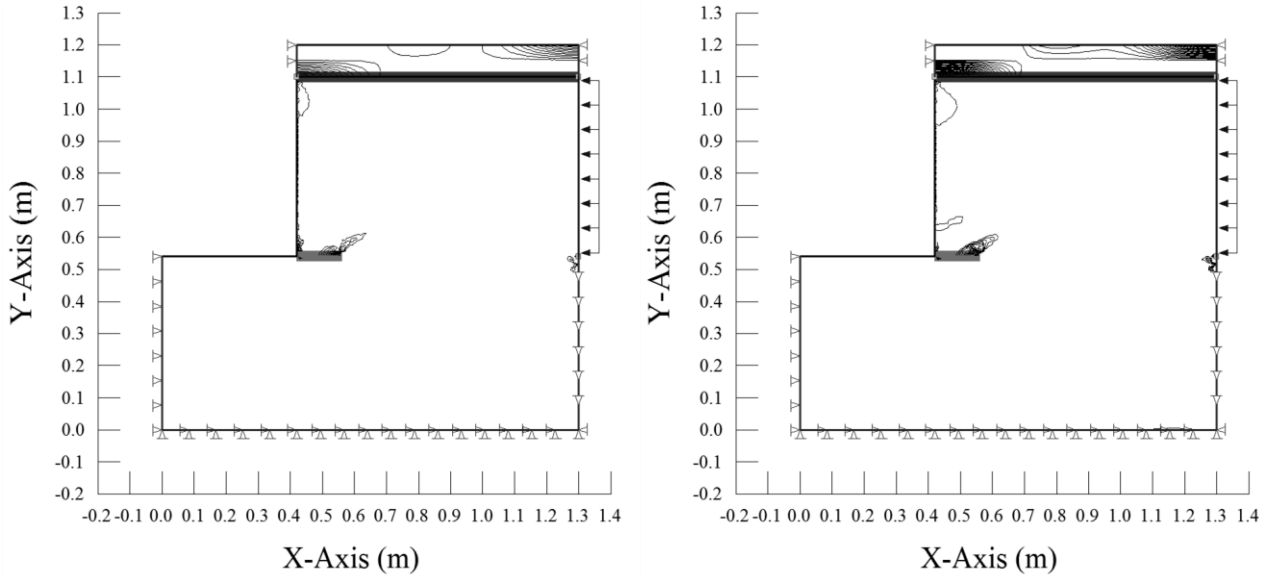

c) Lateral stress = 120-kPa

d) Lateral stress = 160-kPa

Figure 5.26. Vertical Slope FEM Model Analyses with ν = 0.10, Pre-Existing Toe Crack with a 25% Cohesive Strength Reduction, and Negative X-Stress Contours (10-kPa) Indicating Tension Zones.

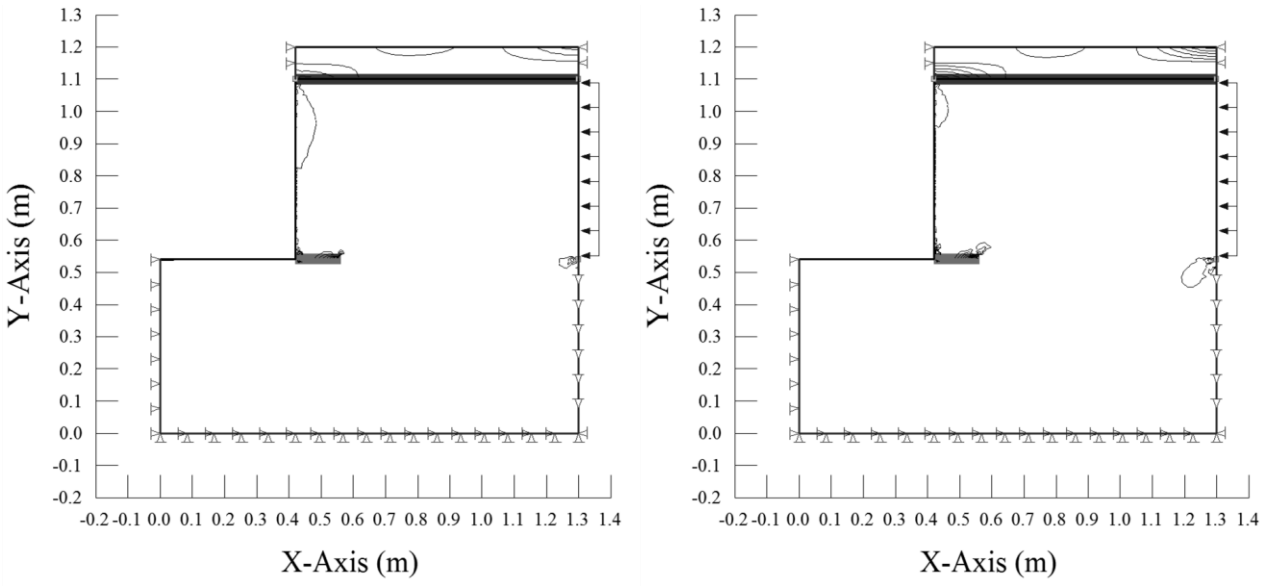

a) Lateral stress = 40-kPa

b) Lateral stress = 80-kPa

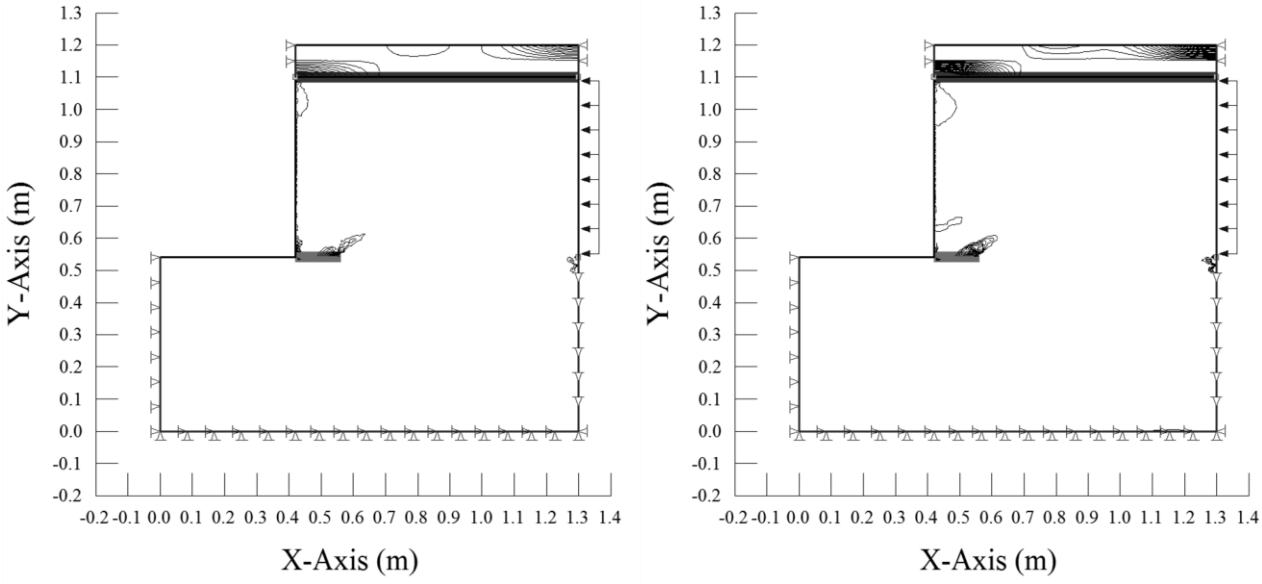

c) Lateral stress = 120-kPa

d) Lateral stress = 160-kPa

Figure 5.27. Vertical Slope FEM Model Analyses with ν = 0.10, Pre-Existing Toe Crack with a 50% Cohesive Strength Reduction, and Negative X-Stress Contours (10-kPa) Indicating Tension Zones.

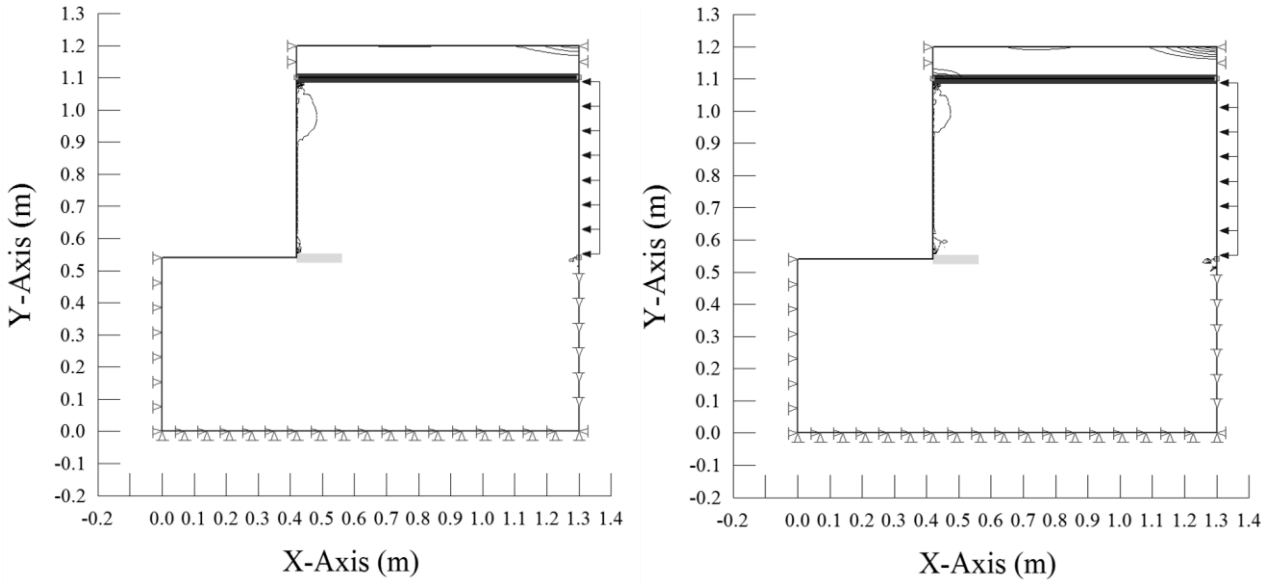

a) Lateral stress = 40-kPa

b) Lateral stress = 80-kPa

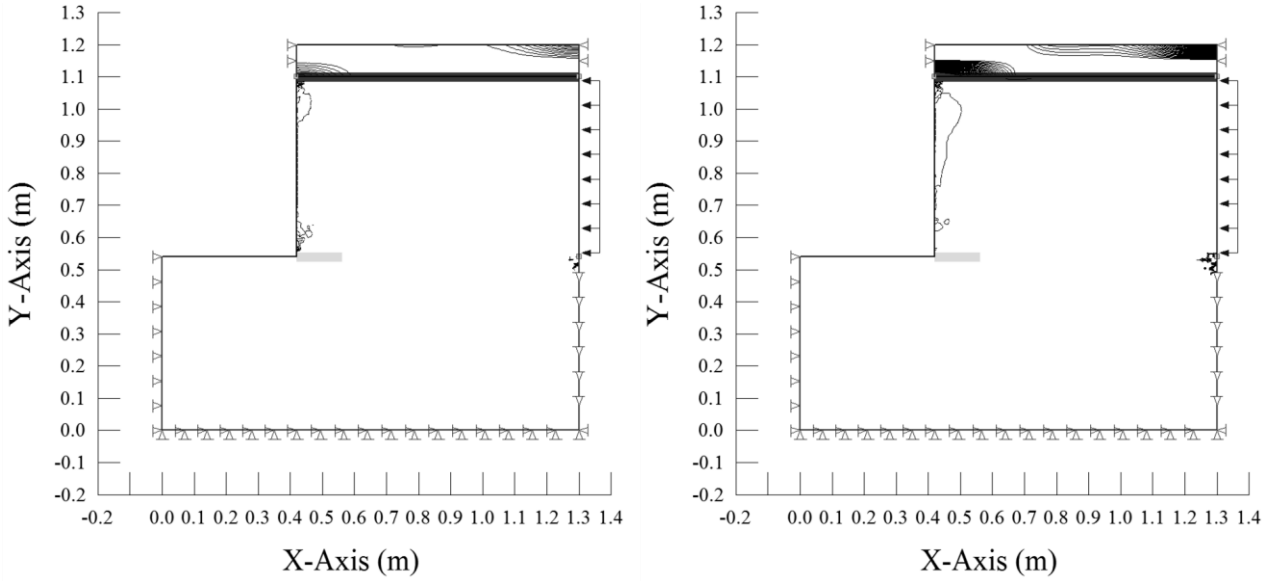

c) Lateral stress = 120-kPa

d) Lateral stress = 160-kPa

Figure 5.28. Vertical Slope FEM Model Analyses with ν = 0.45, No Pre-Existing Toe Crack and Negative X-Stress Contours (10-kPa) Indicating Tension Zones.

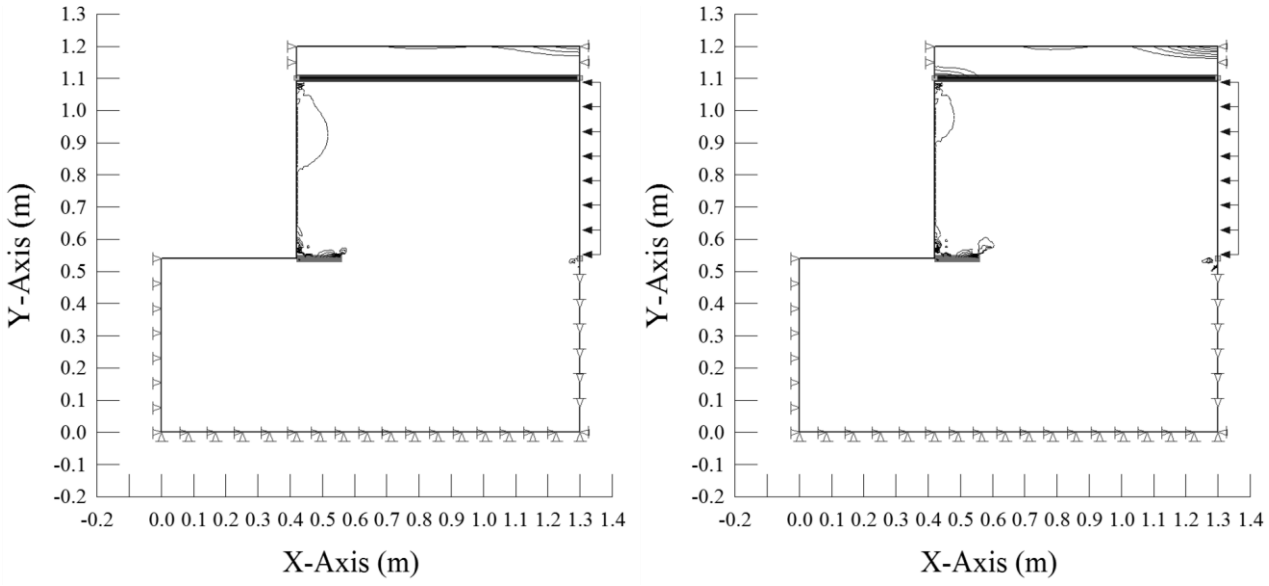

a) Lateral stress = 40-kPa

b) Lateral stress = 80-kPa

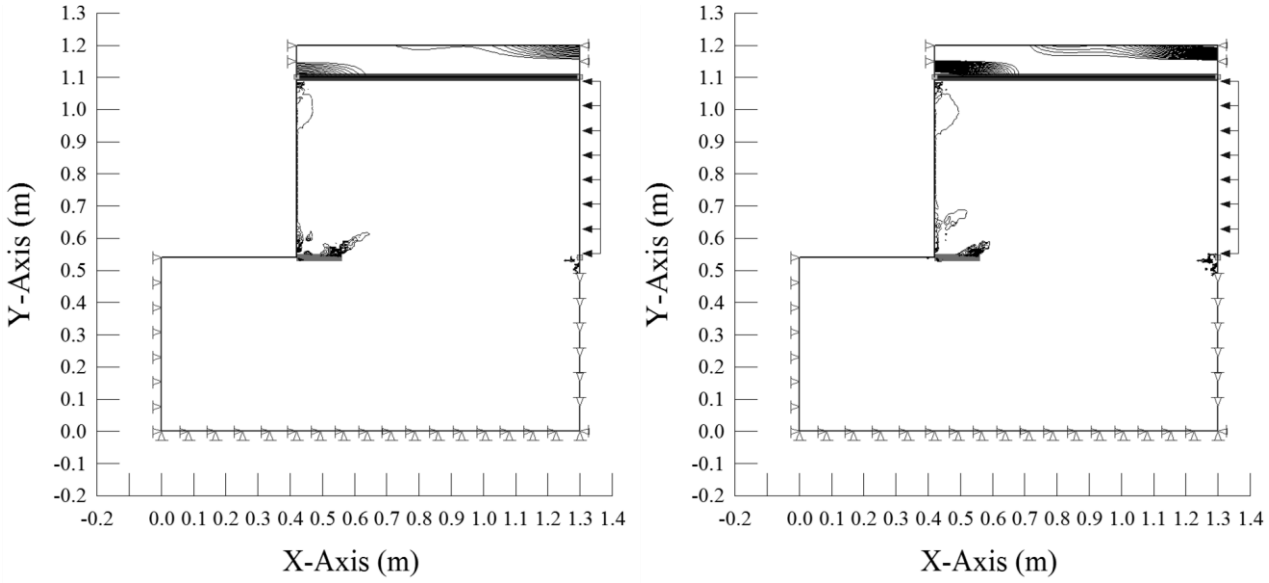

c) Lateral stress = 120-kPa

d) Lateral stress = 160-kPa

Figure 5.29. Vertical Slope FEM Model Analyses with ν = 0.45, Pre-Existing Toe Crack with a 25% Cohesive Strength Reduction, and Negative X-Stress Contours (10-kPa) Indicating Tension Zones.

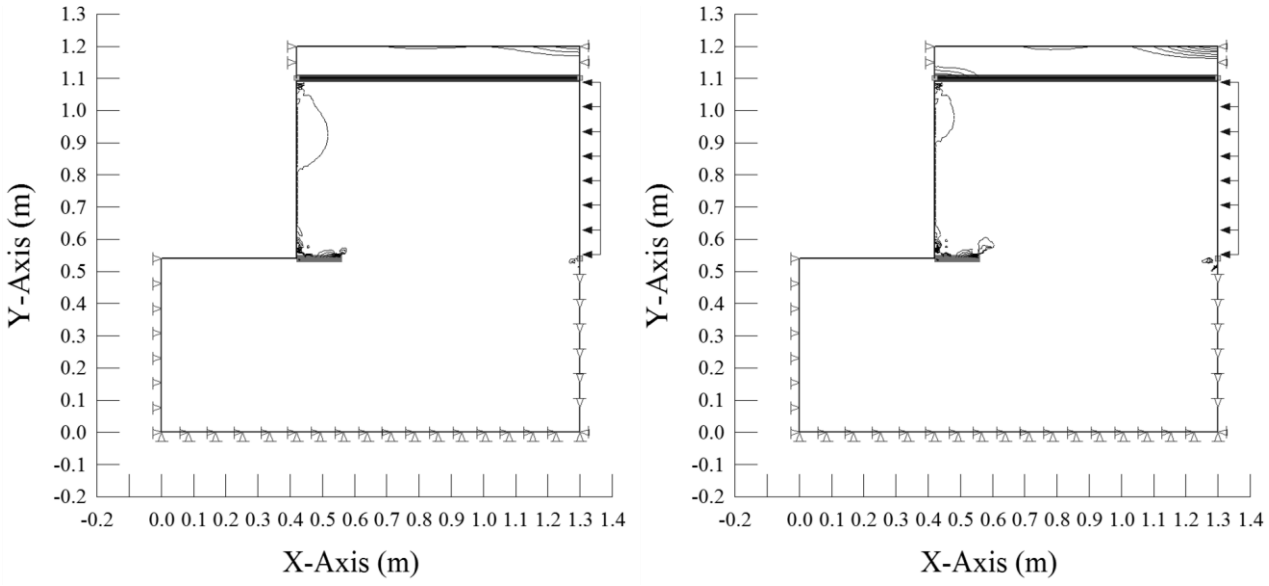

a) Lateral stress = 40-kPa

b) Lateral stress = 80-kPa

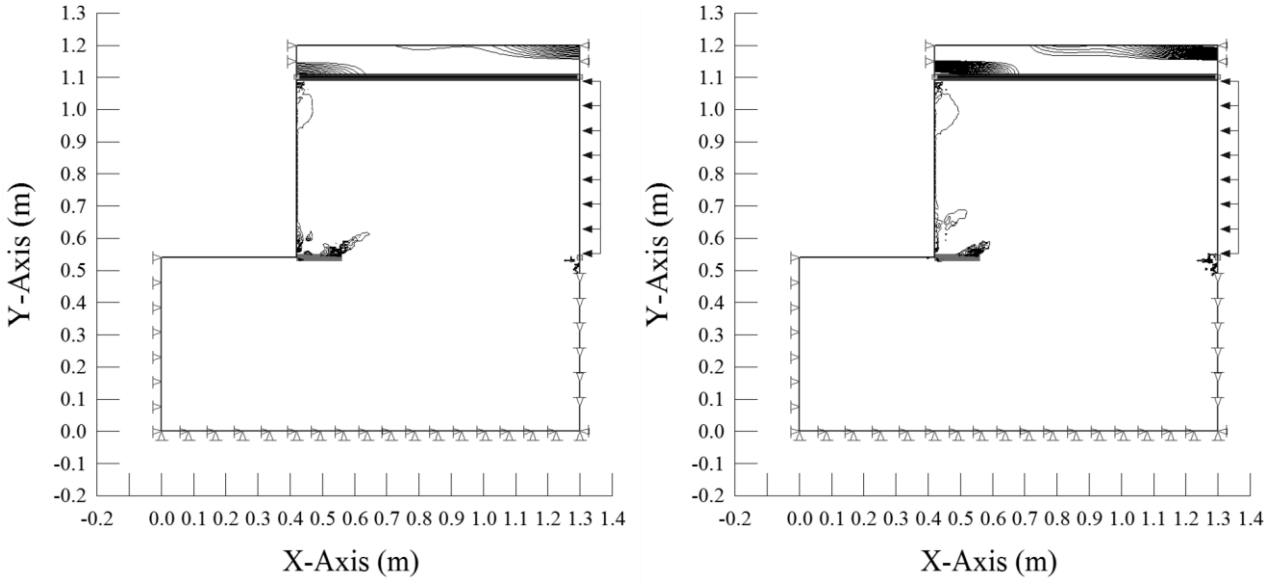

c) Lateral stress = 120-kPa

d) Lateral stress = 160-kPa

Figure 5.30. Vertical Slope FEM Model Analyses with ν = 0.45, Pre-Existing Toe Crack with a 50% Cohesive Strength Reduction, and Negative X-Stress Contours (10-kPa) Indicating Tension Zones.

5.3.1.1 Discussion of Findings. The homogeneous vertical slope model considered a pre-existing closed crack at the toe of slope. Linear elastic fracture mechanics theory indicated that crack propagation in a brittle material will occur in a radial direction from the tip and propagate in a direction in which σ_θ reaches its maximum value, which was shown to occur at $\theta = 70.5°$. The FEM models indicated that crack propagation did occur in a radial direction from the tip and the following findings are noted:

- FEM analyses for both the $\nu = 0.10$ and 0.45 resulted in nearly identical rates and direction of failure plane propagation.

- FEM models with a pre-existing toe crack exhibited similar failure plane propagation rate and direction that were independent of the reduction in cohesive strength along the slip element; that is, both the 25% cohesive reduction and the 50% cohesive reduction resulted in nearly identical rates and direction of failure plane propagation.

- FEM analyses for the simulated vertical slope model indicated the significance of an existing toe crack. The FEM models with an existing toe crack exhibited tangential stress fields that would cause a failure plane to propagate in a radial direction whereas the simulated slopes with no pre-existing toe crack did not exhibit any significant tangential stresses.

- FEM analyses indicated that initial failure plane propagation occurred in a radial direction from the tip and propagated at approximately 54° with respect to the x-axis. Figure 5.31 presents a plot of shear stress along the x-axis beginning at the tip of the slip element for $\nu = 0.10$ and considered a 25% cohesive strength reduction along the slip

element. Review of Figure 5.31 indicates that although there is stress concentrations at the tip of the crack, as encountered in the FEM shear models, the shear stresses at or near the slip element for the vertical slope model do not increase above the undrained shear strength until the second lateral stress increment. However by the second lateral stress increment, the FEM models indicated that crack propagation had already occurred in a radial direction (Figure 5.26 (b)). This finding was also noted for $\nu = 0.45$ cases. This indicates that crack propagation occurred in a radial direction from the crack tip prior to horizontal propagation.

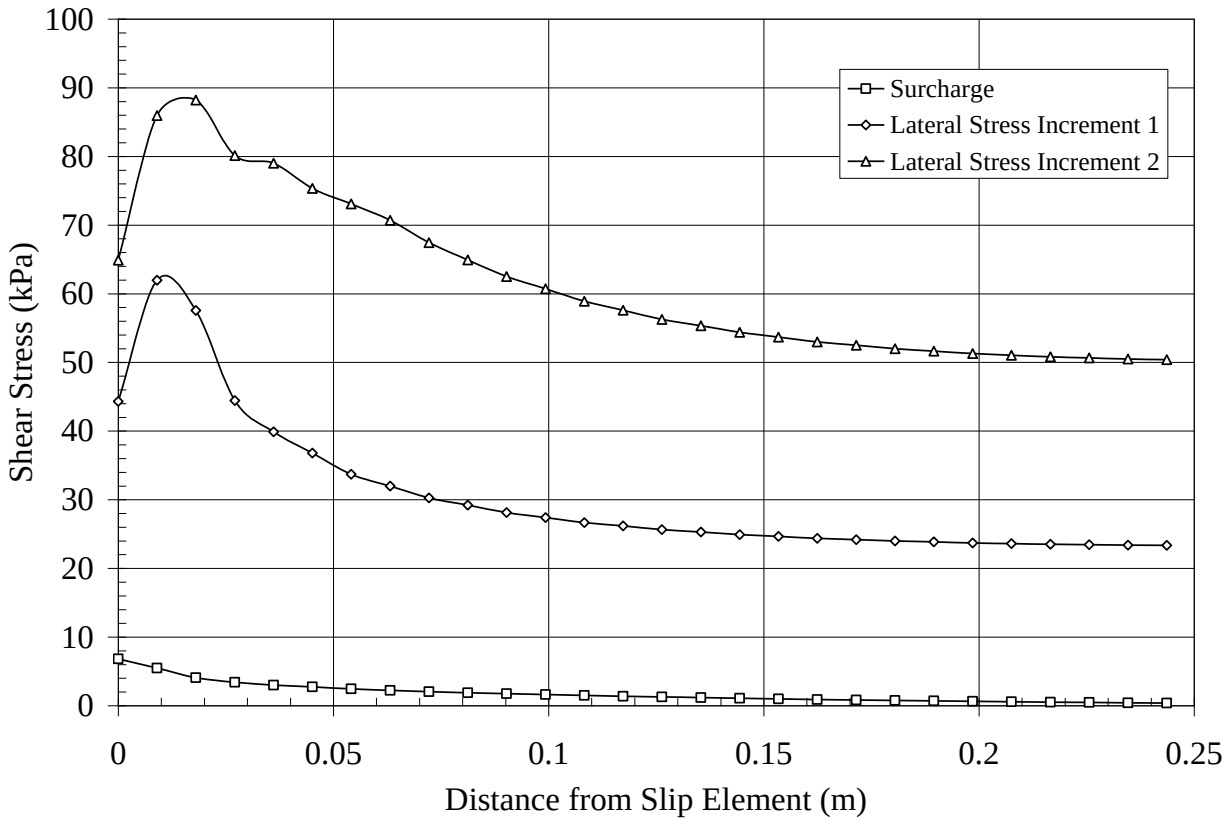

Figure 5.31. Shear Stress along a Horizontal Plane from the Tip of the Slip Element for $\nu = 0.10$ and a 25% Cohesive Strength Reduction along the Slip Element.

5.4 SUMMARY OF FINDINGS

FEM models were created to replicate the laboratory test program observations and study closed crack propagation under $\tau_{r\theta}$ and σ_{θ} loading conditions. The FEM models consisted of two shear models and one vertical slope model and utilized a slip element to represent an idealized crack. The shear models consisted of clay on clay and sand on clay to create two different interfaces along the potential failure plane. The vertical slope model consisted of clay on clay with a pre-existing toe crack. A summary of the findings from the FEM analyses is as follows:

- FEM analyses for the shear models replicated the laboratory test program observations regarding horizontal crack propagation for both the clay on clay and sand on clay shear models.

- FEM analyses for the shear models with $\nu = 0.10$ indicated that the rate of failure plane propagation occurred in a manner that was independent of the magnitude of shear strength reduction along the slip element; that is, both the 25% and 50% reductions in cohesive shear strength models resulted in nearly identical rates of failure plane propagation whereas the no shear strength reduction model required additional shear strain to achieve complete propagation of the failure plane across the model.

- FEM analyses for the shear models with $\nu = 0.45$ produced different results for the clay on clay and sand on clay models. The clay on clay shear models underwent crack propagation that was independent of the slip element; that is, the no shear strength, 25% and 50% shear strength reduction resulted in nearly identical rates of failure plane propagation. This result is attributed to the volumetric strain tending toward zero and the material becoming incompressible. However, when the FEM model incorporated an

upper sand section, the rate of failure plane propagation occurred in a manner that was independent of the magnitude of shear strength reduction along the slip element; that is, both the 25% and 50% reductions in cohesive strength models resulted in nearly identical rates of failure plane propagation whereas the no shear strength reduction model required additional shear strain to achieve complete propagation.

- The FEM shear models exhibited similar shear strain requirements as laboratory models; that is, the clay on clay model for both the laboratory and FEM model required less shear strain, compared to the sand on clay models, to develop the horizontal failure plane.

- The FEM model for the homogeneous vertical slope indicated crack propagation in a radial direction from the tip as predicted by fracture mechanics. Linear elastic fracture mechanics indicated that crack propagation would occur at 70.5° whereas the FEM models indicated 54±°. FEM analyses for both the $\nu = 0.10$ and 0.45 resulted in nearly identical failure plane propagation rate and direction.

- The FEM models for the homogeneous vertical slope with a pre-existing toe crack exhibited similar failure plane propagation rate and direction that were independent of the reduction in cohesive strength along the slip element.; that is, both the 25% cohesive reduction and the 50% cohesive reduction resulted in nearly identical rates and direction of failure plane propagation.

- The FEM models for the homogenous vertical slope indicated the significance of an existing toe crack. The FEM models with an existing toe crack exhibited tangential stress fields that could cause a failure plane to propagate in a radial direction whereas the

simulated slopes with no pre-existing toe crack did not exhibit any significant tangential stresses.

FEM models were developed in an effort to replicate the observed laboratory results and therefore validate their use for additional fracture mechanics studies. The FEM models and the principles of fracture mechanics exhibited general agreement with the laboratory testing program.

6.0 EVALAUTION OF THEORETICAL $\phi = 0°$ SLOPES USING FINITE ELEMENT METHODS

At-rest lateral earth pressures exist in clay soils and develop under long-term conditions as the soil is deposited and acted upon by changes in loading. Excavation into these material results in the release of confining stress along the slope face. The release of horizontal confining stress, or lateral stress relief (LSR), will produce an outward deflection along the slope face that drastically alters the in-situ stresses within the backslope region. FEM analyses are used to investigate the impact that LSR has on the stability of $\phi = 0°$ slopes.

6.1 INTRODUCTION OF FINITE ELEMENT MODELS

FEM models were developed for Vertical (90°), ¼H:1V (76°) and ½H:1V (63°) slopes. The FEM models used standardized material properties for all models developed in this research. The use of standardized material properties allowed comparison between models to observe failure plane propagation behavior under different load and geometric conditions. The geotechnical values used for the FEM laboratory models are shown in Table 6.1. These values were derived from laboratory testing of a geologic stratum known locally as the Pittsburgh Red Beds, which were discussed under Section 5.1.1.

Table 6.1. Geotechnical Parameters and Values Used for the FEM Models.

Geotechnical Parameter	Material and Parameter Values	
	Clay	Sand
E, Modulus of Elasticity	177,100 kPa	44,375 kPa
k_o, lateral earth pressure	1, 2, and 3	0.54
ν, Poisson's Ratio	0.40	0.35
c, Cohesion	86.2 kPa	0
ϕ, Friction Angle	0°	30°
ψ, Dilation Angle	0°	0°
γ, Unit Weight	20.42 kN/m^3	18 kN/m^3
θ, Slope Angle	90°, 76°, and 63°	--

FEM models used a two dimensional mesh with isoparametric elements that consisted of either six node triangles or eight node quadrilaterals. The analyses employed an elastic-plastic constitutive model which described an elastic-perfectly plastic relationship. Dunlop and Duncan (1970), Smith and Hobbs (1974), Griffiths and Lane (1999), and Griffiths (2000) indicated that this constitutive model is most appropriate for clay slopes under undrained conditions where both stress-strain relationships and the failure criterion are expressed in terms of total stresses.

As noted in Table 6.1, the FEM considered three different values, namely a k_o = 1, 2, and 3. Regarding overconsolidated clays, the at-rest lateral earth pressure coefficient is closely related to the stress history of the soil. Brooker and Peck (1993) reported that a k_o = 2.0 is generally associated with overconsolidated clays while Craig (1992) reported that k_o = 2.8 for London Clay with an OCR = 25. As such, a k_o value for a clay material as large as 3 is considered entirely appropriate for this study.

6.1.1 Initial FEM Analyses

FEM analyses were conducted for Vertical, ¼H:1V and ½H:1V slopes. The typical FEM model developed for a vertical excavation is shown as Figure 6.1. As indicated in Table 6.2, this slope had a factor of safety of 2.0 using Culmann's (1866) method and 1.34 using Terzaghi's (1943) method. Left and right boundaries were placed at a distance greater than three times the slope height to eliminate their influence (Dunlop and Duncan, 1969). In-situ stress conditions in the FEM model were first established without any disturbance or excavation (Duncan, 1996). Elements were subsequently removed and the slope face was allowed to relax under LSR.

The initial horizontal movement along the slope face due to LSR without regard for the development of shear zones is shown as Figure 6.2. These results represent consistent behavior with published case studies that indicate slight bulging near the toe of slope (Skempton and LaRochelle, 1965; Duncan and Dunlop, 1969; and Burland, et al, 1977). LSR also created significant changes to k_o in the backslope of the excavated face, as shown in Figure 6.3.

It should be noted that an unsupported vertical cut is not analogous to a retained excavation since the stress conditions are different. This impacts both the critical height and shape of the sliding surface (Terzaghi, 1943). An unsupported vertical excavation results in normal stress along the slope face that are equal to zero and the soil located above the potential failure surface is in a state of elastic equilibrium while the retained section is acted upon by compressive stresses in the lower region. This condition impacts both the height and shape of the sliding surface.

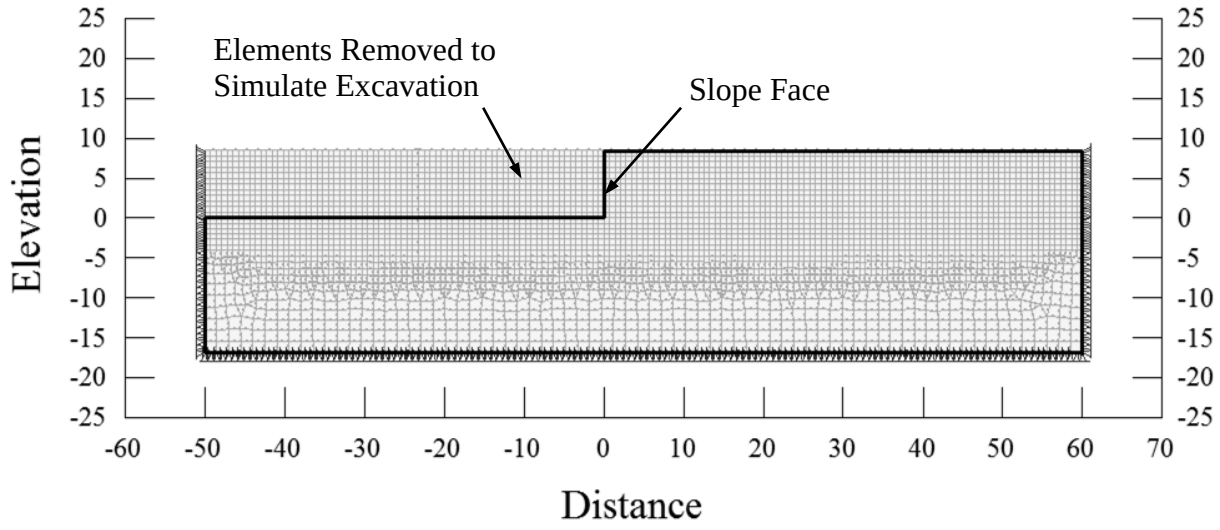

Figure 6.1. Typical FEM Model Used to Establish Initial Stress Conditions for a Clay Slope on Clay Base.

Table 6.2. FEM Model Critical Slope Height Parameters.

Critical Slope Height Parameters	Culmann's (1866) Method	Terzaghi's (1943) Method
Geotechnical Parameters	c = 86.2 kPa, γ = 20.42 kN/m^3	
Critical Height (m)	$H = \frac{4(86.2\ )}{20.42} = 16.9m$	$H = \frac{2.67(86.2)}{20.42} = 11.3m$
Slope Height used in FEM Analyses (m)	$8.45m$	
Theoretical Factor of Safety	$\frac{16.9}{8.45} = 2.0$	$\frac{11.3}{8.45} = 1.34$

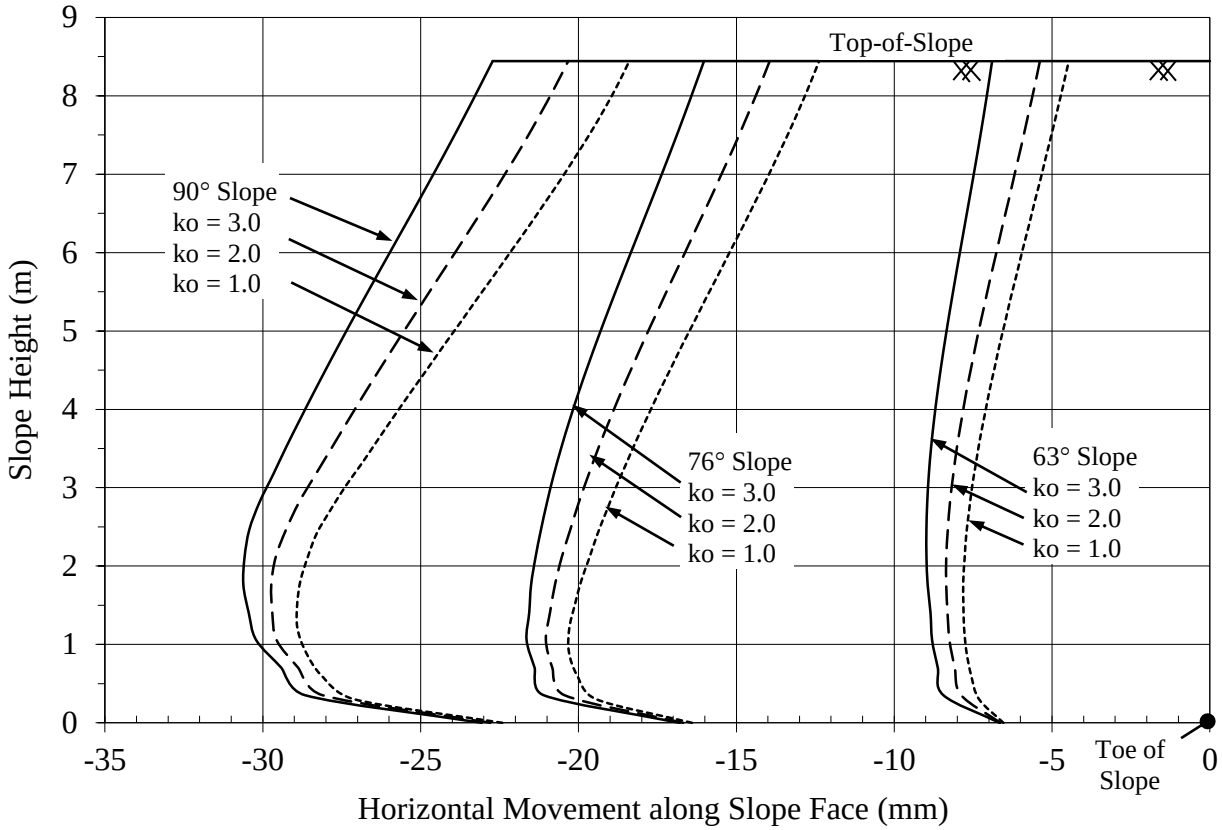

Figure 6.2. Horizontal Movement of the Slope Face from LSR Neglecting Shear Zones.

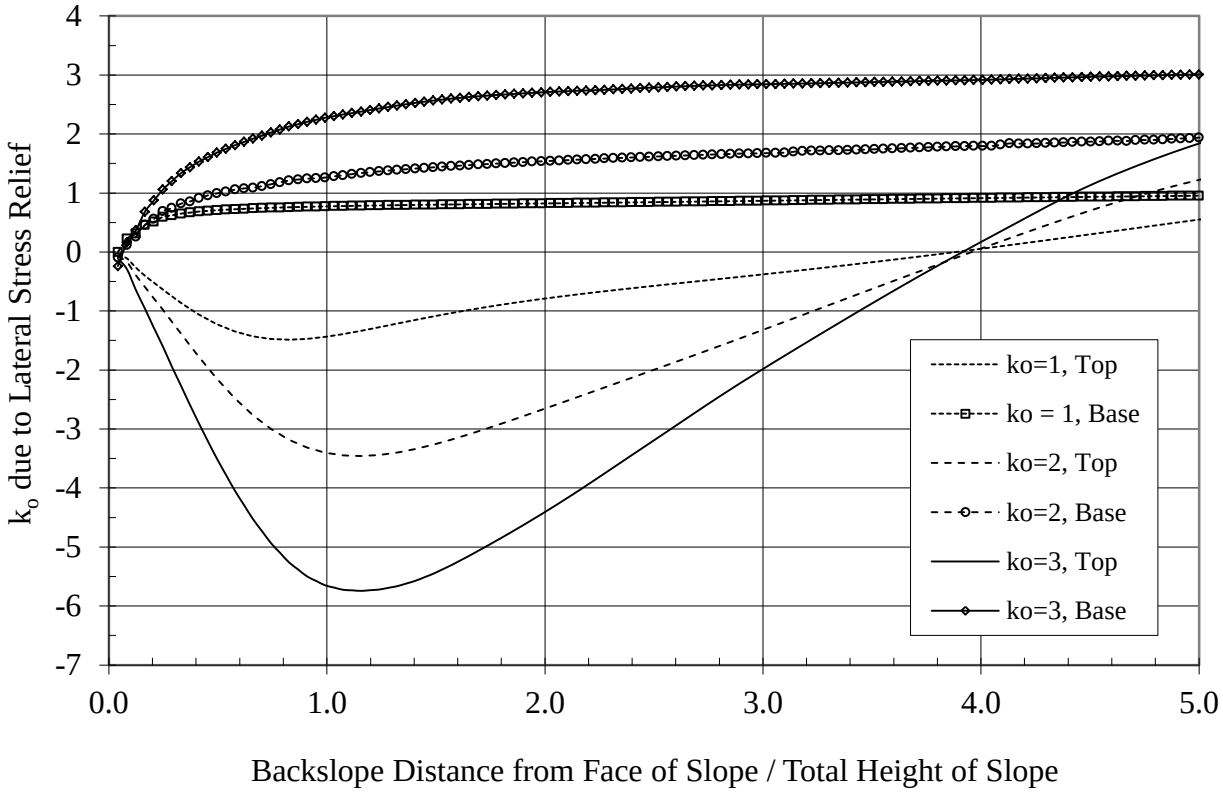

Figure 6.3. Impact of k_o from Lateral Stress Relief on a Vertical Slope without Consideration for Shear Zones.

Review of Figure 6.3 indicated that the lateral stress relief from an unsupported excavation impacted k_o for a distance of two to three times the slope height at the base of the excavation and the influence increased significantly at the top of the slope in the tension zone. Clough and O'Rourke (1990) note that the settlement profile behind a braced or anchored wall can extend behind the backslope a distance up to two times the depth of the excavation. However, when a retaining structure is not involved and the wall face is allowed to undergo LSR, studies performed herein suggest that distance for an unsupported cut is significantly greater at four times the slope height and strongly dependent on k_o. The extent of this influence is in general agreement with published case studies, which indicate that excavations underlain by a great depth of overconsolidated clay show backslope movements extending to more than three times the depth of the excavation (Burland, et al, 1977; Sills, et al, 1977; and Burland and Hancock, 1977).

6.1.2 Evaluation of FEM Stress Conditions

Stresses developed by the FEM models were evaluated at Gauss points to determine if shear planes developed using Mohr-Coulomb failure criterion. Figure 6.4(a) indicates the total stress for a theoretical element representative of an overconsolidated clay with k_o = 3.0. LSR altered the initial stress conditions as shear stresses developed within the soil mass. A failure plane, or crack, was considered to develop if Gauss point stresses exceeded the failure criterion, as shown on Figure 6.4(b).

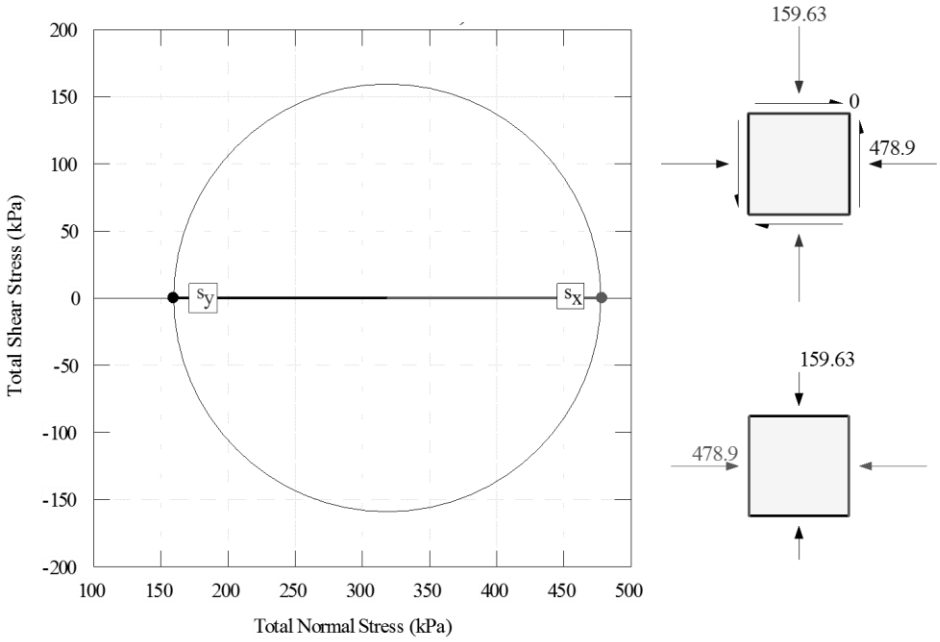

(a) Initial Stress Conditions Prior to LSR

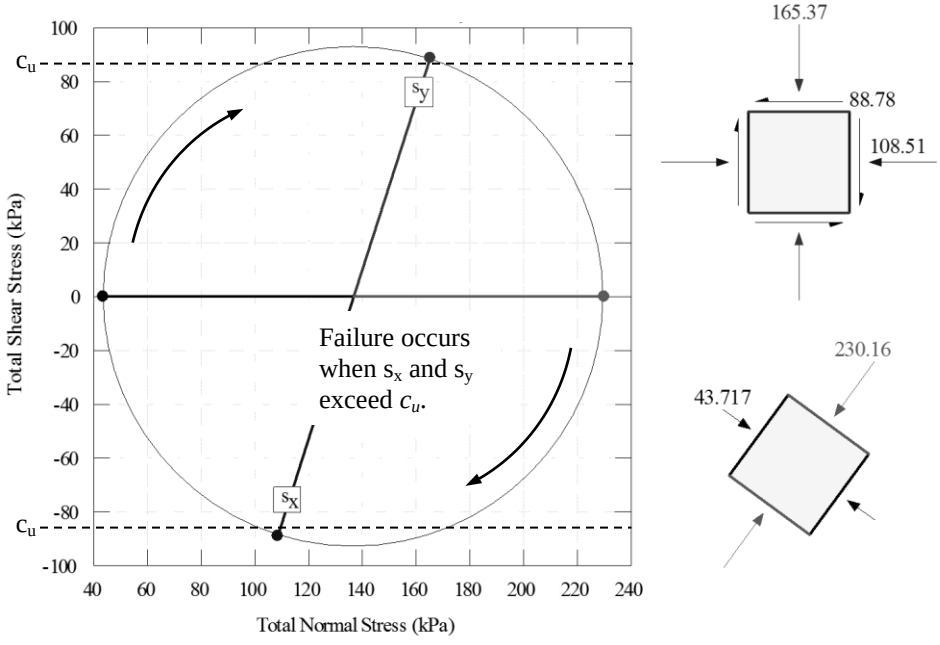

(b) Stress Conditions after LSR

Figure 6.4. Total Stress for a Theoretical Element with k_o = 3.0.

Vertical, horizontal, and tensile stresses were evaluated at each stage and the model was re-meshed to model crack propagation (Hellen, 2001; Griffiths, 2009). The FEM model developed areas or stress bulbs where the σ_θ (i.e., tensile strength) and / or $\tau_{r\theta}$ (i.e., shear strength) stresses would exceed the allowable value. When this occurred, a failure or crack was considered to develop in this region. Although actual failure planes develop from Riedel and Thrust discontinuities coalescing to form an undulating, continuous sliding surface (Skempton, 1966), these bulb failure regions were generally modeled as a single failure plane that would produce a kinetically viable failure plane to cause slope failure.

Closed cracks were modeled using slip elements with an increased mesh concentration to investigate failure plane propagation. A separate FEM model from the one presented in Figure 6.1 was developed to investigate the failure plane propagation; this model used a finer mesh concentration to capture the stress concentrations created by the failure plane "cracks". Vertical, horizontal, and shear stresses were evaluated at each stage and the model was re-meshed to model crack propagation (Hellen, 2001). Based on research conducted by Bazett, et al (1961), Skempton and LaRochelle (1965), and Burland, et al (1977), the analyses considered a reduction in the undrained shear strength along a slip element of 50%. It should be noted that research presented herein also demonstrated that as long as a reduction in shear strength occurred, the magnitude of that reduction did not significantly influence the rate and direction of failure plane propagation.

Angled cracks that initiated at the toe of slope were modeled as frictionless elements where negative lateral stress developed, indicating a gap condition. Frictionless elements are also justified by field observations from Skempton and LaRochelle (1965) where they discuss clay "burst" that occurred at the toe of excavation in London Clay. The London Clay was seen to

bulge and cracking extended into the slope face from the toe. Tensile criterion was based on a correlation study performed Fang and Fernandez (1981). Their research related unconfined compressive strength to tensile strength and resulted in a tensile strength of -41 kPa for the material noted in Table 6.1.

6.2 CLAY SLOPE ON CLAY BASE

The horizontal movement at the slope face due to LSR significantly altered the backslope conditions and created shear and tension cracks in the soil mass. Studies performed herein indicated that the initial direction of crack propagation was strongly dependent on k_o, with two principal failure planes developing in the soil mass at the toe of slope and one failure plane developing in the backslope along the crest. The failure planes are described as follows:

- *Horizontal Failure Plane*. The first failure plane, or crack, was attributed to differential strain-induced movement and extended in a general horizontal direction into the backslope at the base of the excavation. The length of this crack was dependent on k_o; the greater the k_o, the longer the horizontal crack extended into the backslope. This result is consistent with published case histories (Burland, et al, 1977).

- *Inclined Failure Plane*. The second failure plane was attributed to shear-induced changes created by LSR and extended in an upward angle from the toe of slope. The angle of the critical failure plane was also strongly dependent on k_o and the angle became steeper with increasing k_o. This behavior was consist with Skempton and LaRochelle (1965) in which

they discussed clay "burst" where the toe of excavation in London Clay was seen to bulge and that cracking extended into the slope face from the toe.

- *Tension Crack.* The final failure plane developed as a result of LSR which created a tension zone in the backslope that could initiate tension cracking.

Table 6.3 provides a summary of the FEM analyses for the clay slope on clay base. Appendix D contains the FEM analysis output figures.

Table 6.3. Summary of Finite Element Results for Clay Slope on Clay Base.

Slope Face Angle	Limit Equilibrium Factor of Safety	k_o	Slope Conditions due to Initial LSR			Slope Conditions due to Progressive Slope Failure	
			Initial Height of Failure Plane / Total Slope Height	Failure Plane Angle (wrt horizontal)			
				$\alpha_{Minimum}$	$\alpha_{Maximum}$	Did Slope Failure Occur ?	Depth of Tension Crack / Total Slope Height
90°	2.0	1.0	< 0.10	45°	45°	No	0.45
		2.0	0.13	46°	59°	Yes	0.46
		3.0	0.21	55°	77°	Yes	0.48
76° (¼H:1V)	2.6	1.0	< 0.10	45°	46°	No	N/A
		2.0	0.12	50°	60°	No	0.34
		3.0	0.22	50°	77°	Yes	0.47
63° (½ H:1V)	3.2	1.0	< 0.10	45°	46°	No	N/A
		2.0	< 0.10	50°	59°	No	0.27
		3.0	0.23	51°	77°	No	0.47

The development of the failure planes was attributed to LSR and considered Mohr-Coulomb failure criterion with stresses obtained at Gauss points. It is important to note that Table 6.3 indicated only one critical inclined failure plane. However, FEM analyses encountered numerous failure planes in the backslope, but these failure planes were disregarded in subsequent analyses since their impact on overall stability was considered kinematically unviable to overall

slope failure. Further investigation of the critical inclined failure planes noted in Table 6.3 revealed that they are consistent with the classical solutions regarding the stability of unsupported vertical cuts when k_o = 1, which results in an α = 45° (Culmann, 1866; Taylor, 1937; and Terzaghi, 1943). However, as k_o increased, the angle of the failure plane also increased and initial cracking extended to approximately ¼ of the total slope height, which is consistent with field observations from Skempton and LaRochelle (1965) and Burland, et al, 1977).

6.2.1 Sequence of Crack Propagation due to Lateral Stress Relief

FEM analyses were conducted for Vertical, ¼H:1V and ½H:1V slopes. Based on these FEM studies, the general sequence of crack propagation for a vertical slope is shown as Figure 6.5 and is summarized as follows:

1. Lateral stress relief resulted in the formation of a horizontal and inclined crack that initiated at the toe and extended into the backslope. Both the crack length and angle were directly related to k_o. In addition, lateral stress relief resulted in a tension zone at the crest of slope which initiated tension cracking (Figure 6.5(a));

2. The horizontal, inclined, and tension cracks propagated simultaneously due to stress concentrations. A toe failure developed that resulted in a wedge of material falling away from the slope due to negative vertical as well as lateral stress conditions. The toe failure tended to reduce propagation of the inclined crack, however, the tensile cracking continued to advance as the material "unzipped" itself (Figure 6.5(b));

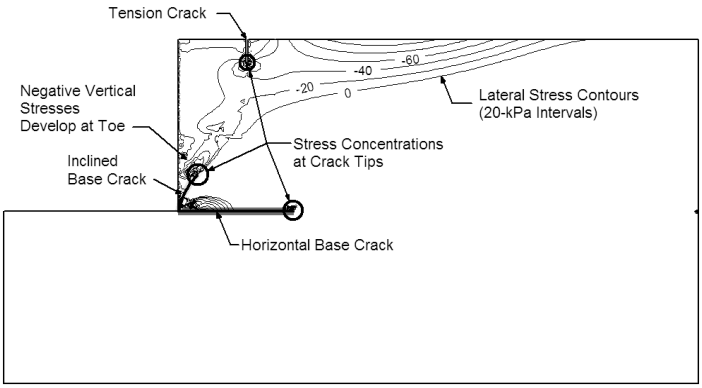

(a) LSR Results in Horizontal and Inclined Crack at Toe along with Tension Crack at Crest.

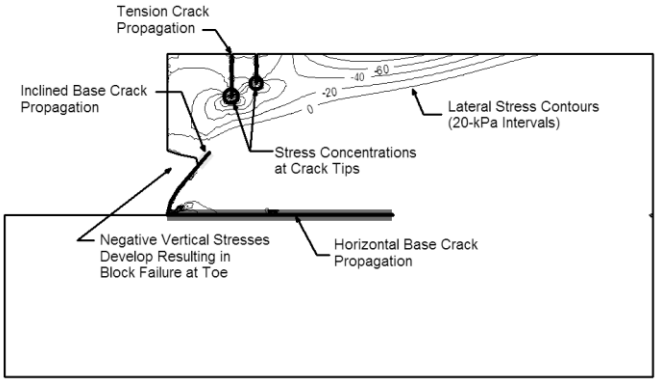

(b) Horizontal, Angle, and Tension Cracks Propagate Simultaneously due to Stress Concentrations; Negative Vertical Stresses Result in a Toe Failure.

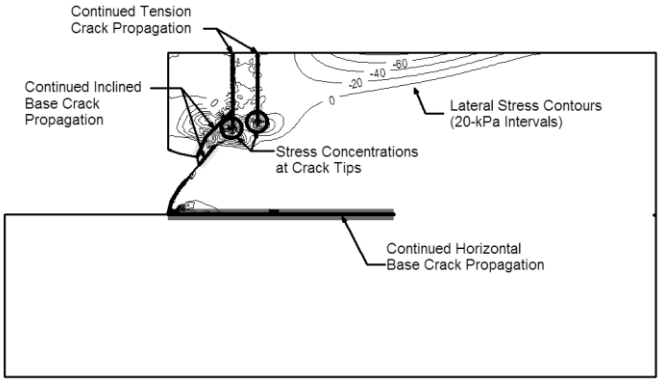

(c) Propagation of the Angle Crack Extending to the Tension Crack Resulting in Slope Failure.

Figure 6.5. Progressive Failure Propagation for a Vertical Slope with k_o = 3.0.

3. Tensile crack propagation generally occurred at a greater rate than angle crack propagation;

4. Ultimate slope failure was attributed to a sudden propagation of the angle crack that extended to the tension crack (Figure 6.5(c)).

Analyses indicate that the ¼H:1V slope remained relatively stable when k_o = 1 and 2, but failed when k_o = 3. Analyses also indicated that the ½H:1V slope remained stable for k_o = 1, 2 and 3. However, it is important to note that all three slopes (i.e., Vertical, ¼H:1V and ½H:1V) developed horizontal and inclined cracks at the toe due to initial LSR. Although FEM analyses did not predict failure in all of the models, one should not conclude that failure would not occur for these slopes. The FEM models did not consider long-term phenomena such as creep and the gradual destruction of diagenetic bonds, which can explain the long-term failures.

The progressive slope movement predicted by FEM after each iteration due to crack propagation for vertical slopes with k_o = 1, 2, and 3 is shown on Figure 6.6. FEM predicted a stable slope when k_o = 1.0, which is in accordance with classical solutions (Culmann, 1866; Taylor, 1937; and Terzaghi, 1943). However, FEM analyses indicated progressive slope failure when k_o = 2 and 3. It should also be noted that at slope failure, the depth of the tension crack varied from approximately 0.45H to 0.48H of the slope height, in accordance with Terzaghi's (1943) assumption.

Figures 6.7 and 6.8 present the progressive slope movement predicted by FEM after each iteration due to crack propagation for ¼H:1V and ½H:1V slopes, respectively. FEM predicted slope failure when k_o = 3.0 and a stable slope when k_o = 1 and 2 for the ¼H:1V slope. FEM predicted a stable slope when k_o = 1, 2, and 3 for the ½H:1V slope.

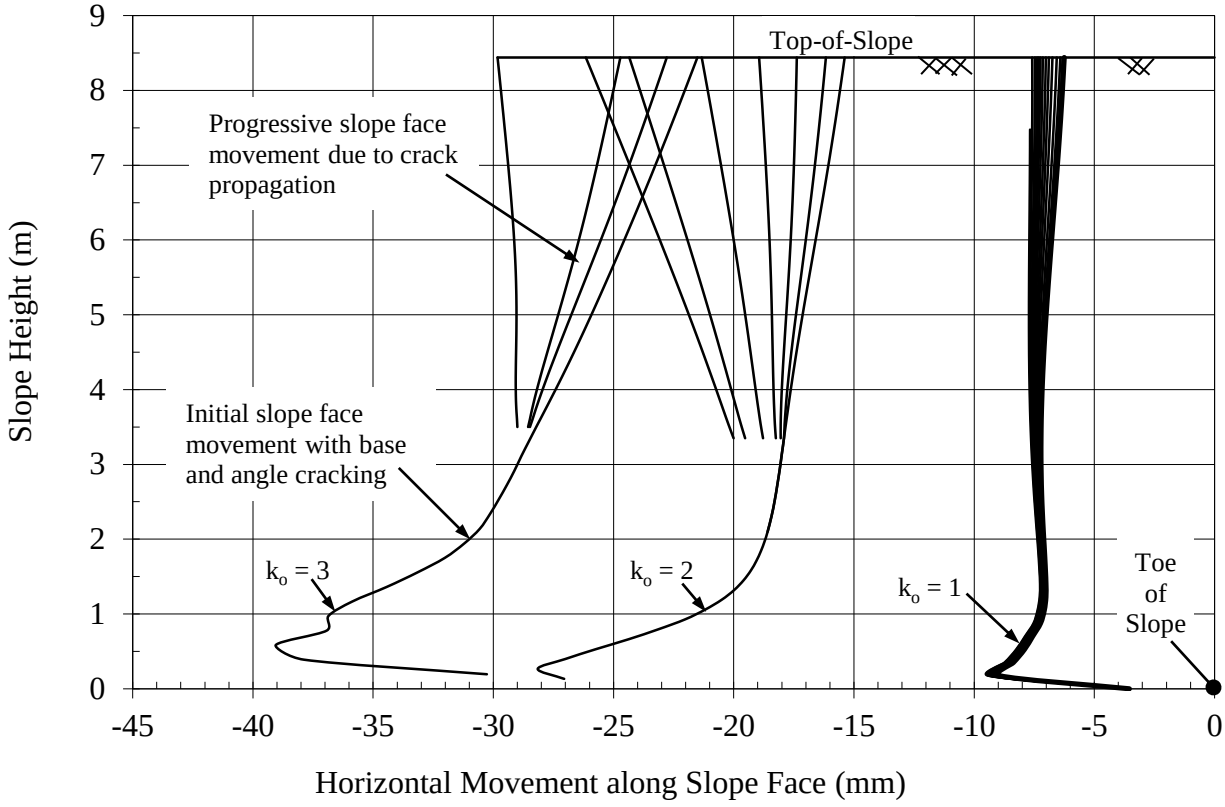

Figure 6.6. Progressive Horizontal Movement along a Vertical Slope Face Predicted by FEM.

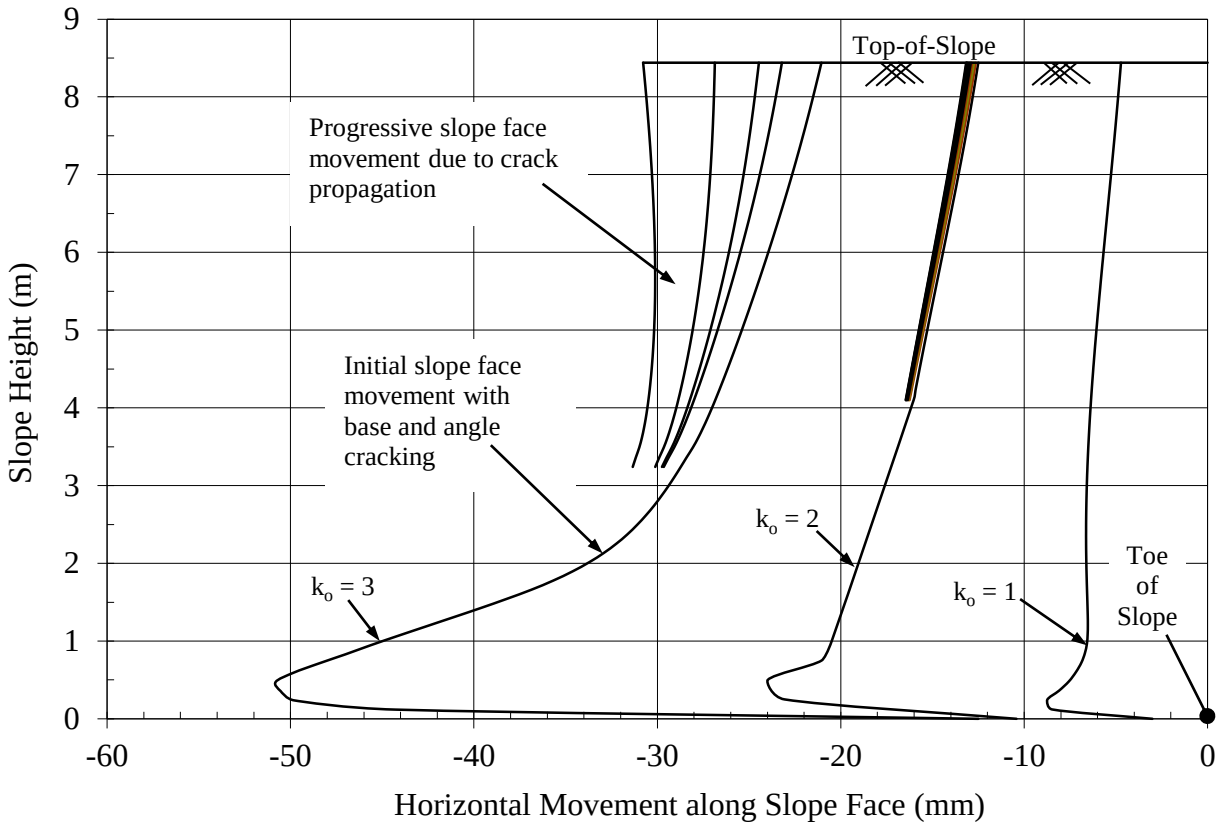

Figure 6.7. Progressive Horizontal Movement along a ¼H:1V Slope Face Predicted by FEM.

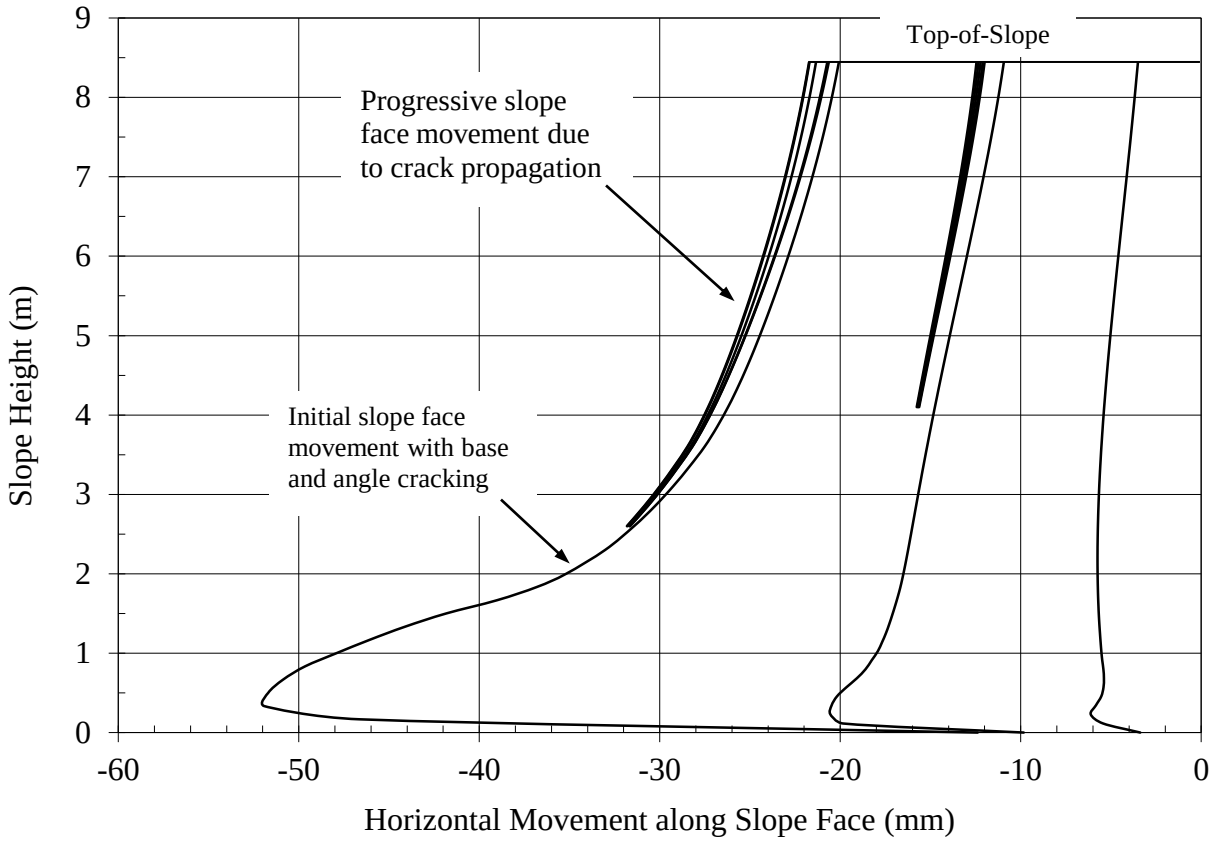

Figure 6.8. Progressive Horizontal Movement along a ½H:1V Slope Face Predicted by FEM.

6.3 CLAY SLOPE ON CLAY BASE WITH OPEN TOE CRACK

An open toe crack can develop in both natural and excavated slopes. An open toe crack can develop from such processes as erosion from wave action, differential weathering of moisture sensitive materials, over-excavation, and mining activities. Open toe cracks that develop from differential weathering are common with the moisture sensitive strata of western Pennsylvania (Kutschke, et al, 2007, 2007, 2007, and 2008). Shotcrete and dental concrete are commonly used to seal these strata and minimize continued development in excavated slopes, as exampled by Figure 6.9 obtained from the Pennsylvania Department of Transportation (PennDOT, 1950). This construction detail was used during the widening of the Boulevard of the Allies in Pittsburgh, PA to minimize weathering of an existing open crack created by differential weathering between the Wellersburg Claystone and Morgantown Sandstone.

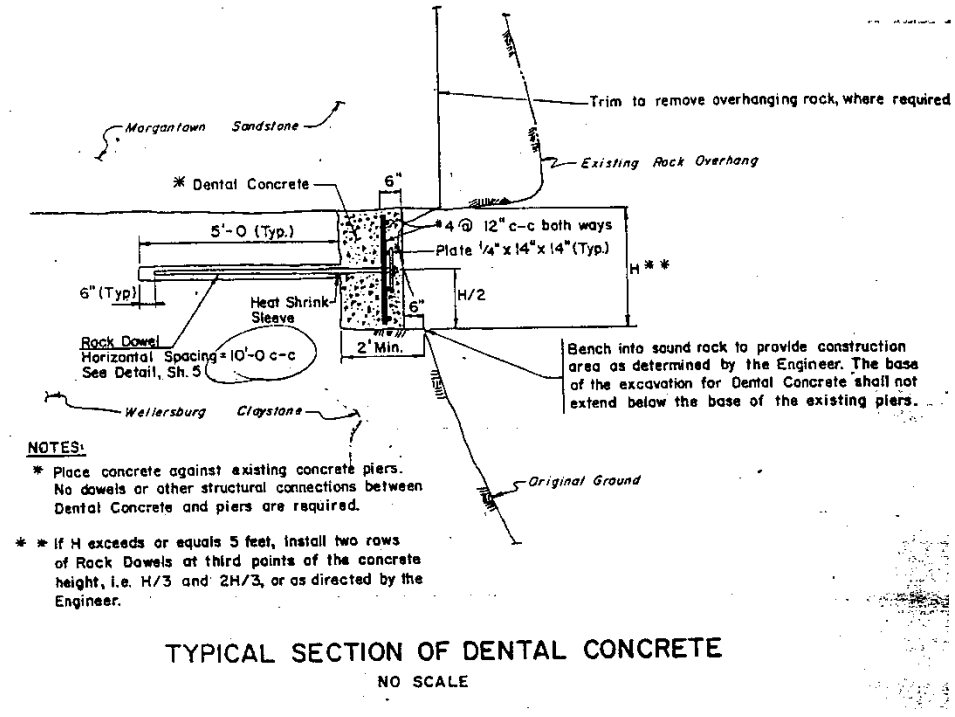

Figure 6.9. PennDOT Design Detail to Minimize Continued Development of a Toe Crack.

6.3.1 FEM Modeling of an Open Toe Crack

FEM analyses were conducted for a vertical slope with an open toe crack. The FEM models used the standardized material properties as noted in Table 6.1 and the slope height as noted in Table 6.2. The models used a two dimensional mesh with isoparametric elements consisting of either six node triangles or eight node quadrilaterals and employed an elastic-plastic constitutive model. FEM analyses considered three different values of k_o, namely 1, 2, and 3. Toe cracks were defined by the variable *Crack*, expressed as follows:

$$Crack = {H_{crack}}/{L_{crack}}$$

where H_{crack} is the crack height and for this research was maintained at 1-unit and L_{crack} is the crack length which was the variable (e.g., when *Crack* = 0.25, the crack was four times longer than it was higher). FEM analyses considered *Crack* = 0.25, 0.33 and 0.50, indicating that the length of the crack was 4, 3, and 2 times longer than it was higher, respectively.

The typical FEM model developed for a vertical excavation with a *Crack* = 0.25 is shown as Figure 6.10. Left and right boundaries were placed at a distance greater than three times the slope height to eliminate their influence (Dunlop and Duncan, 1970). In-situ stress conditions in the FEM model were first established without any disturbance or excavation (Duncan, 1996). Elements were subsequently removed and the slope face was allowed to relax under LSR.

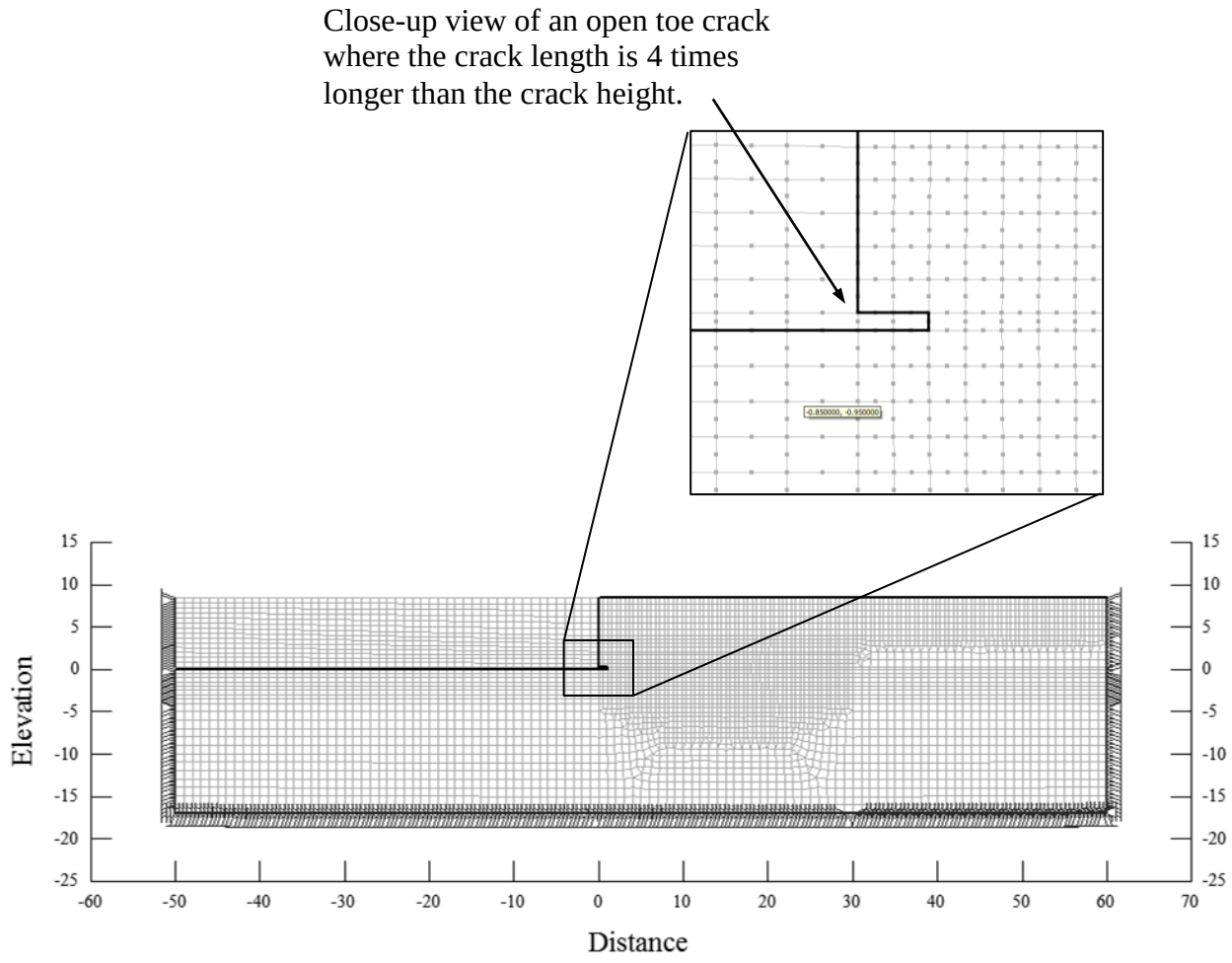

Figure 6.10. Typical FEM Model developed for a Vertical Excavation with *Crack* = 0.25.

6.3.2 FEM Analyses for Slope with an Open Toe Crack

FEM analyses were conducted for vertical slopes with an open toe crack. Appendix E contains the FEM output sheets. The initial horizontal movements along the slope face due to lateral stress relief without regard for the development of shear zones are shown as Figure 6.11. Movement was very similar to the clay slope on clay base analyses that neglected base cracking. Review of Figure 6.11 indicated that horizontal slope face movement was related to the crack length. A longer crack resulted in more outward slope face movement since the cantilevered open toe crack offered no resistance to movement. Failure plane development at the toe of slope due to lateral stress relief for a clay slope with an open crack occurred in a similar manner to crack propagation within a clay slope with a closed toe crack. Fracture mechanics principles indicated that an open or closed crack would propagate in a similar fashion under Mode II loading conditions.

The open toe crack combined with lateral stress relief created significant changes to k_o in the backslope of the excavated face, as shown in Figure 6.12 through 6.14. The toe crack had negligible impact on k_o near the base and middle of the slope. However, the toe crack had significant influence on k_o near the crest of the slope where the maximum tension zone occurred at 1.0H to 1.2H, where H is the total slope height. As the crack length increased, the magnitude of negative lateral earth pressure along the crest also increased, which is intuitively correct. A *Crack* = 0.50 resulted in a maximum k_o value of -2.0, while a *Crack* = 0.25 resulted in a k_o value of -2.7 for an initial k_o = 1.0, as shown on Figure 6.12. A similar conclusion was also noted in Figure 6.13 and 6.14.

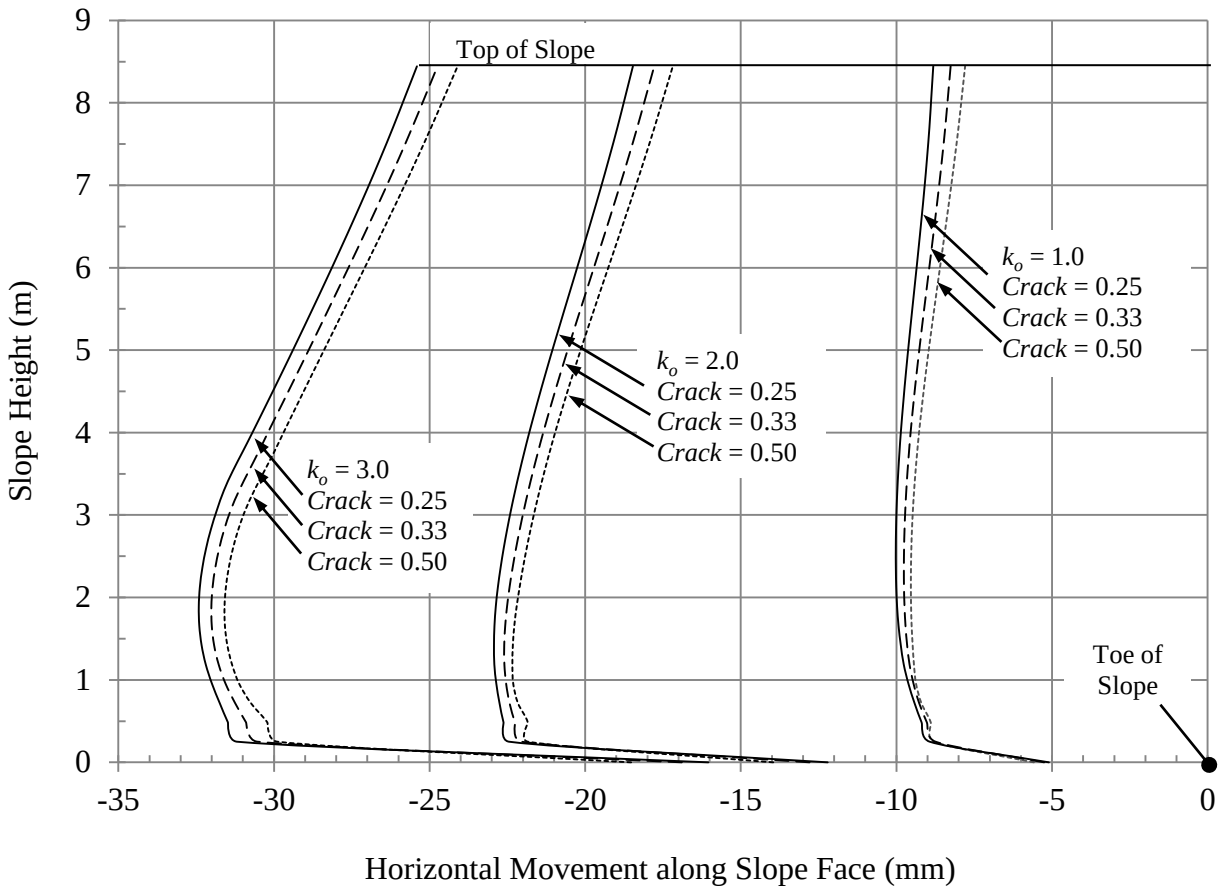

Figure 6.11. Initial Horizontal Movement due to LSR along a Vertical Slope Face with an Open Toe Crack and Neglecting the Development of Shear Zones.

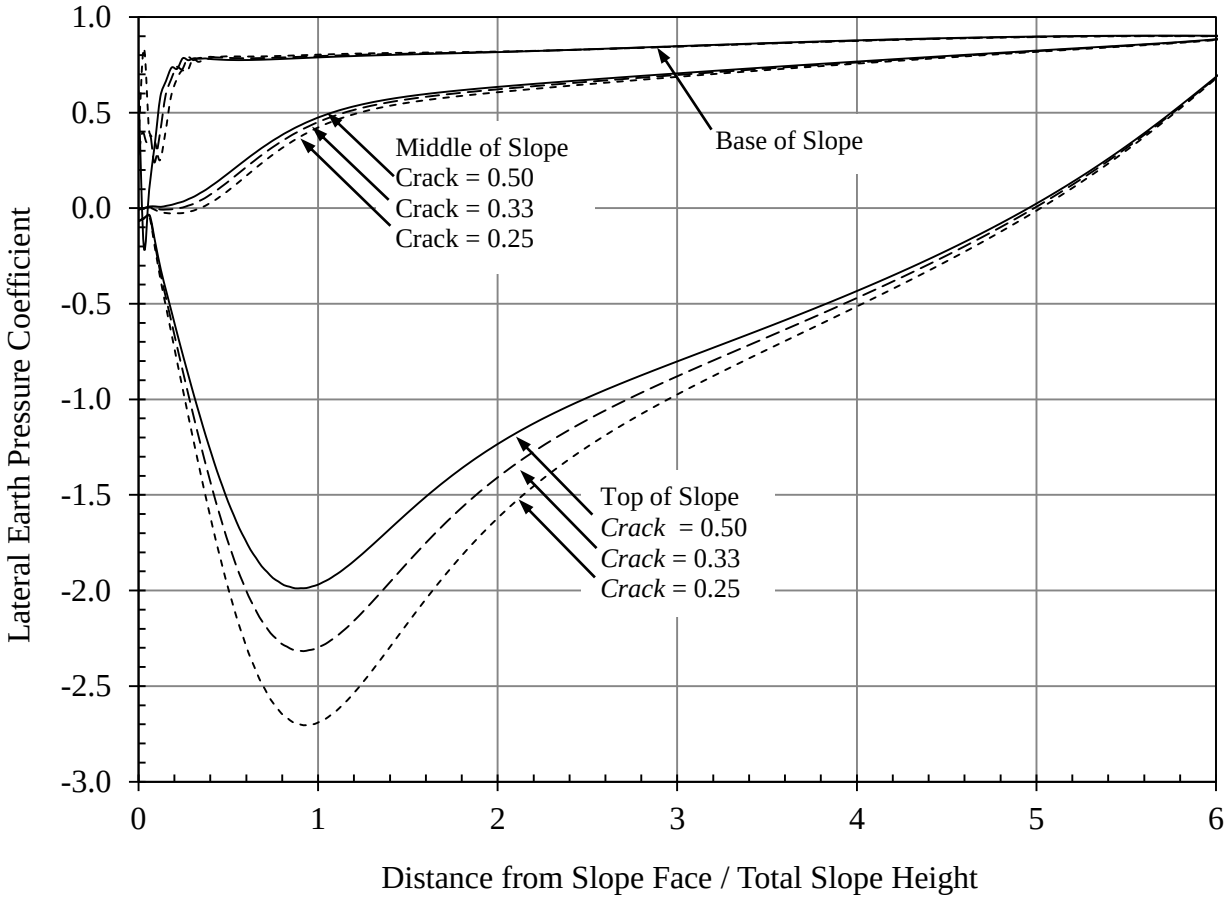

Figure 6.12. Variation of the Lateral Earth Pressure Coefficient for a Vertical Slope subjected to LSR with an Initial k_o = 1.0.

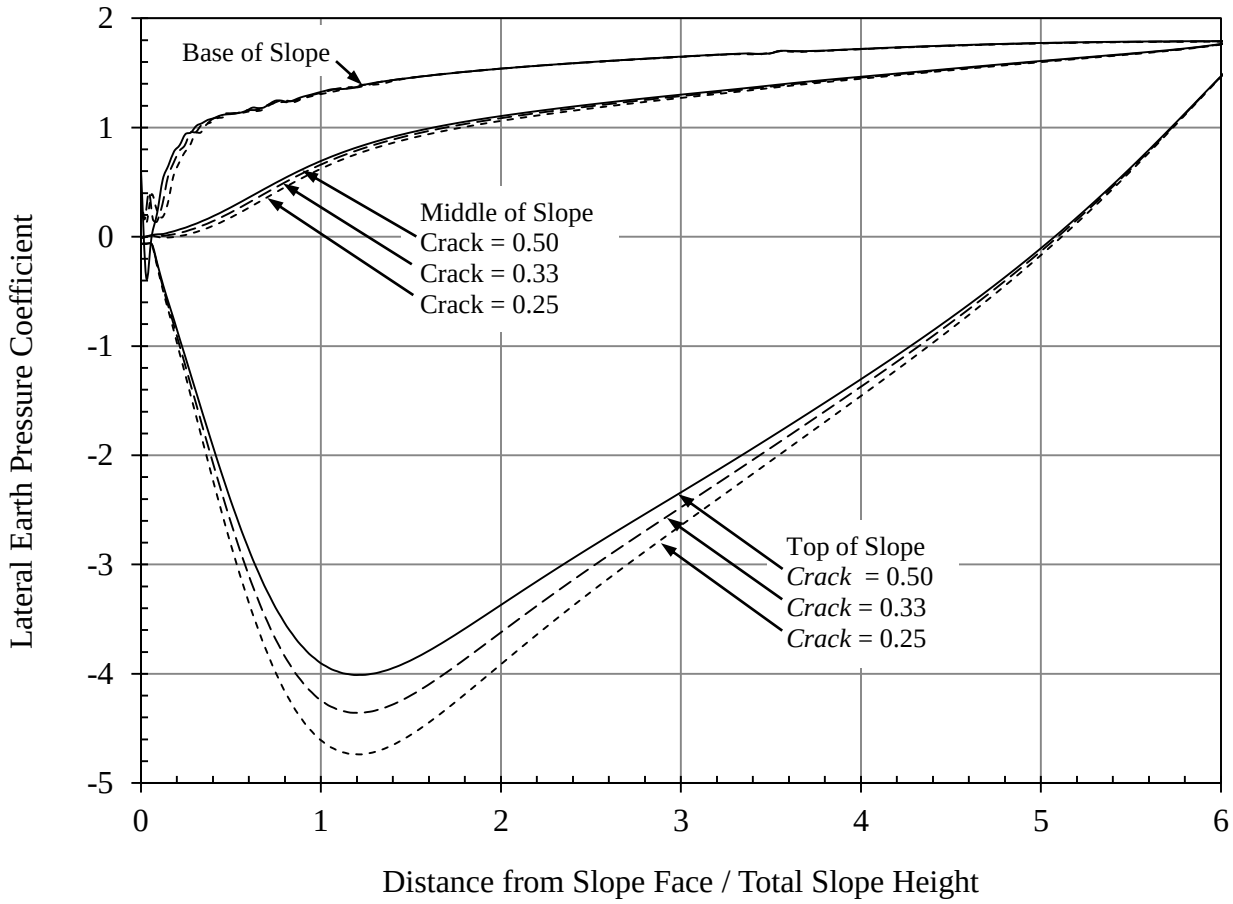

Figure 6.13. Variation of the Lateral Earth Pressure Coefficient for a Vertical Slope subjected to LSR with an Initial k_o = 2.0.

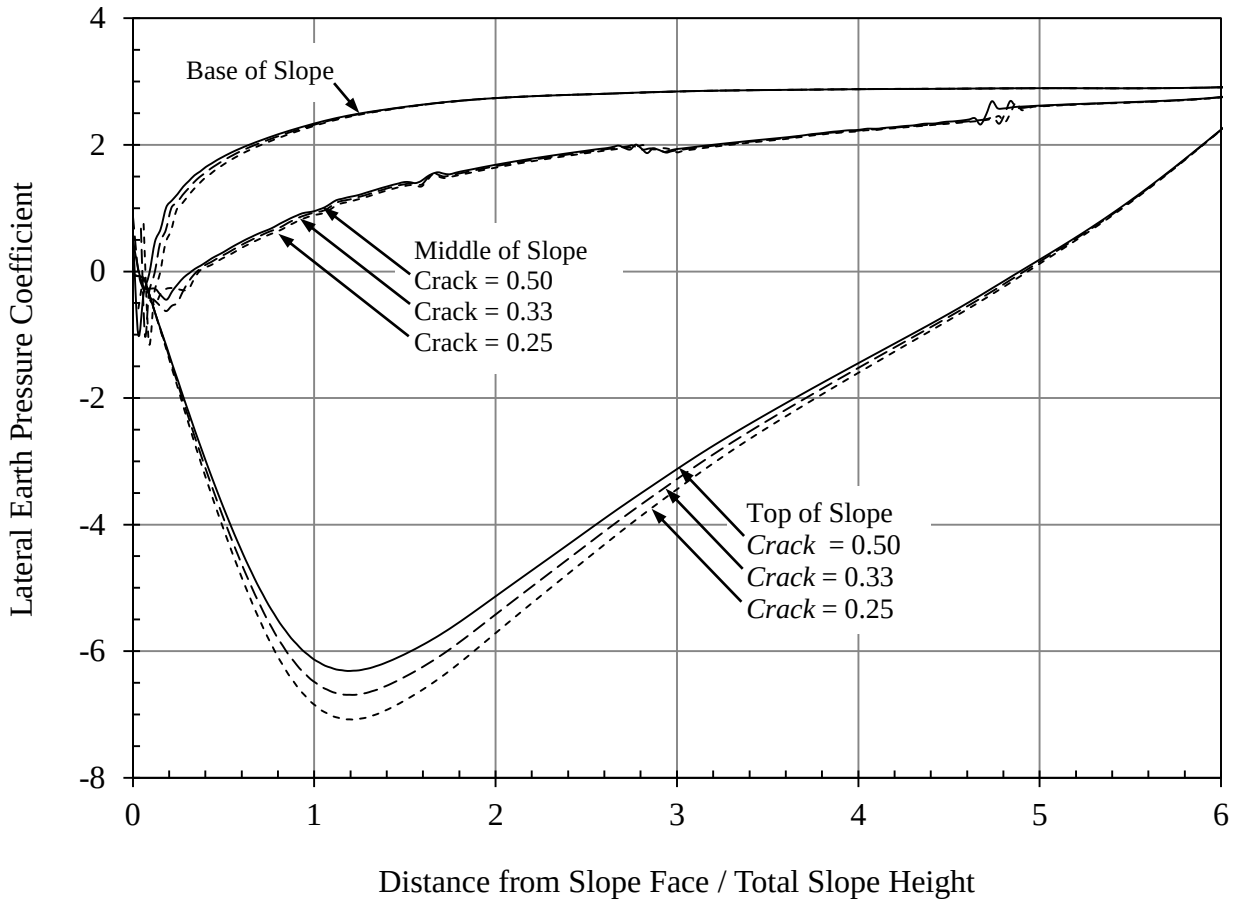

Figure 6.14. Variation of the Lateral Earth Pressure Coefficient for a Vertical Slope subjected to LSR with an Initial k_o = 3.0.

The *Crack* geometry condition influenced the depth of the initial tension zone from LSR, as summarized in Table 6.4. Table 6.4 also presents the depth of the initial tension zone for vertical clay slope on a clay base with no open toe crack at the base of the slope. An open toe crack increased the depth of the initial tension zone from LSR. This is significant since the clay slope on clay base FEM models with a closed crack indicated that tensile crack propagation generally occurred at a greater rate than angle crack propagation. As such, vertical clay slopes with an open toe crack would undergo an increased rated of crack propagation.

Table 6.4. Depth of Initial Tension Crack along Backslope for Vertical Clay Slope on Clay Base without and with an Open Toe Crack.

k_o	Depth of Initial Tension Crack due to LSR / Total Height of Slope		
	Without Open Toe Crack	With Open Toe Crack	
1.0	< 0.10	*Crack* = 0.50 0.33 0.25	0.03 0.06 0.09
2.0	0.13	*Crack* = 0.50 0.33 0.25	0.15 0.17 0.19
3.0	0.21	*Crack* = 0.50 0.33 0.25	0.21 0.22 0.23

6.4 CLAY SLOPE ON SAND BASE

FEM models were developed for Vertical, ¼H:1V and ½H:1V clay slopes on a sand base. The FEM models used standardized material properties as noted in Table 6.1 and the clay slope height as noted in Table 6.2. FEM models used a two dimensional mesh with isoparametric elements consisting of either six node triangles or eight node quadrilaterals. The analyses employed an elastic-plastic constitutive model for both the sand and clay. Several FEM models were developed for this research with only the variable being the lateral earth pressure coefficient that considered k_o = 1, 2, and 3, and the slope angle which considered β = 90°, 76°, and 63°.

6.4.1 FEM Analyses for Clay Slope on Sand Base

The typical FEM model developed for a vertical excavation is shown as Figure 6.15. As indicated in Table 6.2, this slope had a factor of safety of 2.0 using Culmann's (1866) method and 1.34 using Terzaghi's (1943) method. Left and right boundaries were placed at a distance greater than three times the slope height to eliminate their influence (Dunlop and Duncan, 1970). In-situ stress conditions in the FEM model were first established without any disturbance or excavation (Duncan, 1996). Elements were subsequently removed and the slope face was allowed to relax under LSR. Appendix F contains the FEM output sheets.

The initial horizontal movement along the slope face due to lateral stress relief without regard for the development of shear zones is shown as Figure 6.16. These results represent consistent behavior with published case studies which indicate slight bulging near the toe of slope (Skempton and LaRochelle, 1965; Duncan and Dunlop, 1969; and Burland, et al, 1977). It

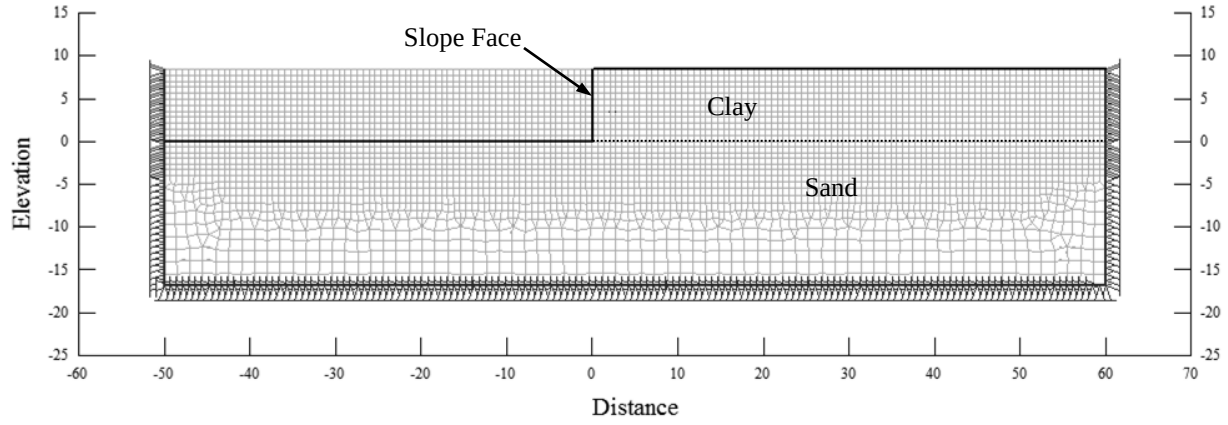

Figure 6.15. Typical FEM Model Used to Establish Initial Stress Conditions for a Clay Slope on Sand Base.

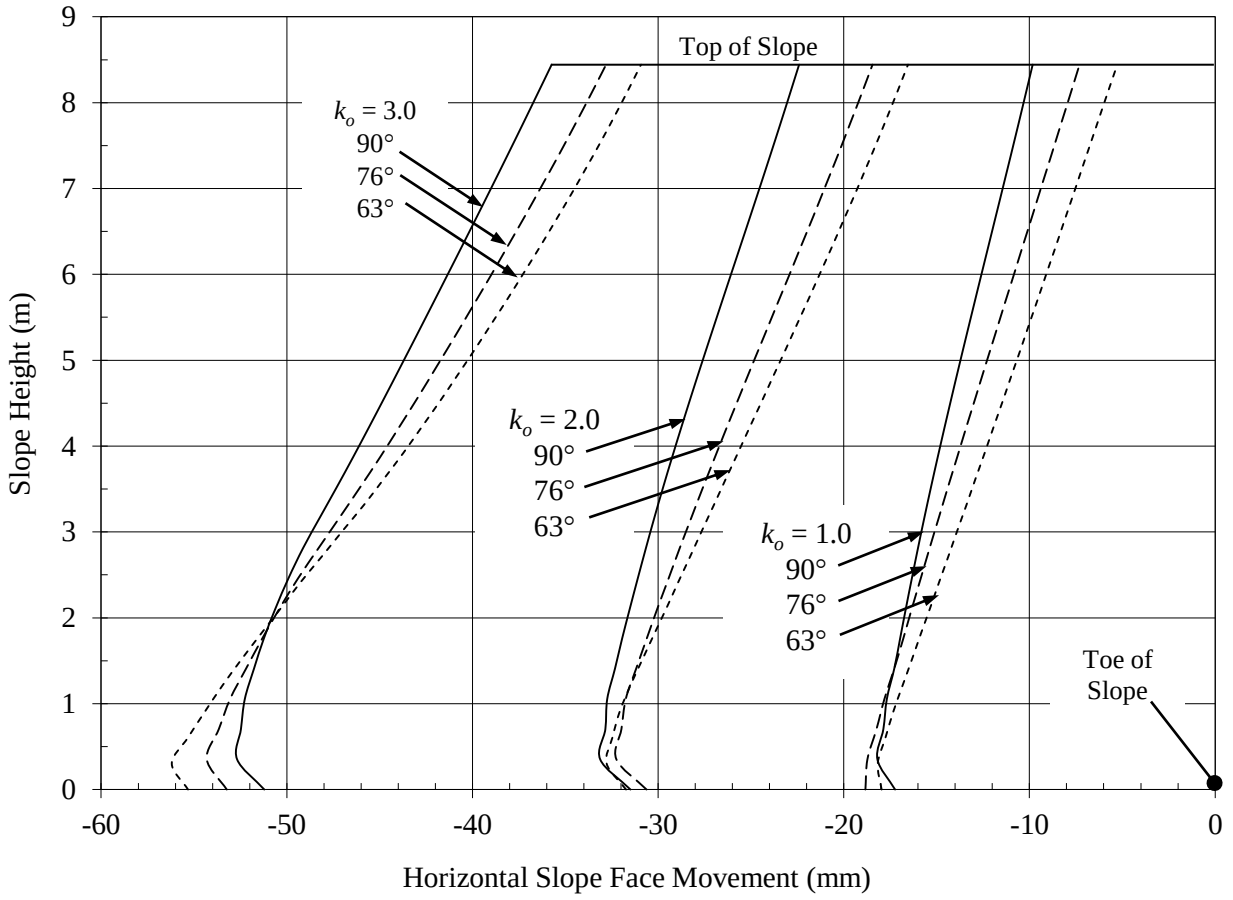

Figure 6.16. Horizontal Slope Face Movement from LSR Neglecting Shear Zones.

is interesting to note that the slope face movement for the clay slope on sand base had larger displacements than the slope face movement for the clay slope on clay base; refer to Figure 6.17 for a direct comparison. The larger horizontal slope face movement created significant changes to k_o in the backslope of the excavated face. The variation of k_o along the top of slope from initial LSR without regard for the development of shear zones is shown as Figure 6.18. Review of the Figure 6.18 indicated that the greatest impact on k_o from LSR was for the vertical slope and the impact decreased with decreasing slope angle. LSR for the vertical slope created a significant tension zone in the backslope region that resulted in k_o decreasing from the initial value of k_o = 3, to a LSR value of k_o = -7.0±. This is significant since tensile crack propagation generally occurred at a greater rate than angle crack propagation. However, the impact of LSR on k_o decreased with a decreasing slope angle. A slope angle of ½H:1V actually experienced a slight increase in k_o near the slope face, which has been attributed to rebound of the slope face from removal of the overburden material.

The horizontal slope face movement also created differential movement between the upper clay slope and lower sand base, as shown on Figure 6.19. The differential movement for the vertical slope extended approximately 1.5H back into the backslope region for the vertical slope face and approximately 1.0H for the ¼H:1V slope. This finding in consistent with a published case history for a near vertical clay slope on a sand base in which the ground within a region of about 1.0 to 1.5 times the depth away from the face appeared to move as a block sliding on a horizontal shear band formed by bedding planes near the base of the excavation (Burland, et al, 1977).

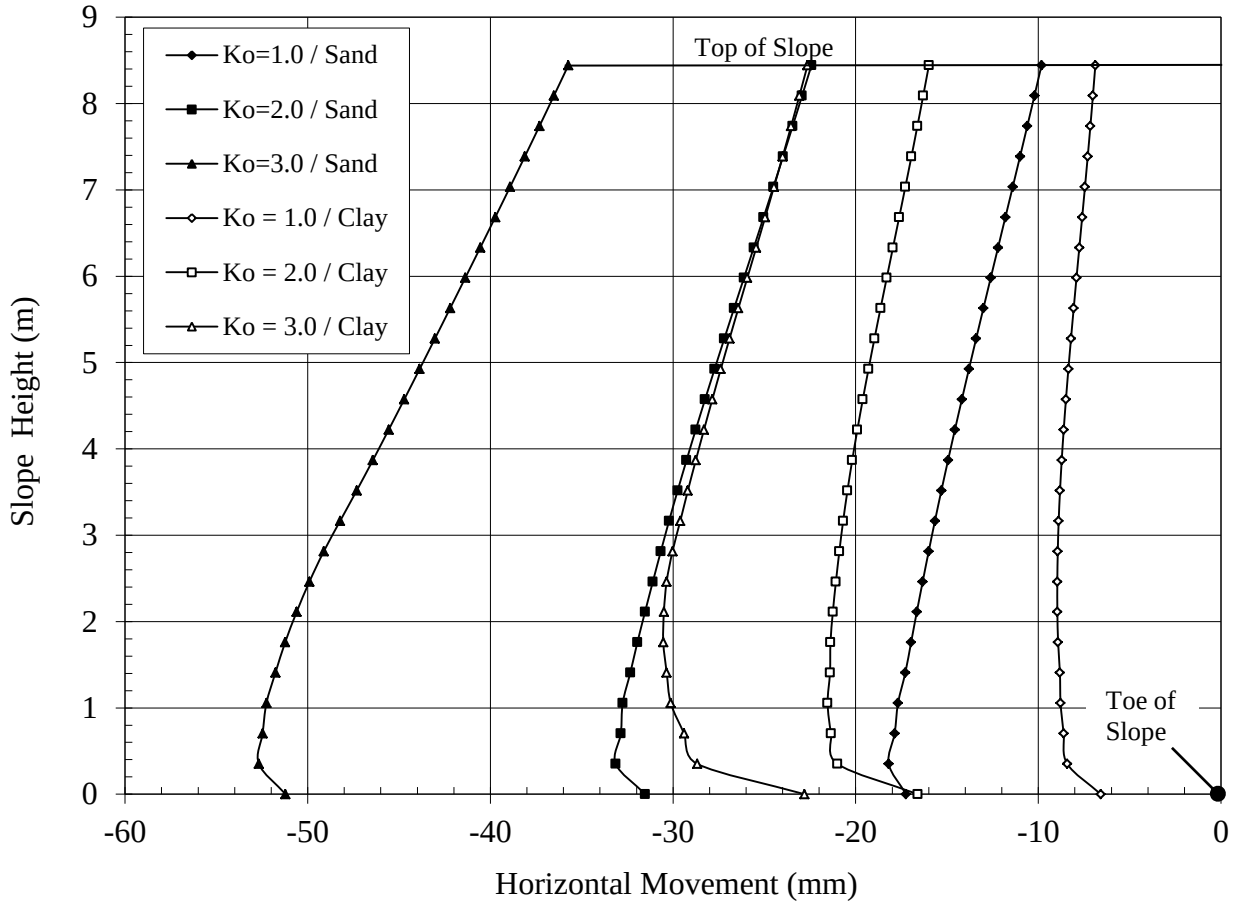

Figure 6.17. Comparison of Horizontal Slope Face Movement due to LSR between Vertical Clay Slopes on Sand and Clay Bases Neglecting Shear Zones.

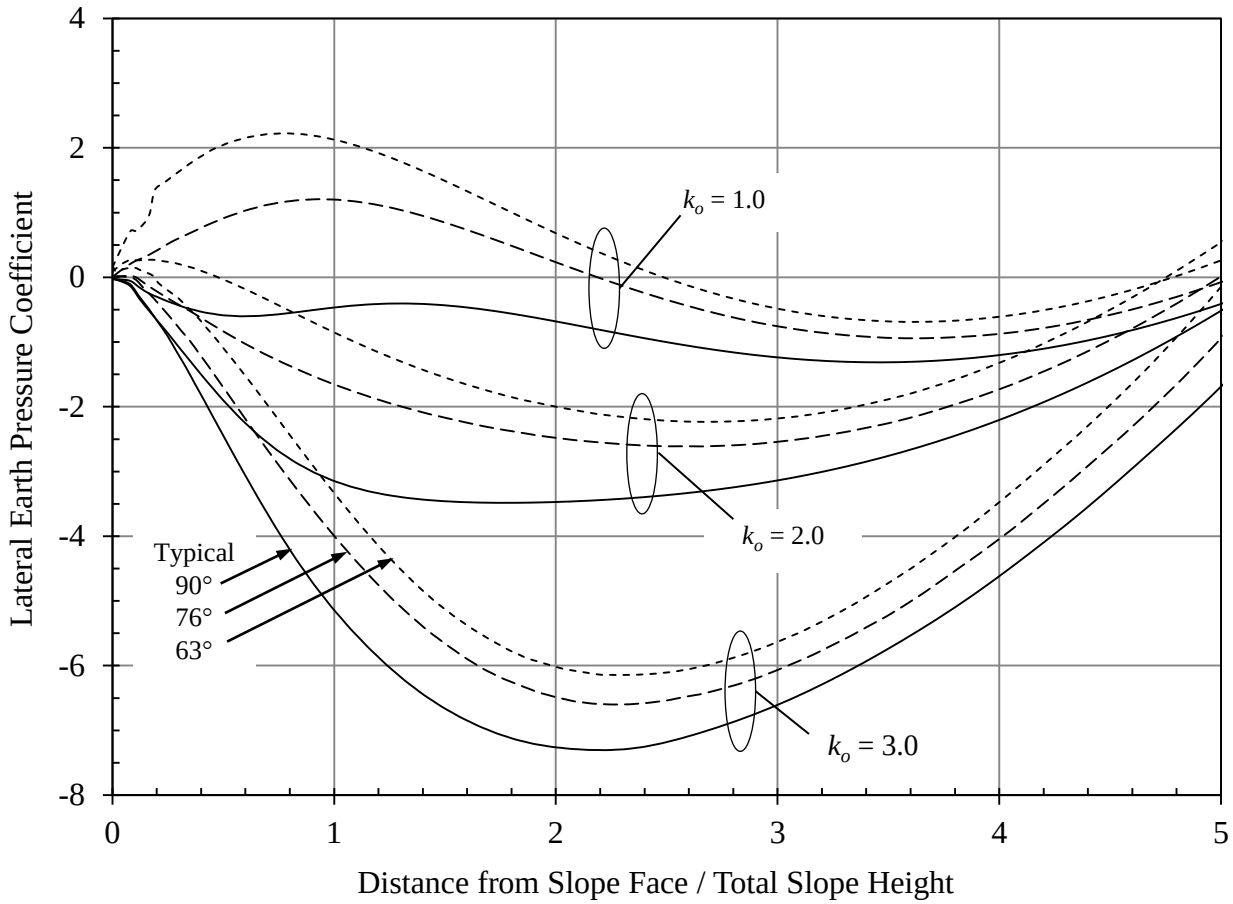

Figure 6.18. Variation of Lateral Earth Pressure along Top of Slope from LSR for a Vertical Clay Slope on Sand Base.

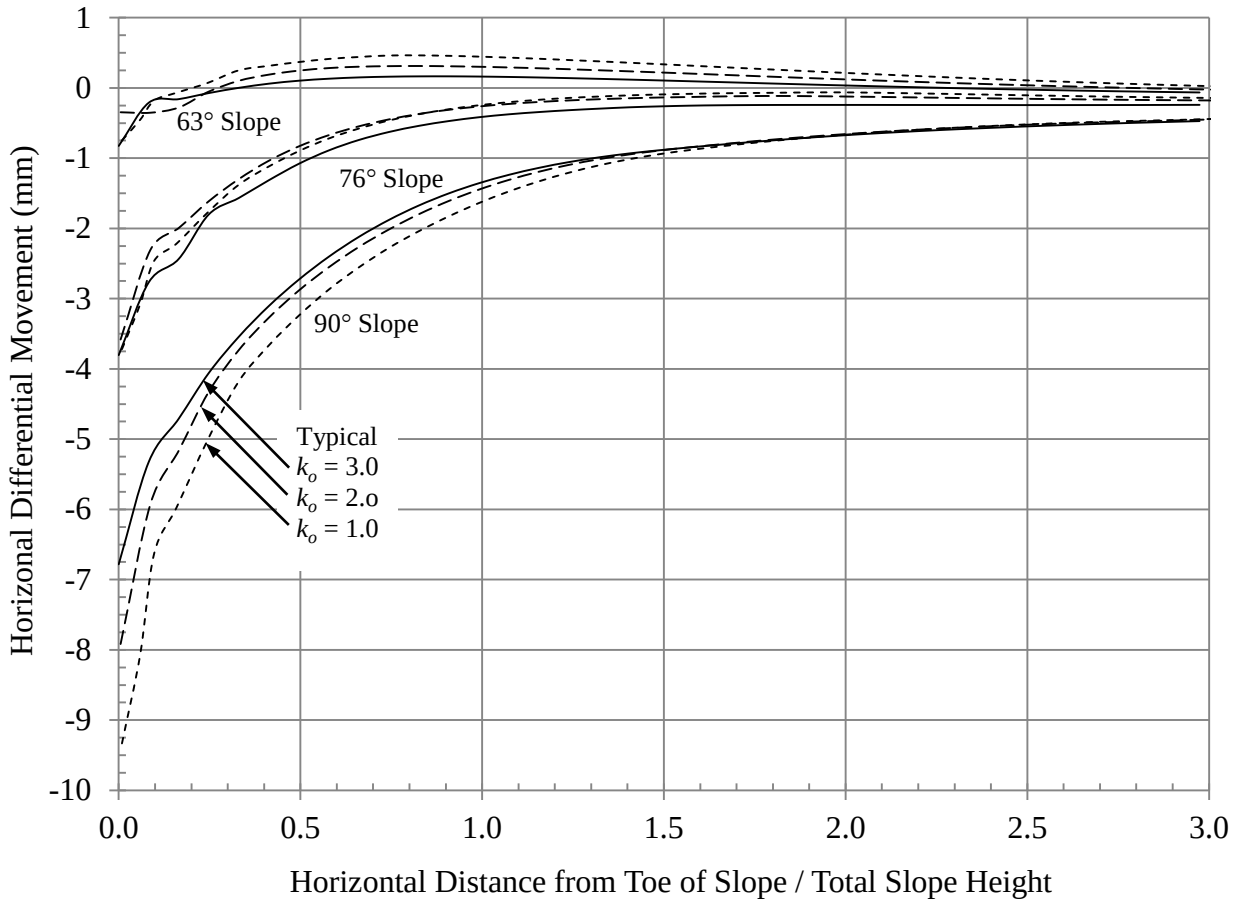

Figure 6.19. Differential Horizontal Movement due to LSR along the Interface between the Upper Clay and Lower Sand.

6.5 SUMMARY OF FEM

LSR for clay slopes significantly altered the backslope conditions and created shear and tension cracks in the soil mass. The initial direction of crack propagation was strongly dependent on k_o, with two principal failure planes developing in the soil mass at the toe of slope and one failure plane developing in the backslope along the crest, as shown on Figure 6.20. The failure planes are described as follows:

- *Horizontal Failure Plane*. The first failure plane, or crack, was attributed to differential strain-induced movement and extended in a general horizontal direction into the backslope at the base of the excavation. This result was consistent with the principles of fracture mechanics for shear induced failure in which the failure plane propagated along the pre-existing horizontal failure plane. The length of this crack was dependent on k_o; the greater the k_o, the longer the horizontal crack extended into the backslope.

- *Inclined Failure Plane*. The second failure plane was attributed to shear-induced changes created by LSR and extended in an upward angle from the toe of slope. This result was consistent with the general principles of fracture mechanics, although the crack propagation angle was not in strict conformance. The angle of the critical failure plane was also strongly dependent on k_o and the angle became steeper with an increasing initial k_o. The crack did not propagate along a constant angle, rather it generally became flatter as it progressed into the backslope.

- *Tension Crack.* The final failure plane developed as a result of LSR which created a tension zone in the backslope that could initiate tension cracking. Tension crack

propagation adhered to the principles of fracture mechanics which indicates that the cracks would tend to propagate vertically with the crack plane.

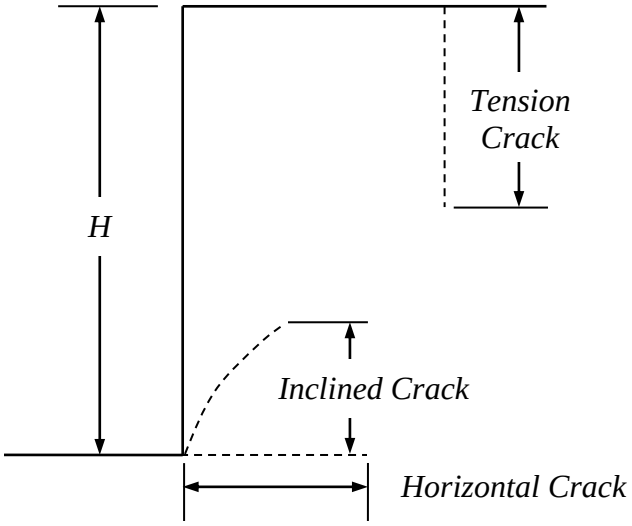

Figure 6.20. Failure Planes Created by Lateral Stress Relief.

FEM analyses indicate a strong relationship between overall slope stability and the initial k_o value. A vertical slope remained stable for k_o = 1.0, as predicted by classical methods. However, LSR resulted in the formation of toe and tension cracks that lead to eventual slope failure for vertical slopes with initial k_o = 2 and 3. The ¼H:1V slope remained relatively stable when k_o = 1 and 2, but failed when k_o = 3. Analyses also indicated that the ½H:1V slope remained stable for k_o = 1, 2 and 3.

7.0 MODIFICATION OF LIMIT EQUILIBRIUM STABILITY ANALYSES

Conventional limit equilibrium methods of slope stability analysis for unsupported vertical cuts in cohesive material only consider the development of a tension zone (Terzaghi, 1943). However, FEM analyses preformed herein indicate that LSR resulted in the formation of tension and toe cracks that lead to the eventual slope failure for vertical as well as inclined slopes. LSR for clay slopes significantly altered the backslope conditions and created shear and tension cracks in the soil mass. The initial direction of crack propagation was strongly dependent on k_o. As such, the limit equilibrium equations for the stability of analyses for unsupported vertical cuts in cohesive material need to consider the impact of LSR.

7.1 VERTICAL SLOPES

Conventional limit equilibrium methods of slope stability analysis for unsupported vertical cuts in cohesive material only consider the development of a tension zone (Terzaghi, 1943). The derivation of this equation was provided under Section 1.2.3 and is presented as Equation 7-1 for ready reference.

$$H_{CRITICAL} = \frac{2.67 c_f}{\gamma} \qquad 7\text{-}1$$

Equation 7-1 does not consider the development of shear zones that occur from lateral stress relief at the toe of slope. Review of Figure 7.1 indicated that continued propagation of H_I would produce a kinematically viable failure plane that would result in overall slope failure. Terzaghi (1943) noted that the curvature of the sliding surface through a vertical bank can be disregarded since the mathematical difference between a curved and plane failure surface is, for practical purposes, negligible. Applying this same assumption, the conditions for stability of a vertical slope has been modified to account for the inclined toe crack that develops from LSR.

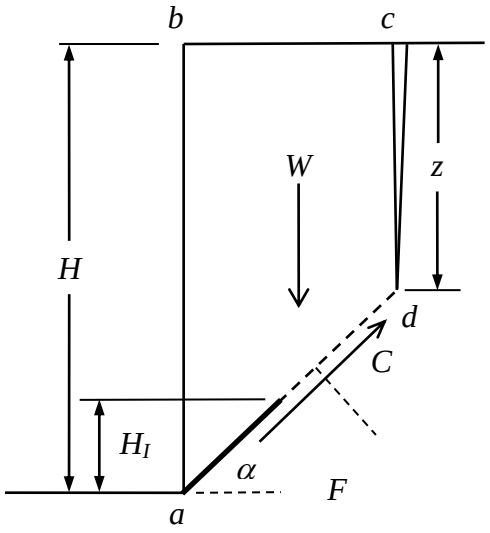

Figure 7.1. Vertical Slope with Plane Failure Surface, Tension and Toe Crack.

Recall that the mass of soil (W) defined by block $\overline{abcd}$ was expressed as:

$$W = \frac{\gamma\left(H^2 - z^2\right)}{2\tan\alpha} \qquad 7\text{-}2$$

The sliding resistance (C) has been modified to account for the toe crack and is given by:

$$C = \frac{c_f}{\sin\alpha}\left(H - H_I - z\right) \tag{7-3}$$

H_I is subtracted from the overall slope height and does not provide shear resistance. FEM modeling indicated that k_o at the toe developed negative vertical and lateral stresses that resulted in a section of the material dislodging from the slope face. Skempton and LaRochelle (1965) confirm this finding in which they discussed clay "burst" where the toe of excavation in London Clay was seen to bulge and that cracking extended into the slope face from the toe.

At limit equilibrium, the sum of the forces on the sliding plane must equal 0. Therefore, combining Equation 7-2 and Equation 7-3 resulted in the following expression:

$$\frac{\gamma\left(H^2 - z^2\right)}{2\tan\alpha}\sin\alpha - \frac{c}{\sin\alpha}\left(H - H_I - z\right) = 0 \tag{7-4}$$

Manipulating Equation 7-4 produces the following expression, which is similar to Equation 1-49, but considers the impact of toe cracking due to LSR:

$$\left(H^2 - z^2\right)\sin 2\alpha - \frac{4c_f}{\gamma}\left(H - H_I - z\right) = 0 \tag{7-5}$$

Based on laboratory testing using gelatin samples, Terzaghi (1943) made the assumption that $z = H/2$. FEM studies performed herein indicate that this assumption was appropriate as the depth of the tension crack varied from 0.45H to 0.48H for a vertical slope when k_o varied from 1.0 to 3.0, respectively. Therefore Equation 7-5 may be simplified as follows:

$$\left(H^2 - \frac{H^2}{4}\right)\sin 2\alpha - \frac{4c_f}{\gamma}\left(H - H_I - \frac{H}{2}\right) = 0 \tag{7-6}$$

which reduces to the following expression:

$$\left(\frac{3H^2}{4}\right)\sin 2\alpha = \frac{4c_f}{\gamma}\left(\frac{H}{2} - H_I\right) \qquad 7\text{-}7$$

FEM studies performed herein indicated that two parameters noted in Equation 7-7 are dependent on k_o, namely the angle of the failure plane (α) and height of the inclined failure plane (H_I). Recall that Table 6.3 summarized the FEM values for α and H_c from initial LSR and these values are presented in Table 8.1 for ready reference.

Table 7.1. FEM Results for Clay Slope on Clay Base due to Initial LSR.

k_o	Slope Conditions due to Initial LSR		
	Height of Failure Plane / Total Slope Height (H_I)	Failure Plane Angle	
		$\alpha_{Minimum}$	$\alpha_{Maximum}$
1.0	< 0.10	45°	45°
2.0	0.13	46°	59°
3.0	0.21	55°	77°

The maximum angle of the failure plane occurred immediately at the toe of slope in direct relation to k_o. Review of the FEM analyses indicted that k_o increased rapidly and achieved a value of k_o = 1.0 within 0.1 to 0.2H for all values of k_o at the toe of slope, as noted in Figure 6.3. As such, the minimum angle of the failure plane was chosen for use in Equation 7-7 since this value would most accurately represent the overall failure plane conditions. Utilizing the values noted in Table 7.1 for H_c and $\alpha_{Minimum}$, Equation 7-1 may be expressed as noted in Figure 7.3 where the solution has been expressed in terms of the Stability Factor, N_s. As noted in Figure

7.3, the solution considered that when k_o = 1.0, the limit equilibrium case was appropriate. The initial height of the failure plane was less than 0.1H when k_o = 1.0 and FEM analyses indicated agreement with the limit equilibrium solution. As such, no further modification of this expressed was considered for k_o = 1.0.

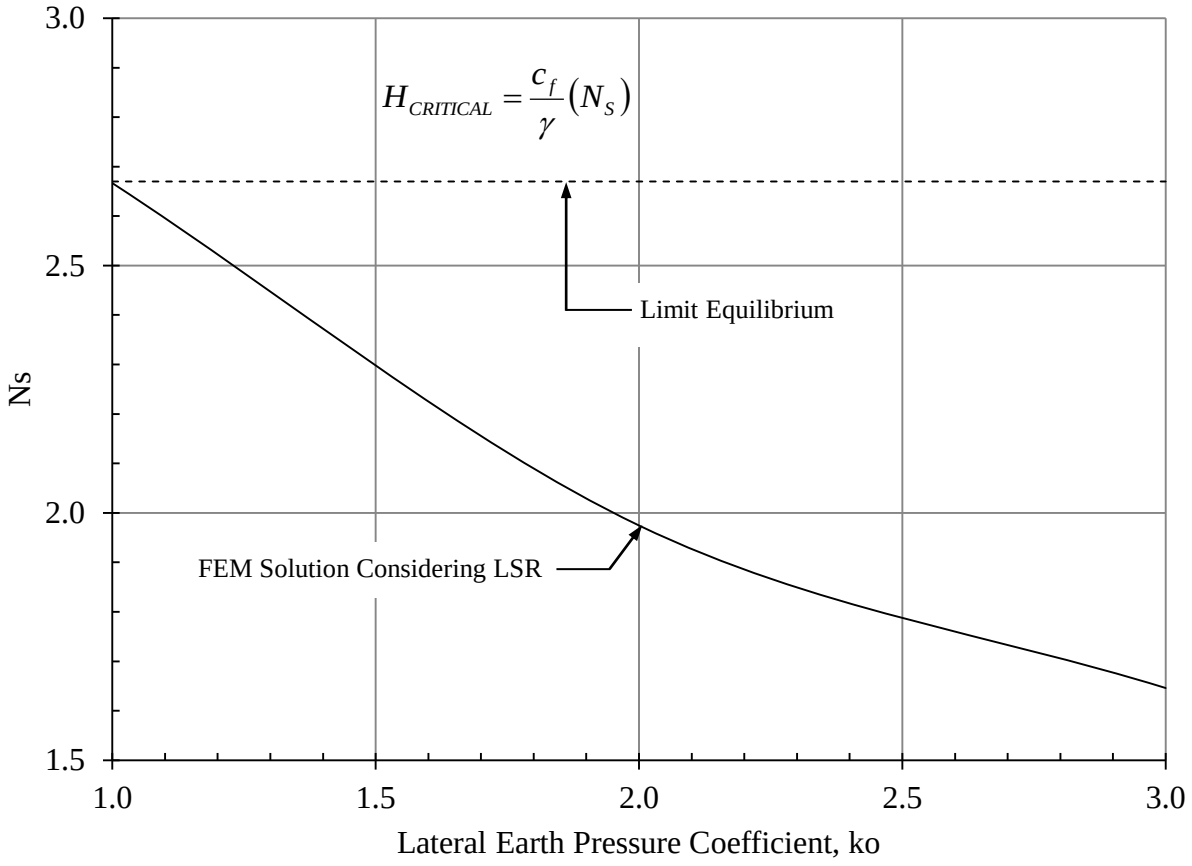

Figure 7.2. N_s as a Function of k_o considering LSR.

Table 7.2 presents the revised critical height values based on the critical height parameters used for this study, and employing the revised N_s value noted in Figure 7.2. The revised parameters indicate a critical height that is less than the critical height used in the FEM analyses. As such, the revised N_s values indicate slope failure, as predicted by the FEM analyses.

Table 7.2. Revised Critical Height Values for a Vertical Slope.

Critical Slope Height Parameters	k_o = 3.0	k_o = 2.0
Geotechnical Parameters	c = 86.2 kPa, γ = 20.42 kN/m^3	
N_s (based on LSR)	1.64	1.97
$H_{CRITICAL}$	6.9 m	8.3 m
Slope Height Used in FEM Analyses	8.45 m	8.45 m
Factor of Safety	0.82	0.98

7.2 INCLINED SLOPES

The limit equilibrium solution for the stability of $\phi = 0°$ slope was developed by Terzaghi (1943) and was shown as Equation 1-59, and repeated as Equation 8-8 for ready reference.

$$H_c = \left(\frac{c_u}{\gamma}\right) N_s \qquad 7\text{-}8$$

Terzaghi (1943) developed values of N_s for various slope angles and the stability factor varied linearly from 3.85 at $\beta = 90°$ to 5.52 at $\beta = 53°$. However, the solution did not account for tension cracking or toe cracking due to LSR. FEM analyses indicate that an inclined toe crack can develop as well as a tension crack due to LSR. Figure 7.3 presents an inclined slope with both a tension crack as well as a toe crack. Fellenis (1927), Taylor (1937, 1948); Terzaghi

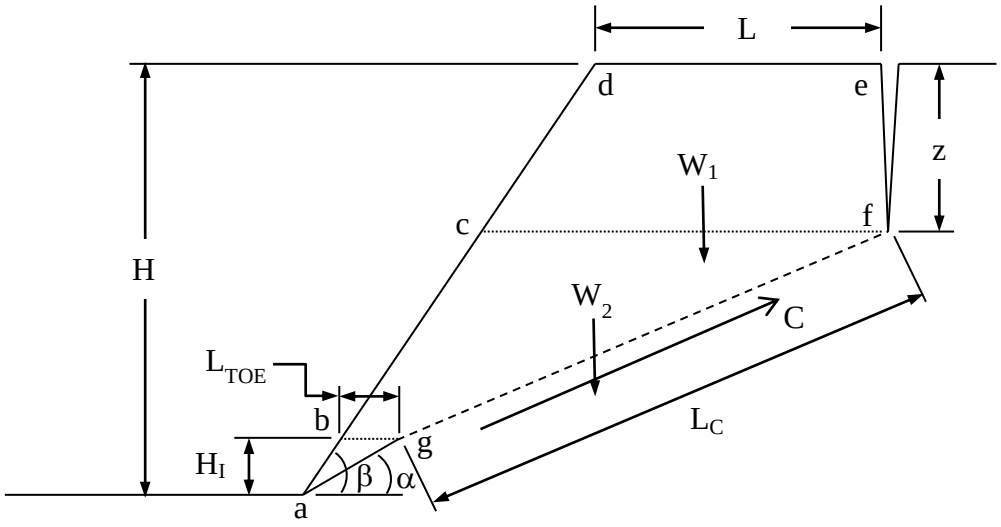

Figure 7.3. Inclined Slope with Plane Failure Surface and Tension Crack.

1943), and Terzaghi and Peck (1967) have shown that when the slope face angle is greater than 53°, the failure surface is a circular arc that extends from the crest to the toe of slope. The inclusion of tension and toe crack would reduce the length of shear resistance since a tension crack could offer no shear strength resistance.

The mass of soil defined by area $\overline{cdef}$ may be expressed as:

$$W_1 = 0.5(z)(\gamma)\left[L + \left(L + \frac{z}{\tan(\beta)}\right)\right] \quad 7\text{-}9$$

where z = depth of the tension crack, L = distance from the crest to the tension crack, γ = soil unit weight, and β = slope face angle. Equation 7-9 may be manipulated into the following:

$$W_1 = \gamma\left(zL + \frac{z^2}{2\tan(\alpha)}\right) \quad 7\text{-}10$$

The mass of soil defined by area $\overline{bcfg}$ may be expressed as:

$$W_2 = 0.5(\gamma)(H - H_I - z)\left[\left(L + \frac{z}{\tan(\alpha)}\right) + L_{TOE}\right] \quad 7\text{-}11$$

where H_I = height of toe crack due to LSR, and L_{TOE} is horizontal distance between the slope face and the toe crack at the height of H_I. L_{TOE} may be expressed by the following expression using the Law of Sines as follows:

$$\frac{L_{TOE}}{\sin(\beta-\alpha)} = \frac{\left({}^{H_I}/_{\cos(90-\beta)}\right)}{\sin(\beta)} \quad 7\text{-}12$$

Solving for L_{TOE},

$$L_{TOE} = \left[\frac{\frac{H_I}{\cos(90-\beta-\alpha)}}{\sin(\alpha)}\right][\sin(\beta-\alpha)] \quad 7\text{-}13$$

The triangular area defined by $\overline{abg}$ is neglected in this derivation. FEM modeling indicated that k_o at the toe generally developed negative vertical and lateral stresses that resulted in a section of the material dislodging from the slope face. This conclusion is also confirmed by Skempton and LaRochelle (1965) in which they discussed clay "burst" where the toe of excavation was seen to bulge and that cracking extended into the slope face from the toe.

The sliding resistance is defined by the undrained shear strength at failure (c_f) acting along the failure plane L_C. Terzaghi (1943) noted that the curvature of the sliding surface through a vertical bank could be disregarded. By similar extension, the failure surface connecting the toe crack and the tension crack for an inclined slope was considered to be a plane failure surface. The length of this failure surface is expressed by the following:

$$L_C = \sqrt{x^2 + y^2} \quad 7\text{-}14$$

in which the variables x and y are defined by the following equations:

$$x = (H)\tan(90-\beta) + L - \frac{H_I}{\tan(\alpha)} \quad 7\text{-}15$$

$$y = H - z - H_I \quad 7\text{-}16$$

At limit equilibrium, the sum of the forces on the sliding plane must be equal to zero, which results in the following:

$$(W_1 + W_2)\sin(\alpha) - (c_f)(L_C) = 0 \qquad 7\text{-}17$$

In order to reduce Equation 7-17 into simplest form, the terms H_I, L, and z are normalized with respect to the total slope height, H. The normalized values are shown in Table 7.4. The values noted in Table 7.4 were based on the FEM analyses for a Clay Slope on Clay Base. The toe crack height and depth of tension crack were presented in Table 6.3. The distance from the slope crest to minimum lateral earth pressure coefficient is presented as Figure 7.4. The tension crack was assumed to occur along the crest where the lateral earth pressure coefficient was at the greatest negative value (indicating maximum tension).

Table 7.3. Toe Crack Height, Distance from Crest to Toe Crack, and Depth of Tension Crack Normalized to Total Slope Height.

Slope Angle	Lateral Earth Pressure	Normalized to Total Slope Height		
		Toe Crack Height	Distance from Crest to Tension Crack	Depth of Tension Crack
(β)	(k_o)	(H_I)	(L)	(z)
90° Vertical	1	0.08H	0.83H	0.03H
	2	0.13H	1.24H	0.07H
	3	0.21H	1.24H	0.08H
76° ¼H:1V	1	0.07H	2.41H	0
	2	0.12H	1.26H	0.08H
	3	0.22H	1.18H	0.08H
63° ½H:1V	1	0.07H	2.84H	0
	2	0.07H	1.48H	0.03H
	3	0.23H	1.03H	0.08H

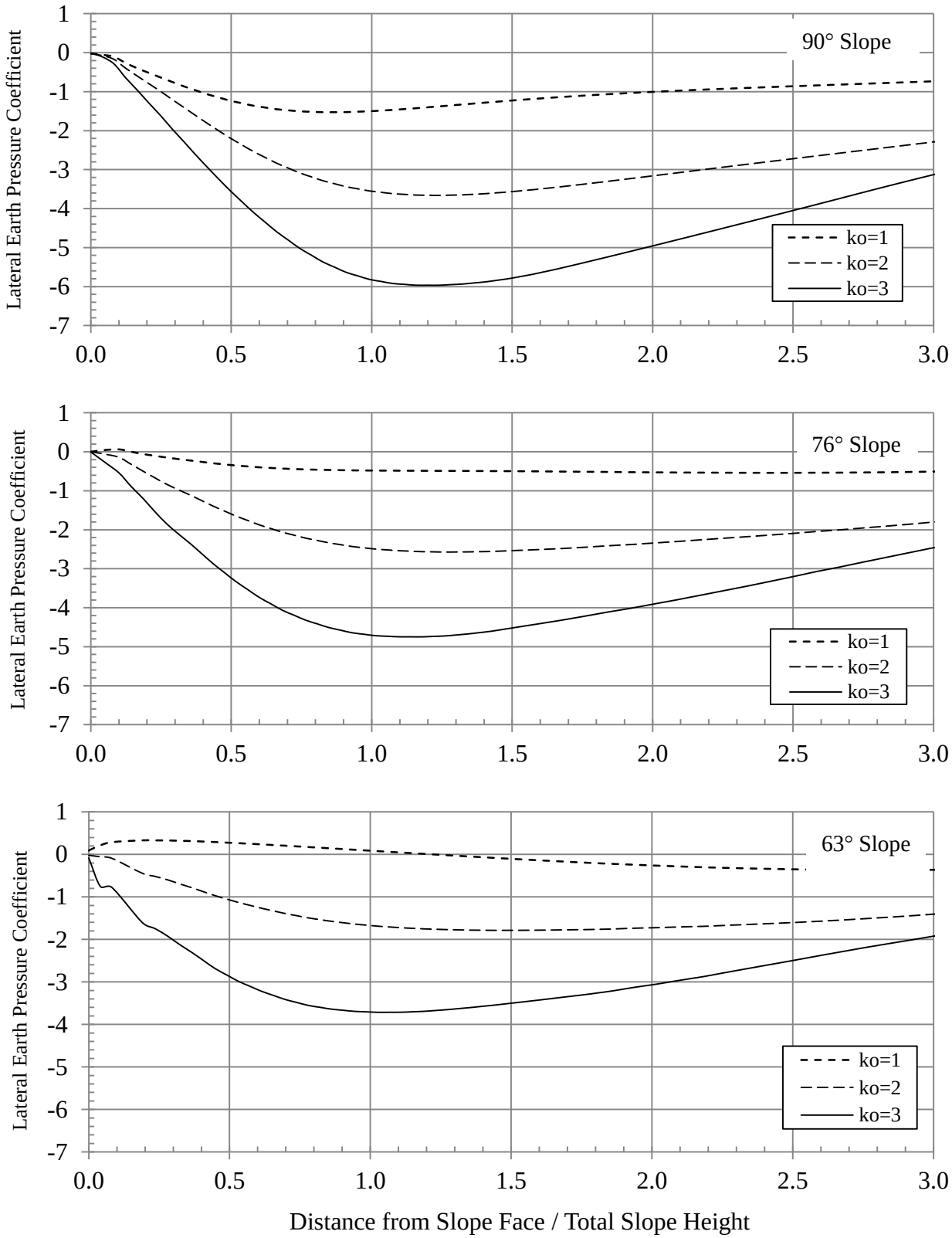

Figure 7.4 Variation of Lateral Earth Pressure due to LSR along the Top of Slope.

Equation 7-17 is now readily solved with the only unknown variables consisting of c, γ and H, as all other variables are normalized with respect to H. Figure 7.5 presents the solution to Equation 7-17 in graphical form. It should be noted that the initial height of the failure plane was less than 0.1H for all cases when k_o = 1.0 and FEM analyses indicated negligible tension zones. As such, no further modification was considered for k_o = 1.0.

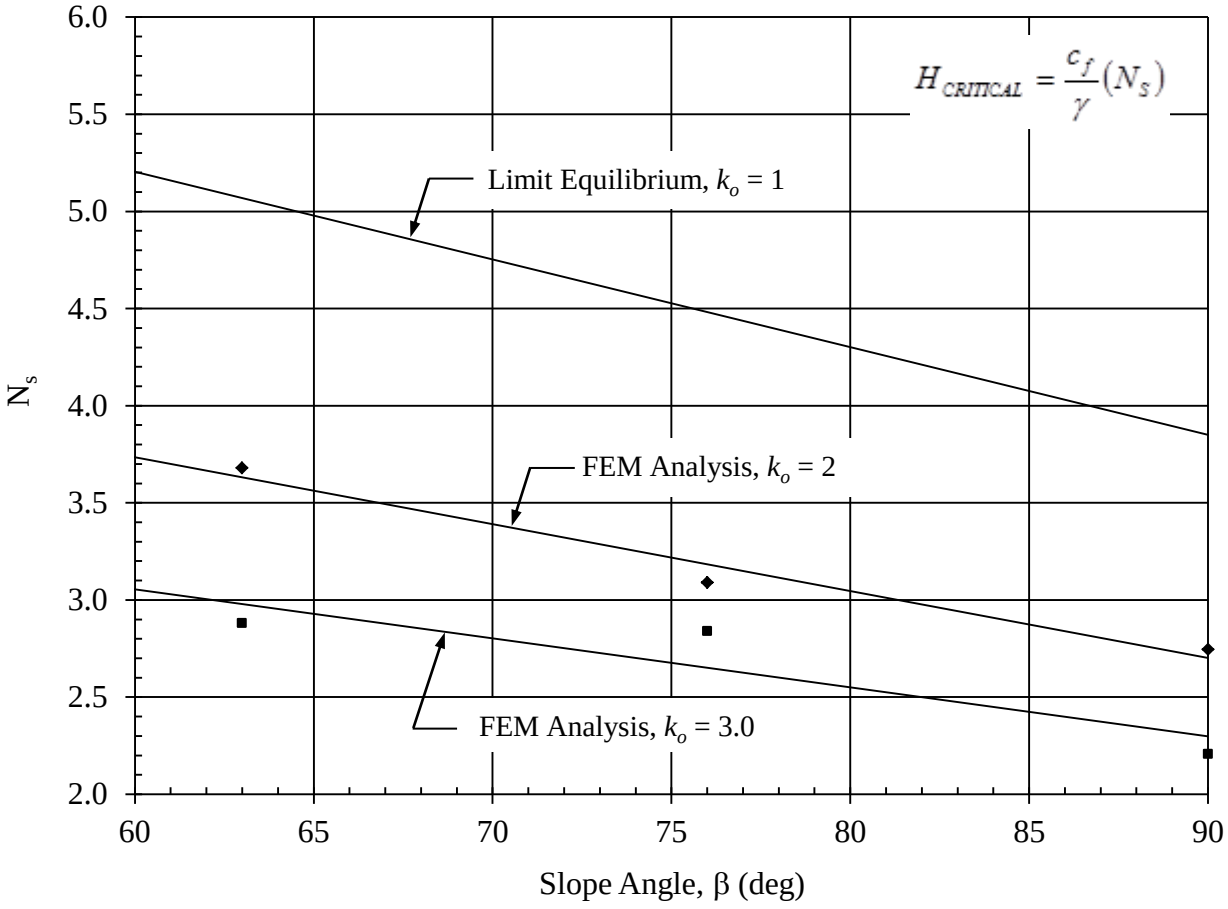

Figure 7.5. N_s as a Function of k_o considering LSR for Inclined Slopes.

As noted below, the critical height for the ¼H:1V slope was 18.9-meters, based on equation 1-59 and using the stability factor presented in Figure 1.6.

$$H_c = \left(\frac{86.2}{20.42}\right)(4.48) = 18.9$$

The actual height used in the FEM analysis was 8.45-meters, which resulted in a factor of safety of 18.9 / 8.45 = 2.24. However, this solution did not account for the effects of LSR on the overall stability of the slope. Recall that FEM analyses indicated that slope failure did occur for the ¼H:1V slope when k_o = 3.0, but remained stable for k_o = 2 and 1. As such, it is expected that the factor of safety for a ¼H:1V slope when k_o = 3.0 would be very close to unity. Table 7.4 presents the revised critical height value and employed the revised N_s value noted in Figure 7.5 for the ¼H:1V slope. Review of Table 7.4 indicated a considerable reduction in the factor of safety value.

Table 7.4. Revised Critical Height Values for ¼H:1V Slope.

Critical Slope Height Parameters	k_o = 3.0	k_o = 2.0
Geotechnical Parameters	c = 86.2 kPa, γ = 20.42 kN/m^3	
N_s (based on LSR)	2.65	3.18
$H_{CRITICAL}$	11.1	13.4
Slope Height Used in FEM Analyses	8.45 m	8.45 m
Factor of Safety	1.31	1.59

8.0 EVALUATION OF CASE HISTORIES USING FINITE ELEMENT METHODS

FEM models were developed to evaluate the failure of two stiff clay slopes; the Oxford Slope and the Conemaugh Slope. The Oxford Slope is a published case history of a stiff clay slope that involved a detailed site characterization and instrumentation program (Burland, Longworth and Moore, 1977; Burland and Moore, 1973; and Skempton and Hutchinson, 1969). The Conemaugh Slope is also a published case history of a stiff clay slope and one in which the author has personnel working knowledge of (Kutschke, et al, 2007, 2007, 2007, 2008, and 2010). Finite element models were developed for these two slopes to investigate the effect of lateral stress relief on slope stability.

8.1 OXFORD CLAY SLOPE

Burland, Longworth, and Moore (1977) studied a 29-m deep excavation that occurred in stiff Oxford Clay. Their work was part of a long-term research study that was carried out during 1969 to 1971 at the London Brick Company's Saxon pit near Peterborough, England. The main purpose of their study was to measure the magnitude and extent of the ground movements and to examine the relative influence of material properties and geological factors on deformation behavior. The work conducted by Burland, et al (1977) was the state-of-the-art for that time since the precise observation of movements required the development of new instrumentation and measurement

techniques. Instrumentation was installed to measure ground movement surrounding the excavation (both at surface and at depth) and to investigate factors such as groundwater pressure. The instrumentation consisted of piezometers, precise surveying, photogrammetry, horizontal extensometers, inclinometers, and vertical extensometers. Refer to Burland and Moore (1973) for further details of the installation and performance of the instrumentation used in the Saxon Pit.

The excavation pit consisted of a 3 to 5-m thick mantle of sand, gravel, and weathered clay that overlied the Oxford Clay. These deposits were stripped and placed in an adjoining pit. The Oxford Clay was cut by a mechanical planar along a 25-m high face sloping at 72° with respect to the horizontal. The gantry of the planar guided a continuous chain that carried 30-mm wide chisel bits. The bits would rake down the slope face and break off small lumps of clay. The gantry pivoted about a vertical axis and was mounted on a rail system that traveled parallel to the slope face. The resulting combination of rotation and lateral movement allowed a 10 to 15-m thick slice to be cut from the slope face.

8.1.1 Site Characterization

Site characterization was conducted by Burland, et al (1977), Burland and Moore (1973), and Skempton and Hutchinson (1969), and consisted of office research, field instrumentation, and laboratory testing to characterize the Saxon pit for geotechnical analyses. The office research indicated that structurally, the area was relatively undisturbed with an average tilt of 1° to the south east. Major faults had been recorded around and to the west of Peterborough, but Burland, et al (1977) indicated that no such faulting was evident in the brick pits.

The excavation in the Saxon Pit exposed the Middle and Lower Oxford Clay. The Middle Oxford Clay (MOC) was 8 to 10-m thick and was more plastic than the 17-m thick Lower Oxford Clay (LOC). The Kellaway Bed formation was at the base of the pit and consisted of 3.2-m of thick green-gray sand underlain by 2.1-m of dark blue-grey plastic clay. The Kallaway Beds are underlain by the Great Oolite Series, a heterogeneous limestone stratum, and site investigation generally terminated at this depth.

The MOC and LOC belong to the Callovian stage of the Upper Jurassic and were deposited in quite water in a relatively shallow epicontinental sea flanked by low relief (Hallam, 1975). The Oxford Clays were once deeply buried and as such, are overconsolidated. During the Pleistocene period, glaciers mantled the area with boulder clay, most of which had been eroded and replaced by terrace gravel deposits.

The upper reaches of the MOC are moderately weathered clay with frequent brown-stained fissures and a homogeneous plastic appearance at the slope face. This contrasted with the lower part which was much less fissured and weathered, with a blocky appearance. The clay was classified as highly plastic and was considered to have a stiff consistency (Skempton and Hutchinson, 1969).

The LOC consisted of two lithologic types which contrasted clearly along the excavated face. Dark brown-gray, strongly laminated shales predominate, especially near the base. The LOC is more properly termed a clay-shale from a strength and soil fabric point-of-view. This stratum had a relatively high calcium carbonate content that ranged from 10 to 20% and resulted in local cementing of the soil matrix (Burland, et al, 1977).

8.1.1.1 Geotechnical Properties of the Oxford Clay. Burland, et al (1977) conducted an extensive laboratory testing program to characterize the site for geotechnical analyses. The laboratory test data indicated that the unit weight of the Oxford clays were relatively consistent with depth, averaging 19.9 kN/m^3, for both the MOC and LOC. Index properties displayed small variation with depth, with an average liquid limit of 55% and a plastic limit of 24%, while the clay content was typically greater than 55%. Water content decreased over the same depth from 22 to 18%. The clay near the crest generally had a water content near the plastic limit while the clay near the base had a water content less than the plastic limit and was corresponding more brittle in behavior. Burland, et al (1977) indicated that joints in the LOC frequently appeared to die out in the overlying MOC.

The undrained shear strength progressively increased with depth from 50 kPa to over 1,200 kPa (Burland, et al, 1977). The rate of shear strength increase was proportionally greater in the LOC, as shown in Figure 8.1.

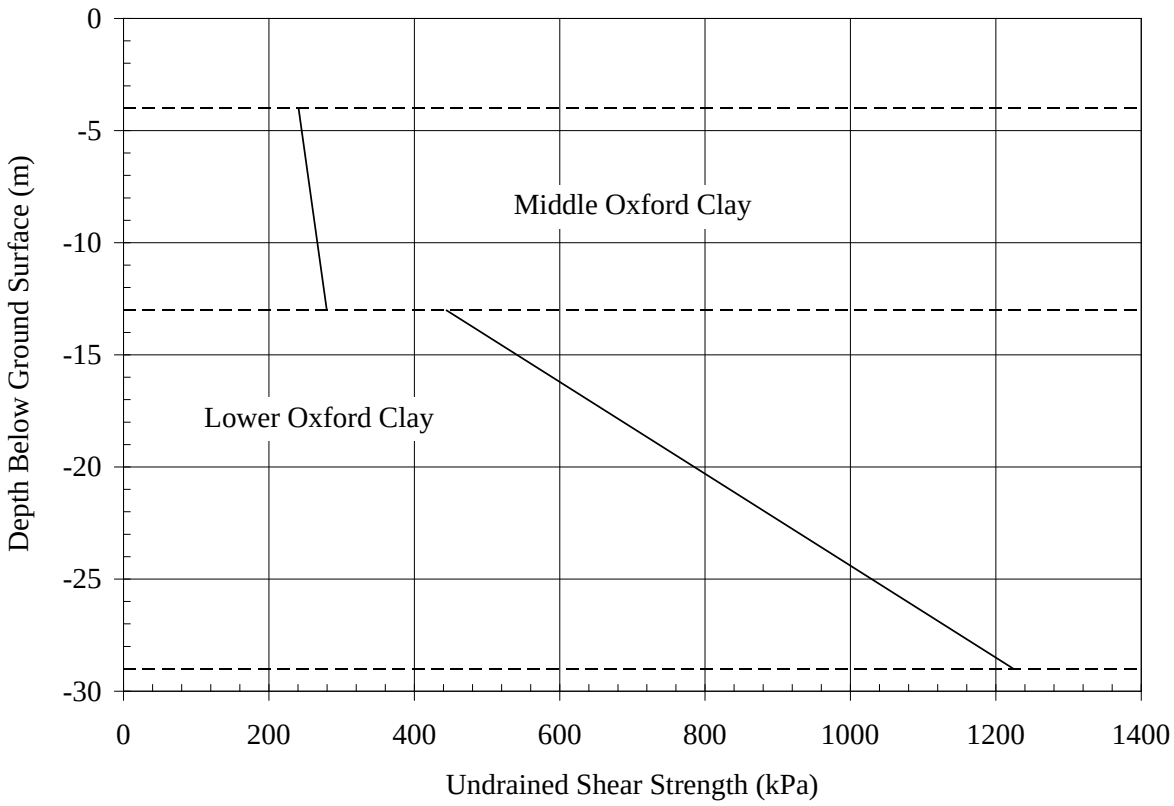

Figure 8.1. Variation of Undrained Shear Strength with Depth for the Oxford Clay.

The Modulus of Elasticity also increased with depth from 20,000 kPa to 150,000 kPa (Burland, et al, 1977). The rate of increase was again higher in the LOC, as shown on Figure 8.2. The ratio of E/c_u displayed no net increase with depth and has an approximate average value of 100.

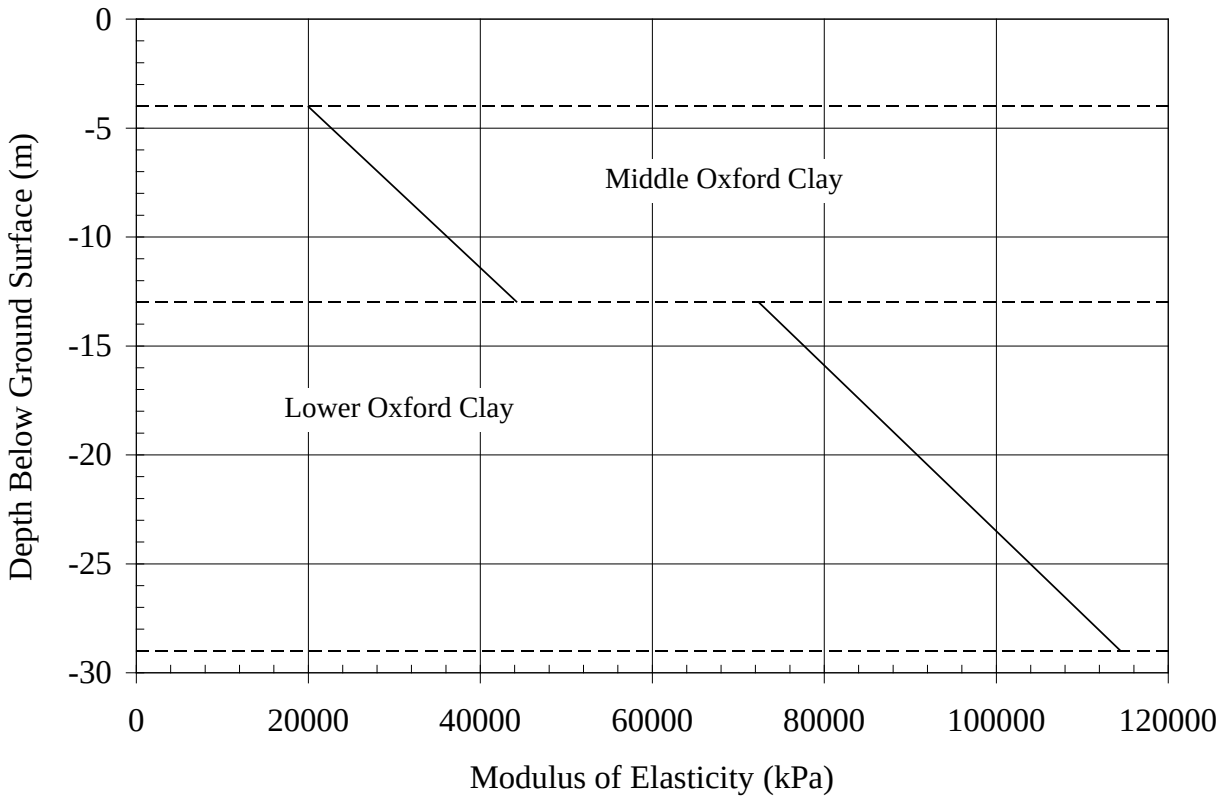

Figure 8.2. Variation of Modulus of Elasticity with Depth for the Oxford Clay.

8.1.1.2 Instrumentation. Instrumentation was installed both at surface and at depth to measure ground movement surrounding the excavation. Instrumentation consisted of piezometers, precise surveying, photogrammetry, horizontal extensometers, inclinometers, and vertical extensometers. Burland, et al (1977) observed that measurements all indicated a mechanism of behavior in which the ground within a region of about 1 to 1.5 times the depth away from the face appeared to move as

a block, sliding on a horizontal shear band formed by bedding planes near the base of the excavation. The magnitude and rate of the horizontal movement of the surface points was dependent on their relative position to the face, the distance the face advanced in a given cut, and the time period between cuts. Measurable movements extend back from the top of the face for a distance of about 2.5 times the depth of the excavation. Burland, et al (1977) also indicated that at distances greater than 30-m from the slope face, that the vertical movements were approximately the same as the horizontal movements, whereas closer to the face the horizontal movement dominated.

8.1.2 Finite Element Model

A FEM model was developed to study the influence that lateral stress relief had on the Oxford Slope. Review of the available literature indicated that no numerical model had been developed to study the movement of this slope. The FEM model used a two dimensional mesh with isoparametric elements consisting of either six node triangles or eight-node quadrilaterals. A fine mesh of 29 elements over the slope height was used. Boundary conditions considered the base to be fixed in the horizontal and vertical direction while the sides were only fixed in the horizontal direction. Figure 8.3 presents the FEM model that was used to establish the initial stress conditions.

The FEM model simulated excavation by progressively "turning-off" elements and allowing lateral stress relief to occur. The elements were grouped in regions labeled 1 through 4, as noted in Figure 8.3. The horizontal width of each region was 10-meters to match actual site excavation procedures (Burland, et al, 1977).

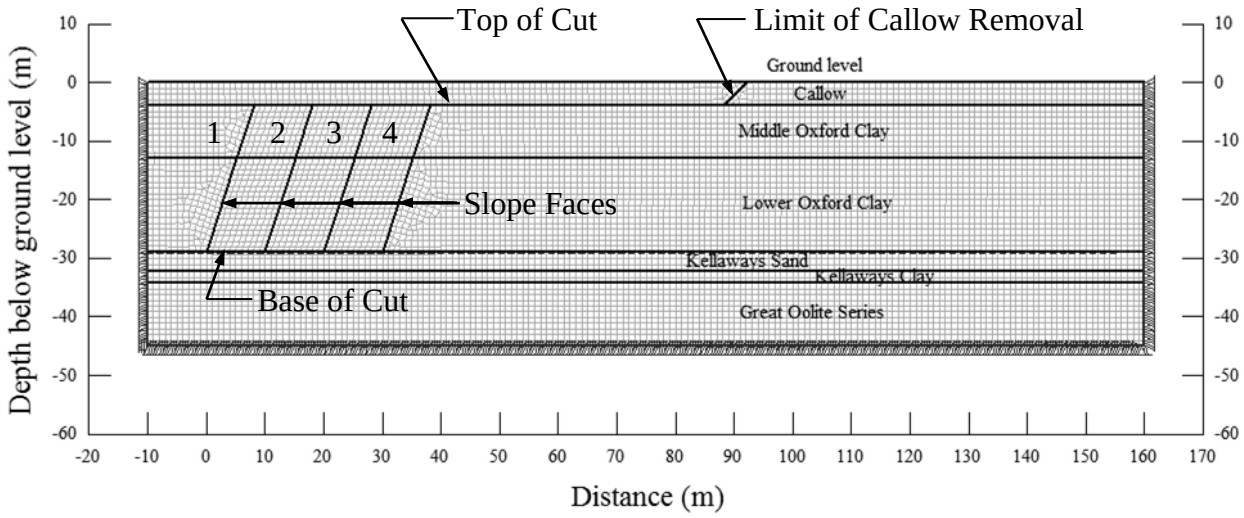

Figure 8.3. Oxford Clay Slope FEM Model.

The FEM analyses closely modeled actual site conditions with staged analyses conducted as follows:

- Stage 1 – Establish in-situ stress conditions;
- Stage 2 – Remove Callow from a distance of -10 meters to 90 meters; and
- Stage 3 – Progressively turn-off elements in Regions 1 through 4 to simulate excavation and allow lateral stress relief.

The clay material utilized an elastic-plastic constitutive model which describes an elastic-perfectly plastic relationship. Stresses are directly proportional to strains until the yield point is reached; beyond yield, the stress-strain curve is perfectly horizontal. Dunlop and Duncan (1970), Smith and Hobbs (1974), Griffiths and Lane (1999), and Griffiths (2000) indicate that this constitutive model is most appropriate for clay slopes under undrained conditions, where both stress-strain relationships and the failure criteria are expressed in terms of total stresses.

The undrained shear strength and Modulus of Elasticity values used in the FEM model are as noted in Figure 8.1 and 8.2, respectively. Table 8.1 presents the geotechnical parameter values used for the Oxford Slope FEM analyses and are based on published data obtained from Burland, et al (1977).

As noted in Table 8.1, the FEM model used a constant unit weight and a constant lateral earth pressure coefficient value for each stratum, so that the initial horizontal and vertical stress increased linearly with depth in each stratum. As an initial analysis verification, the vertical stress values obtained from the FEM model were compared to simple hand calculation values considering the following expression,

$$\sigma = (\gamma)(depth) = \left(19.9\frac{kN}{m^3}\right)(depth)$$

where (σ) is the total vertical stress and (γ) is the unit weight. FEM analyses were conducted using the parameter values noted in Table 8.1. FEM analyses established the in-situ stress conditions during Stage 1 analyses. Figure 8.4 presents the initial in-situ stress conditions along with the hand calculation verification of vertical stress values. The FEM in-situ vertical stress and hand calculation values indicate an exact agreement.

Table 8.1 Geotechnical Parameters and Values Used for the Oxford Slope FEM Model.

FEM Geotechnical Parameters	Geotechnical Strata and Value of Parameter					
	Callow	MOC	LOC	Kellaways Sand	Kellaways Clay	Great Oolite Series
Constitutive Model	Linear Elastic	Elastic Plastic	Elastic Plastic	Linear Elastic	Linear Elastic	Linear Elastic
Modulus of Elasticity, E [MPa]	38.3	Figure 8.2	Figure 8.2	620	620	39,300
Poisson's Ratio, ν	0.35	0.4	0.4	0.25	0.25	0.23
Undrained Shear Strength, c_u [kPa]	--	Figure 8.1	Figure 8.1	--	--	--
Friction Angle, ϕ [deg]	--	0	0	--	--	--
Lateral Earth Pressure Coefficent, k_o	0.54	3.0	2.0	0.33	0.33	0.30
Dilation Angle, ψ [deg]	--	0	0	--	--	--
Unit Weight, γ [kN/m^3]	18.9	19.9	19.9	21.2	21.2	24.4

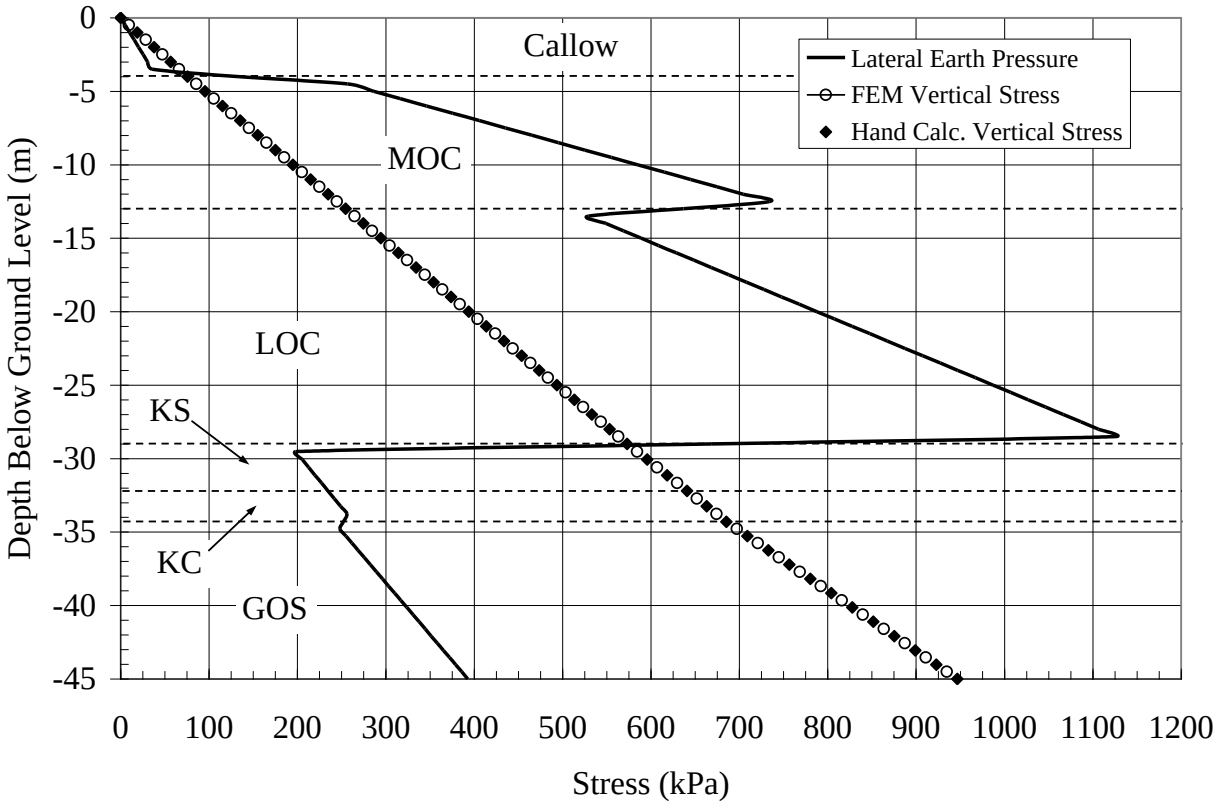

Figure 8.4. FEM In-Situ Horizontal and Vertical Earth Pressures Prior to Excavation.

8.1.2.1 Finite Element Slip Element. The shear strength along a closed crack is generally less than that of the intact clay. Skempton and LaRochelle (1965) indicated that the shear strength developed in London Clay along a closed crack was approximately 55% of the average undrained shear strength of the intact clay. Bazett, et al (1961) indicated that the Leda Clay, near Massena, New York, exhibited a 75% reduction in the undrained shear strength along a closed crack.

As long as there are no overall changes in water content, the undrained shear strength will remain constant regardless of changes in total stress (Skempton and Sowa, 1963). The effective

shear strength values of intact Oxford Clay samples lifted near the base of the excavation are known from shear box tests to be (Burland, et al, 1977):

Peak Values	Residual Values
ϕ' = 27.5°	ϕ' = 13°
c' = 172 kPa	c' = 3.5 kPa

Skempton and LaRochelle (1965) indicated that it is possible to calculate the effective normal pressure (σ') corresponding to the undrained shear strength (c_u) by the following expression:

$$c_u = c' + \sigma' \tan(\phi') \qquad 8\text{-}1$$

Substituting the appropriate peak shear strength values obtained from Burland, et al (1977) and the undrained shear strength at the base of the excavation from Figure 7.1 into Equation 87.1, the following expression was obtained:

$$1224 \text{ kPa} = 172 \text{ kPa} + \sigma' \tan(27.5°)$$

$$\sigma' = 2020 \text{ kPa}$$

The shear strength parameters of a closed fissure are taken as the residual values (Skempton and LaRochelle, 1965). Therefore, with the same effective pressure, the average undrained strength along a closed fissure may be expressed as (Skempton and LaRochelle, 1965):

$$c_u = 3.5 \text{ kPa} + (2020 \text{ kPa}) \tan(13°)$$

$$c_u = 470 \text{ kPa}$$

which is a 62% reduction of the undrained shear strength along a closed fissure. This result is in general agreement with studies performed by Bazett, et al (1961) and Skempton and LaRochelle (1965).

Burland, et al (1977) indicated that the shear strength of the Oxford Clay will reduce from peak to residual within 3 to 4-mm of movement. This research considered that 4-mm of differential movement is sufficient to develop a 62% reduction in the undrained shear strength. As such, FEM analyses incorporated a slip element with a shear strength reduction of 62% when differential movement exceeded 4-mm.

8.1.3 Finite Element Model Results

The FEM analyses were conducted in stages to simulate actual field condition procedures. Figure 8.5 through 8.9 present the FEM results with displacement meshing using a 10X magnification to aid visual observation. Review of these figures indicated that the slope face appears to move as a block, which is in close agreement with field observations conducted by Burland, et al (1977). A graph of the slope face movement after each excavation is presented as Figure 8.10. This figure indicates that the first initial cut resulted in the largest slope face movement, which is as expected since this initial excavation would produce the largest release of lateral stress; an inherit characteristic of the FEM model. However, the magnitude of successive movements reduced and reached a relative uniform displacement with the 3rd and 4th cuts. These last cuts essentially produced identical outward slope face movements. Further examination of Figure 8.10 indicated that there is significant differential movement at the toe of slope between the LOC and the Kellaways Sand. It is this differential movement that resulted in propagation of

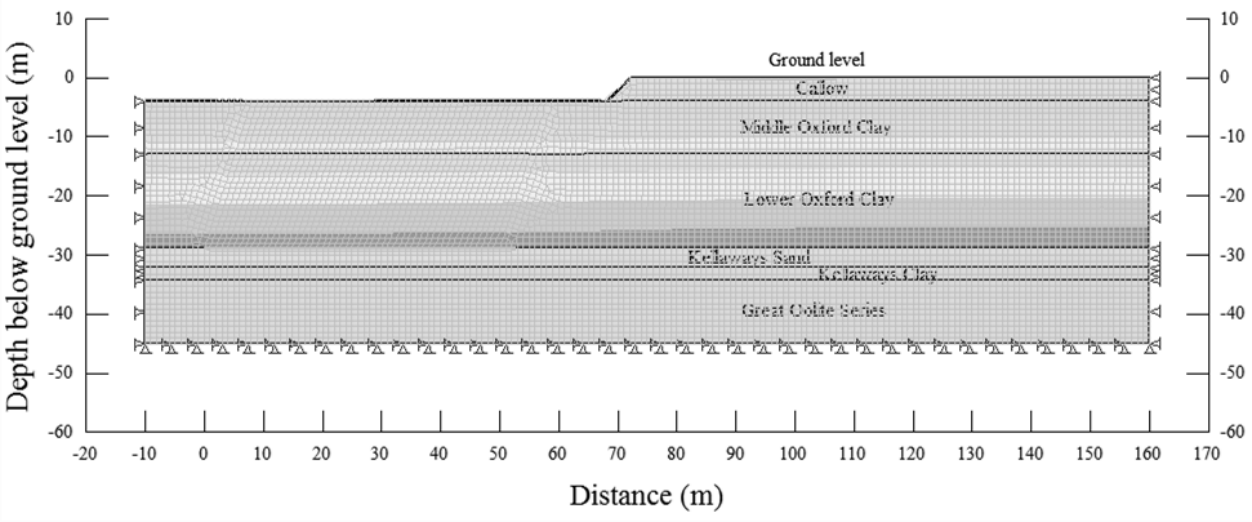

Figure 8.5. FEM Stage 1 Analysis – Mesh Deformation after Removal of Callow.

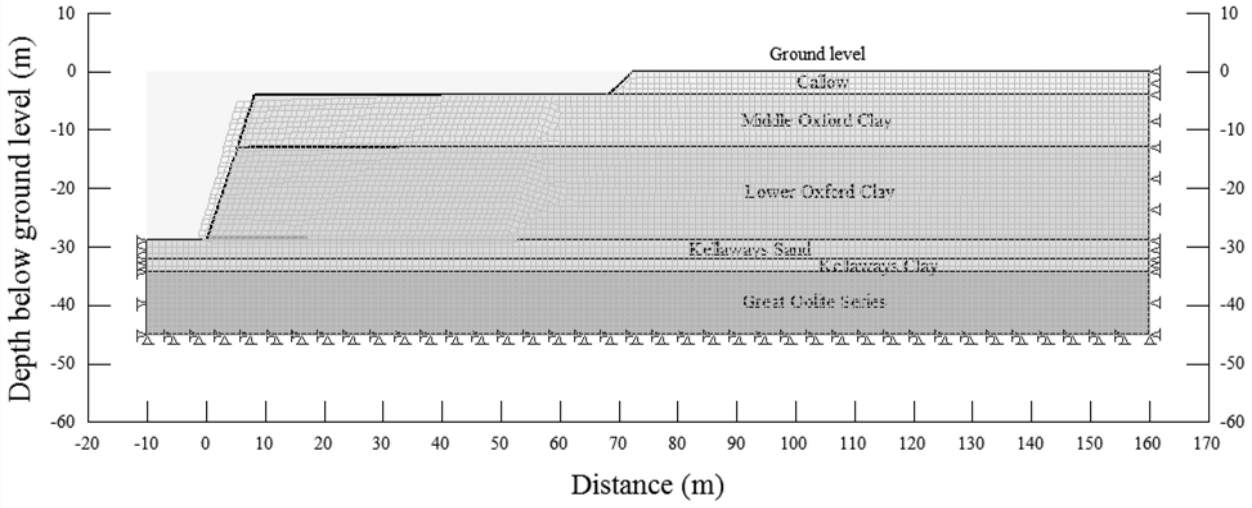

Figure 8.6. FEM Stage 2 Analysis – Mesh Deformation after First Cut.

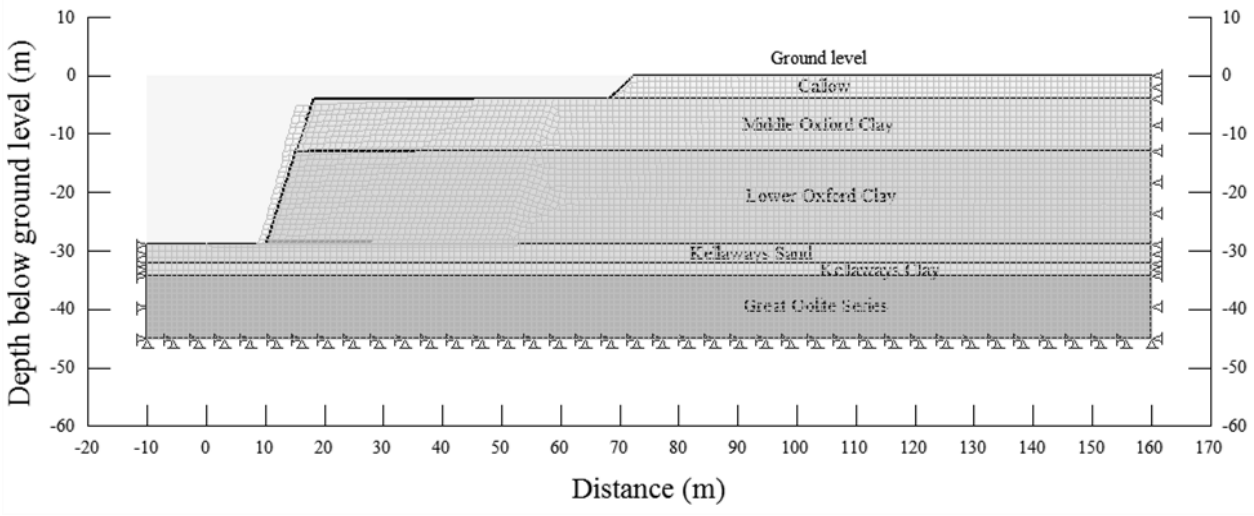

Figure 8.7. FEM Stage 3 Analysis – Mesh Deformation after Second Cut.

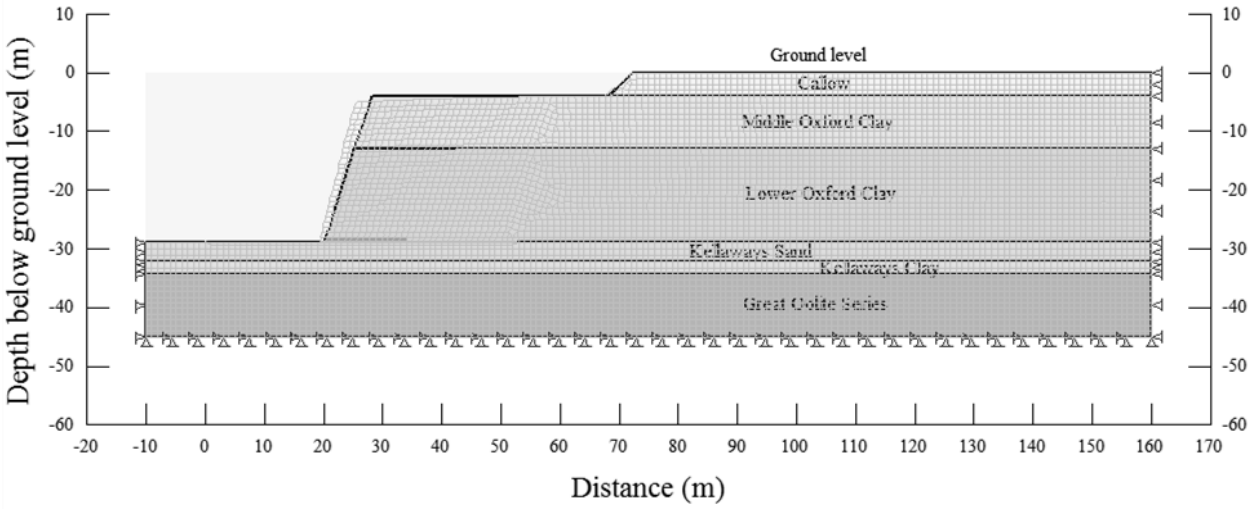

Figure 8.8. FEM Stage 4 Analysis – Mesh Deformation after Third Cut.

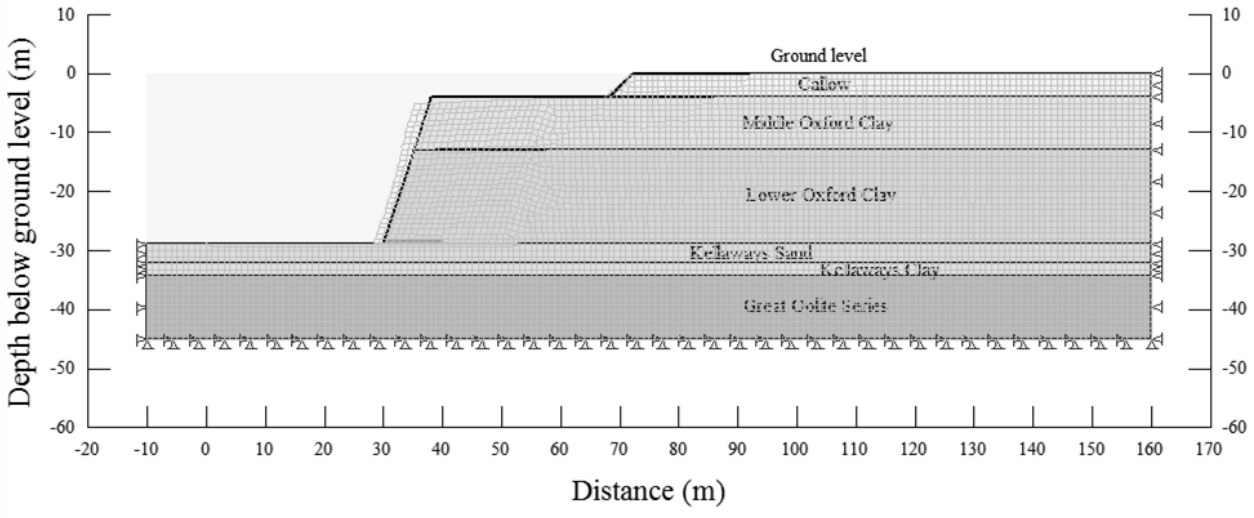

Figure 8.9. FEM Stage 5 Analysis – Mesh Deformation after Fourth Cut.

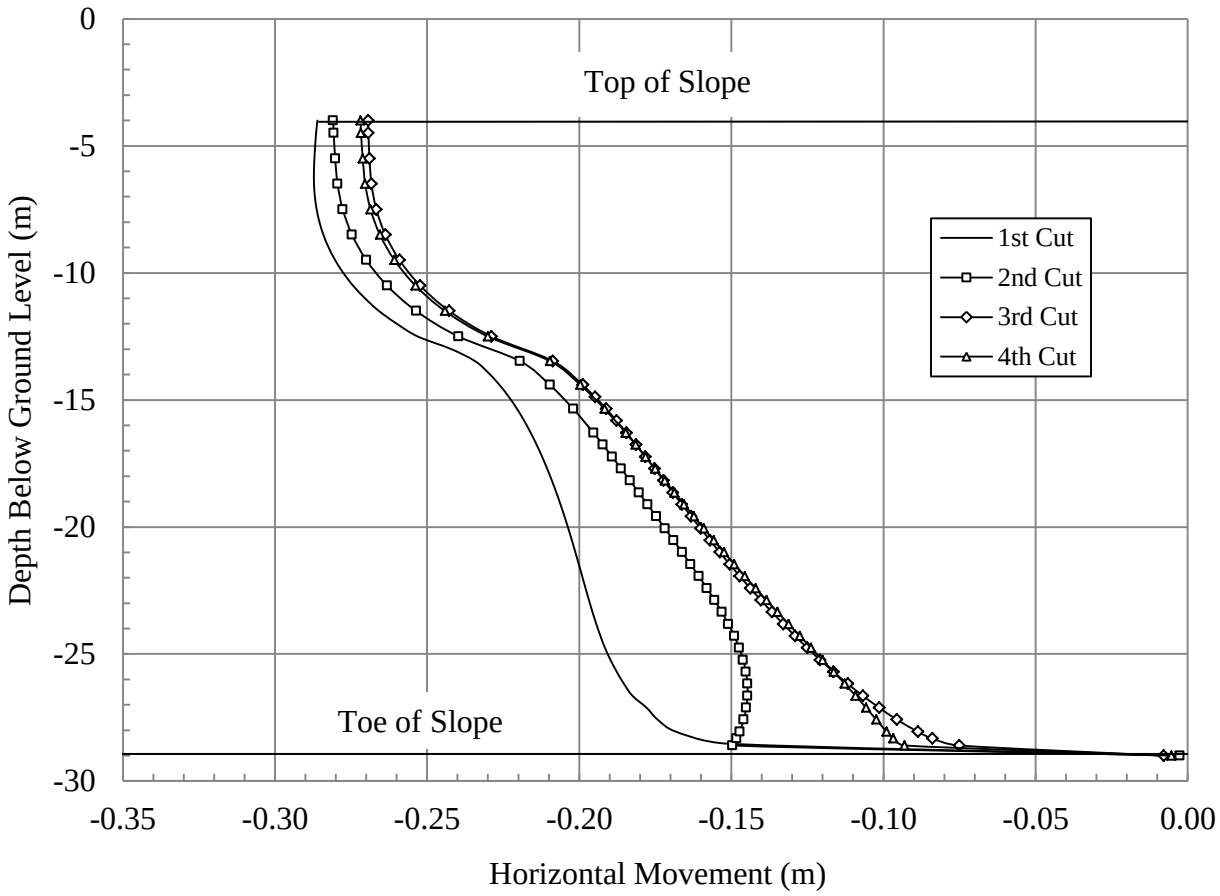

Figure 8.10. Individual Slope Face Movements After Each Cut.

a closed crack, which was modeled in the FEM analyses with a slip element. A slip element was incorporated into the FEM model after review of differential displacement from the prior excavation. For example, the 1st cut indicated that differential movement extended a distance of 0.9H into the slope. Therefore the slip element for the 2nd cut extended 0.9H into the slope from the toe of the 1st Cut. The FEM model then "turned-off" the elements within Region 2 to simulate the next cut. This process was repeated for successive stages. It should be noted that Burland, et al (1977) indicated that slope face movements at the base typically ranged from 0.15 to 0.20 m, which is in close agreement with the FEM analyses.

The differential movement for each successive cut is presented as Figure 8.11. The variation in the magnitude of the differential displacement at the face of the excavation is attributed to the length of the slip element from each resulting cut. However, it is significant to note that the differential displacements all converge at 0.8H. Burland, et al (1977) indicated that the ground within a region of 1.0H from the face appeared to move as a block and these FEM analyses indicate a similar conclusion.

FEM analyses indicate that the Oxford Slope is essentially a shear model in which excessive shear strains created and caused lateral propagation of a horizontal failure plane. Figure 8.12 provides the FEM lateral earth pressures near the crest and base of the slope after each cut. Negligible tensile stresses developed along the crest of the slope and the FEM models all converge in a uniform manner. However, larger tensile stresses developed at the base of the slope for the 1st and 2nd cut; again an inherit characteristic of the FEM model which undergoes a significant lateral stress relief with the first cut. The FEM again converged on a solution after

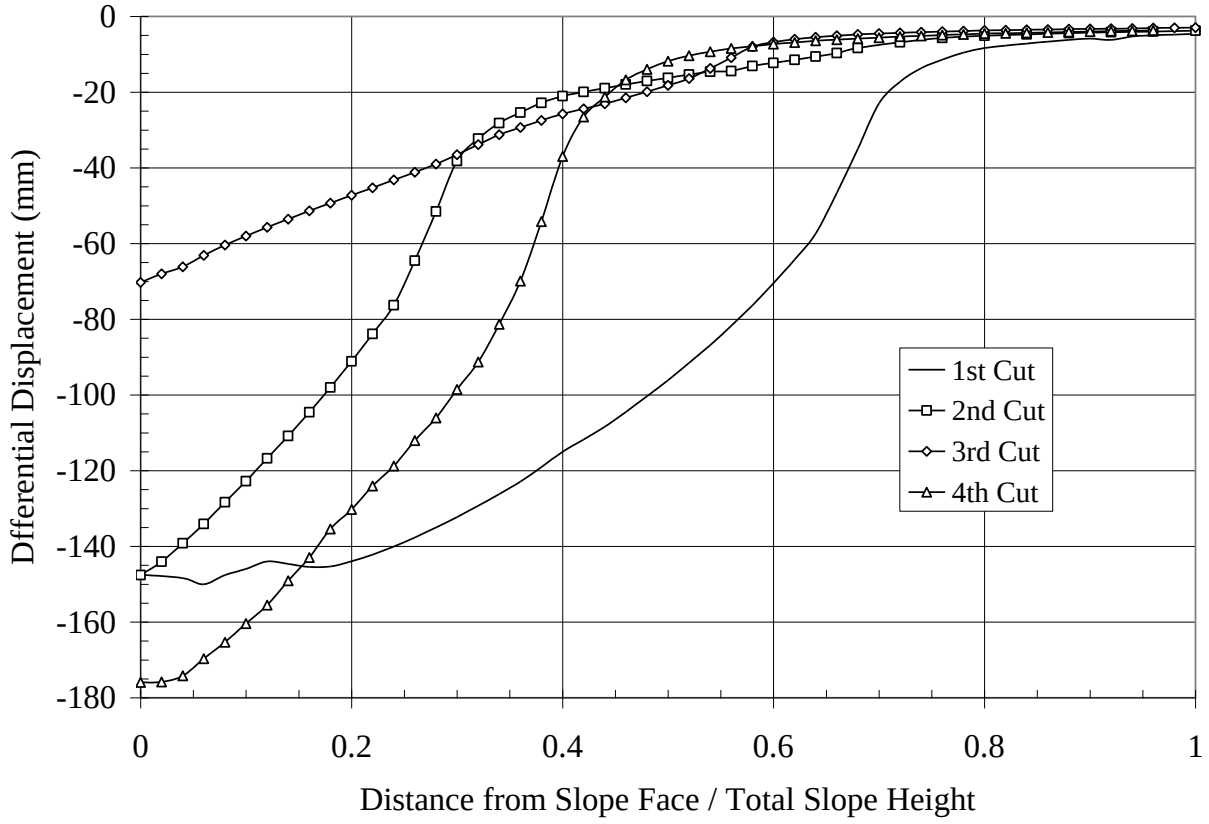

Figure 8.11. Differential Movement between LOC and Kellaways Sand.

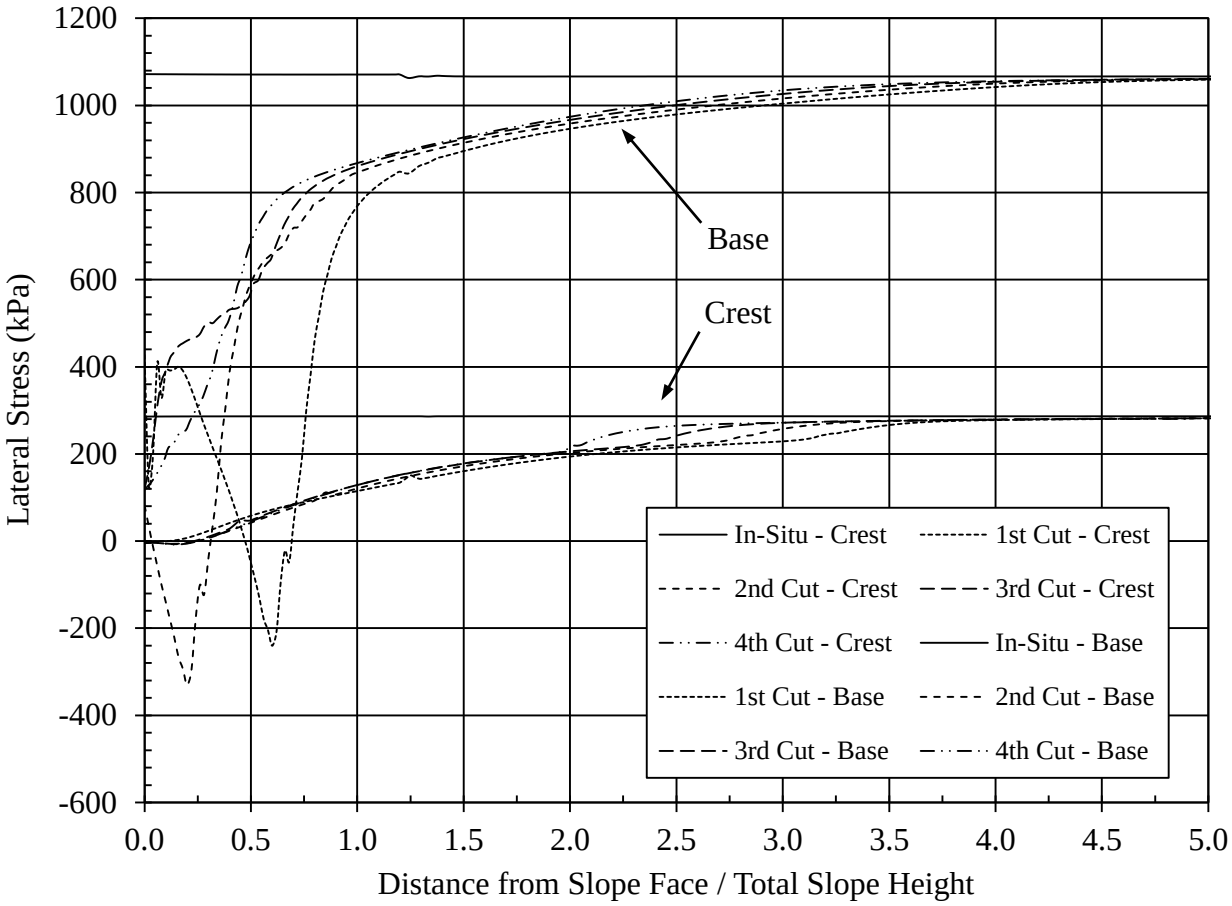

Figure 8.12. Lateral Earth Pressure in Backslope Region after each Successive Cut.

subsequent excavations, approximately 1.0H. Beyond 1.0H, the FEM indicated that the lateral earth pressures along the base are essentially equivalent, irrespective of the excavation sequence. The larger tensile stress near the slope face may cause crack propagation at an inclined angle, but these cracks are relatively close to the slope face and would be removed during subsequent excavations.

Burland, et al (1977) indicated that the horizontal stress change is usually the largest and horizontal movements tend to dominate in excavations of overconsolidated clay. However, Burland, et al (1977) also recorded settlement along the crest of the slope that ranged from about 100 to 150 mm. Figure 8.13 indicates the FEM settlement profile along the crest of the slope for each cut. These results are in excellent agreement with the observation recorded by Burland, et al (1977).

Burland, et al (1977) indicated that measureable horizontal movements extended to a distance of about 2.5H from the slope face. This result is similar to Sills, et al (1977), and Burland and Hancock (1977) in which they note that when an excavation into overconsolidated clay is underlain by a great depth of similar material, the horizontal movement extended to more than 3.0H from the slope face. Figures 8.14 and 8.15 indicate the FEM variation of lateral earth pressure along a horizontal plane at the mid-height of the MOC and LOC. FEM analyses converge at 3.0H, which is slightly greater than observed by Burland, et al (1977).

The FEM analyses indicated that the Oxford Slope behaved as a shear model. Tensile stresses at the base and crest of slope were not sufficient to create inclined or vertical cracking, respectively. Crack propagation at the base of the slope was attributed to the release of lateral

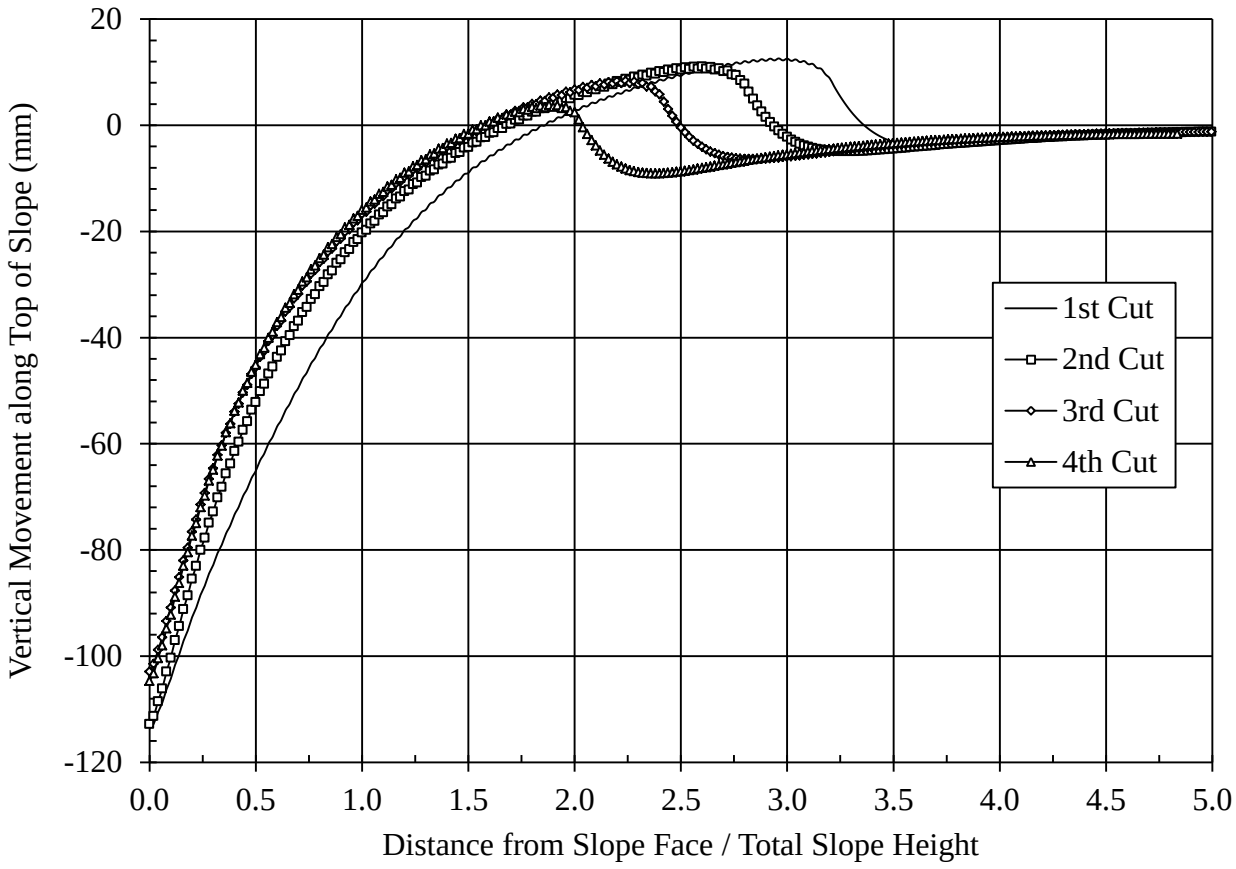

Figure 8.13. Vertical Movement Along Top of MOC After Each Cut.

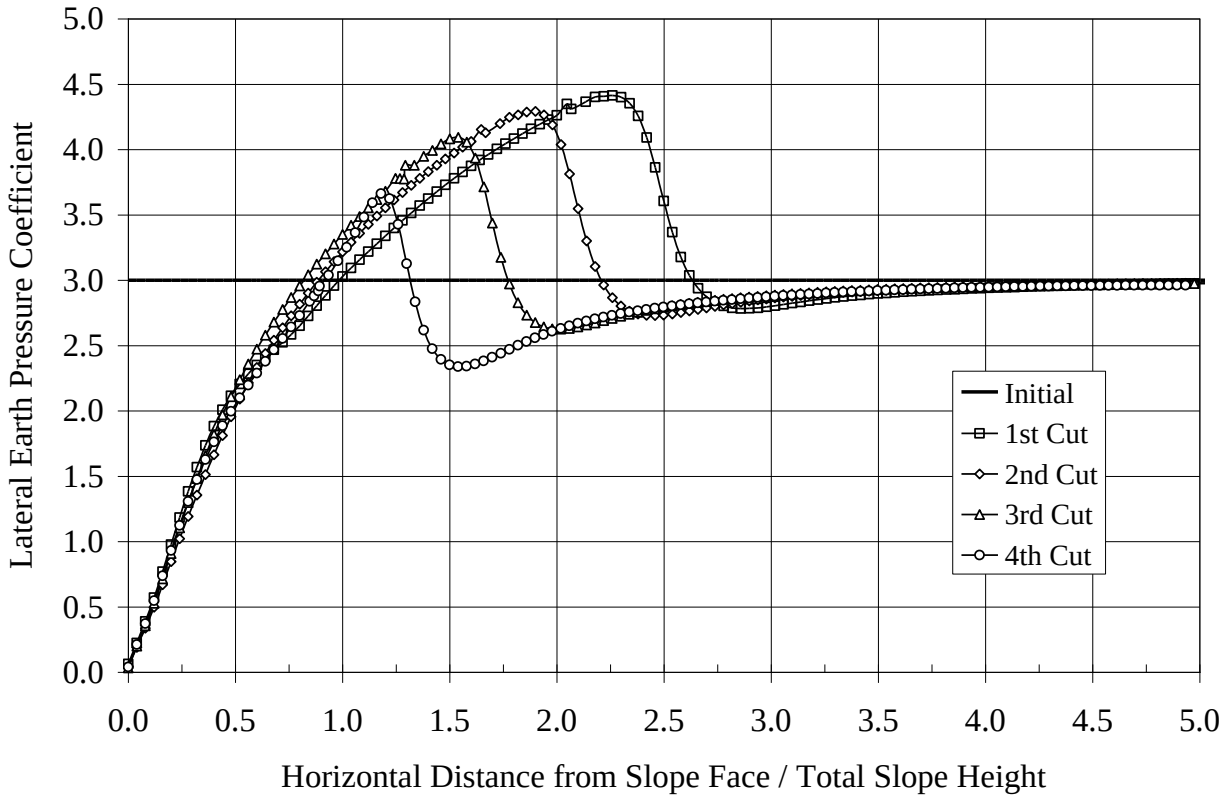

Figure 8.14. Variation of Lateral Earth Pressure at Mid-Height of MOC.

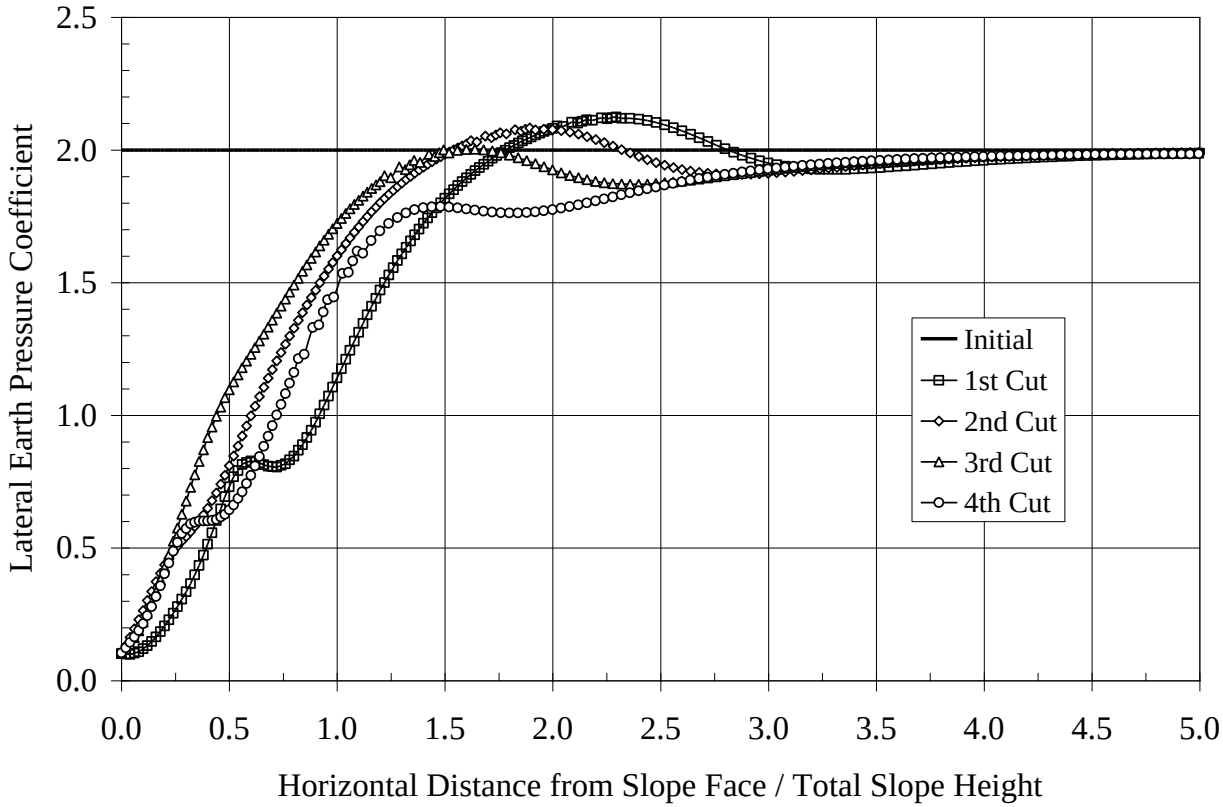

Figure 8.15. Variation of Lateral Earth Pressure at Mid-Height of LOC.

earth pressure that resulted in excessive shear strains from differential movement. It is these shear strains that created a closed crack and it was the continuing shear strains from subsequent cuts that propagated the crack. Propagation occurred along the plane of the existing crack due to excessive shear strain, similar to the laboratory shear model. The closed crack propagated before the LOC reached the peak shear stress due to differential shear strain. Figure 8.16 and Figure 8.17 present the shear stress contours for the 3rd and 4th cut. These two figures indicate that the magnitude of shear stress was not sufficient to cause failure, rather the material was brittle enough that failure occurred due to differential shear strain and as evidenced by the laboratory model, crack propagation should and did occur along the pre-existing failure plane.

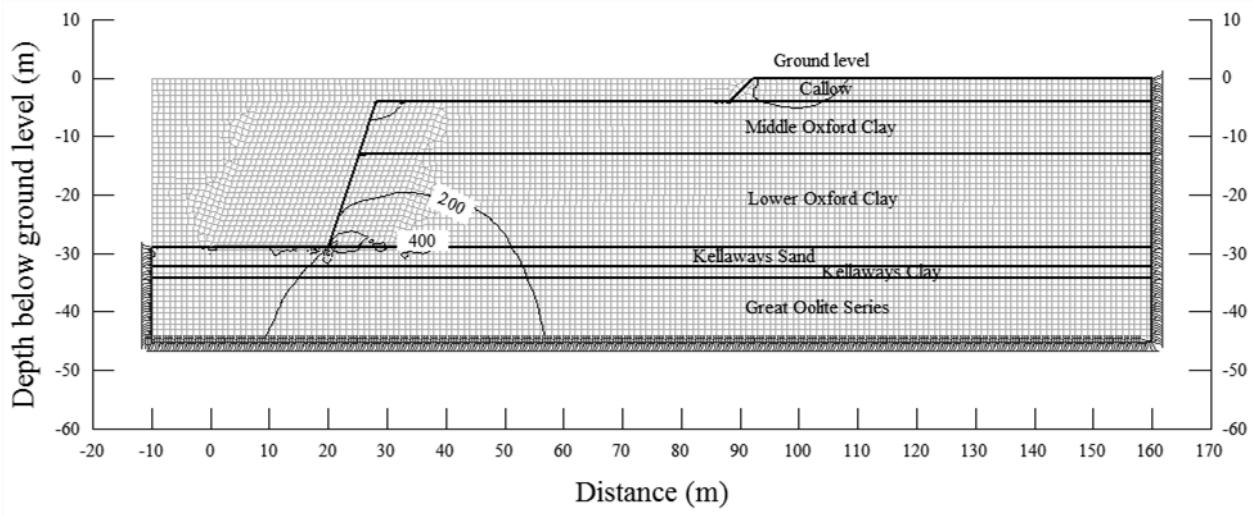

Figure 8.16. Shear Stress Contours (200 kPa) at the 3rd Excavation Stage.

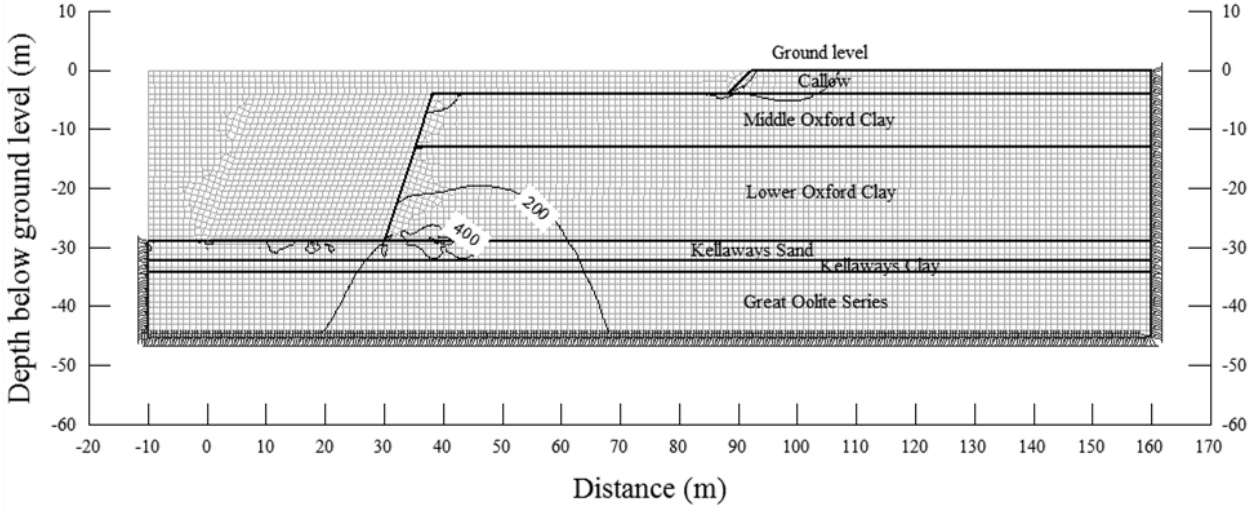

Figure 8.17. Shear Stress Contours (200 kPa) at the 4th Excavation Stage.

8.2 CONEMAUGH SLOPE

The Conemaugh Slope is a published case history that involved a 29± m excavation into residual stiff clay and sedimentary rock units located in Indiana County, Pennsylvania (Kutschke, et al, 2007, 2007, 2007, 2008, and 2010). The Conemaugh Slope was part of a larger project that involved 8.7-km of new railroad track construction. The overall project required the removal of 1.1 million m^3 of soil and sedimentary rock and resulted in cut slopes as deep as 46-m and fill slopes as high as 14-m. Right-of-way restrictions limited rock cut slope angles to those steeper than traditionally used for these slide prone and highly erodible geologic strata. Cut slopes were designed to fit within the proposed right-of-way by developing countermeasures to minimize weak rock degradation, installing sub-horizontal drains to lower groundwater levels, and developing an instrumentation program consisting of inclinometers and piezometers to monitor slope movement and water levels. The innovative geotechnical design efforts for this project resulted in considerable construction cost savings for the owner and earned local, state, and national awards from the American Society of Civil Engineers and the American Council of Engineering Companies. Figure 8.18 presents an aerial view of the Conemaugh Slope during construction.

8.2.1 Geologic Conditions

The Conemaugh Slope is associated with the Conemaugh Group, Glenshaw Formation, Pennsylvanian Period. The constituents are described as interbedded, strong and weak sedimentary rocks with considerable horizontal and vertical variation in strength and deformability but with a general tendency for vertical repetition of behavioral characteristics

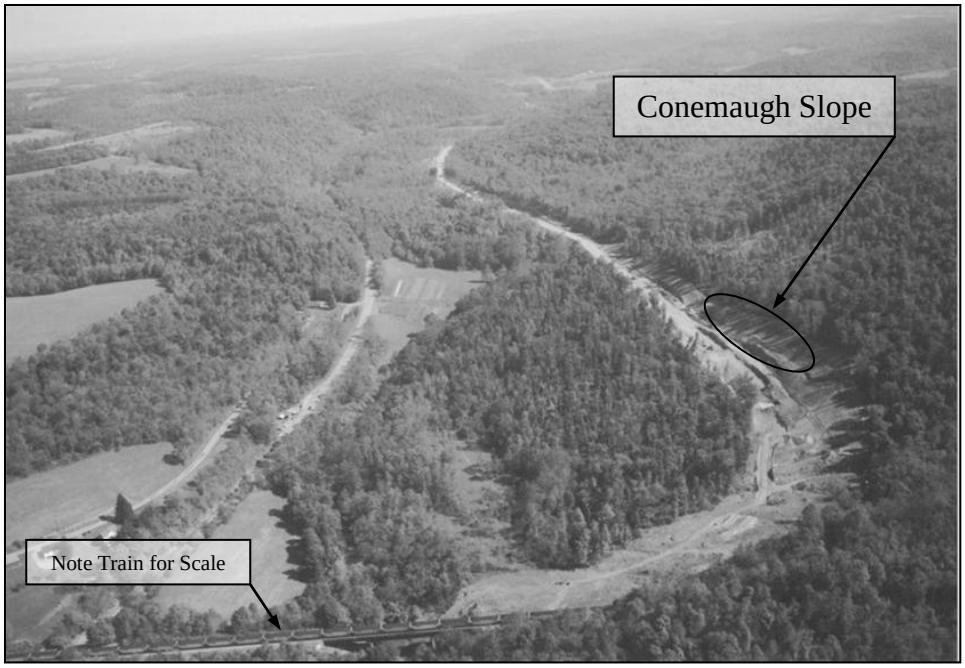

Figure 8.18. Aerial View of Conemaugh Slope During Construction (viewed looking east).

(Hamel, 1998). Structural features of the subject area include the Elders Ridge Synclinal Axis (to the northwest) and the Jacksonville Anticlinal Axis (to the southeast), both of which are oriented on a southwest-northeast trend. The dip of the bedding plane is about 3° to the northwest at the project corridor. The site soils are comprised of residual materials derived from weathering of the underlying bedrock.

A characteristic feature of the Conemaugh Group is the presence of mudrocks (particularly massive claystone) that have undergone oxidation to impart a predominantly red color. The local term "Pittsburgh Red Beds" is often used to refer to these weak, highly erodible claystone units that disintegrate rapidly upon exposure to form red-brown sandy, silty clay of medium plasticity (Hamel and Flint, 1972). The red beds are usually penetrated by a myriad of randomly oriented, closely spaced fractures, often with slickensided surfaces. The Pittsburgh Red Beds, along with

other unnamed red bed formations of the Conemaugh Group, have caused numerous slope stability problems that have attributed to the 3,000 recent and 12,000 historic landslide noted throughout the region (Ackenheil, 1954; Gray, et al. 1978; Hamel and Flint, 1972; Wu, et al. 1987, Hamel and Adams, 1981, and Pomeroy, 1982).

8.2.2 Conemaugh Slope Geometry

The Conemaugh Slope was designed as a 17.8-m high rock slope constructed at 3/4H:1V with an intermediate 4.5-m wide horizontal bench followed by a 10.9-m high soil slope excavated at 2H:1V. Available test borings indicated that the excavation would expose claystone associated with the Pittsburgh Red Beds, a weak and highly erodible rock unit. In order to protect this stratum and prevent it from undermining more resistant material, a shotcrete slope protection system (SSPS) that consisted of shotcrete, wire mesh, and rock anchors was applied to this stratum immediately after excavation (Kutschke, et al, 2007). However, construction encountered discontinuous rock strata that resulted in a design change. The as-built slope, which was modified during construction, consisted of 12.2-m high rock slope with a 4.5-m wide horizontal bench. The resulting 16.8-m high soil slope was excavated at 1H:1V for a height of 6.9-m, with the remaining slope excavated at 2H:1V. The as-built slope is shown as Figure 8.19 and the generalized cross section used for finite element analyses is shown as Figure 8.20.

8.2.3 Project Instrumentation

Three inclinometer casings and three standpipe piezometers were installed along the Conemaugh Slope. The piezometers were located immediately adjacent to the inclinometer casings since it is not practical to use an inclinometer casing as an observation well. The depths of the

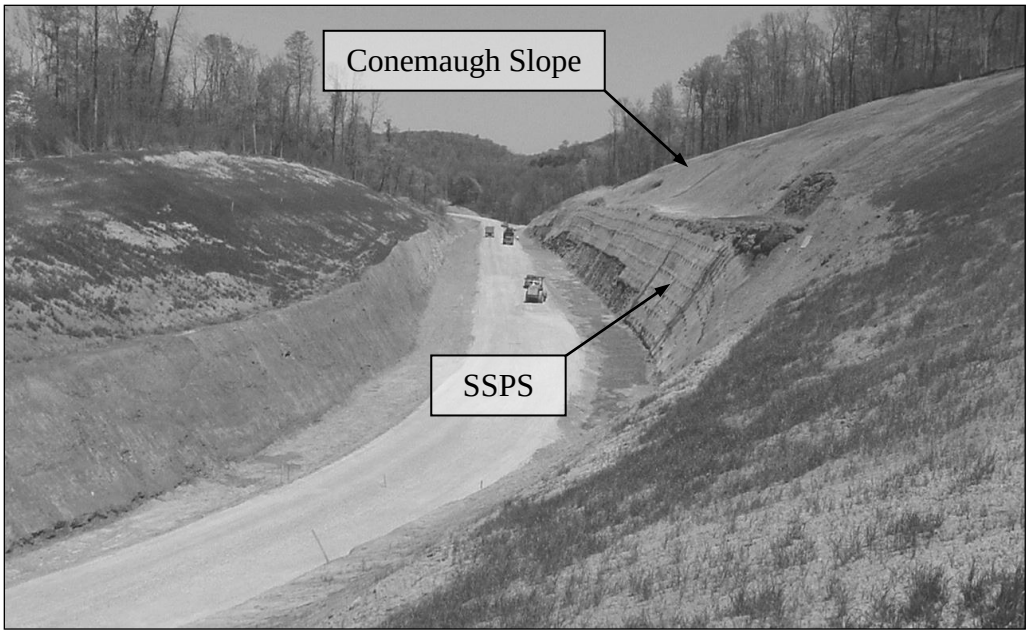

Figure 8.19. Cross Section View of Conemaugh Slope Prior to Slope Failure.

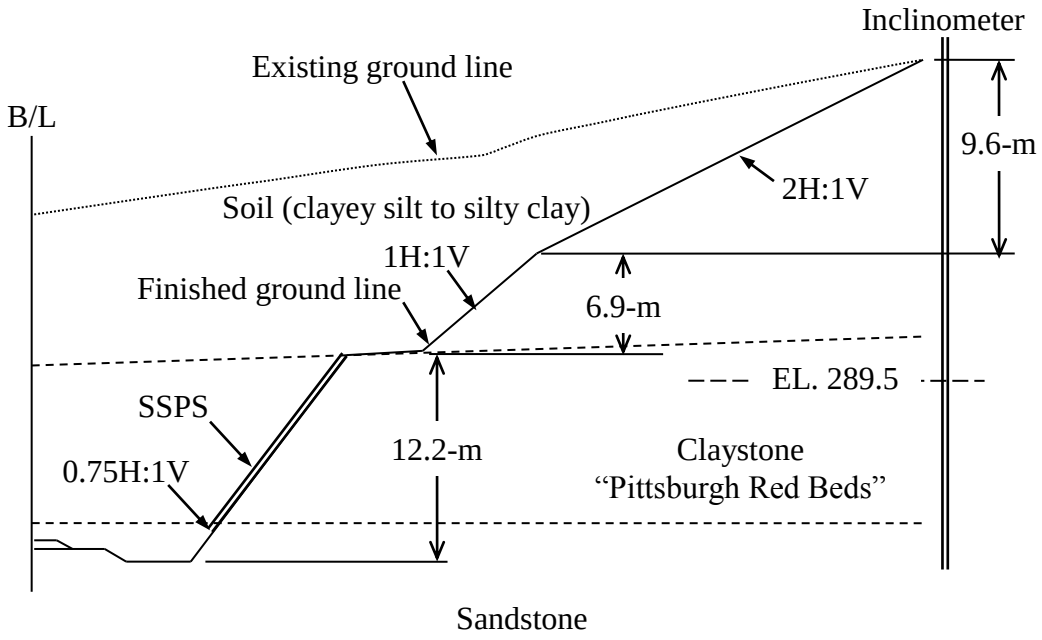

Figure 8.20. As-Built Conemaugh Slope Cross Section.

inclinometer casings and corresponding standpipes ranged from 29 to 35-m, typically extending at least 3-m below the proposed track elevation into the underlying sandstone. In all cases, the casings were located approximately 3-m beyond the crest of the proposed cut slope, as noted in Figure 8.21. The locations of the two inclinometers (I-2 and I-3) relative to the Conemaugh Slope are shown as Figure 8.21.

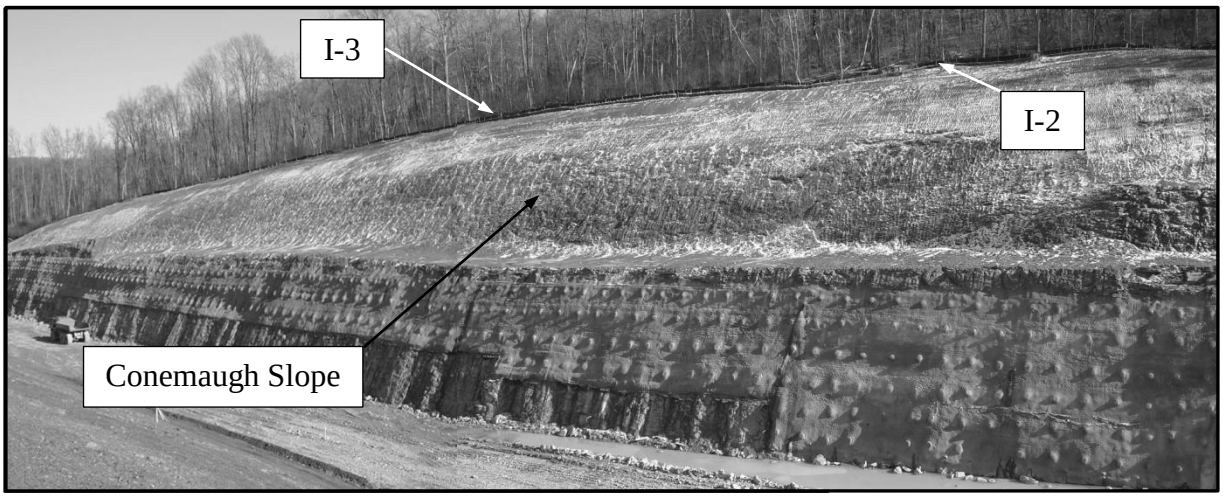

Figure 8.21. Inclinometer Locations along Conemaugh Slope.

The inclinometer casings were installed in 15.2-cm diameter drill holes and tremie grouted with cement-bentonite grout mix. The grout mix design was selected to ensure strength compatibility with the in-situ materials. The standpipe piezometers consisted of Schedule 80 PVC pipe installed in 7.6-cm diameter drill holes and the annulus was backfilled with coarse aggregate, sand, bentonite, and grout. Special attention was given to grouting the soil-rock interface in order to prevent hydraulic communication between surface water and deeper aquifer(s) that may be confined.

Installation of all instrumentation was completed prior to the beginning of excavation work so that stable baseline inclinometer and groundwater readings could be obtained. After obtaining two to three sets of initial baseline inclinometer readings, subsequent readings were taken twice a week in areas where excavation work was occurring. The frequency of readings was periodically increased in response to suspected slope movements.

In response to the deep adjacent excavations, the inclinometers all indicated the development of slope movements occurring at distinct zones. Because these movements stabilized following the completion of the cut, they have been attributed to relief of confining pressure coupled with vibrations from blasting operations. Inclinometers I-2 and I-3 indicated distinct movement at approximate El. 289.5-m. The inclinometer plot for I-2 is shown as Figure 8.22. This elevation corresponded to movement within the claystone stratum. Dunnicliff (1993) indicated that time rate of movement is a particularly important parameter regarding inclinometer plots. Time rate of movement plots are created from inclinometer data and provide important information regarding the rate of movement, in which the figure will clearly indicate an increasing or decreasing slope movement. Figure 8.23 presents a time rate of movement plot for the Conemaugh Slope at El. 289.5, and it clearly illustrates lateral stress relief that occurred during excavation. Upon completion of excavation, the rate of movement decreased and approached an asymptotic value. The excavation depths noted in Figure 8.23 represent an approximate rate of excavation as construction did not occur along neat stages, but rather by bulk excavation focused in select areas.

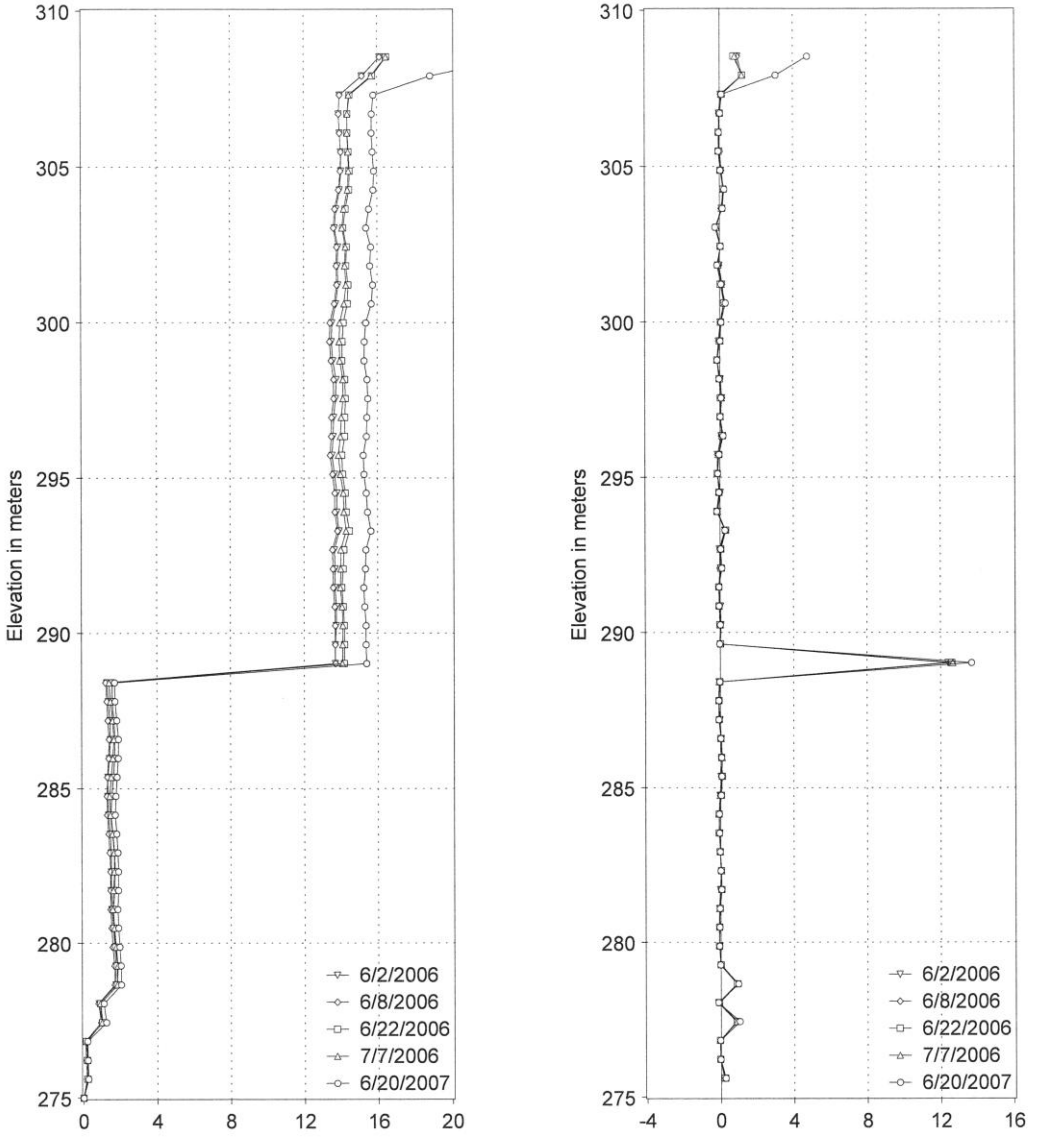

(a) Cumulative Displacement (mm)

(b) Incremental Displacement (mm)

Figure 8.22. Inclinometer Plot for I-2.

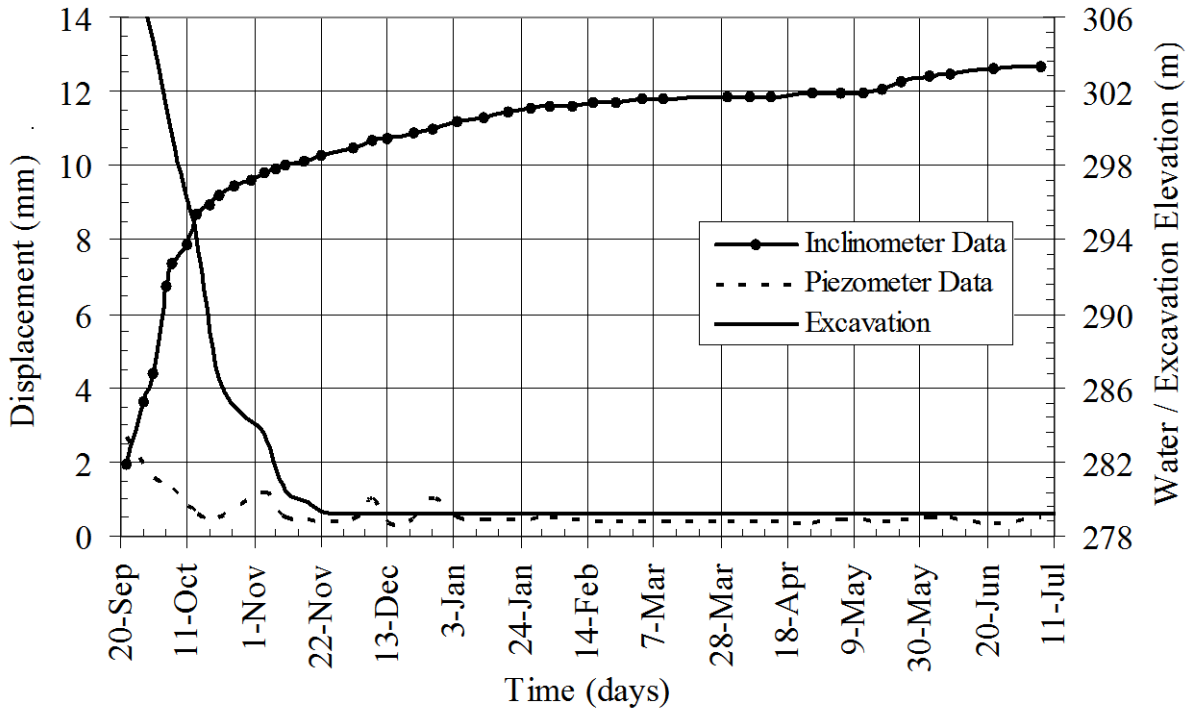

Figure 8.23. Conemaugh Slope Time Rate of Movement at El. 289.5±.

A soil slide involving approximately 6,200± m^3 occurred during approximately 6 months after construction. The slide occurred in-front of and down slope of the inclinometers, as shown on Figure 8.24(a). The main scarp daylighted in front of the inclinometer casings. The slide did not pass through the inclinometer casings and the inclinometers did not notice any pre-slide movement. The slide had a near vertical main scarp that had an approximate height of 7.6 m, as noted in Figure 8.24(b). Slope failure occurred in the soil, not in the underlying claystone, with the toe of the slide at approximate El. 291-m.

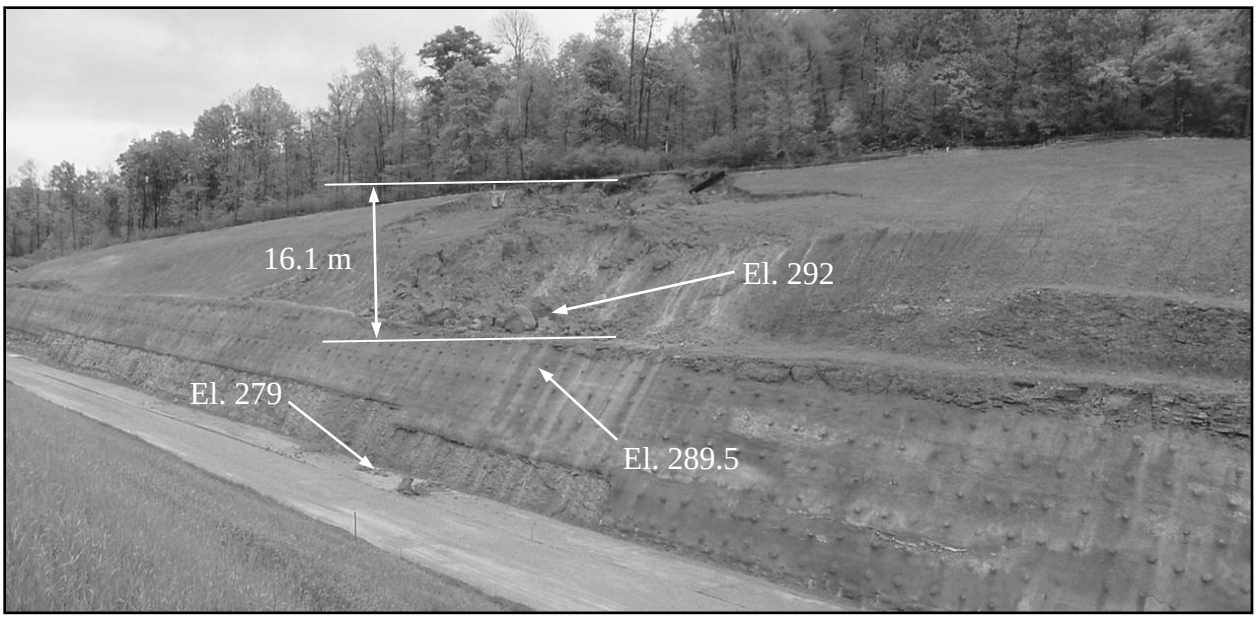

(a) Overview of slope.

(b) View of 7.6 meter tall main scarp.

Figure 8.24. Conemaugh Clay Slope Failure.

8.2.4 Site Characterization for Finite Element Analyses

Available subsurface information indicated three significant strata, namely: residual soil that consisted of clayey silt to silty clay which weathered from the underlying parent rock. The soil was underlain by claystone units that were situated over sandstone. URS (2005) presented a detailed discussion regarding the soil properties and laboratory test data.

8.2.4.1 Residual Soil. Pre-slide test borings obtained for the Conemaugh Slope indicated that the material generally consisted of clayey silt to silty clay with trace shale fragments. This material is believed to be residual material that weathered from the underlying Pittsburgh Red Bed. Standard penetration testing indicated uncorrected blow counts that ranged from 6 to greater than 50 blows per foot, but generally around 22 indicating a very stiff consistency. The low N-values were generally encountered near surface and increased with depth.

The soil properties used for the FEM models were derived from laboratory testing and published correlations (Aplan, 1967; Holtz and Kovacs, 1981; Mayne, 1984; AASHTO, 1996; Bowles, 1996, and URS, 2005). Laboratory testing consisted of index property, shear strength, and consolidation testing. It is important to note that the Pittsburgh Red Bed formation is highly variable and generalized data regarding this formation is not practical (Hamel and Flint, 1972; Hamel and Adams, 1981; Hamel, 1998; Kutschke, et al, 2007, 2007; and Hamel, 2009). Shear strength properties depend on whether the stratum is weathered or unweathered (as opposed to colluvial or residual soils derived from this formation) as well as dependent on composition, degree and types of fissures and fractures at both macro & micro levels (Hamel, 2009). Table 8.2 presents the selected values used for the FEM Conemaugh Slope model.

Table 8.2. Geotechnical Parameters and Values for the Conemaugh Slope FEM Model.

Geotechnical Parameter	Value
E, Modulus of Elasticity	177,100 kPa
k_o, Lateral Earth Pressure Coefficient	1.41
ν, Poisson's Ratio	0.4
c, Cohesion	86.2 kPa
ϕ, Friction Angle	0°
ψ, Dilation Angle	0°
γ, Unit Weight	20.42 kN/m^3

8.2.4.2 Bedrock. The residual soil transitioned into claystone rock associated with the Pittsburgh Red Bed formation. The claystone material encountered is generally characterized as gray to red-brown, very soft to soft, completely to highly weathered, very intensely bedded (RD 5°), very close to closely fractured (RD 30° – 60°), with slickensided to slightly rough fracture/joint surfaces. Test boring information indicated percent core recoveries that ranged from 60 to 100 percent, but generally greater than 90 percent, and rock quality designation (RQD) values were typically zero. Beneath the claystone, the test borings encountered shaley to fine-grained sandstone. The rock core characteristics of the sandstone consisted of gray to green gray, medium hard to hard, slightly weathered, intensely bedded (RD 5°), very closely to medium fractured (RD 10°), rough to slightly rough fracture/joint surfaces. Percent rock core recoveries were generally greater than 90 percent and RQD values were generally greater than 68 percent.

Site characterization for FEM modeling of the claystone and sandstone strata consisted of unconfined compressive strength (UCS) testing. The test data was used in conjunction with the Geomechanics Classification System, or Rock Mass Rating (RMR) to characterize the bedrock

(Bieniawski, 1974). Based upon examination of the rock cores and the available laboratory test data, the RMR for the claystone material ranged from 11 to 27, while the sandstone ranged from 54 to 72. The in-situ modulus of the rock relied on the following correlation proposed by Serafim and Pereira (1983):

$$E = 10^{\left(\frac{RMR-10}{40}\right)}$$

where the Modulus of Elasticity is in units of GPa. Shear strength values where developed using the Hoek-Brown strength criterion which resulted in a curved shear strength envelope given by the following equation (Hoek, 1983):

$$\tau = (\cot\phi' - \cos\phi')\frac{m\sigma_{u(r)}}{8} \qquad 8\text{-}2$$

where τ is the shear stress at failure and ϕ' is the instantaneous friction angle at given values of τ and σ'. The value of ϕ' used in Equation 8-2 is given by:

$$\phi' = \arctan\left[\frac{1}{\left(4h\cos^2\theta - 1\right)^{0.5}}\right] \qquad 8\text{-}3$$

where the variables h and θ presented in Equation 8-3 are defined as:

$$h = 1 + \frac{16\left(m\sigma' + s\sigma_{u(r)}\right)}{3m^2\sigma_{u(r)}}$$

$$\theta = \frac{1}{3}\left(90 + \arctan\left[\frac{1}{\left(h^3 - 1\right)^{0.5}}\right]\right)$$

The dimensionless constants *m* and *s* are dependent on rock type and the degree of fracturing of the rock mass (related back to the RMR analysis). The cohesion is the intercept of the line defining the instantaneous friction angle on the shear axis defined by Mohr-Coulomb. The features of the curved shear strength envelope are that at:

- Low normal stress, the blocks of the rocks are interlocked and the friction angle is high.
- High confining stress, the friction angle diminishes and the cohesion progressively increases with the normal stress.

The Hoek-Brown strength criterion for the claystone stratum is presented as Figure 8.25, and Table 8.3 provides the selected values used for the FEM model. The Hoek-Brown strength criterion for the sandstone is presented as Figure 8.26, and Table 8.4 presents the selected values used for the FEM model.

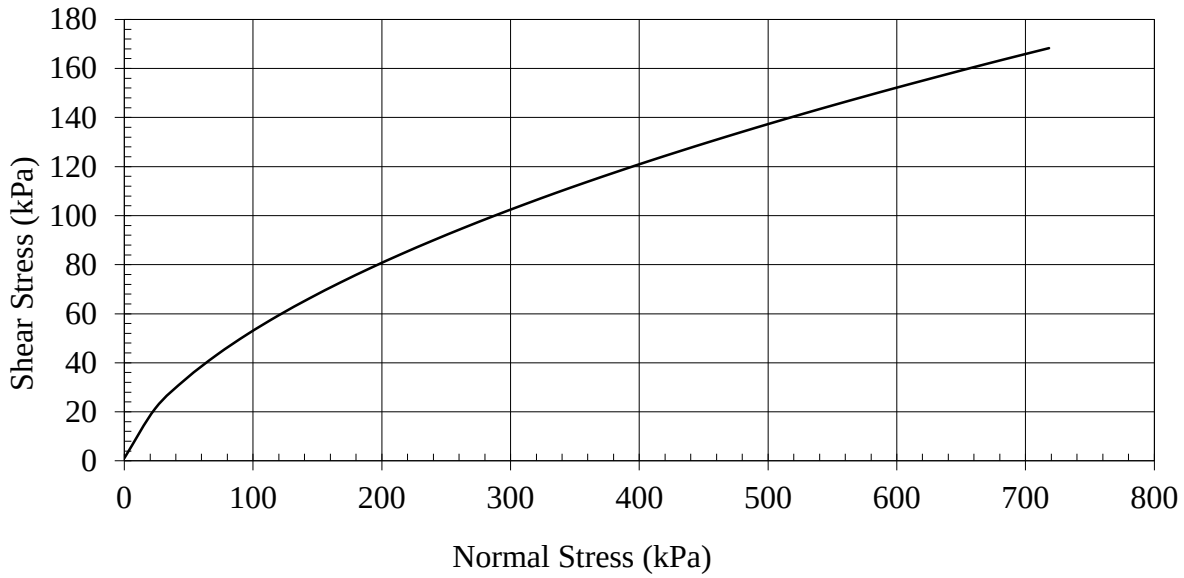

Figure 8.25. Non-Linear Mohr Envelope for Claystone.

Table 8.3. Claystone Geotechnical Parameters and Values for the Conemaugh Slope FEM Model.

Geotechnical Parameter	Value
E, Modulus of Elasticity	1,900,000 kPa
k_o, Lateral Earth Pressure Coefficient	3.0
ν, Poisson's Ratio	0.2
c, Cohesion	10.8 kPa
ϕ, Friction Angle	30°
ψ, Dilation Angle	0
γ, Unit Weight	156 pcf

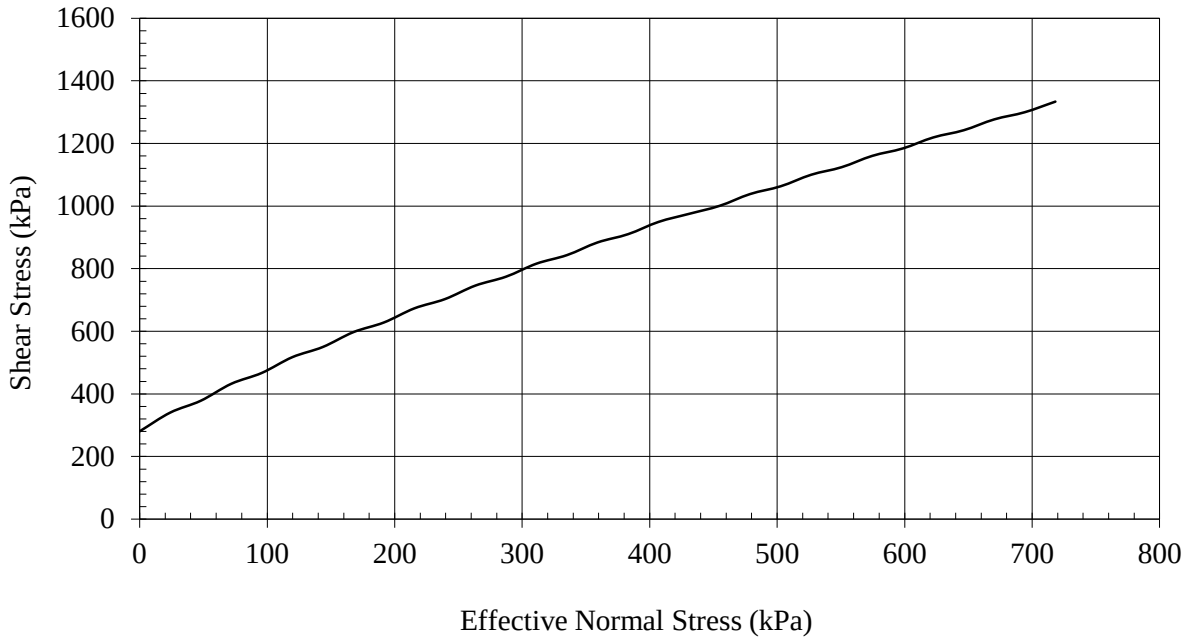

Figure 8.26. Non-Linear Mohr Envelope for Sandstone.

Table 8.4. Sandstone Geotechnical Parameters and Values for the Sandstone Slope FEM Model.

Geotechnical Parameter	Value
E, Modulus of Elasticity	8,840,000 kPa
k_o, Lateral Earth Pressure Coefficient	3.87
ν, Poisson's Ratio	0.3
c, Cohesion	430 kPa
ϕ, Friction Angle	45°
ψ, Dilation Angle	0
γ, Unit Weight	161 pcf

8.2.5 Finite Element Model

The FEM model used a two dimensional mesh with isoparametric elements consisting of six node triangles. Boundary conditions considered the base to be fixed in the horizontal and vertical direction while the sides were only fixed in the horizontal direction. The FEM model used to establish the initial stress conditions is shown as Figure 8.27.

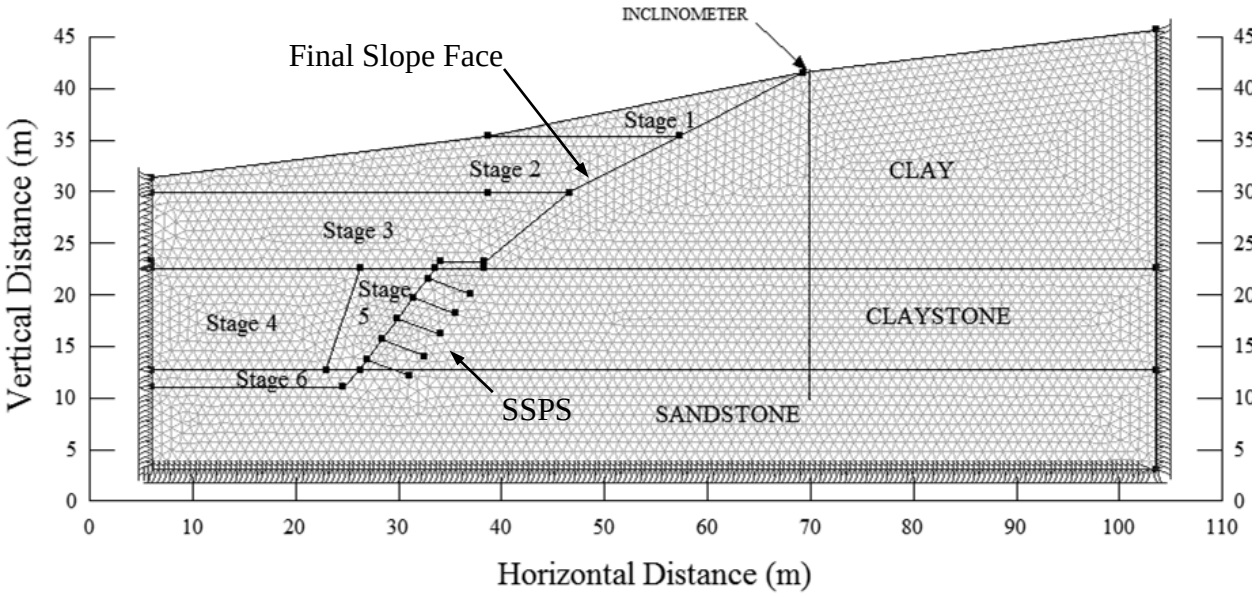

Figure 8.27. Initial FEM Model Indicating Construction Stage Conditions.

The FEM model simulated excavation by progressively "turning-off" elements and allowing lateral stress relief to occur. The elements were grouped in regions labeled Stage 1 through Stage 6, as noted in Figure 8.27. These regions were incrementally removed by "turning-off" the elements and conducting subsequent stress-deformation analyses at each stage. The FEM analyses closely modeled actual excavation conditions with staged analyses. Stage 5 analyses

involved continued excavation along the slope face as well as installation of the SSPS that involved shotcrete and rock anchors (Kutschke, et al, 2007, 2007). These elements were modeled in the FEM analyses using structural beams and structural bars and are noted in Figure 8.27. The rock anchors are passive elements and were not post-tensioned. The slope protection served to minimize weathering of the erodible rock and was not considered in the design to provide structural support (Kutschke, et al, 2007). Stage 6 completed the FEM analyses.

The residual soil and claystone strata were modeled using elastic-plastic material properties in which stresses are directly proportional to stains until the yield point is reached. In accordance with Wyllie and Mah (2006), the sandstone utilized a linear-elastic constitutive model.

The Conemaugh Slope FEM model used a constant unit weight and constant lateral earth pressure coefficient value for each stratum so that the initial horizontal and vertical stress increased linearly with depth in each stratum. As an initial analysis verification, the vertical stress values obtained from the FEM model were compared to simple hand calculation values considering the following expression,

$$\sigma = (\gamma)(depth)$$

where (σ) is the total vertical stress and (γ) is the unit weight of the soil. Figure 8.28 presents the FEM initial vertical stress contours prior to excavation and Figure 8.29 presents the FEM initial horizontal and vertical stress conditions along with the hand calculation verification. The FEM in-situ vertical stress and the hand calculation values indicate an accurate agreement.

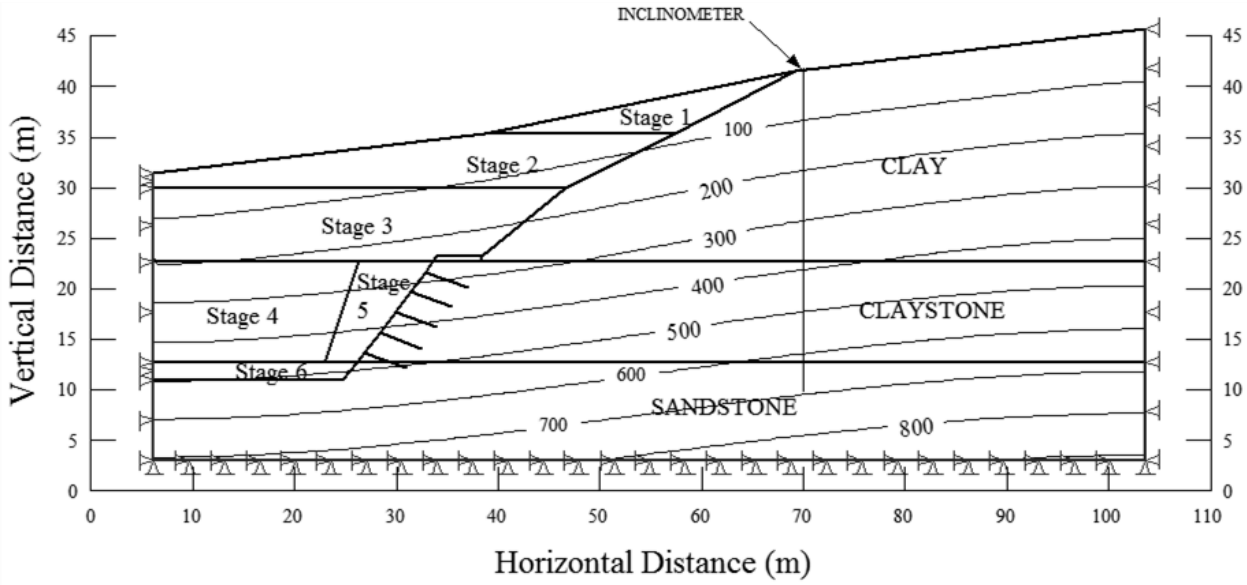

Figure 8.28. Initial Vertical Stress Contours (100 kPa) Prior to Excavation.

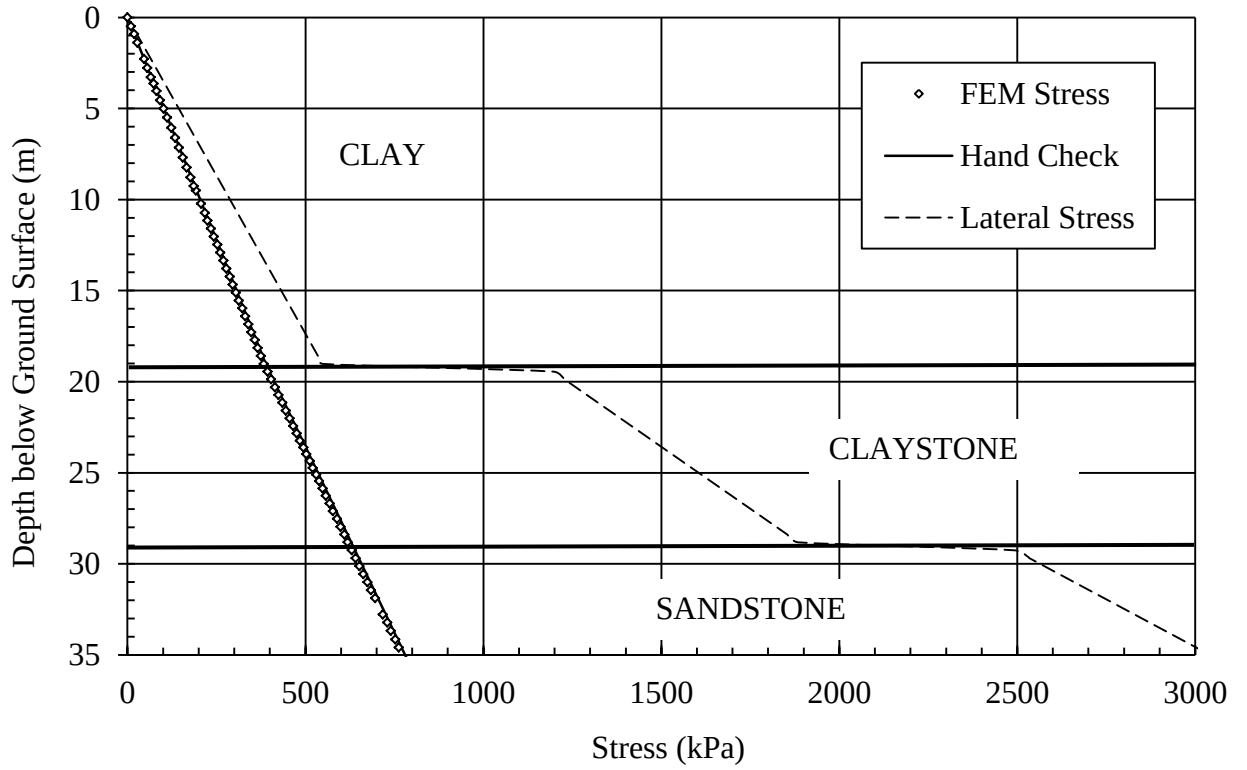

Figure 8.29. FEM Initial Horizontal and Vertical Earth Pressures Along the Inclinometer Prior to Excavation.

8.2.6 Evaluation of Model Results

The FEM analyses were conducted in stages to simulate actual field excavation procedures. Initial analyses were first performed without consideration for pre-existing cracks. Figures 8.30 through 8.32 present the shear stress contours for excavation Stages 1, 2, and 3. Examination of these figures indicated that Stage 1 and Stage 2 excavation did not induce sufficient shear stress to develop a closed crack in the clay stratum. However, review of Figure 8.32 indicated that the shear stress contours are approximately equal to the undrained shear strength of the clay material near the clay-claystone interface. That is, release of confining pressure resulted in outward slope movement that developed excessive shear stress to produce a closed crack. Figure 8.33 provides detailed examination of a stress element near the toe of slope, which clearly indicates a condition that would result in the development of a failure plane. Subsequent analyses utilized a slip element to model the closed crack that extended from the toe of slope and into the backslope region. Based on research conducted by Bazett, et al (1961), Skempton and LaRochelle (1965), and Burland, et al (1977), the analyses used a reduction in the undrained shear strength along a slip element of 50%. Figure 8.34 indicates the FEM outward slope face movement for each excavation stage and incorporated the slip element for the 3rd and subsequent stages. The impact that a closed crack had on the overall slope is noted on Figure 8.35, which compares the slope movement at the 3rd Stage with and without a closed crack. A closed crack resulted in a larger outward slope face movement, which is as expected since there has been a reduction in the overall shear strength resistance of the slope. This research postulated that pre-existing cracks within this slope, combined with the construction induced cracks from lateral stress relief, resulted in overall slope failure. The extent and random direction of the pre-existing cracks in

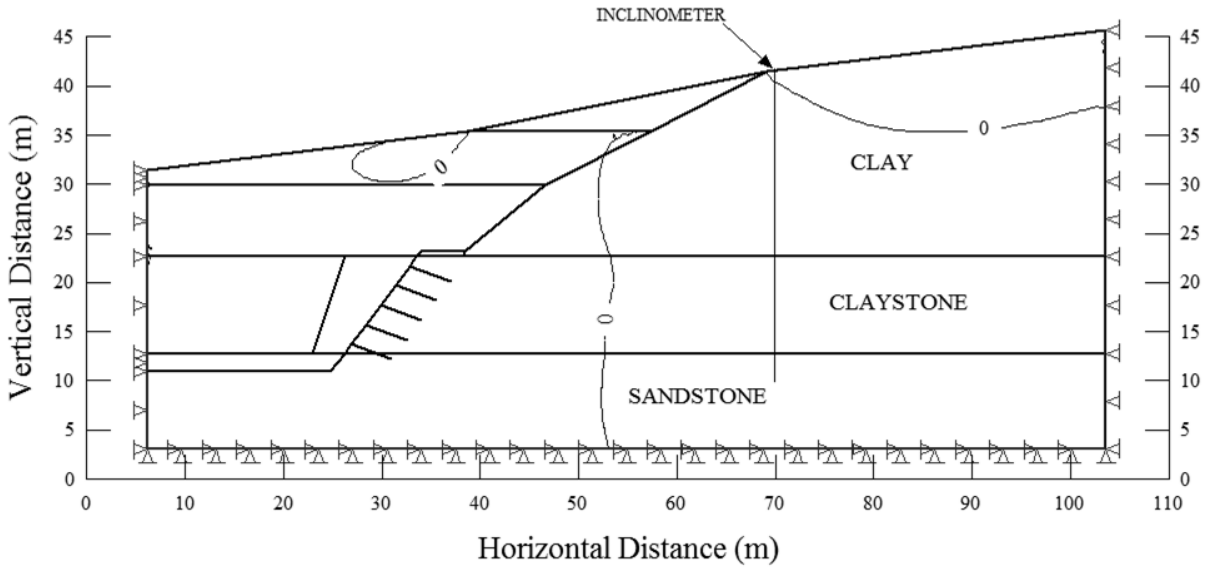

Figure 8.30. Shear Stress Contours (50-kPa) for Stage 1 Excavation with No Pre-Existing Crack.

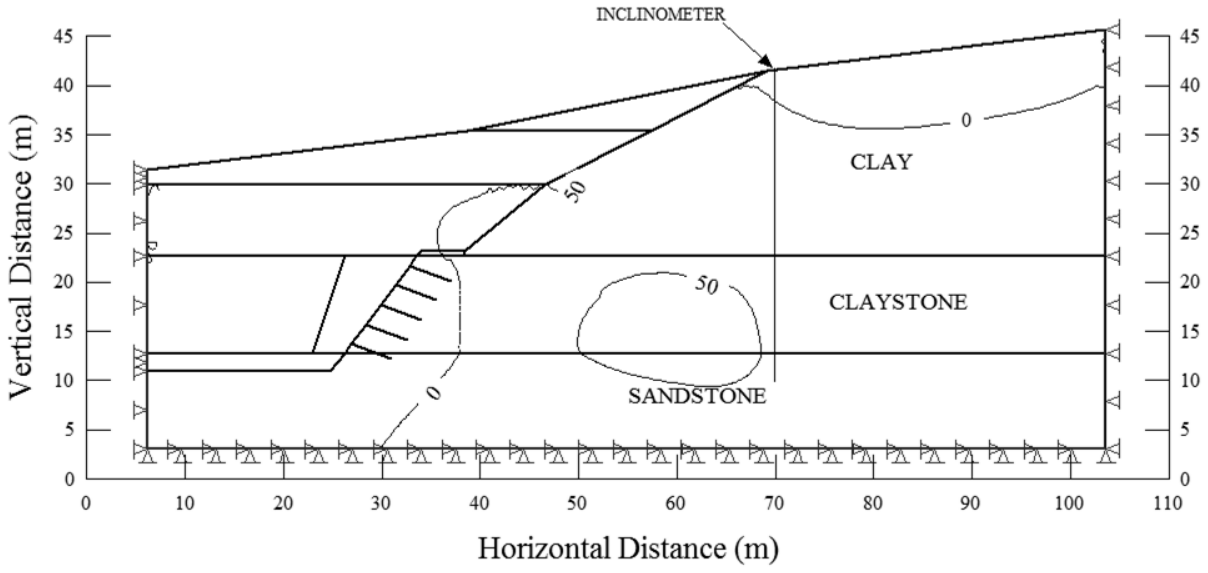

Figure 8.31. Shear Stress Contours (50-kPa) for Stage 2 Excavation with No Pre-Existing Crack.

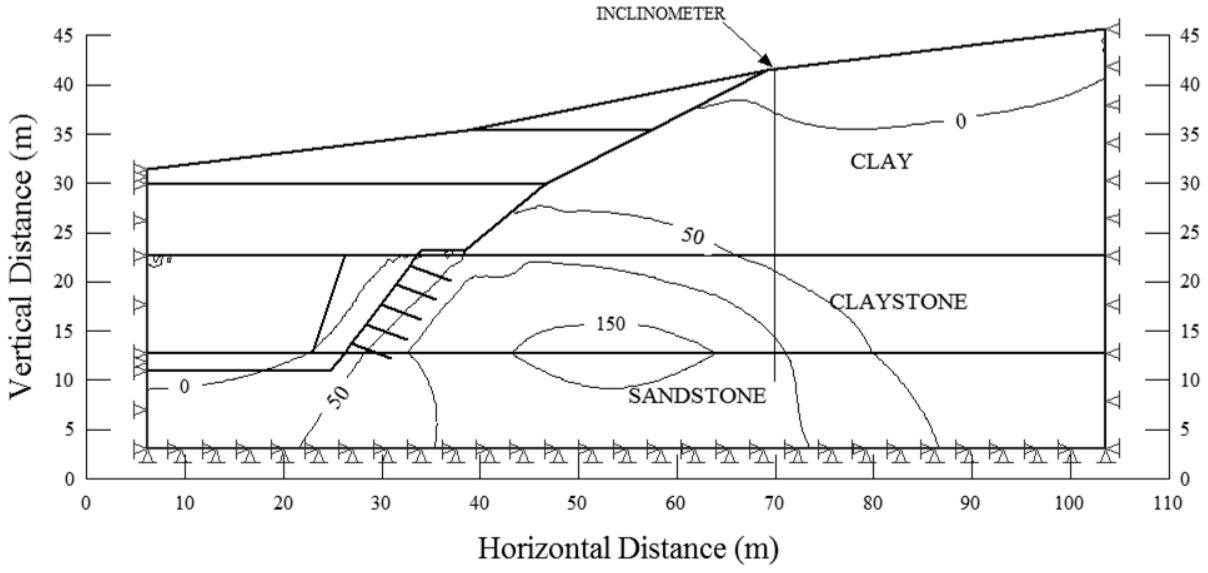

Figure 8.32. Shear Stress Contours (50-kPa) for Stage 3 Excavation with No Pre-Existing Crack.

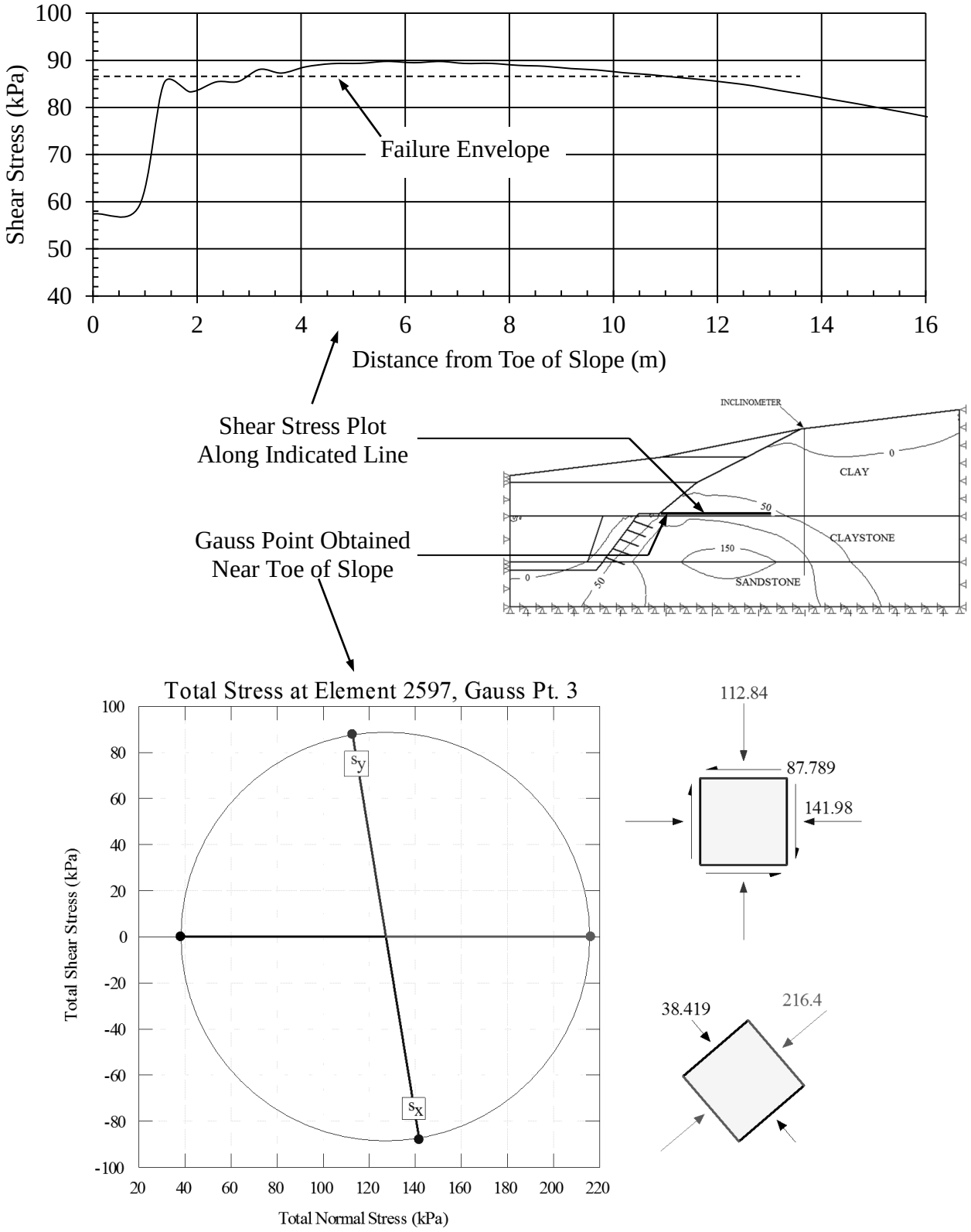

Figure 8.33. Shear Stresses Near Clay – Claystone Interface.

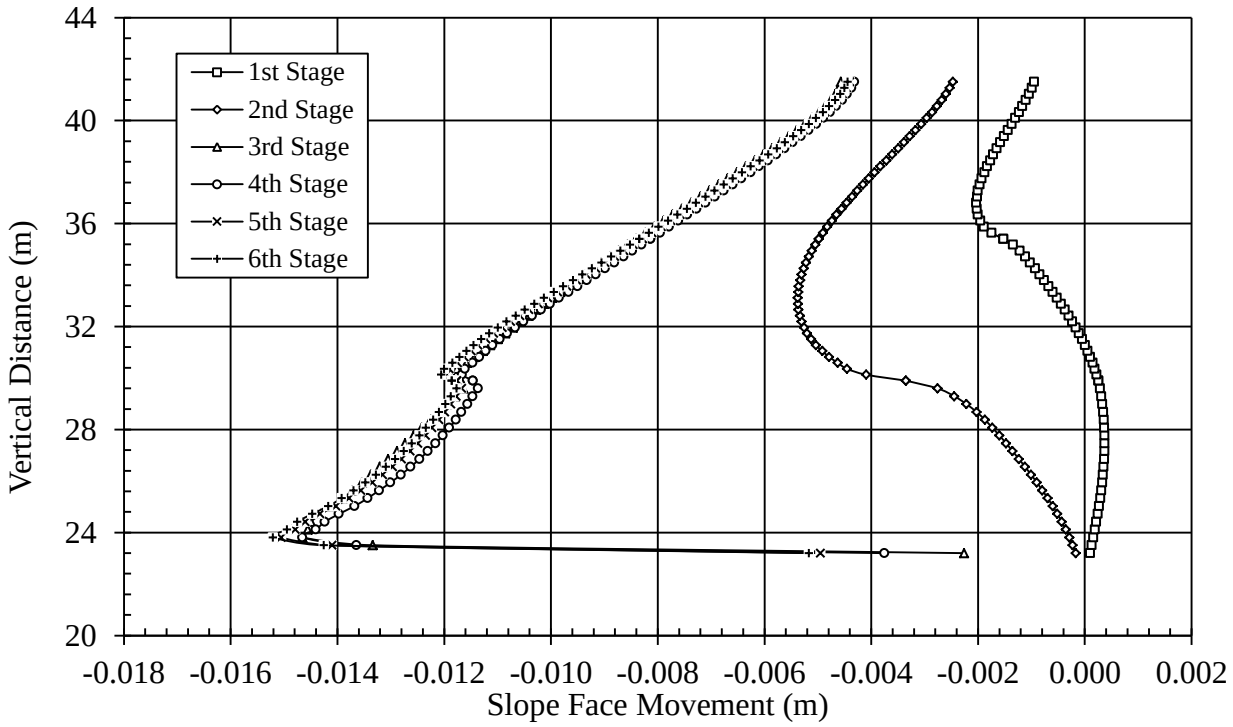

Figure 8.34. FEM Slope Face Movements at Each Excavation Stage.

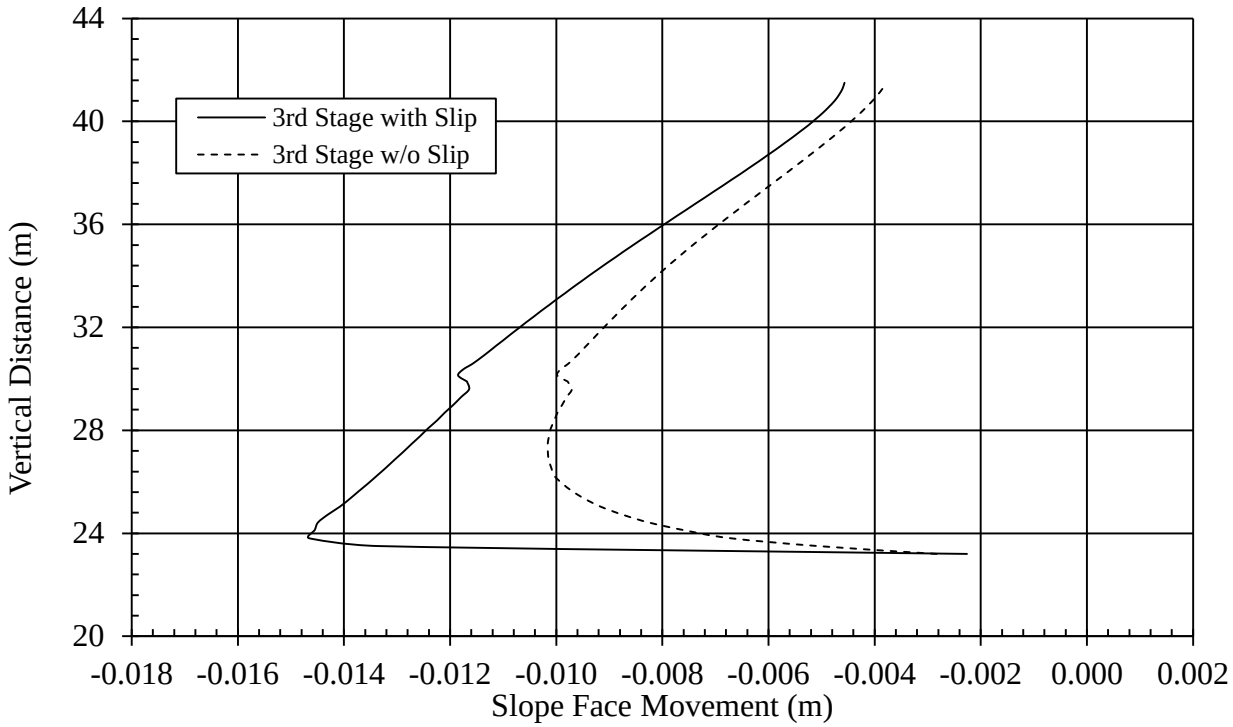

Figure 8.35. FEM Slope Face Movements at Excavation Stage 3.

the clay stratum is difficult to realistically or practically model and was not incorporated into the FEM model.

The release of confining pressure caused by the excavation had a profound impact on the lateral earth pressures in the backslope region. Figures 8.36 to 8.38 present the lateral earth pressure along a horizontal plane at the base of each excavation stage. Figures indicated that:

- At the base of the excavation for Stage 1 and 2, the lateral earth pressure at the toe of excavation increased in response to the material in the backslope region tending to move outward due to release of confining pressure and downward due to gravity. This conclusion is evident in all figures as the material in the toe region becomes compressed as failure would occur at the toe (Fellenius, 1927; Taylor, 1937, 1948; Terzaghi, 1943).
- Excavation significantly impacted the lateral earth pressures from the slope face to a lateral distance that ranged from 1.4 to 1.7H. Beyond this distance, the lateral earth pressures were not significantly impacted by the excavation. As indicated in Figures 8.36 to 8.38, the inclinometer was located outside this region and did not experience any post-construction movement in the soil backslope; this conclusion agrees well with the actual field observations.
- Negative lateral earth pressure developed at the toe of slope for Stage 3, which is different from the first two stages that experience increased lateral earth pressures. This condition is in response to the formation of a toe crack with reduced shear strength properties that allowed for greater toe deflection. This result is consist with Skempton and LaRochelle (1965) where they discuss clay "burst" where the toe of excavation in London Clay was seen to bulge and that cracking extended into the slope face.

Location of horizontal plane used to develop Figure 8.36

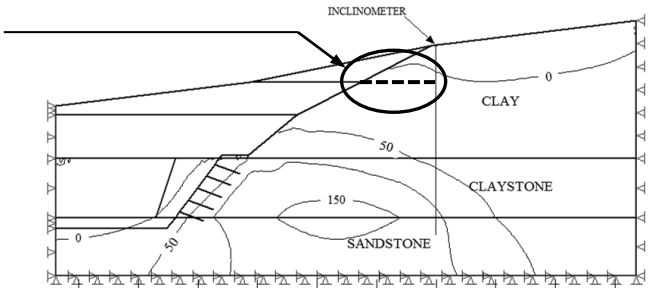

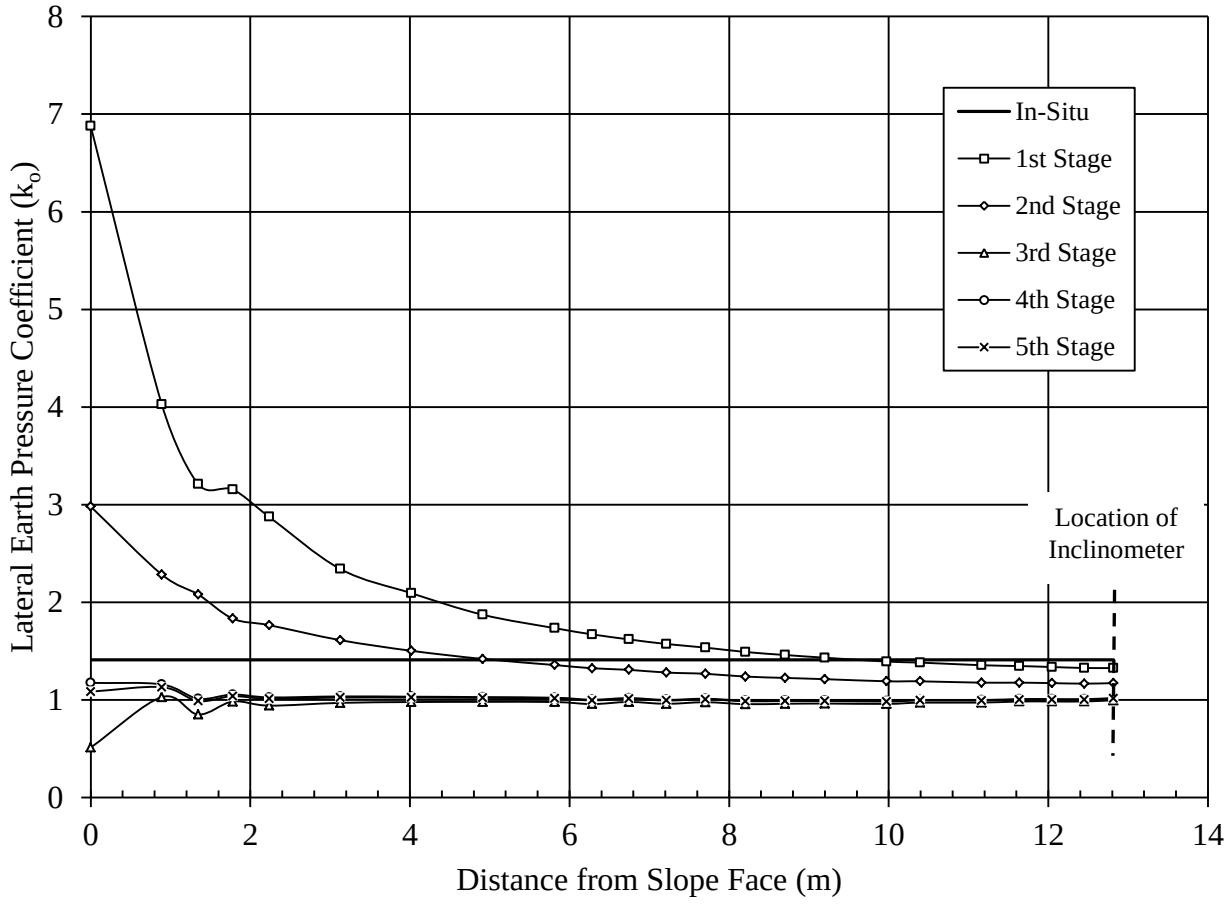

Figure 8.36. Lateral Earth Pressure at Base of 1st Stage along a Horizontal Plane from Slope Face to Inclinometer.

Location of horizontal plane used to develop Figure 8.37

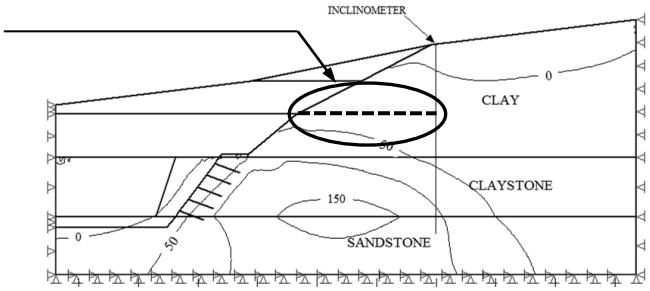

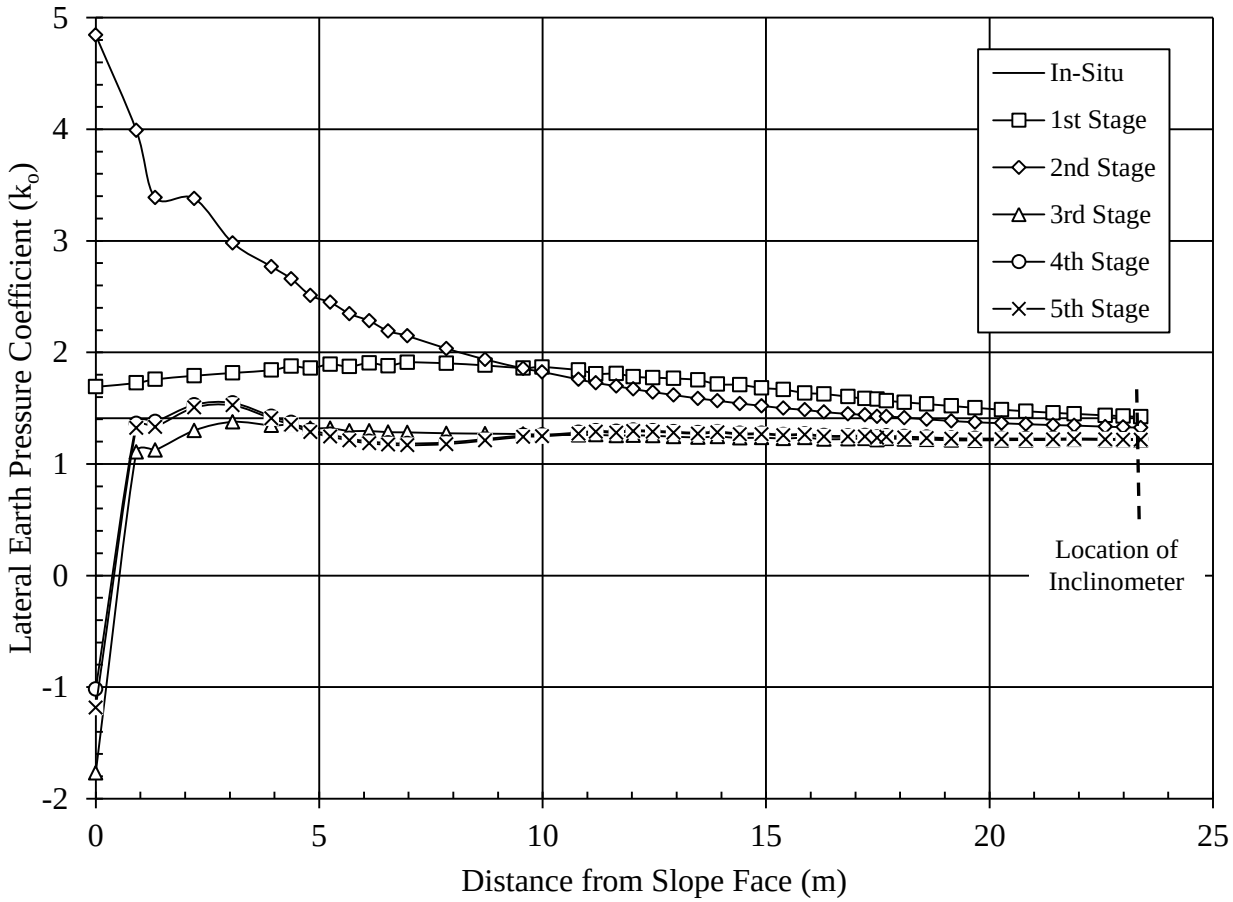

Figure 8.37. Lateral Earth Pressure at Base of 2nd Stage along a Horizontal Plane from Slope Face to Inclinometer.

Location of horizontal plane used to develop Figure 8.38

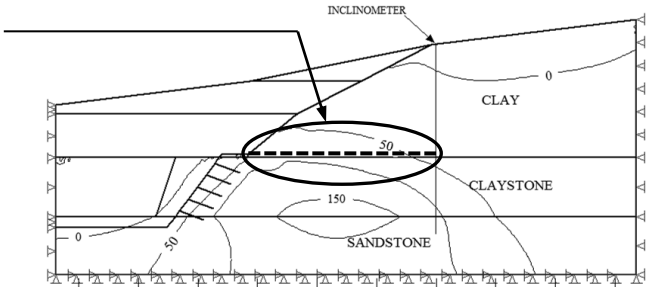

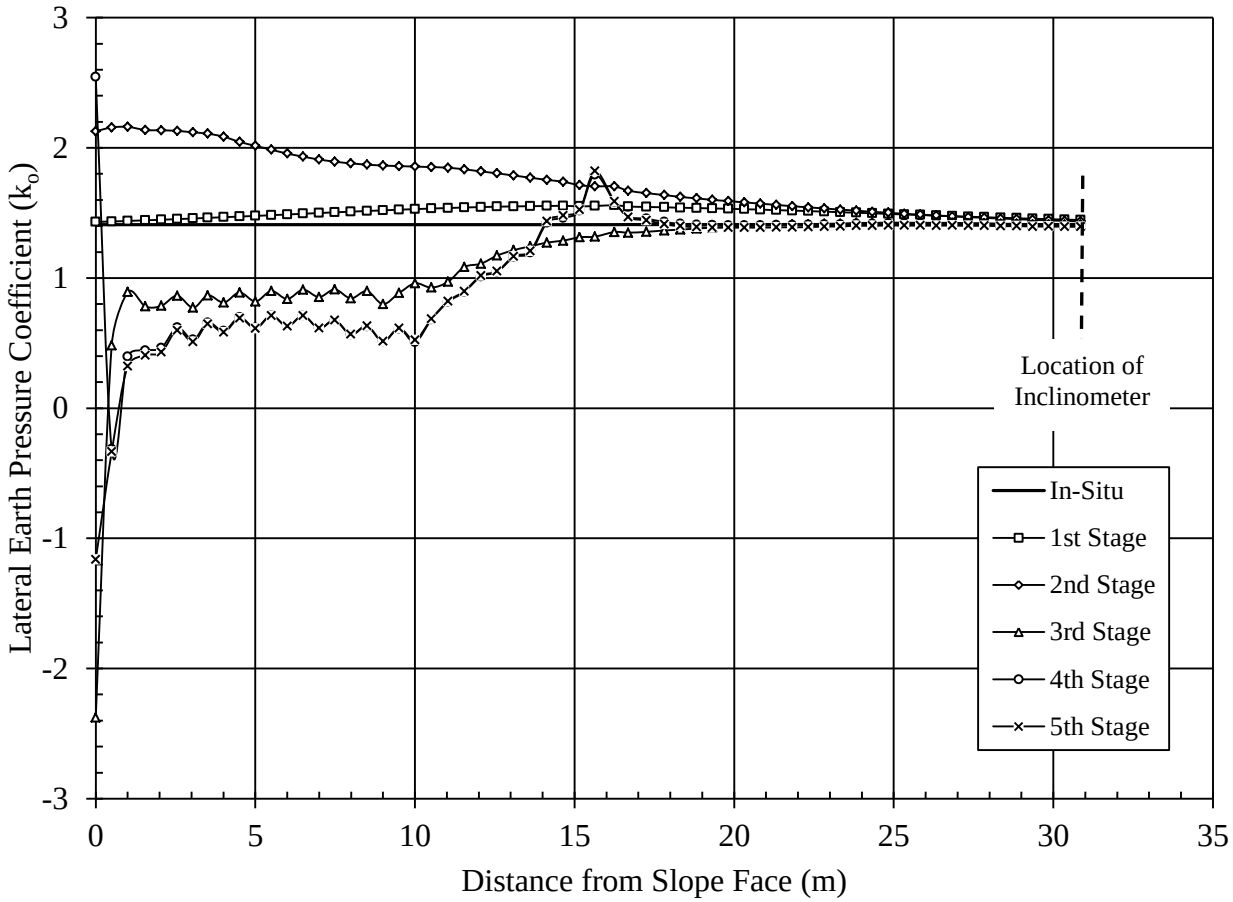

Figure 8.38. Lateral Earth Pressure at Base of 3rd Stage along a Horizontal Plane from Slope Face to Inclinometer.

8.3 SUMMARY

Excavation activities at both the Oxford Slope and the Conemaugh Slope significantly altered the lateral earth pressures within the backslope region. Observations regarding the FEM analyses for these two models are summarized as follows:

Oxford Slope

- The Oxford Slope FEM model exhibited very close agreement to actual measured field displacements. FEM analyses indicate that the Oxford Slope was essentially a shear model in which excessive shear strains created and caused lateral propagation of a horizontal failure plane. Propagation occurred along the plane of the existing crack due to excessive shear strain, similar to the laboratory shear model.
- Tensile stresses at the base and crest of slope were not sufficient to create inclined or vertical cracking. The closed crack propagated horizontally before the LOC reached peak shear stress due to differential shear strain. The magnitude of shear stress was not sufficient to cause failure, rather the material was brittle enough that failure occurred due to differential shear strain and as evidenced by the laboratory model, crack propagation should and did occur along the pre-existing failure plane.

Conemaugh Slope

- LSR resulted in outward slope movement that developed excessive shear stress to produce a closed crack. This research postulated that pre-existing cracks within this slope, combined with the construction induced cracks from lateral stress relief, resulted in overall slope failure. The extent and random direction of the pre-existing cracks in the

clay stratum is difficult to realistically or practically model and was not incorporated into the FEM model.

9.0 CONCLUSIONS

This research used finite element and fracture mechanics analyses as well as laboratory and field studies of slopes in purely cohesive clay ($\phi = 0°$ soil) with either a vertical or an inclined slope face. The analyses indicated that when Lateral Stress Relief (LSR) took place during the excavation of the slopes, the following was produced:

1. Excavation into stiff cohesive material resulted in the outward movement of the new slope face due to LSR. The magnitude of movement was dependent on k_o and this movement could create a discontinuity at the toe of the slope as well as a tension crack at the surface of the backslope. Conventional limit equilibrium methods of slope stability analysis only consider the equilibrium of a soil mass tending to move down slope under the influence of gravity without regard for the in-situ stress conditions or the development of shear zones that occur from LSR. There was very little known about how these two discontinuities formed as well as how they interacted to produce the final failure of the slope. Research presented herein provided insight into the propagation of these shear zones that lead to the progressive failure of $\phi = 0°$ slopes due to LSR.

2. LSR within $\phi = 0°$ slopes significantly altered the backslope conditions and created shear and tension cracks in the soil mass. The initial direction of crack propagation was strongly dependent on k_o, with two principal failure planes developing in the soil mass at

the toe of slope and one failure plane developing in the backslope along the crest. The failure planes that developed due to LSR can be described as follows:

- *Horizontal Failure Plane, H_H, at the toe of the slope*. The first failure plane, or crack, was attributed to differential strain-induced movement and extended in a general horizontal direction into the backslope at the base of the excavation. This result was consistent with the principles of fracture mechanics for shear stress controlled failure in which the failure plane propagated along the pre-existing horizontal failure plane. The length of this crack was dependent on the coefficient of earth pressure at rest (k_o); the greater the k_o, the longer the horizontal crack extended into the backslope.

- *Inclined Failure Plane, H_I, at the toe of the slope*. The second failure plane was attributed to shear-induced changes created by LSR and extended in an upward angle from the toe of slope. This result was consistent with the general principles of fracture mechanics, although the crack propagation angle was not in strict conformance. The angle of the critical failure plane was also strongly dependent on k_o and the angle became steeper with an increasing initial k_o. The crack did not propagate along a constant angle, rather it generally became flatter as it progressed into the backslope.

- *Tension Crack, H_T, at the top of the slope.* The final failure plane developed as a result of LSR which created a tension zone in the backslope that could initiate tension cracking. Tension crack propagation adhered to the principles of fracture mechanics which indicates that the cracks would tend to propagate vertically and normal to the gravity induced tensile stress.

3. FEM analyses indicated a strong relationship between overall slope stability and the initial k_o value. The horizontal, inclined and tension cracks propagated simultaneously due to stress concentrations. A toe failure tended to develop that resulted in a wedge of material falling away from the slope due to negative vertical as well as lateral stress conditions. The toe failure tended to reduce propagation of the inclined crack, however, the tensile cracking continued to advance as the material "unzipped" itself. Tensile crack propagation generally occurred at a greater rate than angle crack propagation and ultimate slope failure was attributed to a sudden propagation of the angle crack that extended to the tension crack.

4. Conventional limit equilibrium methods of slope stability analysis for unsupported vertical cuts do not consider the impact of LSR. Although this condition was found to be appropriate for vertical slopes when k_o = 1.0, research presented herein suggested that LSR can create tension and toe cracks that lead to the eventual slope failure for k_o > 1.0. A modified Stability Factor (N_s) was developed to account for the impact that LSR has on the stability of slopes with vertical as well as for the ones with inclined faces.

This concludes this research on the investigation of LSR on the stability of $\phi = 0°$ slopes using laboratory, fracture mechanics, and finite element method approaches.

APPENDIX A

DERIVATION OF STABILITY NUMBER

Appendix A presents the derivation of the stability number to determine the critical height of a vertical slope (Taylor, 1937). Recall that Equation 1-42 was expressed as follows:

$$H = \frac{c}{\gamma}\left(\frac{\left(\frac{\theta\left(\pi/180\right)}{2\sin^2\theta\sin^2\alpha} \right)}{\left(\frac{\cos(90+\theta-\alpha)}{4\sin\theta\sin\alpha\tan\alpha} + \frac{1}{6\tan^2\alpha} + \frac{1}{12\sin^2\alpha} \right)} \right) \qquad \text{A-1}$$

Equation A-1 may be represented as:

$$H = \left(\frac{c}{\gamma} \right) f(\alpha,\theta) \qquad \text{A-2}$$

The critical height is determined by differentiating Equation A-2 with respect to θ and α as follows:

$$\frac{d}{d\alpha} f(\alpha,\theta) = 0 \text{ and } \frac{d}{d\theta} f(\alpha,\theta) = 0 \qquad \text{A-3}$$

Begin by first differentiating $\frac{d}{d\alpha} f(\alpha,\theta)$, which may be expressed as follows:

$$\frac{dH}{d\alpha} = A - B \qquad \text{A-4}$$

where,

$$A = \frac{\pi(\theta)\left[\frac{\tan^2+1}{3\tan^3\alpha} + \frac{\cos\alpha}{6\sin^3\alpha} - \frac{\sin(90+\theta-\alpha)}{4\sin\alpha\sin\theta\tan\alpha} + \frac{\cos(90+\theta-\alpha)(\tan^2\alpha+1)}{4\sin\alpha\sin\theta\tan^2\alpha} + \frac{\cos(90+\theta-\alpha)\cos\alpha}{4\sin^2\alpha\sin\theta\tan\alpha} \right]}{360(\sin^2\alpha)(\sin^2\theta)\left(\frac{\cos(90+\theta-\alpha)}{4\sin\alpha\sin\theta\tan\alpha} + \frac{1}{6\tan^2\alpha} + \frac{1}{12\sin^2\alpha} \right)^2}$$

and

$$B = \frac{\pi(\theta)\cos\alpha}{180\sin^3\alpha\sin^2\theta\left(\frac{\cos(90+\theta-\alpha)}{4\sin\alpha\sin\theta\tan\alpha}+\frac{1}{6\tan^2\alpha}+\frac{1}{12\sin^2\alpha}\right)}$$

Next, differentiate $\frac{d}{d\theta}f(\alpha,\theta)$, which may also be expressed as follows:

$$\frac{dH}{d\theta} = C + D - E \qquad \text{A-5}$$

where,

$$C = \frac{\pi}{360\sin^2\alpha\sin^2\theta\left(\frac{\cos(90+\theta-\alpha)}{4\sin\alpha\sin\theta\tan\alpha}+\frac{1}{6\tan^2\alpha}+\frac{1}{12\sin^2\alpha}\right)}$$

$$D = \frac{\pi(\theta)\left(\frac{\sin(90+\theta-\alpha)}{4\sin\alpha\sin\theta\tan\alpha}+\frac{\cos(90+\theta-\alpha)\cos\theta}{4\sin\alpha\sin^2\theta\tan\alpha}\right)}{360\sin^2\alpha\sin^2\theta\left(\frac{\cos(90+\theta-\alpha)}{4\sin\alpha\sin\theta\tan\alpha}+\frac{1}{6\tan^2\alpha}+\frac{1}{12\sin^2\alpha}\right)^2}$$

$$E = \frac{\pi(\theta)\cos\theta}{180\sin^2\alpha\sin^3\theta\left(\frac{\cos(90+\theta-\alpha)}{4\sin\alpha\sin\theta\tan\alpha}+\frac{1}{6\tan^2\alpha}+\frac{1}{12\sin^2\alpha}\right)}$$

Equation A-4 and A-5 must both equal zero and these equations are more readily solved using graphical methods. The solution to Equation A-4 and A-5 results in $\alpha = 47.6°$ and $\theta = 15.1°$, as noted in Figure A.1 (Taylor, 1937).

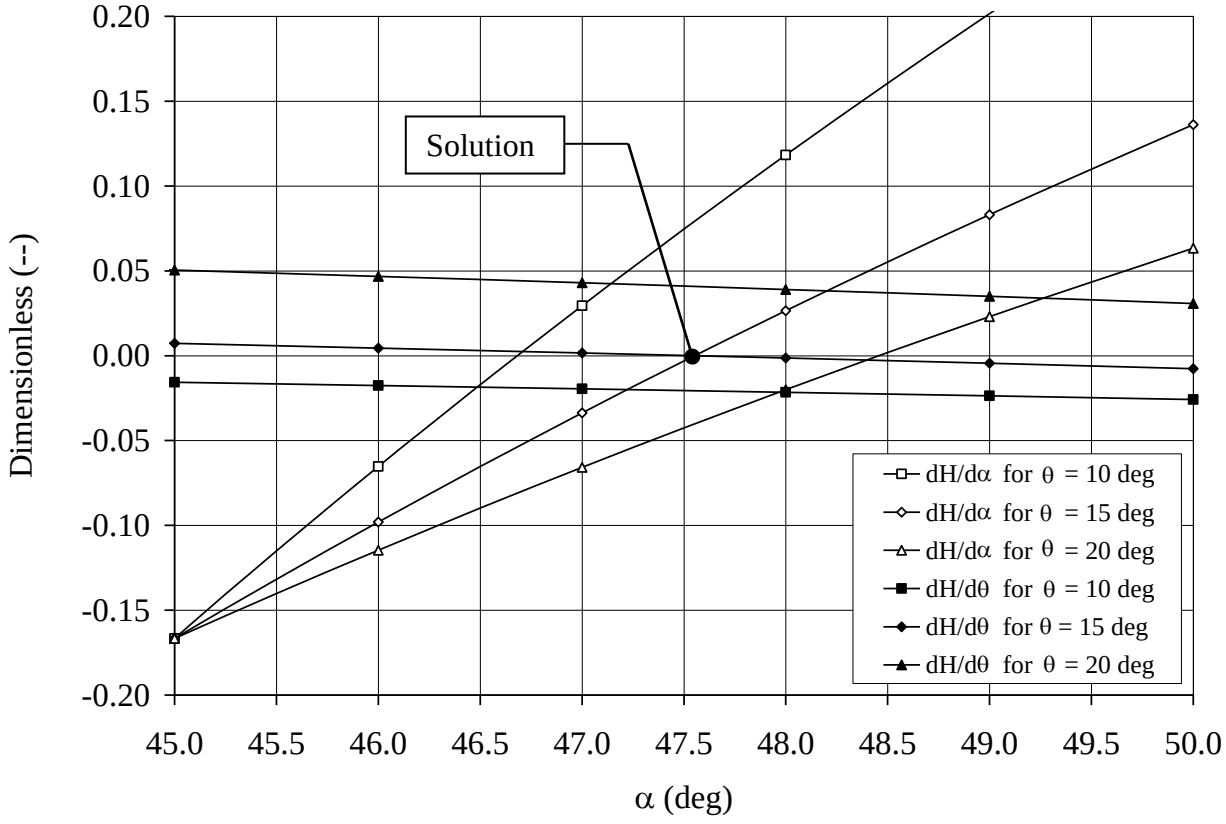

Figure A.1. Graphical Solution to $\frac{d}{d\alpha} f(\alpha,\theta)$ and $\frac{d}{d\theta} f(\alpha,\theta)$

APPENDIX B

FINITE ELEMENT MESH OPTIMIZATION

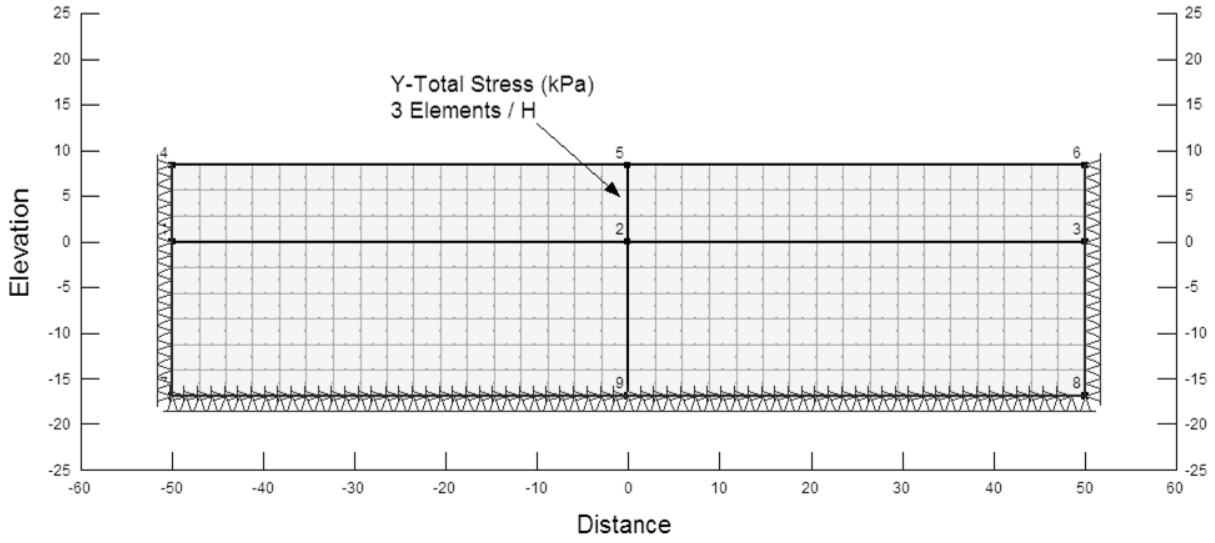

Figure B.1. Typical FEM Before Excavation.

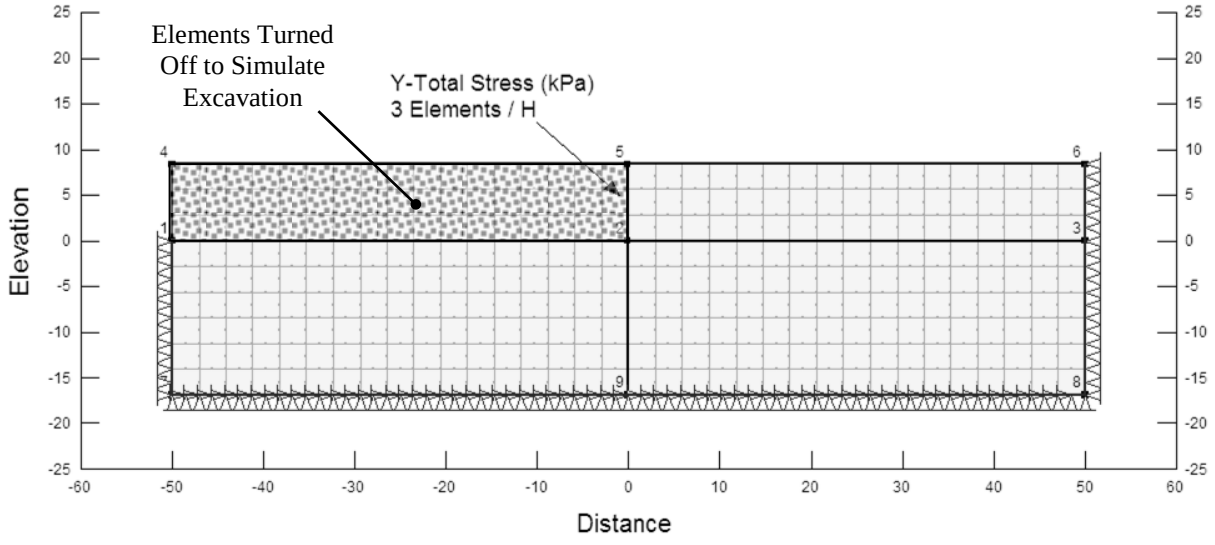

Figure B.2. Typical FEM After Excavation.

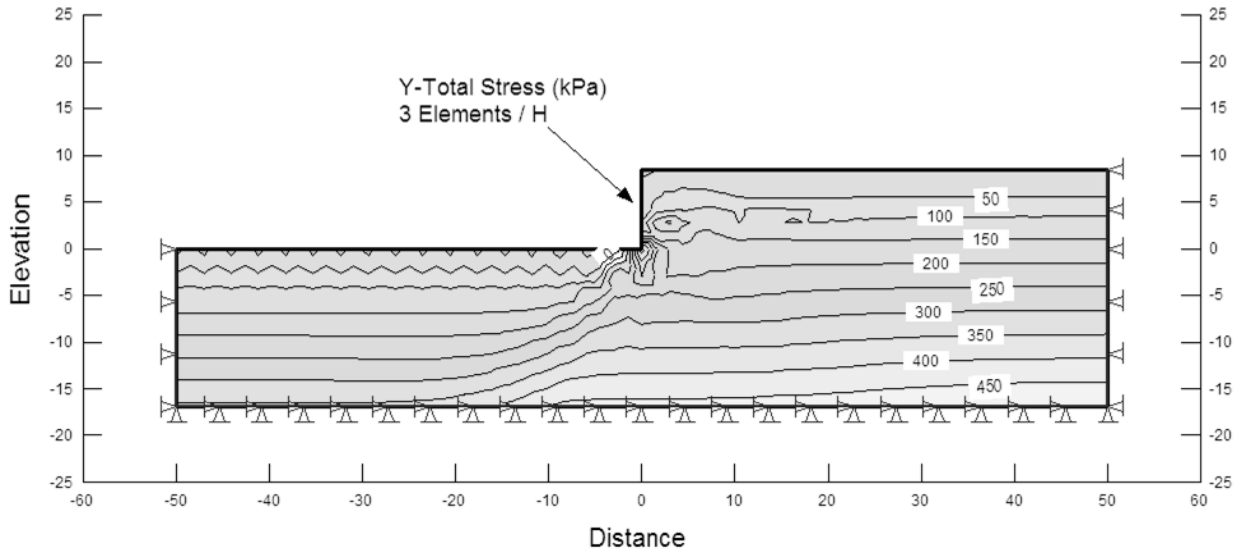

Figure B.3. Vertical stress contours using three, eight-node quadrilateral elements over the slope height.

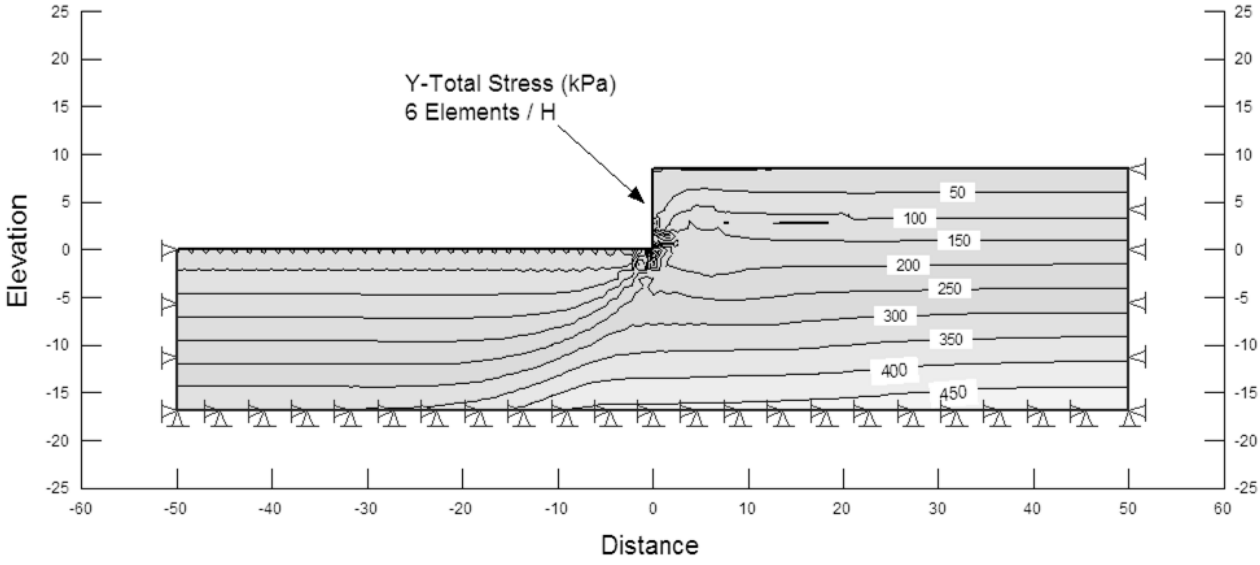

Figure B.4. Vertical stress contours using six, eight-node quadrilateral elements over the slope height.

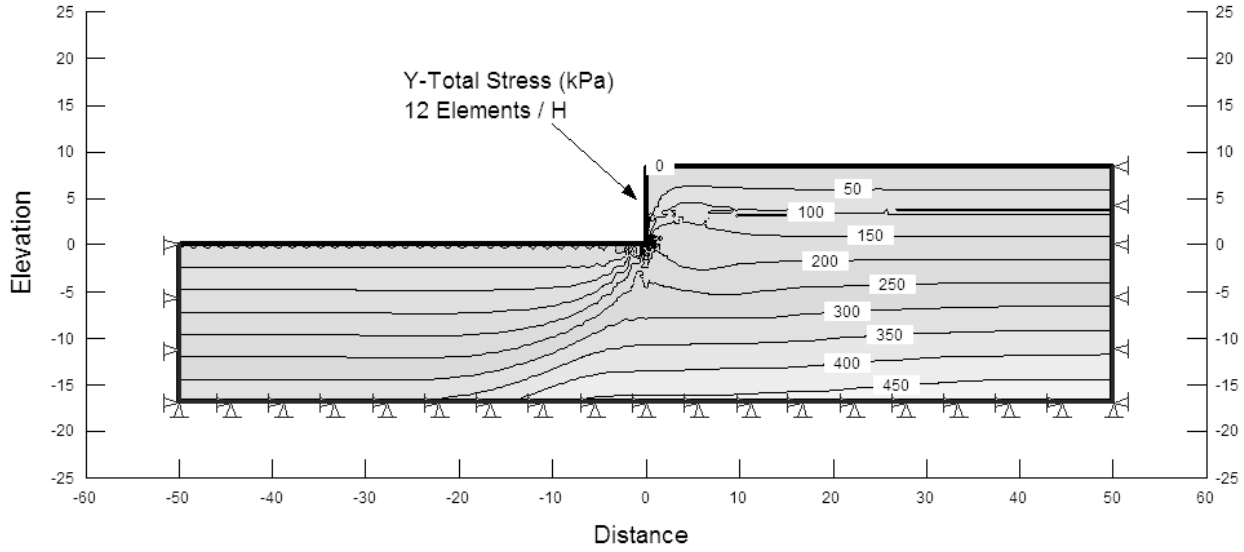

Figure B.5. Vertical stress contours using twelve, eight-node quadrilateral elements over the slope height.

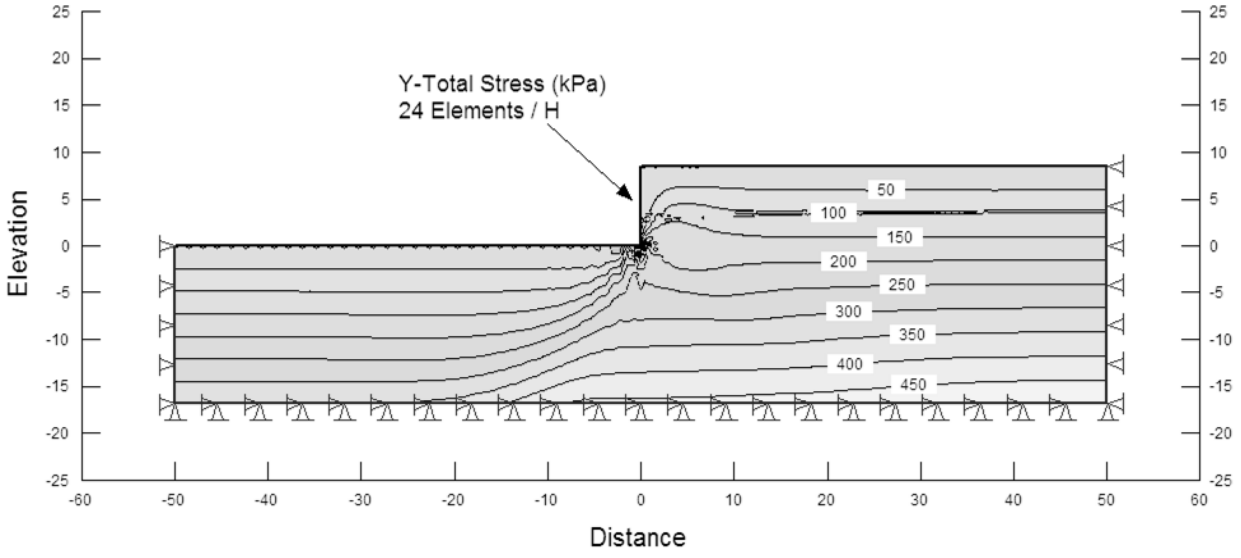

Figure B.6. Vertical stress contours using twenty-four, eight-node quadrilateral elements over the slope height.

APPENDIX C

CLAYEY SAND ON CLAY SHEAR MODEL MOHR-COULOMB GRAPHS

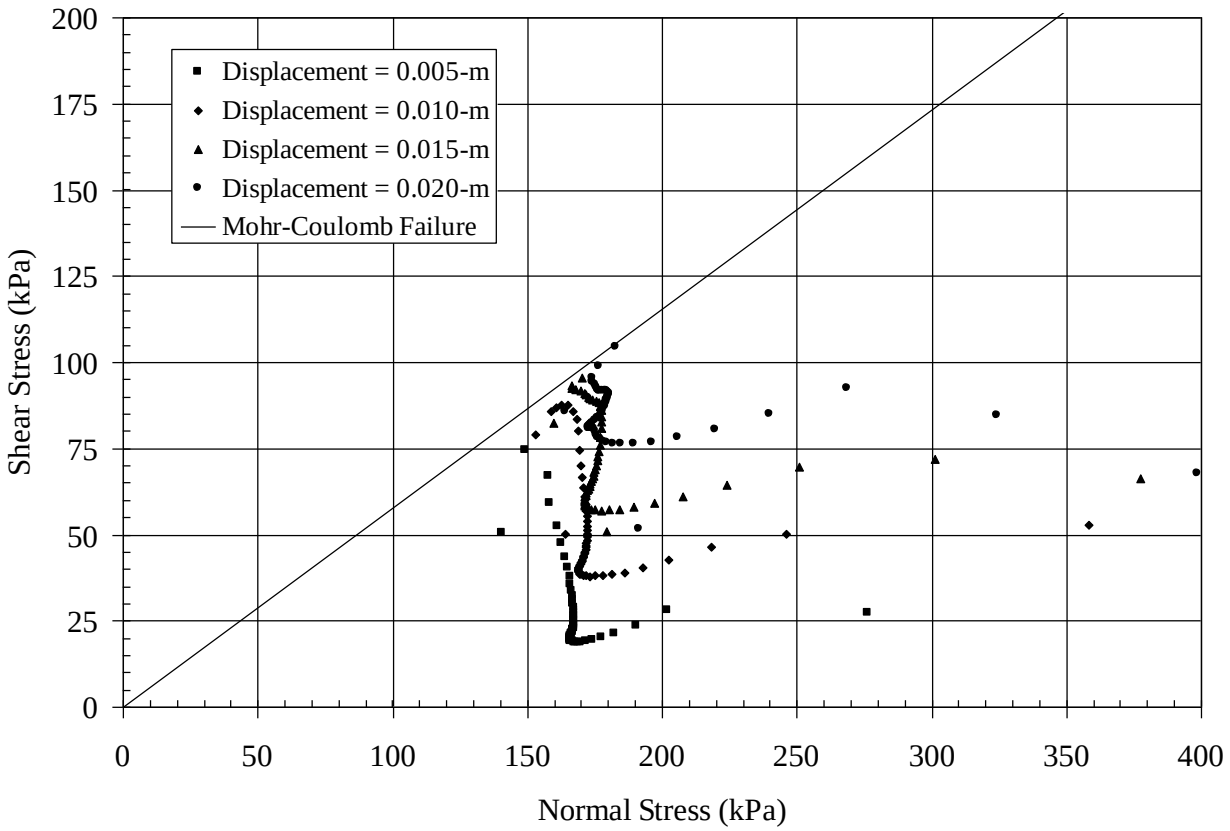

Figure C.1. FEM Shear and Normal Stresses for the Clayey Sand Layer Obtained Directly above the Clayey Sand-Clay Interface with $\nu = 0.10$ for the Clay with No Slip Element Strength Reduction.

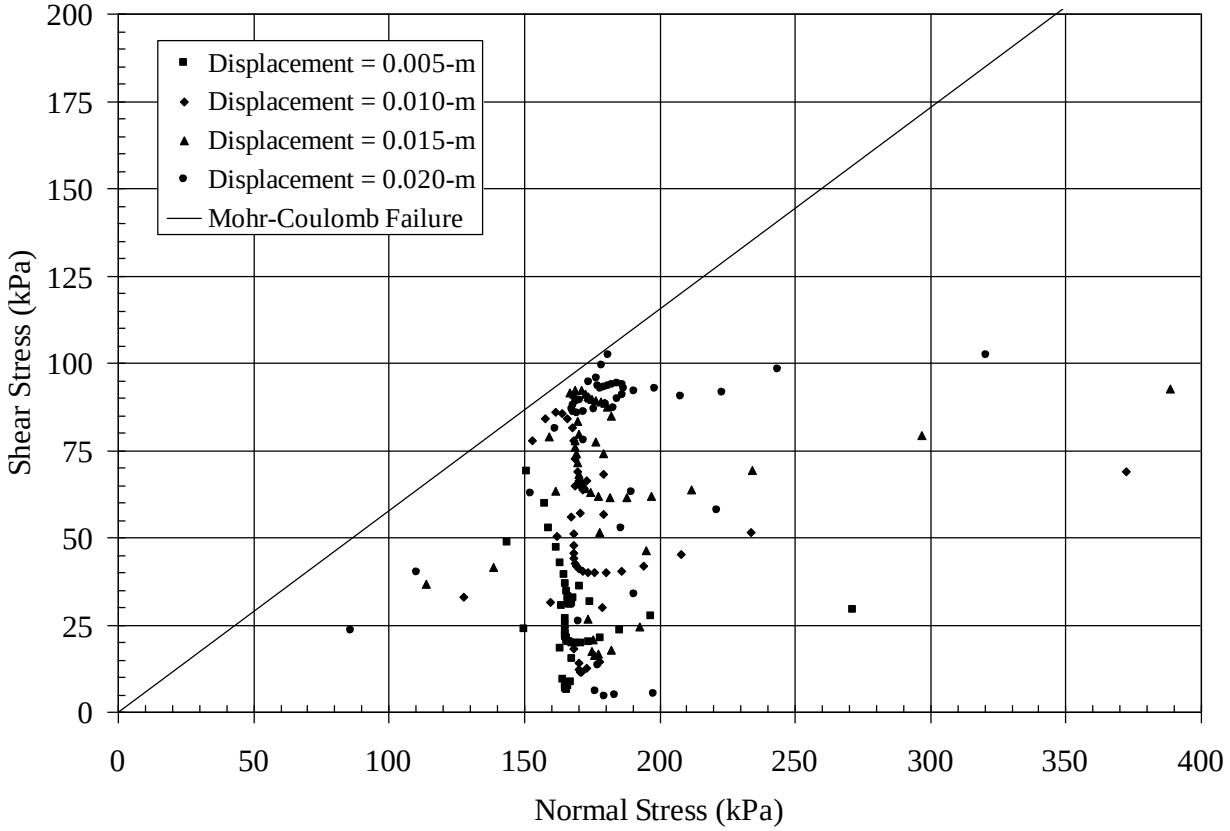

Figure C.2. FEM Shear and Normal Stresses for the Clayey Sand Layer Obtained Directly above the Clayey Sand-Clay Interface with $\nu = 0.10$ for the Clay and 25% Slip Element Strength Reduction.

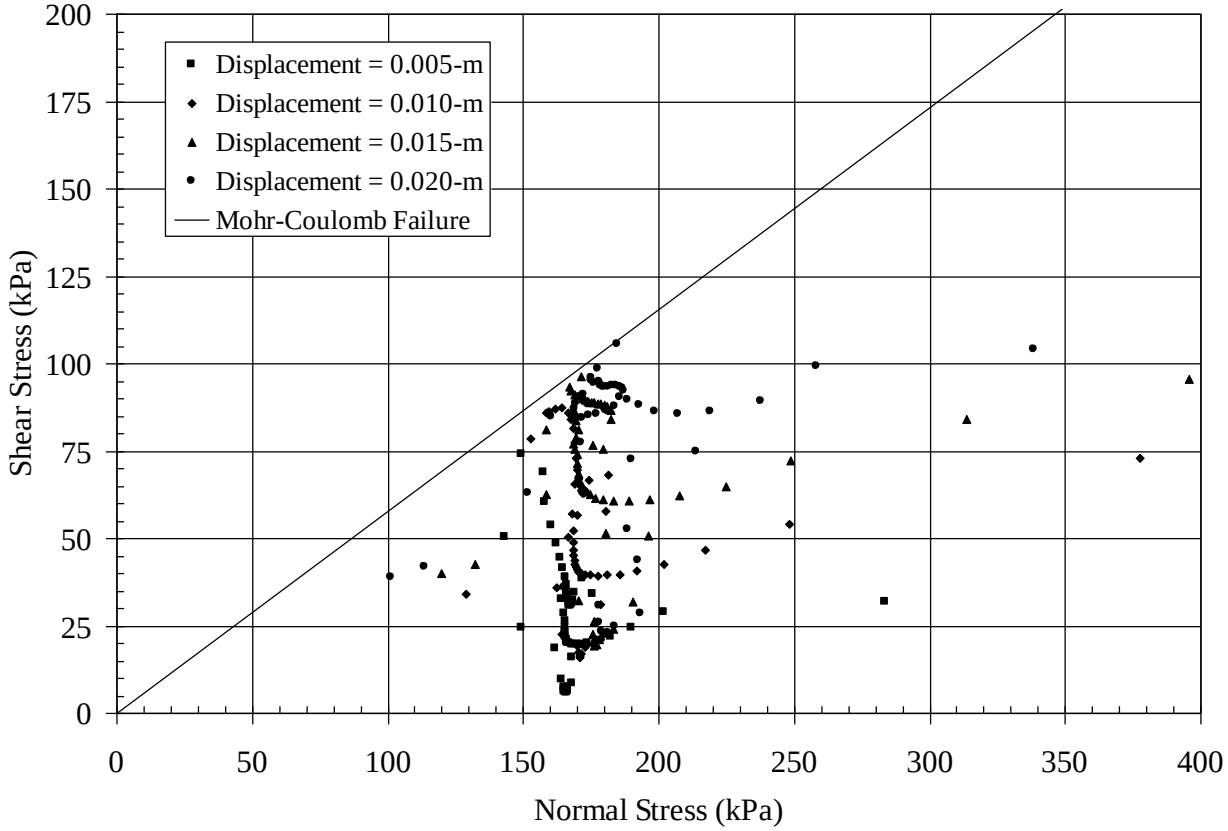

Figure C.3. FEM Shear and Normal Stresses for the Clayey Sand Layer Obtained Directly above the Clayey Sand-Clay Interface with $\nu = 0.10$ for the Clay and 50% Slip Element Strength Reduction.

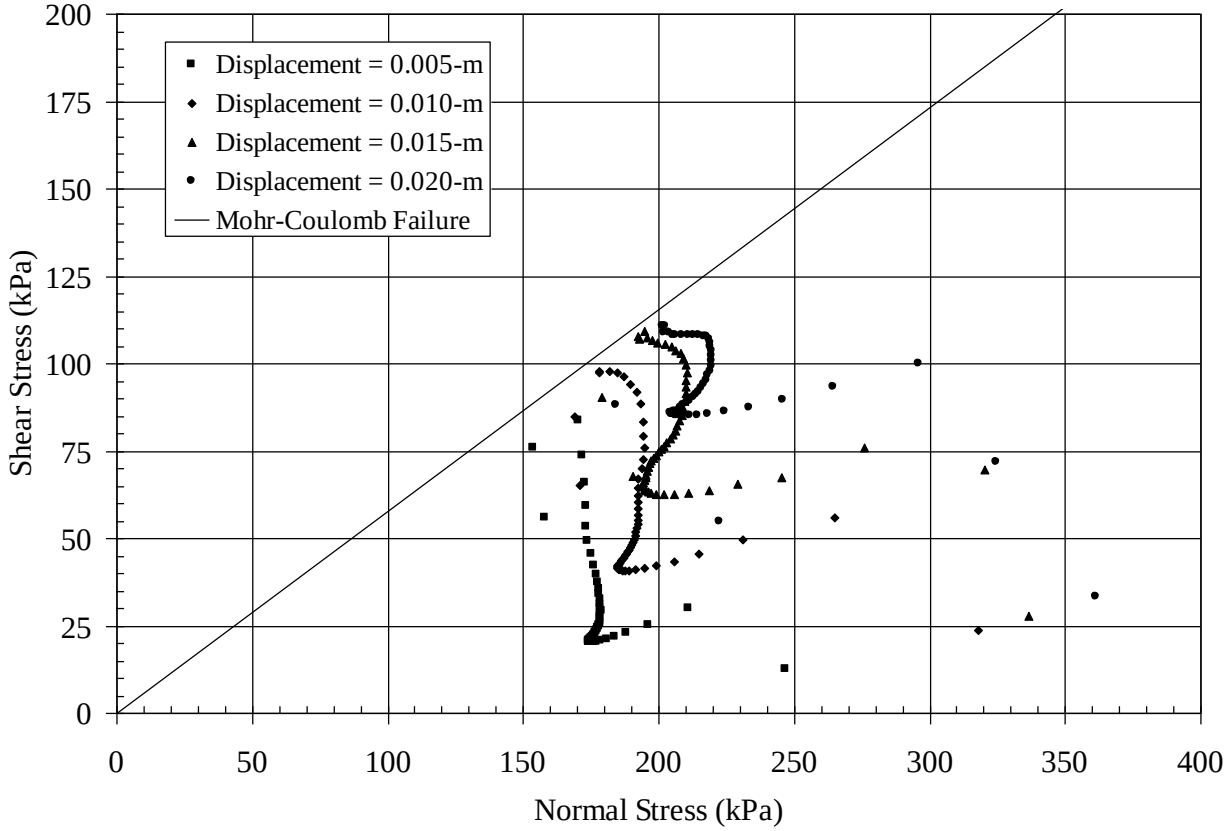

Figure C.4. FEM Shear and Normal Stresses for the Clayey Sand Layer Obtained Directly above the Clayey Sand-Clay Interface with $\nu = 0.45$ for the Clay with No Slip Element Strength Reduction.

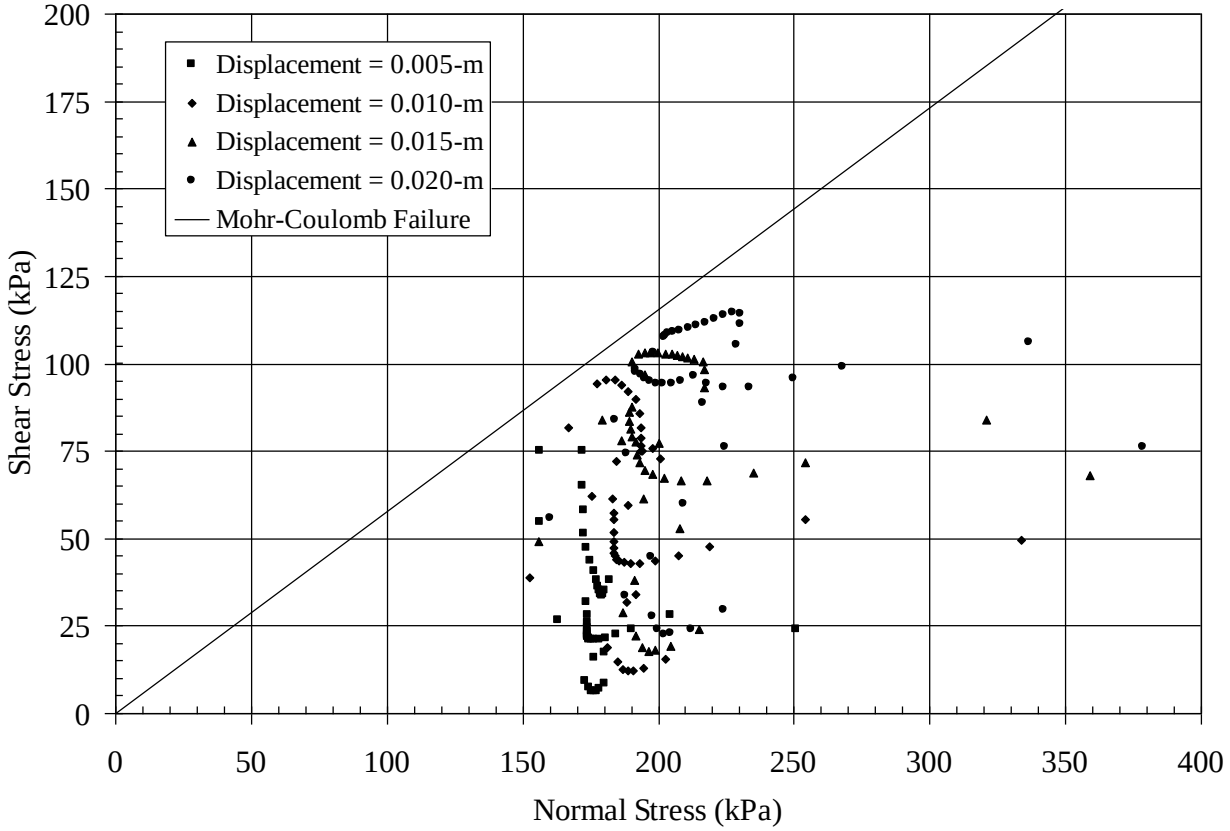

Figure C.5. FEM Shear and Normal Stresses for the Clayey Sand Layer Obtained Directly above the Clayey Sand-Clay Interface with $\nu = 0.45$ for the Clay and 25% Slip Element Strength Reduction.

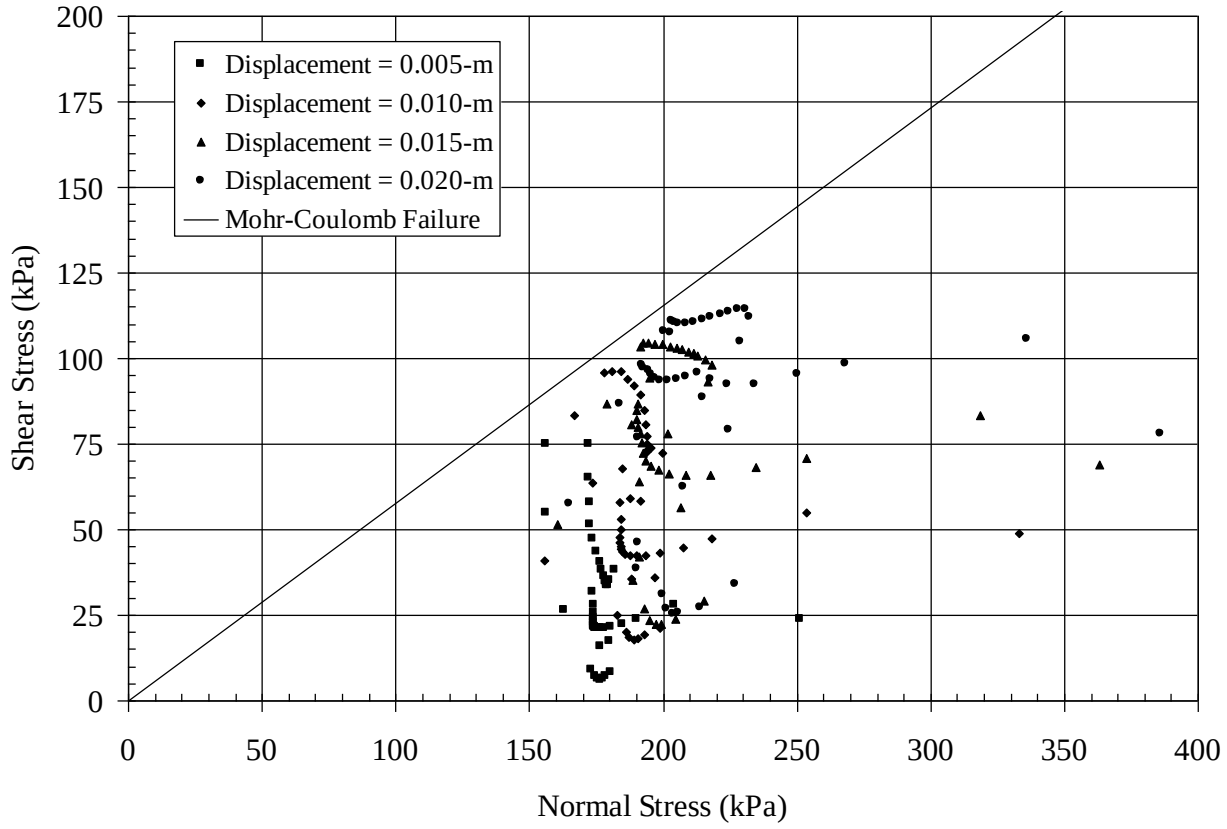

Figure C.6. FEM Shear and Normal Stresses for the Clayey Sand Layer Obtained Directly above the Clayey Sand-Clay Interface with $\nu = 0.45$ for the Clay and 50% Slip Element Strength Reduction.

APPENDIX D

FEM MODELS FOR EVALUATION OF $\phi = 0°$ SLOPES

Vertical Slope FEM Model for k_o = 3.0

Deformation Mesh Displayed at 10X Magnification

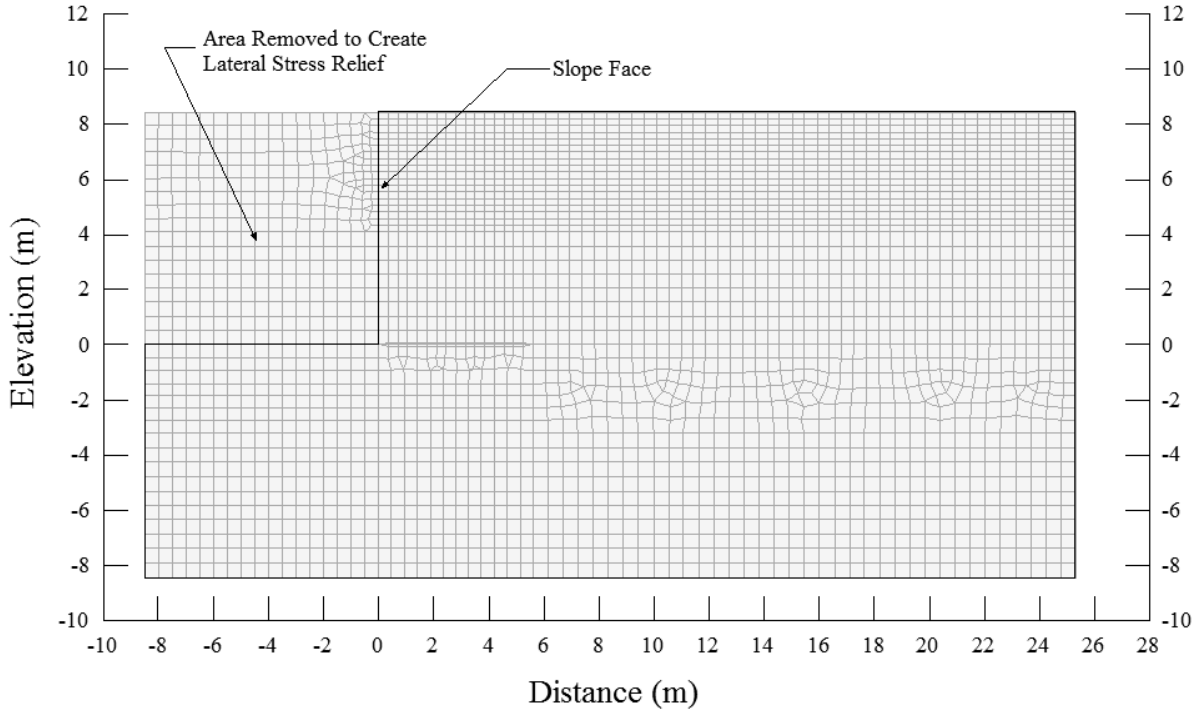

Figure D.1. Initial FEM Model for k_o = 3.0.

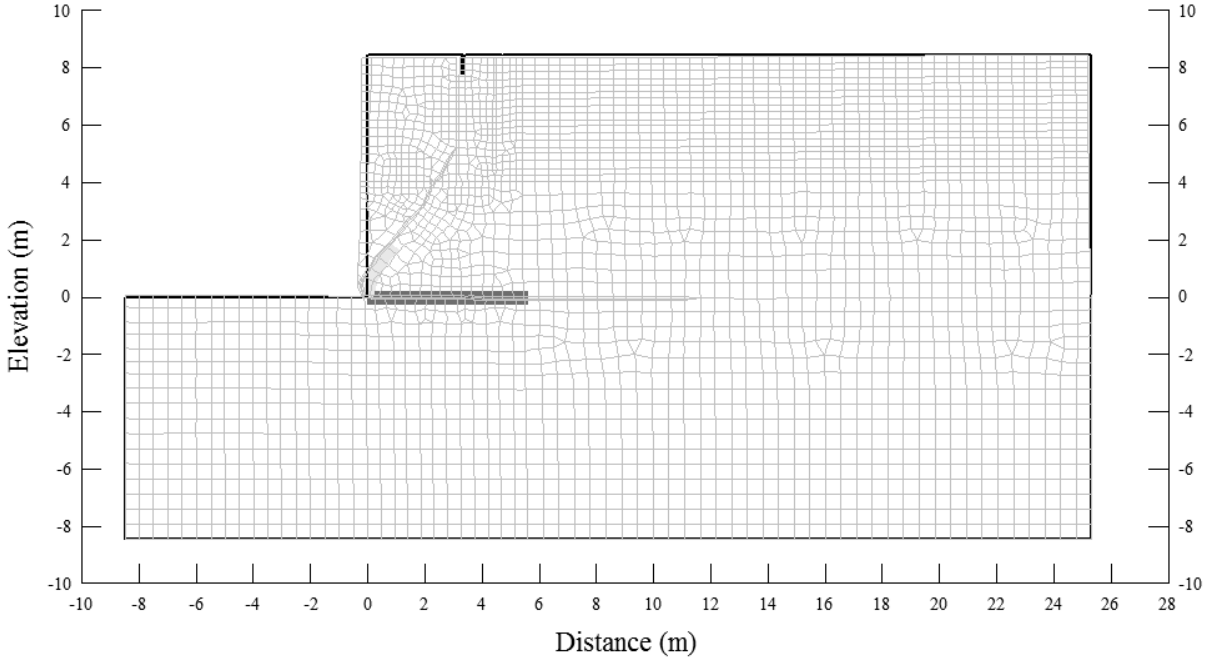

Figure D.2. FEM Model with Onset of Base, Inclined and Tension Cracking due to LSR.

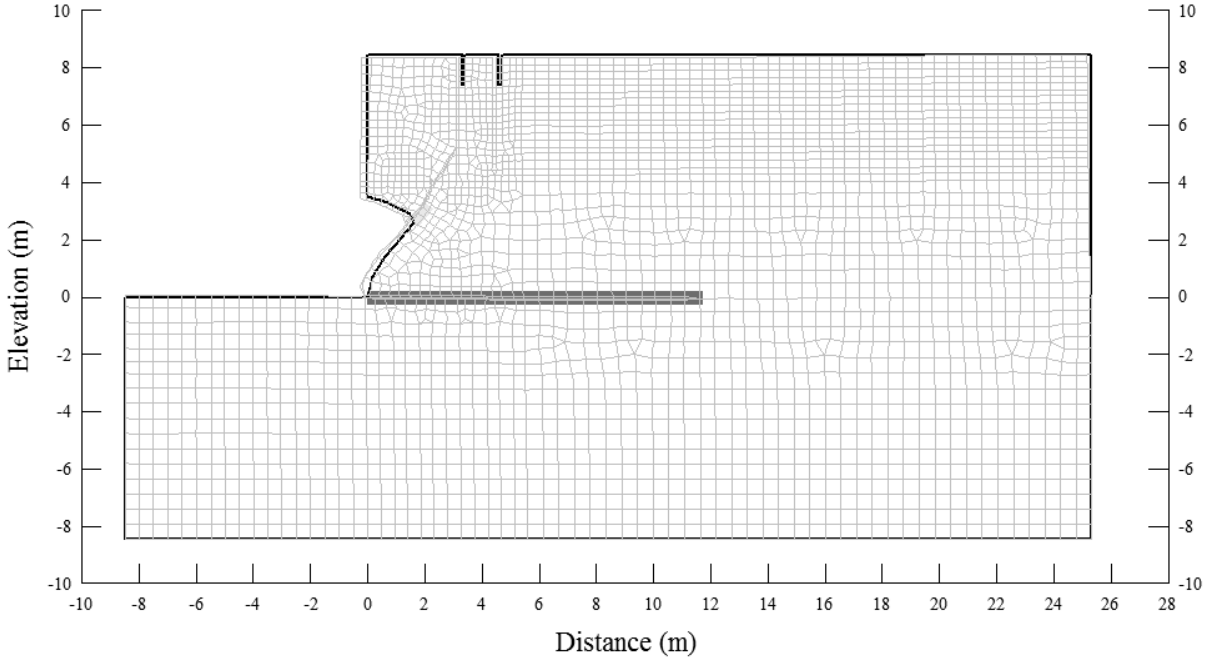

Figure D.3. FEM Model with Propagation of Base, Inclined and Tension Cracking. Inclined Cracking Resulted in Toe Failure and Loss of Material Due to Negative Stresses.

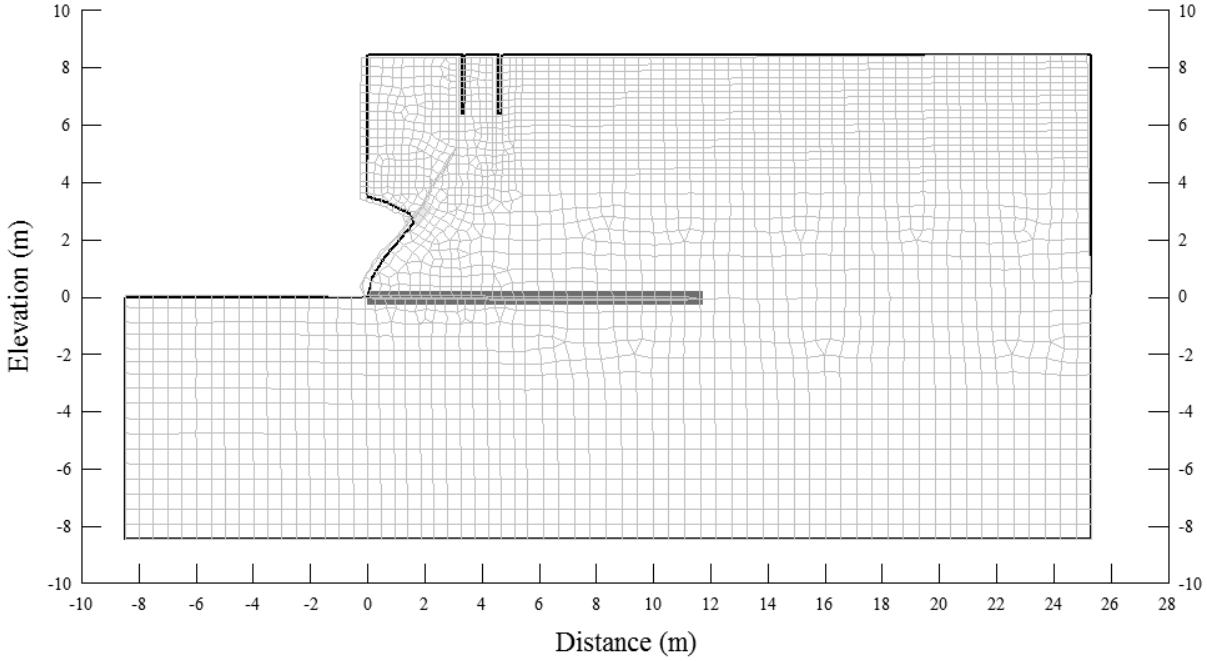

Figure D.4. FEM Model with Continued Propagation of Inclined and Tension Cracking.

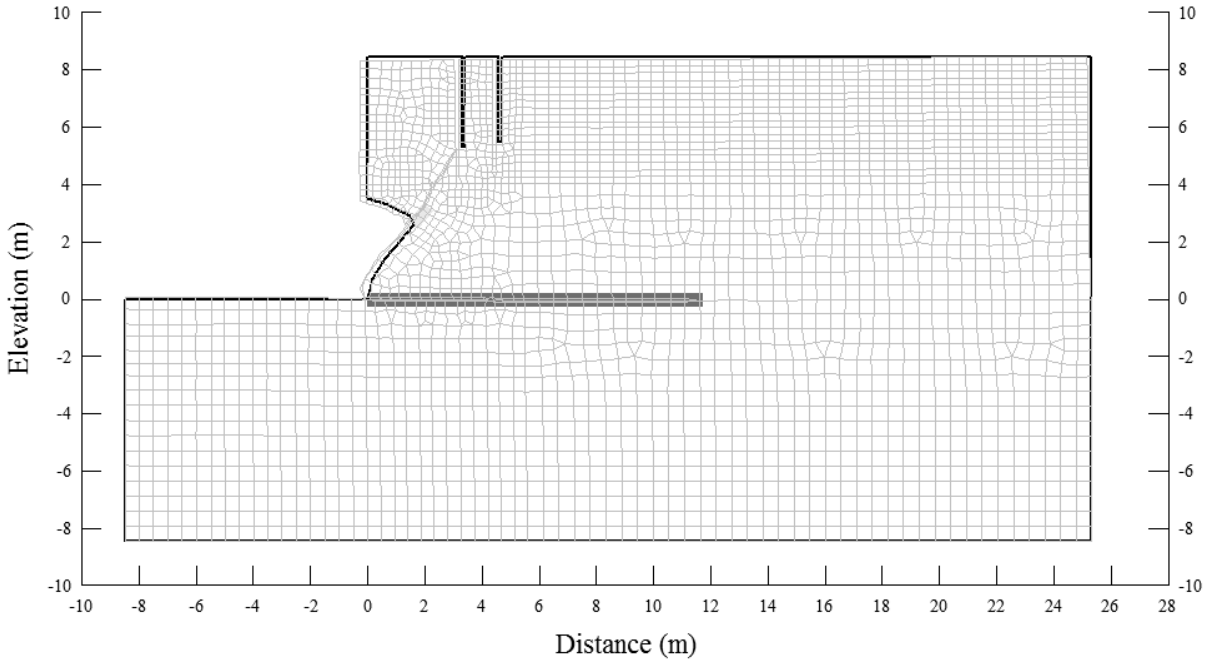

Figure D.5. FEM Model with Continued Propagation of Inclined and Tension Cracking.

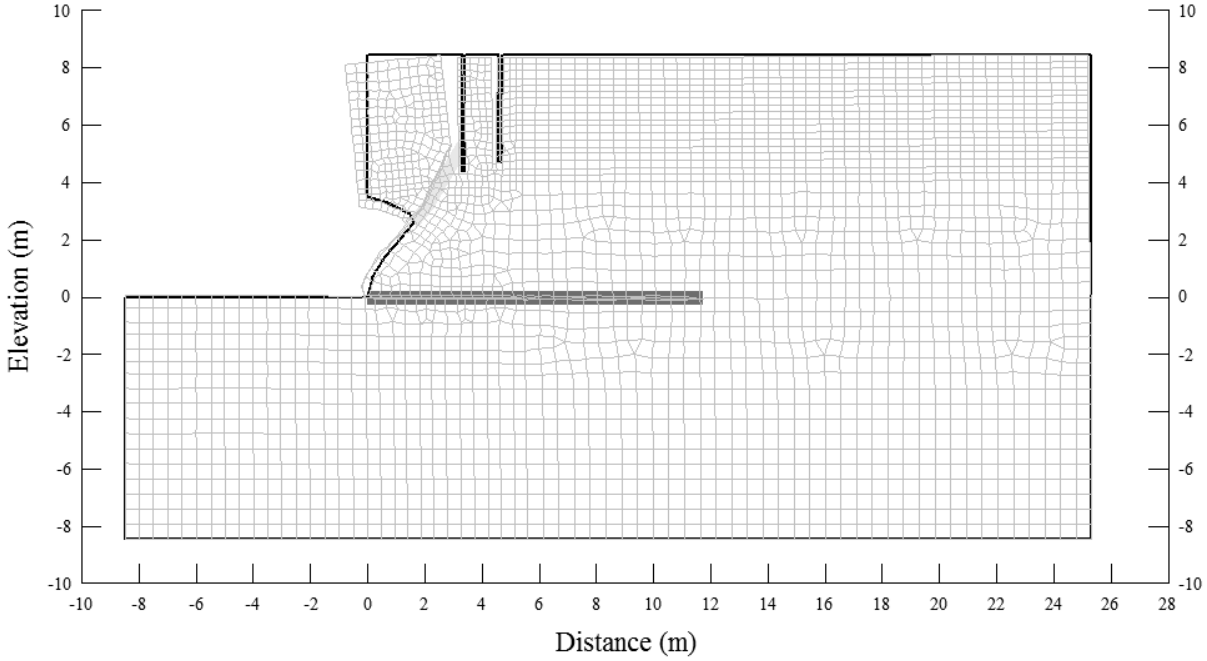

Figure D.6. FEM Model with Continued Propagation of Inclined and Tension Cracking Resulting in Overall Slope Failure.

Vertical Slope FEM Model for k_o = 2.0

Deformation Mesh Displayed at 20X Magnification

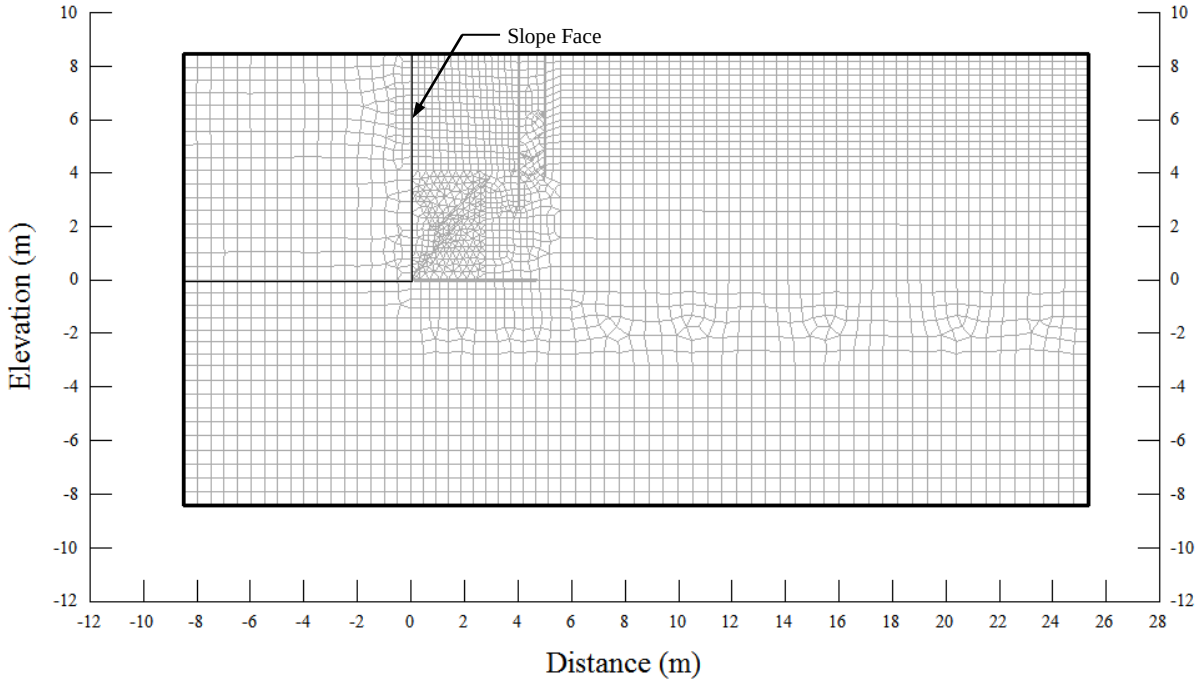

Figure D.7. Initial FEM Model for k_o = 2.0.

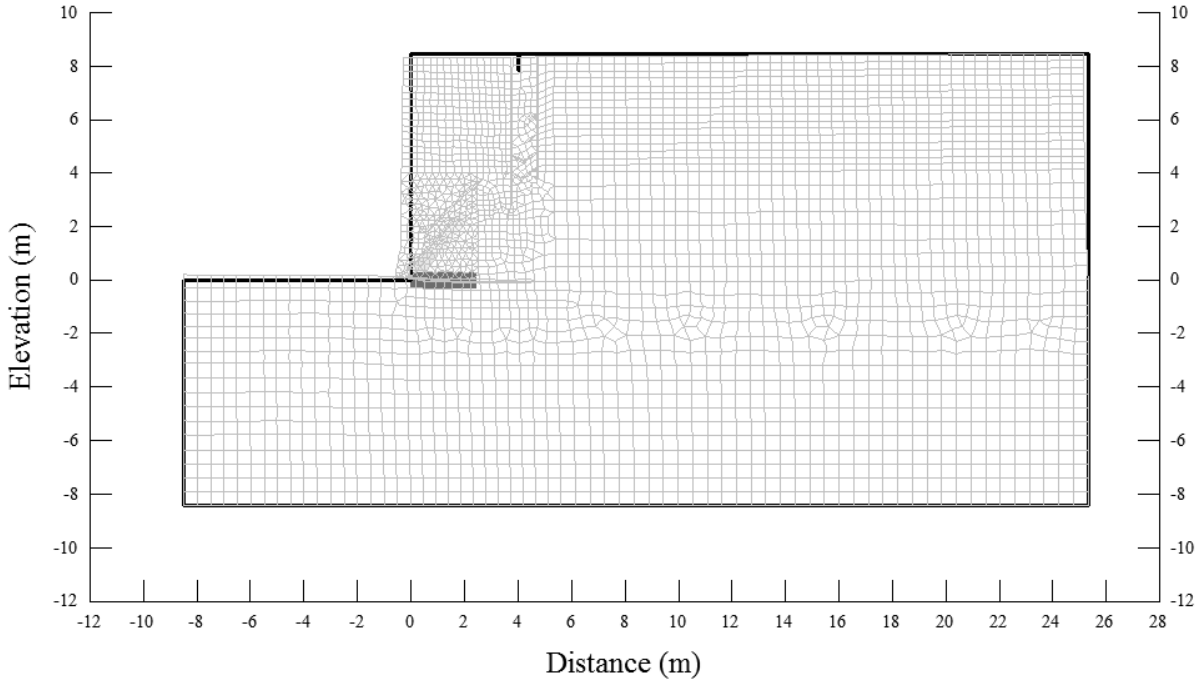

Figure D.8. FEM Model with Onset of Base, Inclined and Tension Cracking due to LSR.

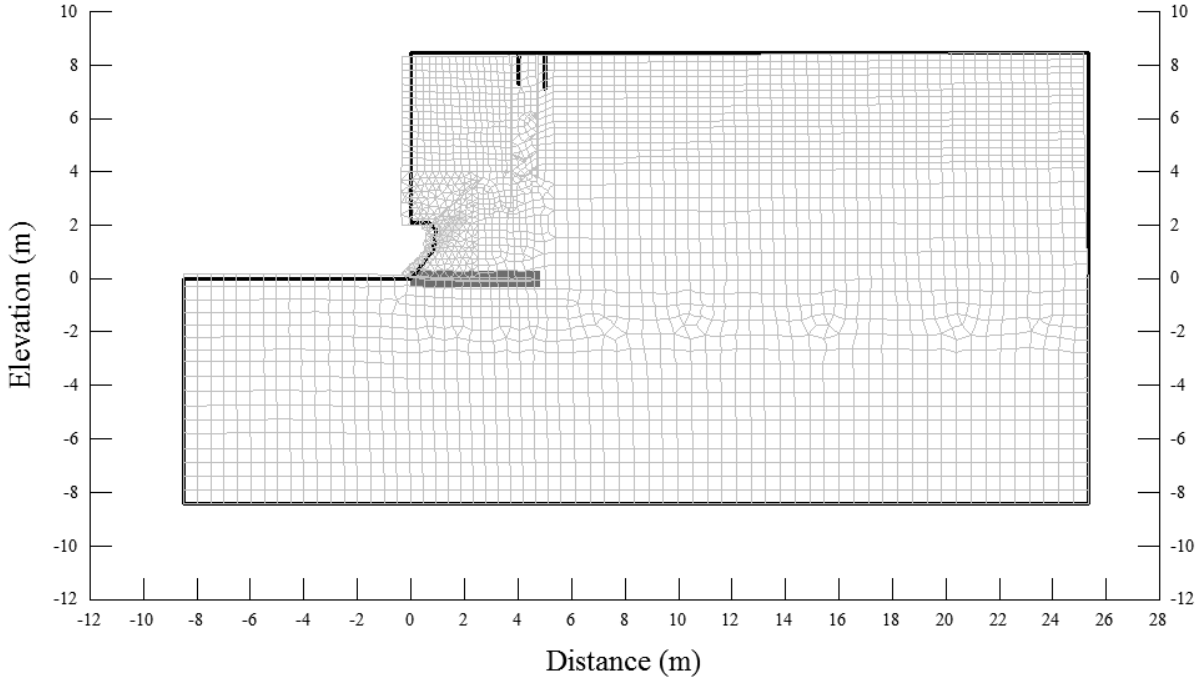

Figure D.9. FEM Model with Propagation of Base, Inclined and Tension Cracking. Inclined Cracking Resulted in Toe Failure and Loss of Material Due to Negative Stresses.

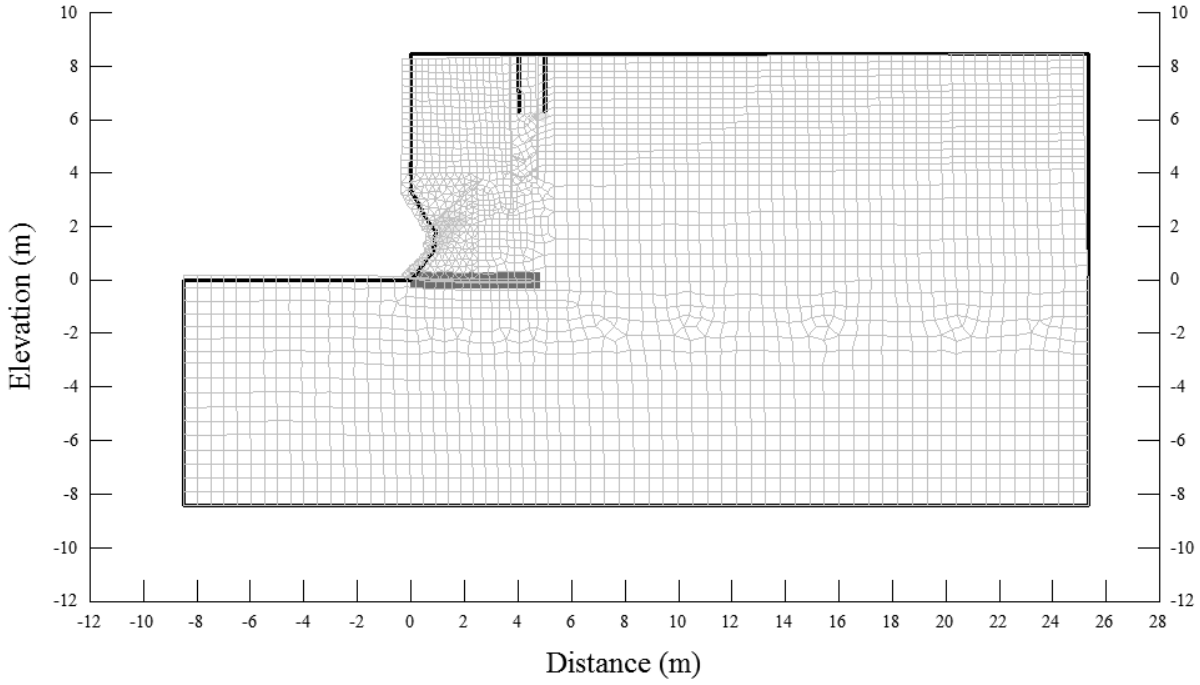

Figure D.10. FEM Model with Continued Propagation of Inclined and Tension Cracking. Inclined Cracking Resulted in Continued Loss of Material at the Toe Due to Negative Stresses.

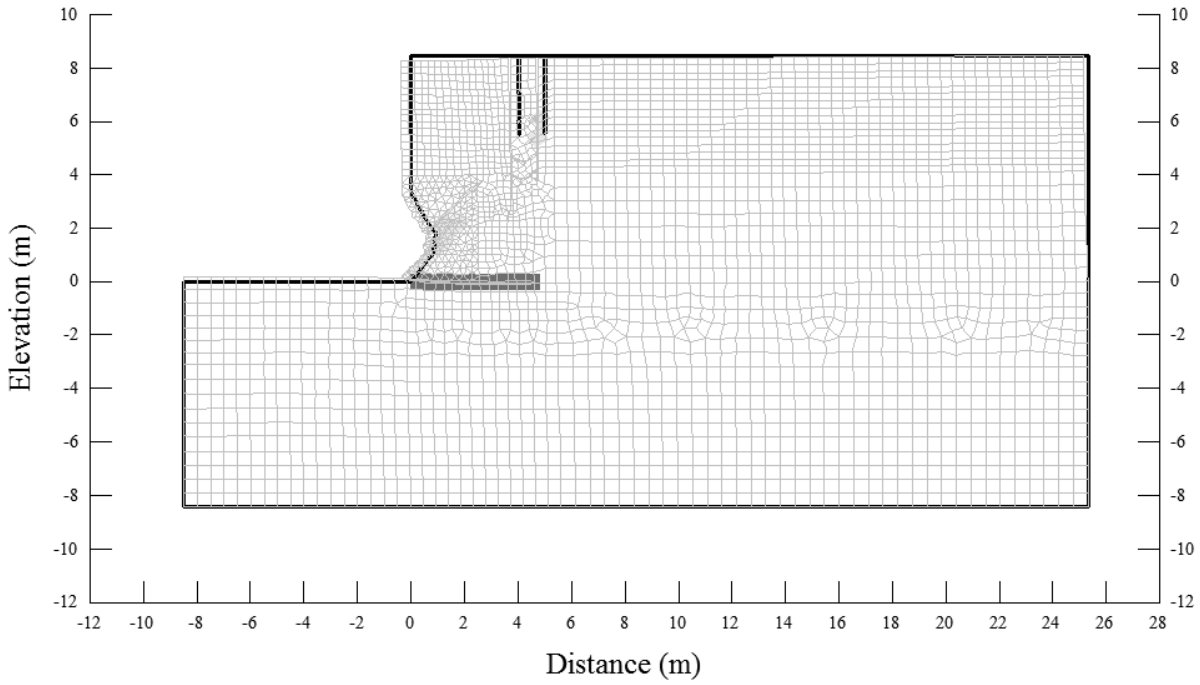

Figure D.11. FEM Model with Continued Propagation of Inclined and Tension Cracking.

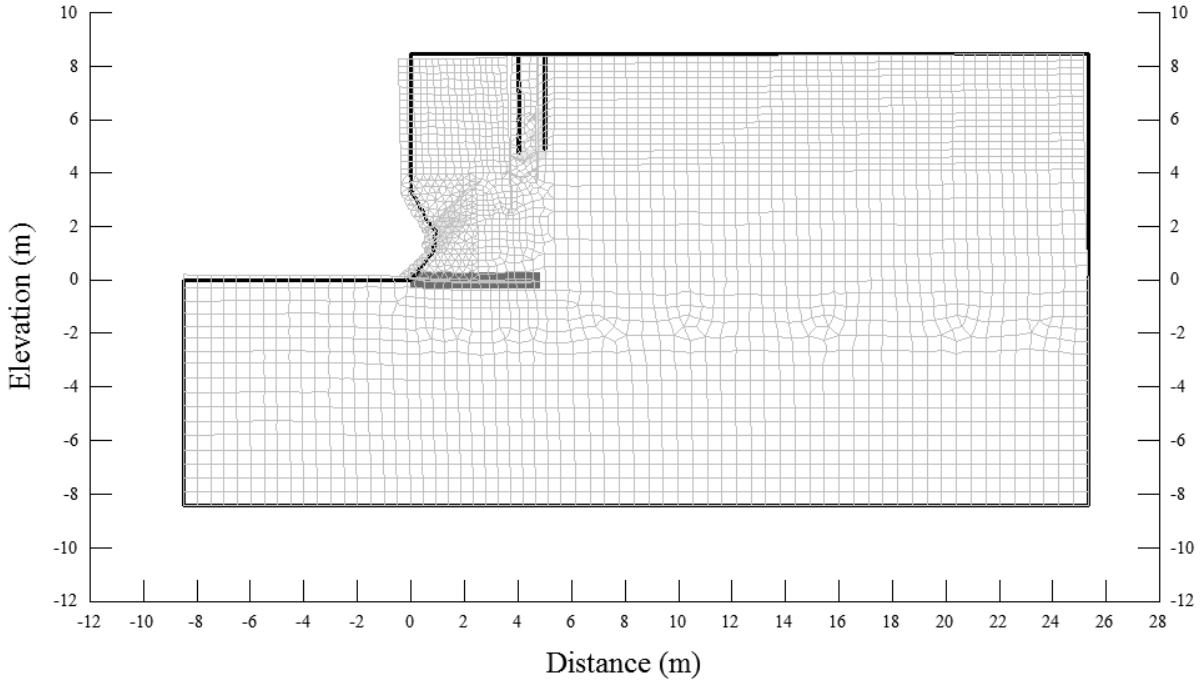

Figure D.12. FEM Model with Continued Propagation of Inclined and Tension Cracking.

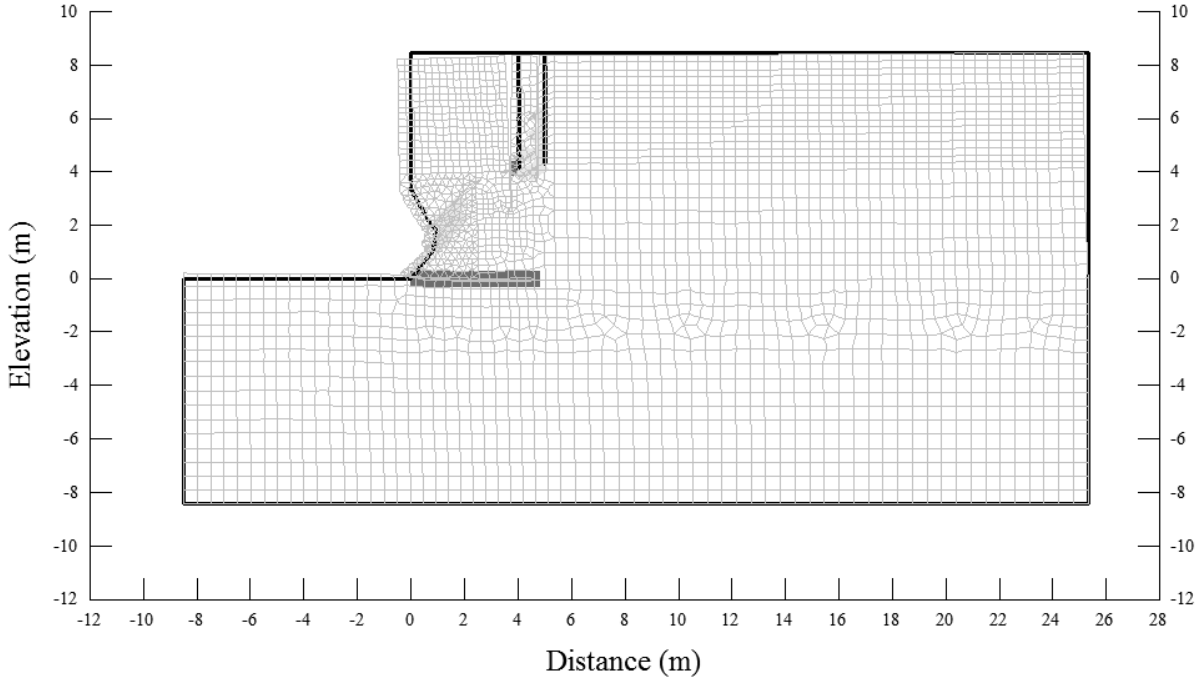

Figure D.13. FEM Model with Continued Propagation of Inclined and Tension Cracking.

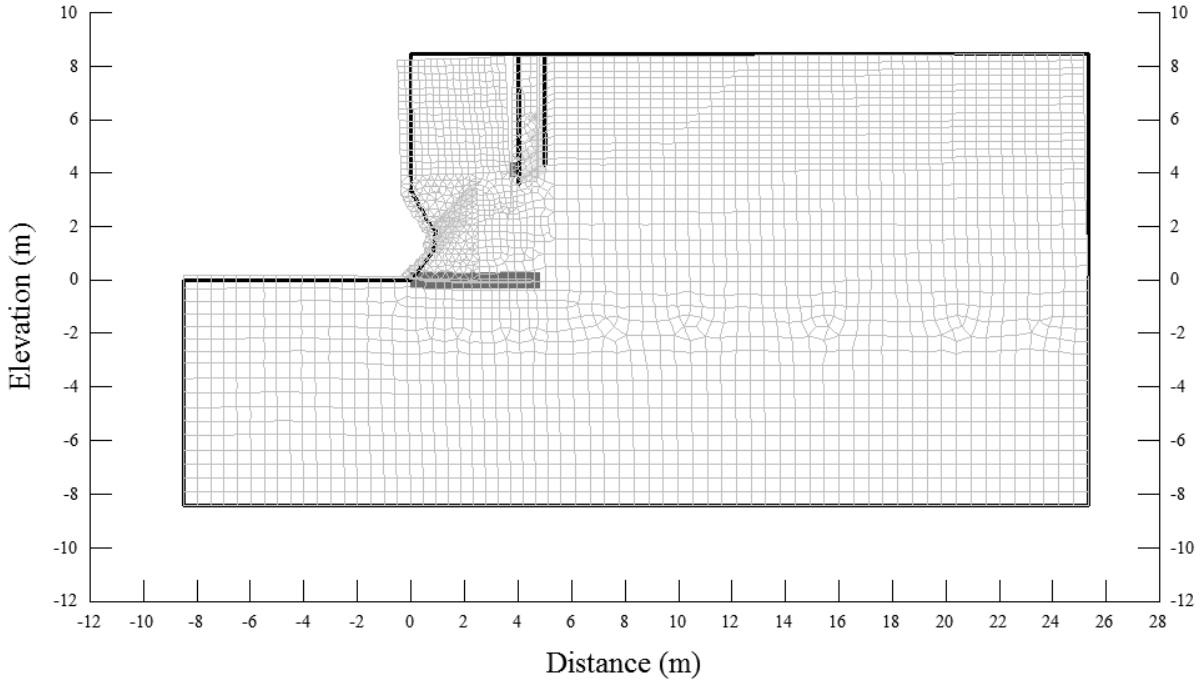

Figure D.14. FEM Model with Continued Propagation of Inclined and Tension Cracking.

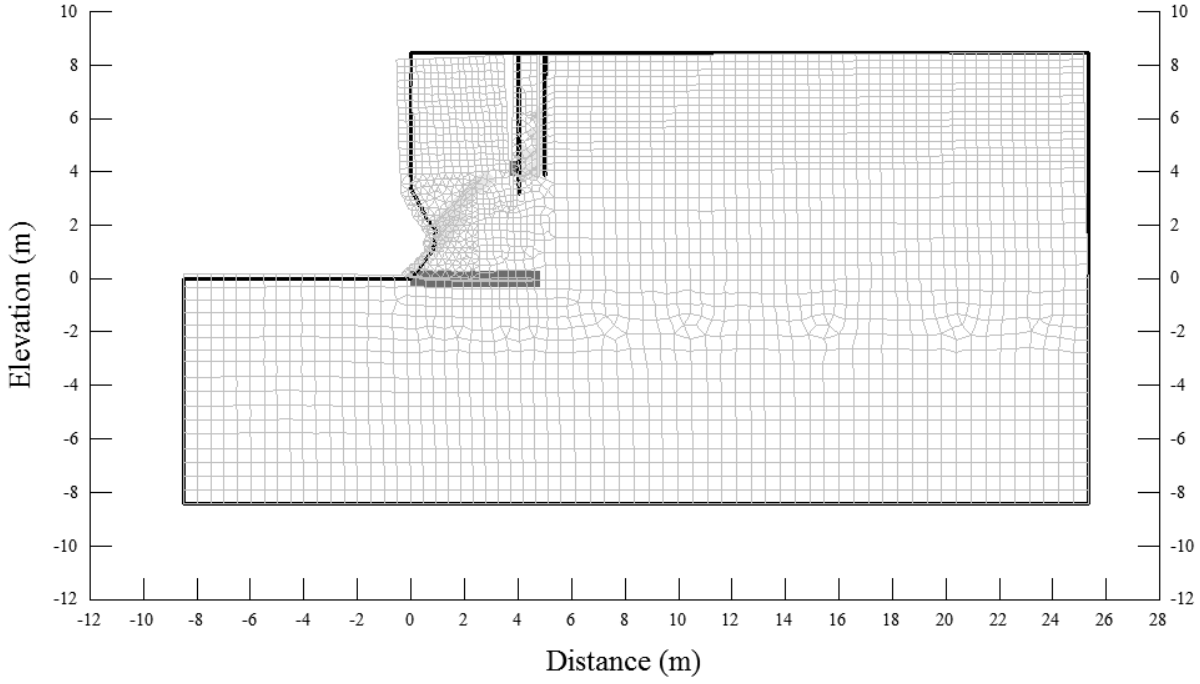

Figure D.15. FEM Model with Continued Propagation of Inclined and Tension Cracking.

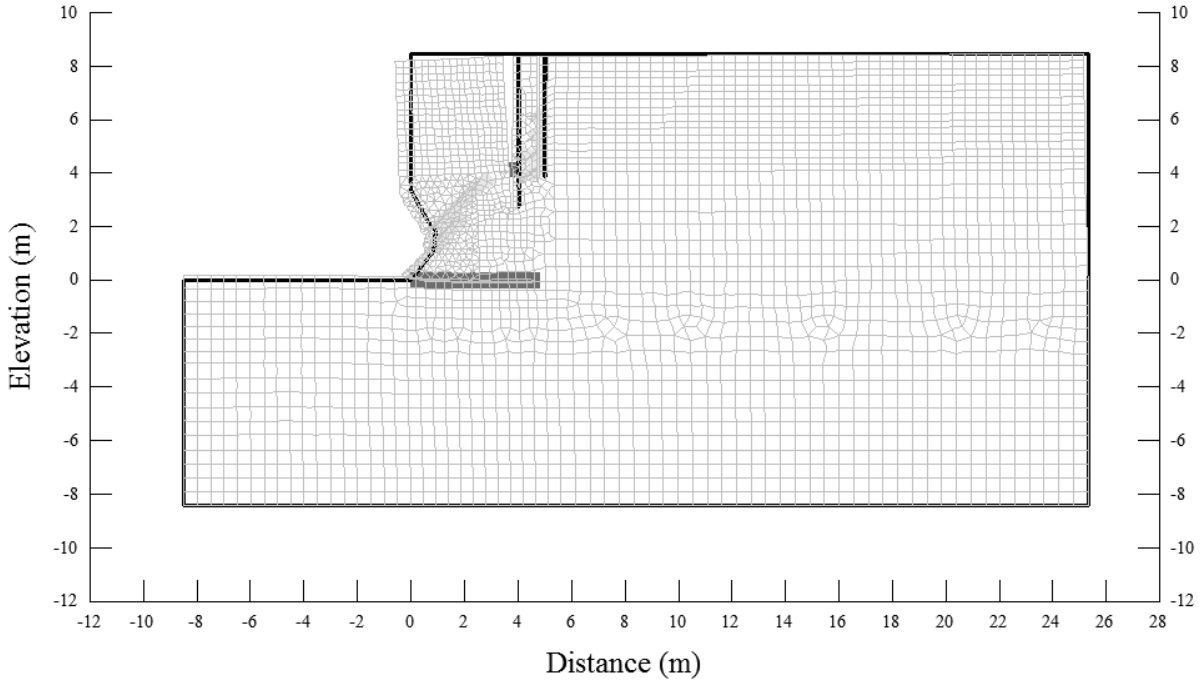

Figure D.16. FEM Model with Continued Propagation of Inclined and Tension Cracking that Resulted in Ultimate Slope Failure.

Vertical Slope FEM Model for k_o = 1.0

Deformation Mesh Displayed at 20X Magnification

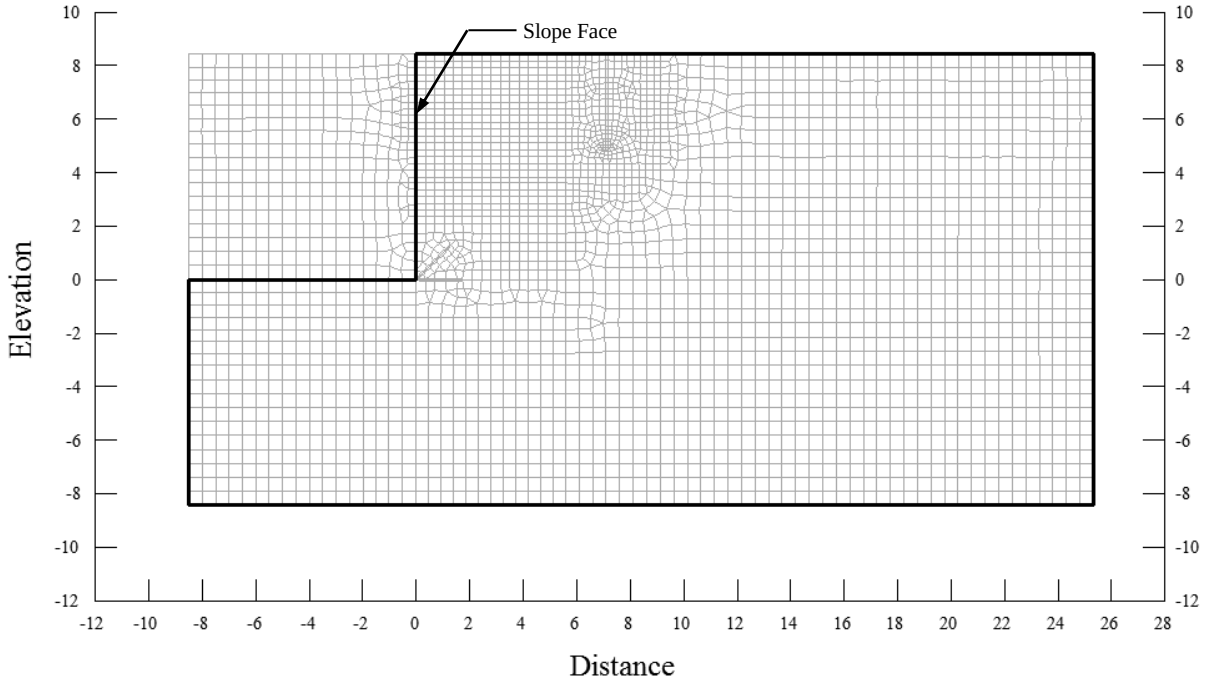

Figure D.17. Initial FEM Model for k_o = 1.0

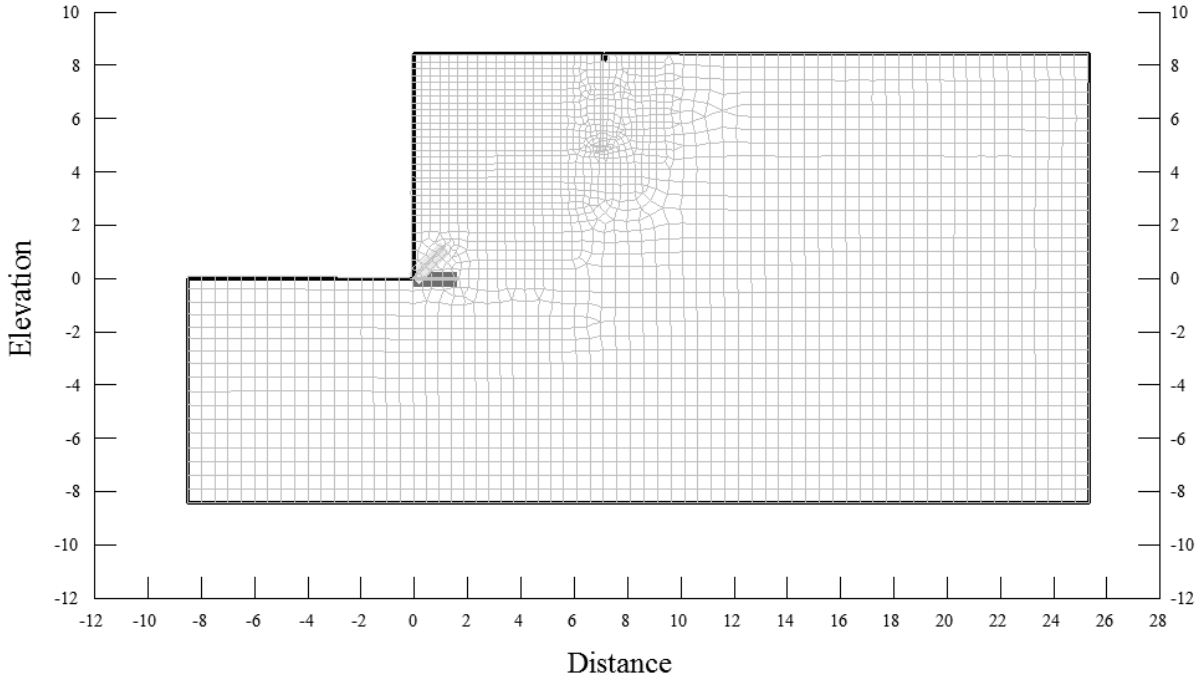

Figure D.18. FEM Model with Onset of Base, Inclined and Tension Cracking due to LSR.

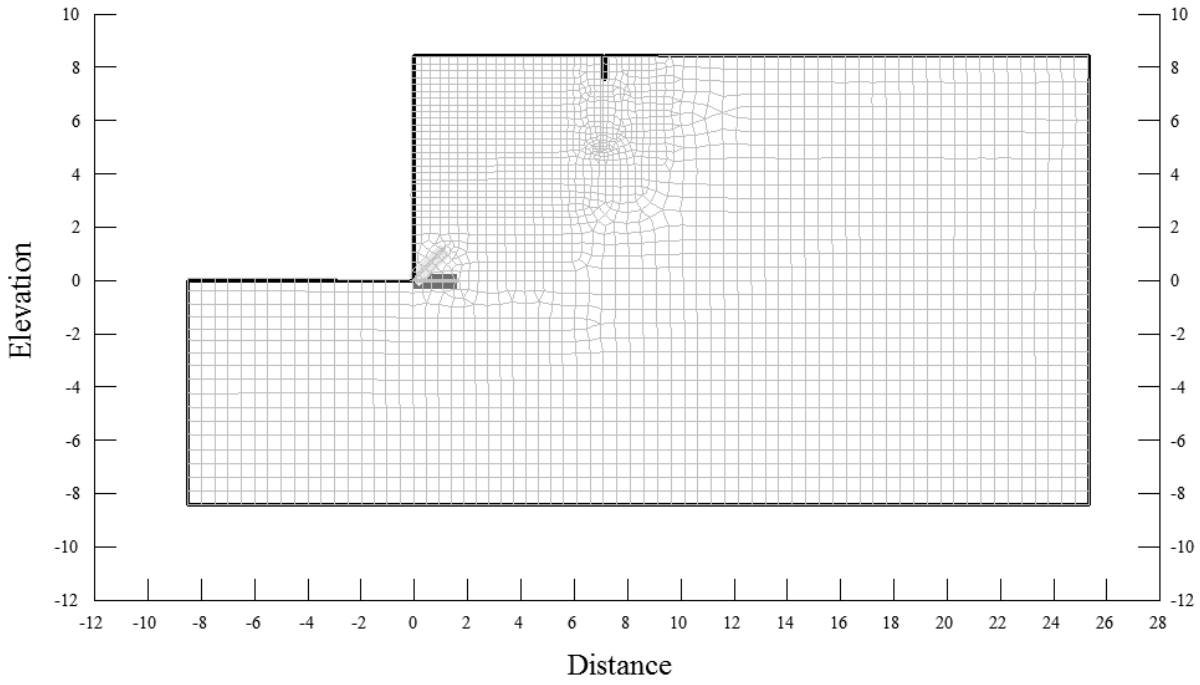

Figure D.19. FEM Model with Continued Propagation of Tension Crack.

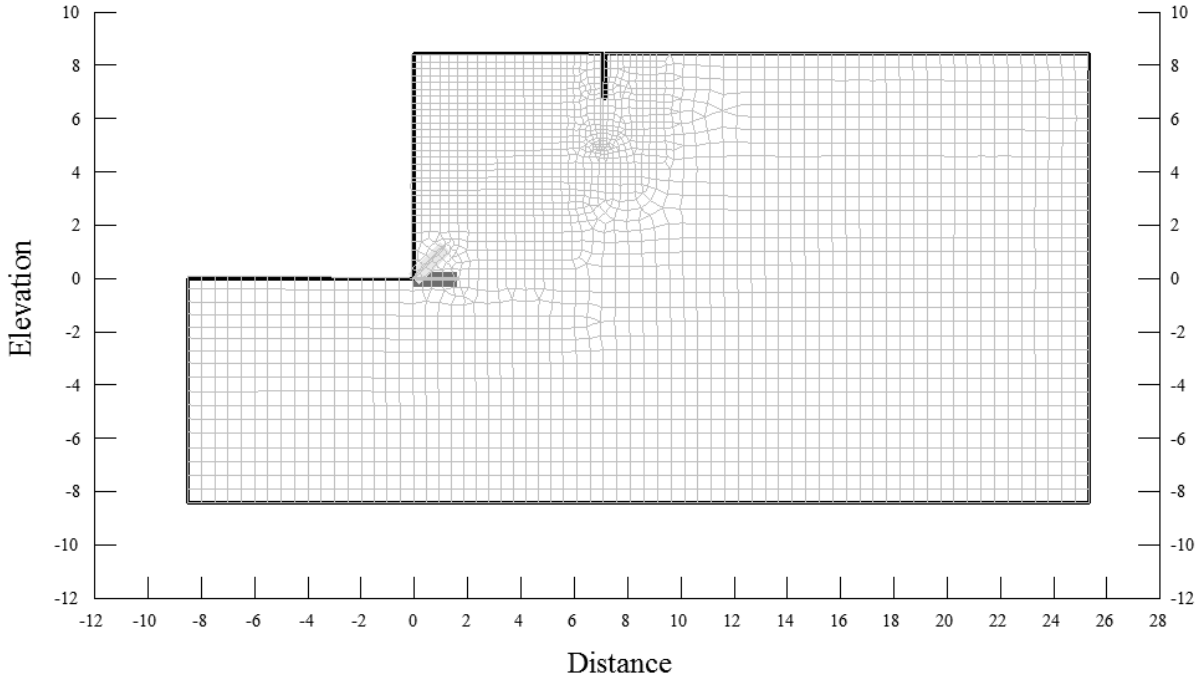

Figure D.20. FEM Model with Continued Propagation of Tension Crack.

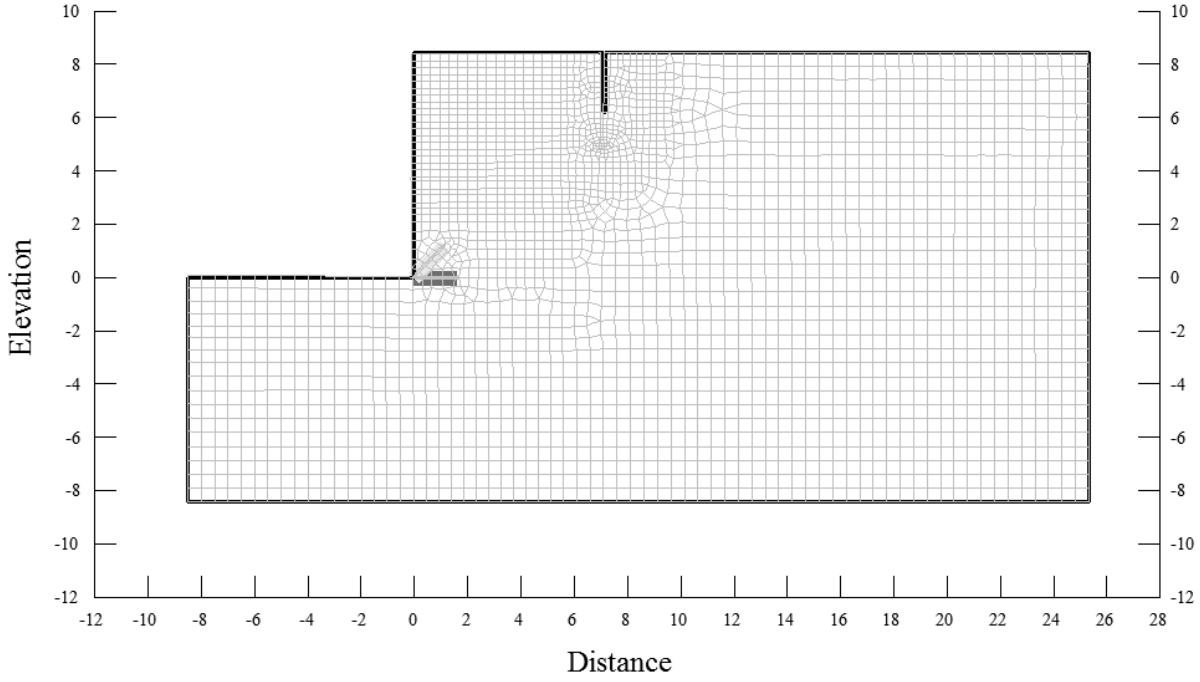

Figure D.21. FEM Model with Continued Propagation of Tension Crack.

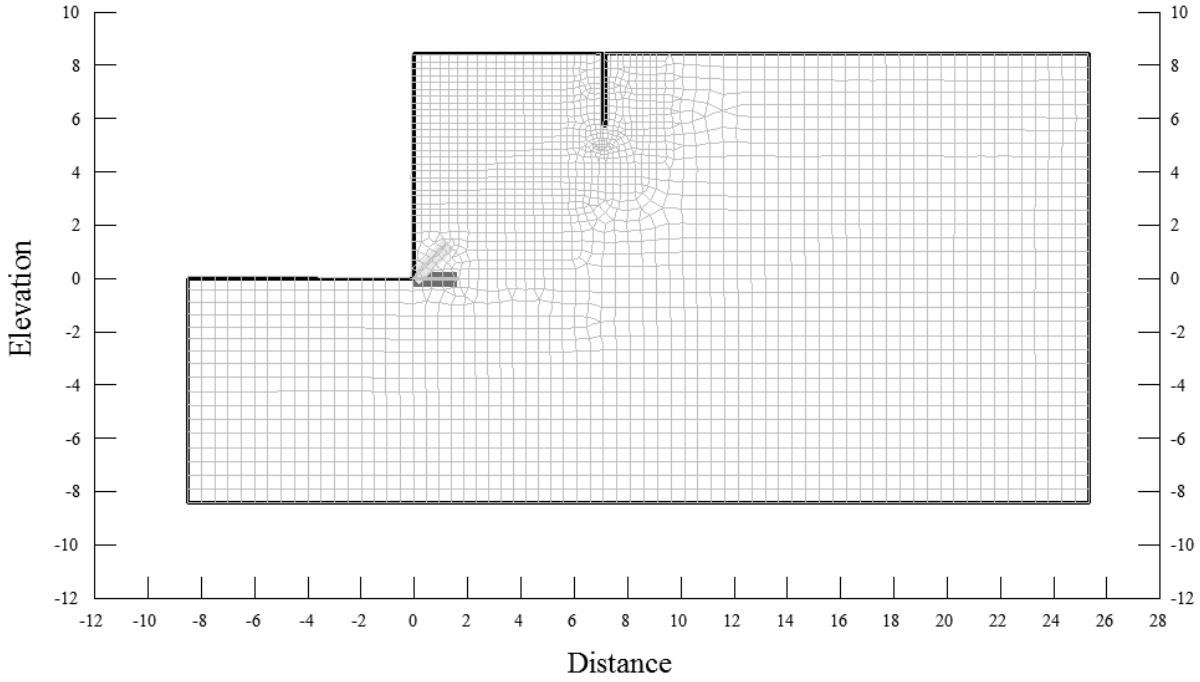

Figure D.22. FEM Model with Continued Propagation of Tension Crack.

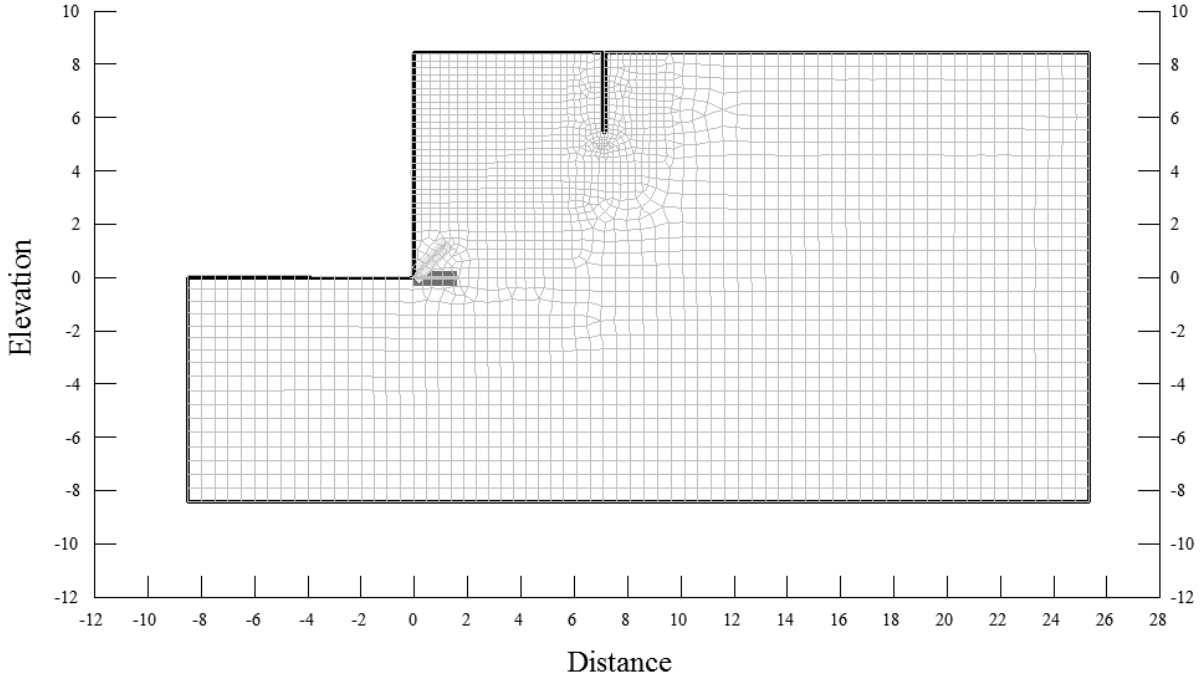

Figure D.23. FEM Model with Continued Propagation of Tension Crack.

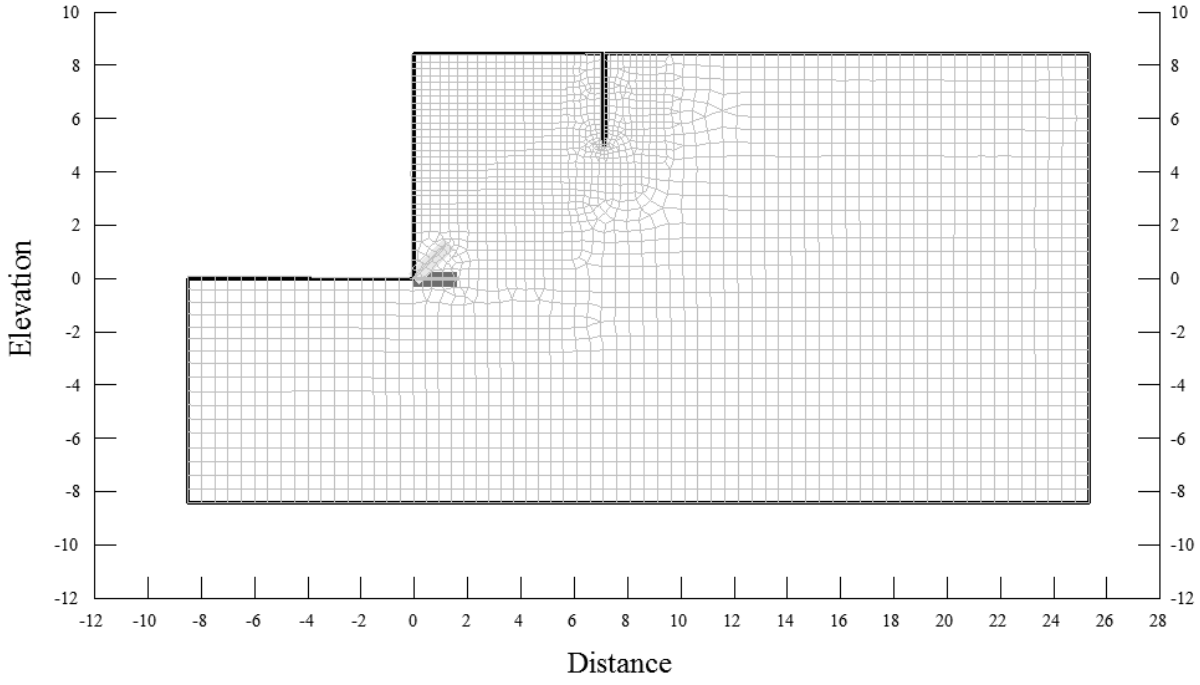

Figure D.24. FEM Model with Tension Crack that has Stabilized.

¼H:1V Slope FEM Model for k_o = 3.0

Deformation Mesh Displayed at 10X Magnification

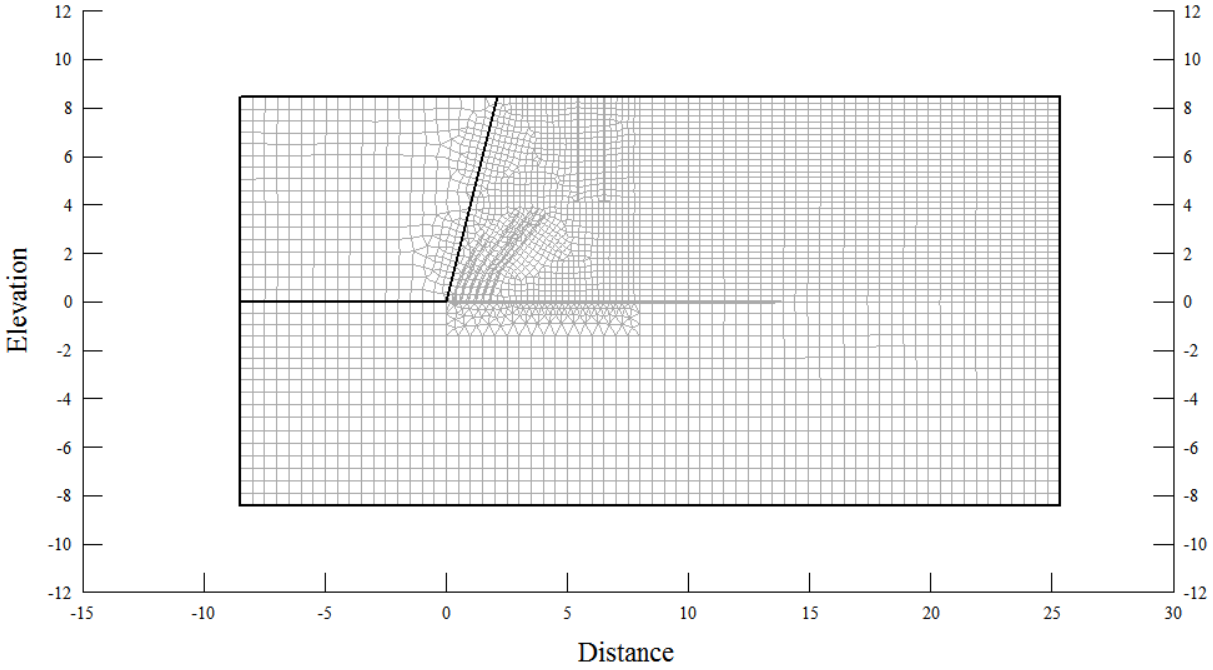

Figure D.25. Initial FEM Model for k_o = 3.0

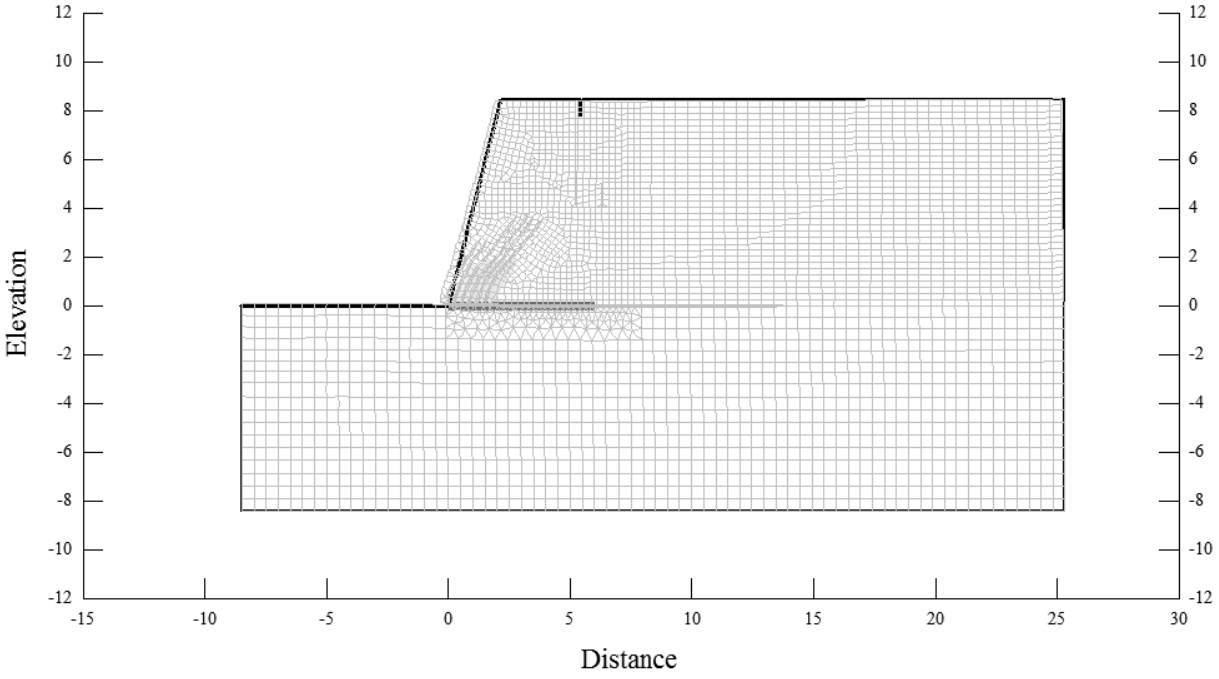

Figure D.26. FEM Model with Onset of Base, Inclined and Tension Cracking due to LSR.

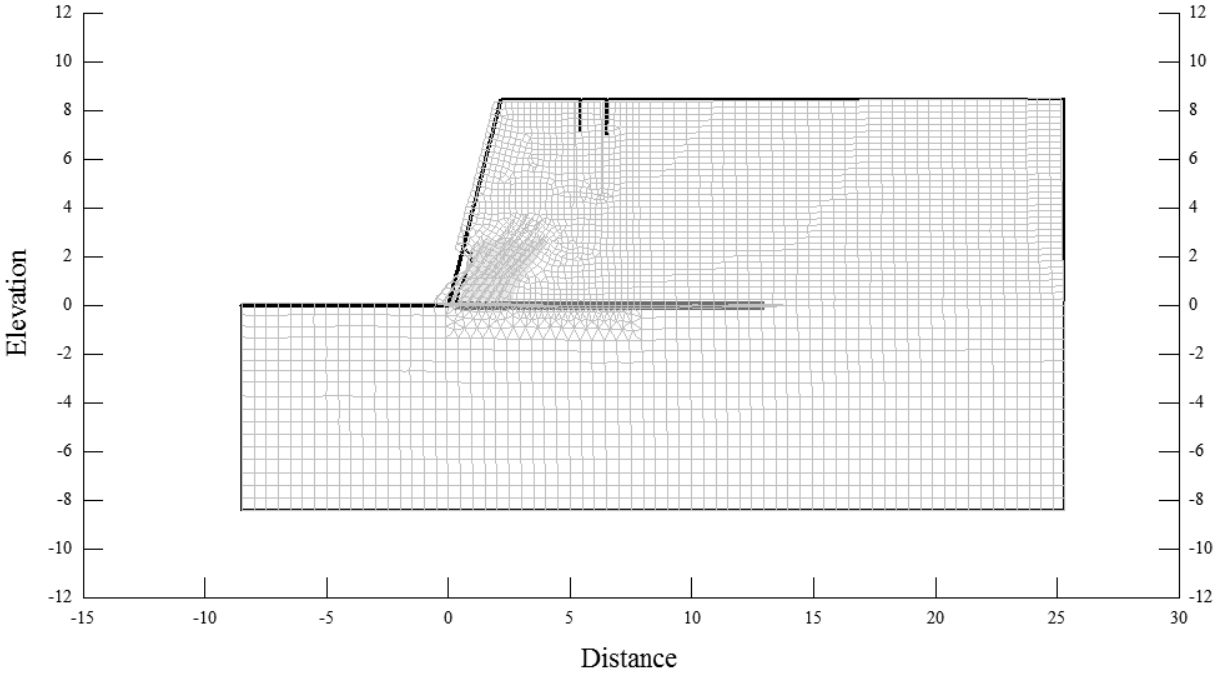

Figure D.27. FEM Model with Continued Propagation of Base, Inclined and Tension Cracking. Inclined Cracking Resulted in Loss of Material at the Toe Due to Negative Stresses.

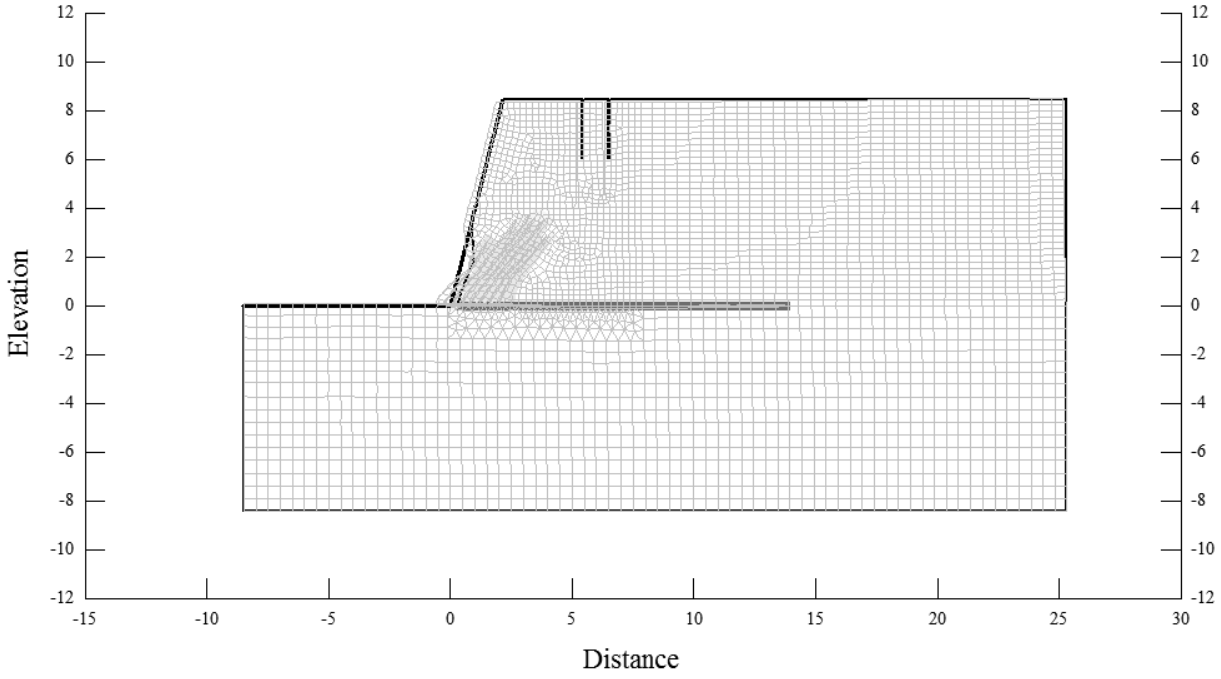

Figure D.28. FEM Model with Continued Propagation of Base, Inclined and Tension Cracking.

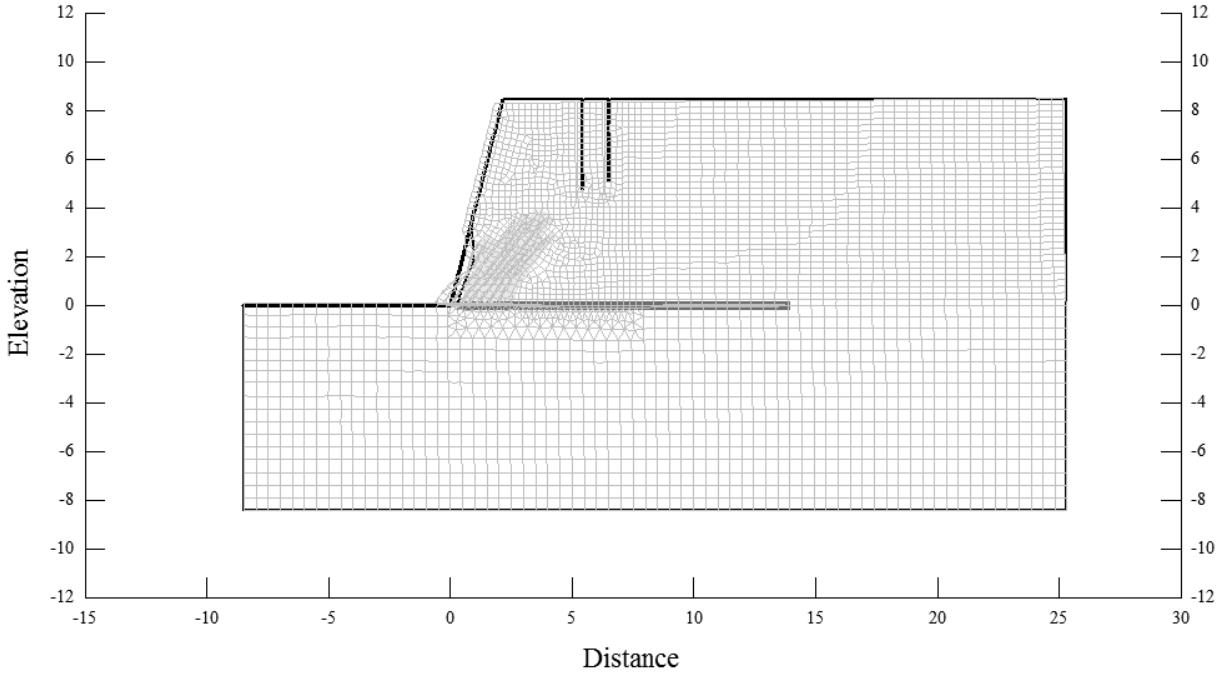

Figure D.29. FEM Model with Continued Propagation of Inclined and Tension Cracking that Resulted in Ultimate Slope Failure.

¼H:1V Slope FEM Model for k_o = 2.0

Deformation Mesh Displayed at 20X Magnification

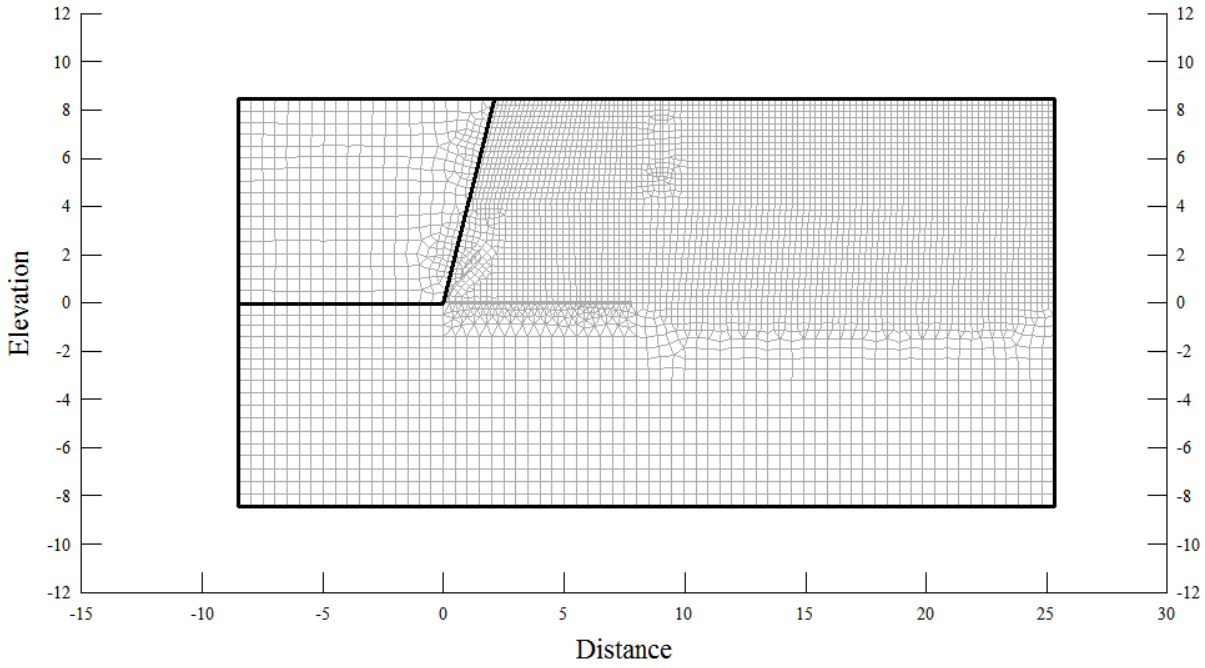

Figure D.30. Initial FEM Model for k_o = 2.0

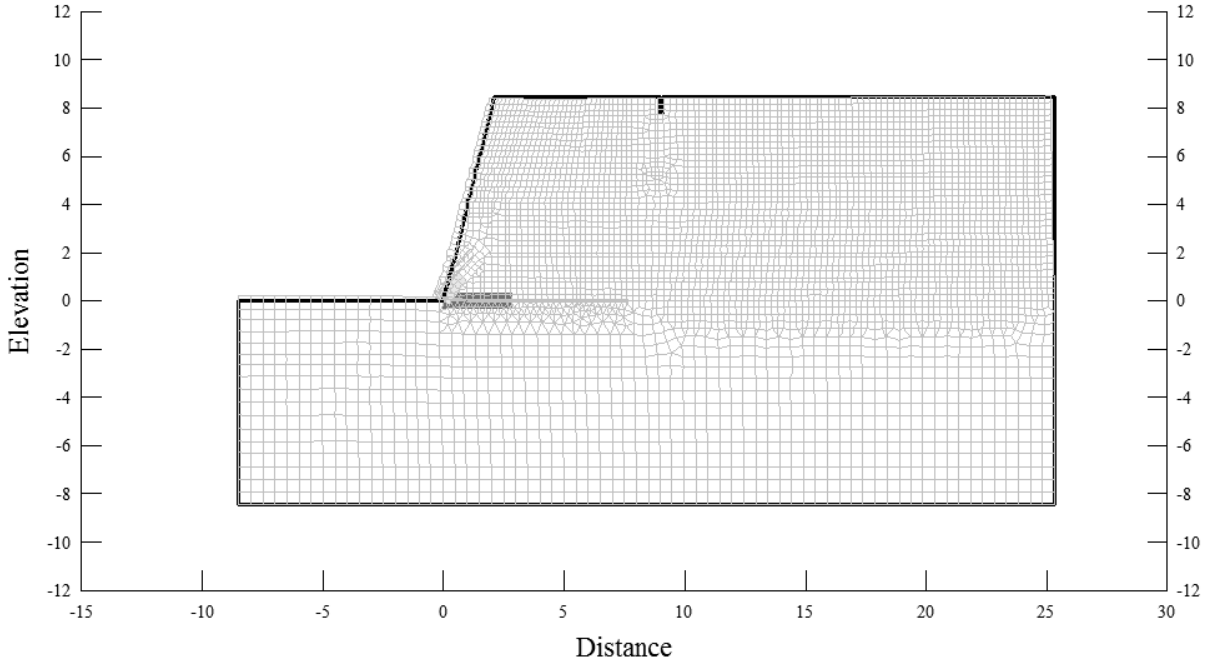

Figure D.31. FEM Model with Onset of Base, Inclined and Tension Cracking due to LSR.

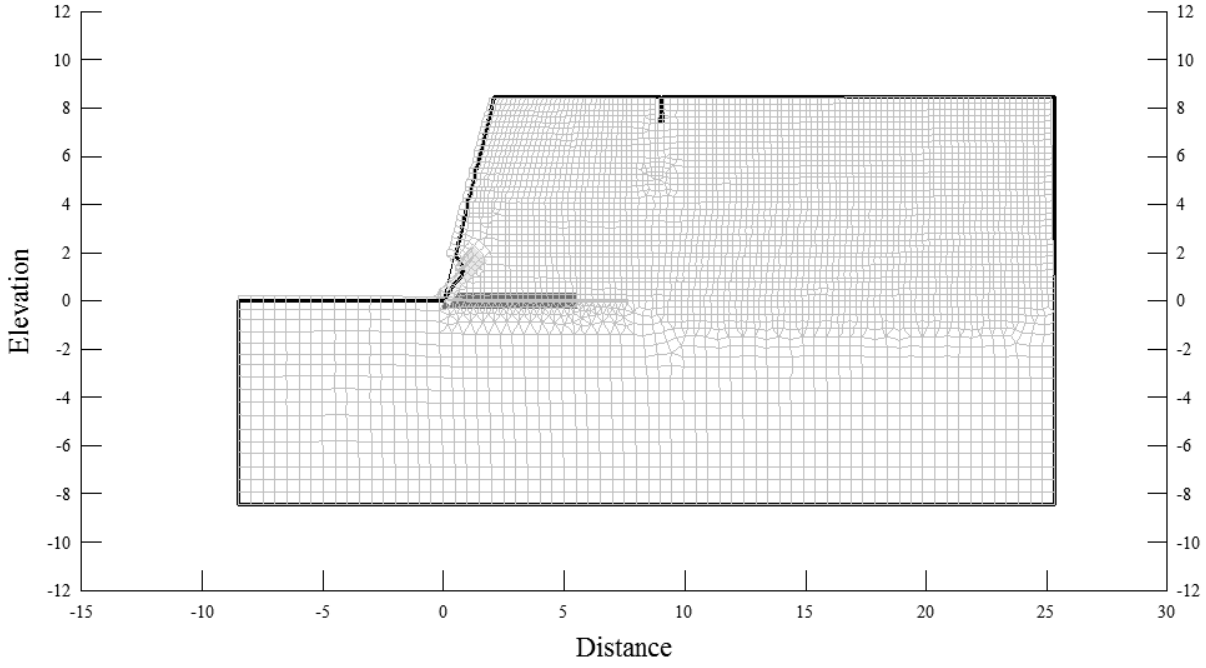

Figure D.32. FEM Model with Continued Propagation of Base, Inclined and Tension Cracking. Inclined Cracking Resulted in Loss of Material at the Toe Due to Negative Stresses.

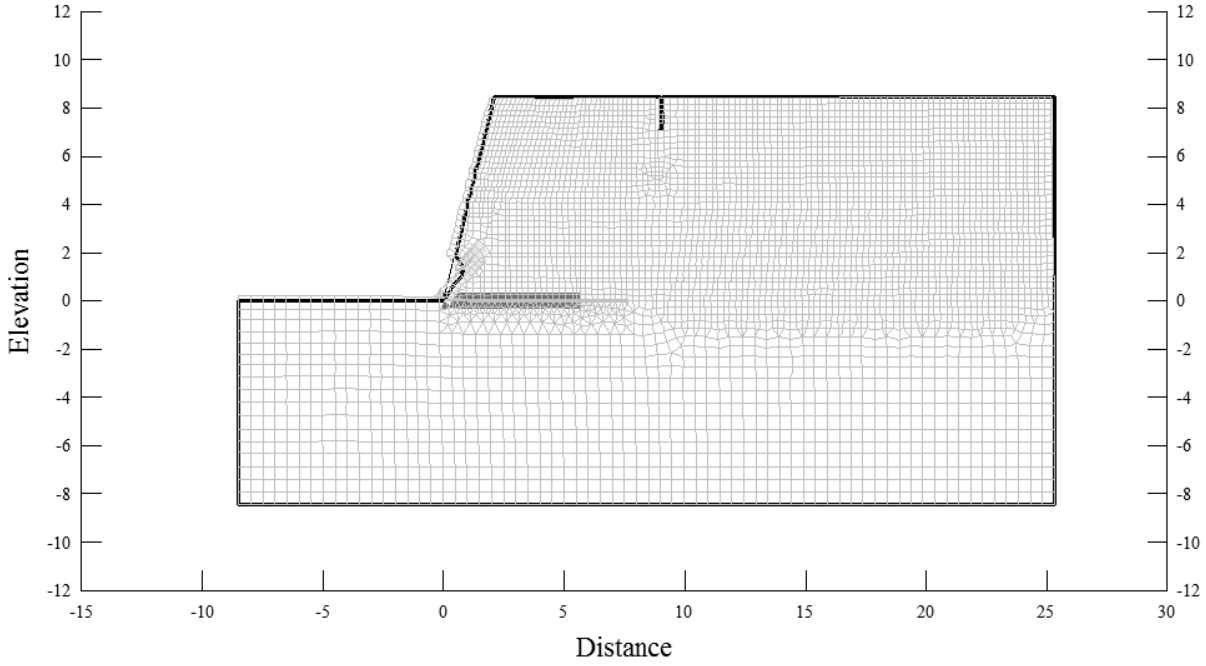

Figure D.33. FEM Model with Continued Propagation of Base, Inclined and Tension Cracking.

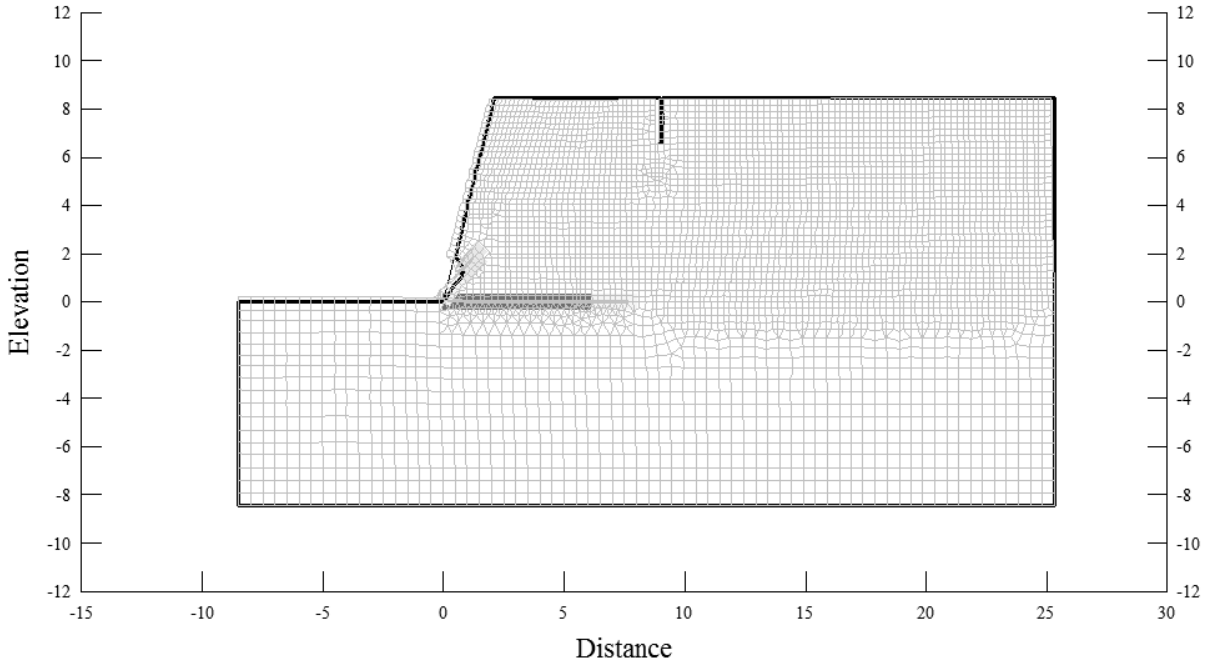

Figure D.34. FEM Model with Continued Propagation of Tension Cracking.

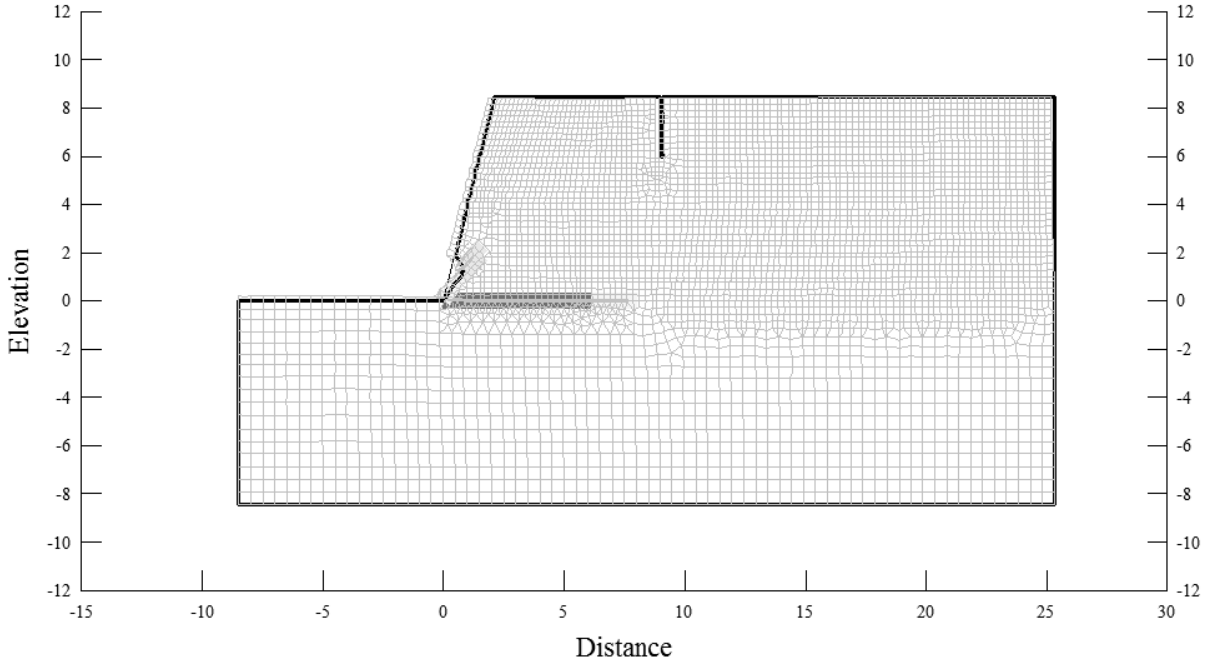

Figure D.35. FEM Model with Continued Propagation of Tension Cracking.

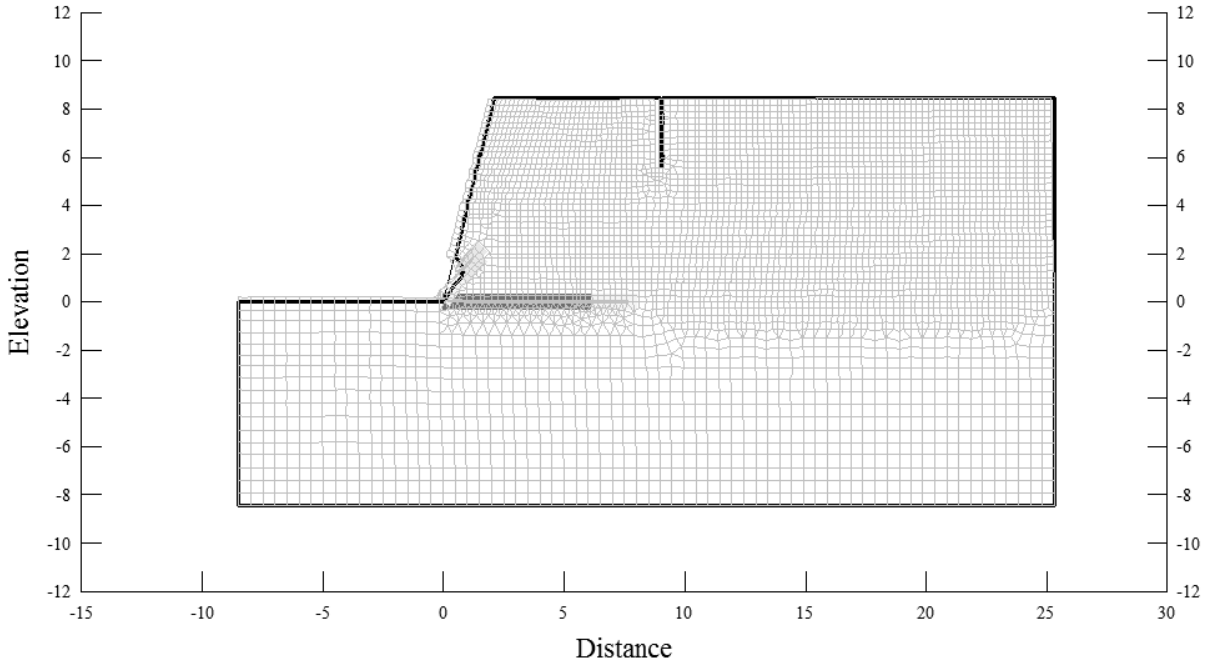

Figure D.36. FEM Model with Stabilization of Base, Inclined and Tension Cracking.

¼H:1V Slope FEM Model for k_o = 1.0

Deformation Mesh Displayed at 20X Magnification

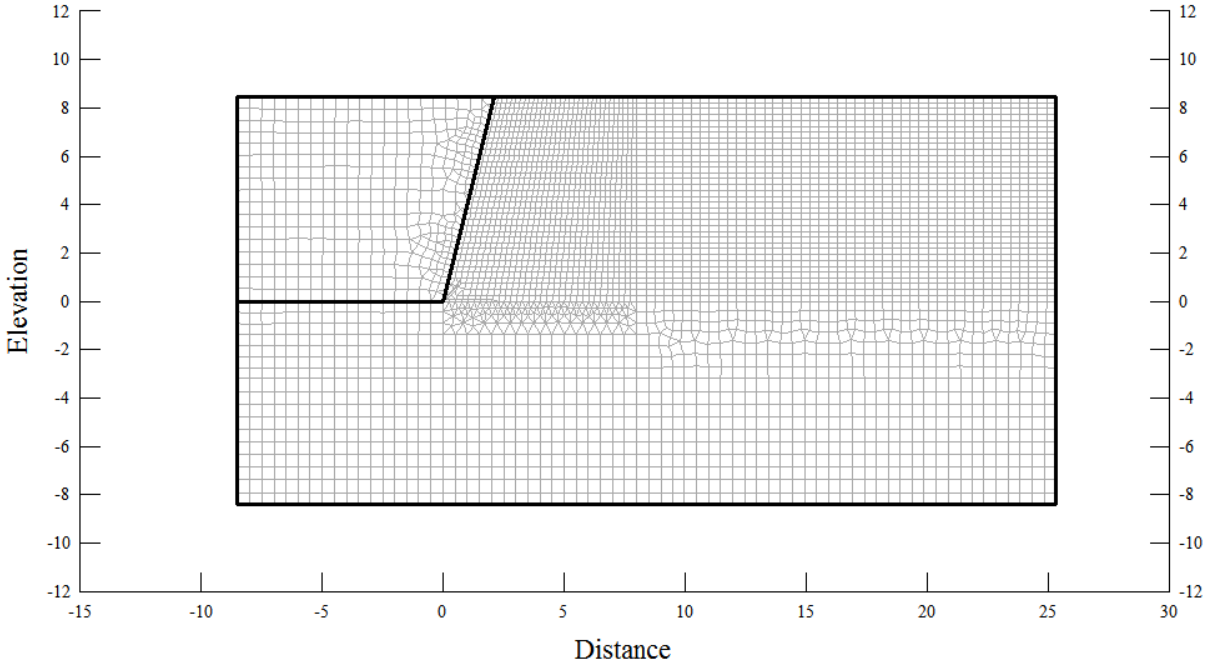

Figure D.37. Initial FEM Model for k_o = 1.0

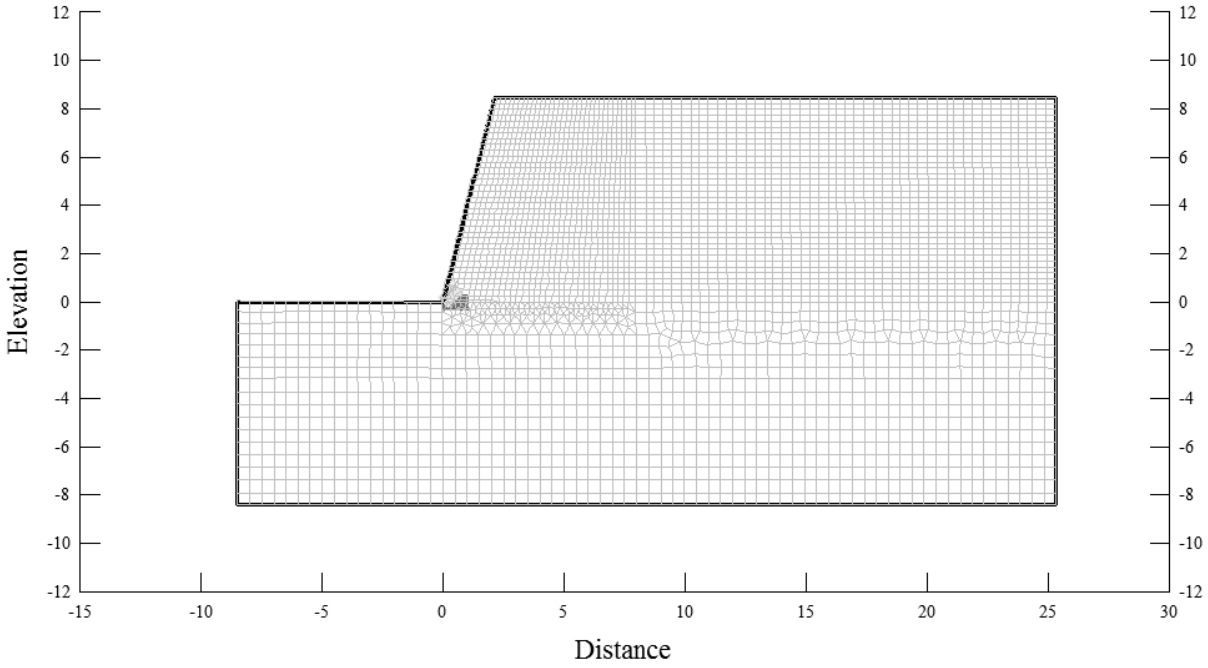

Figure D.38. FEM Model with Onset of Base and Inclined Cracking due to LSR. Lateral Stresses Were Not of Sufficient Magnitude to Produce Tensile Cracking.

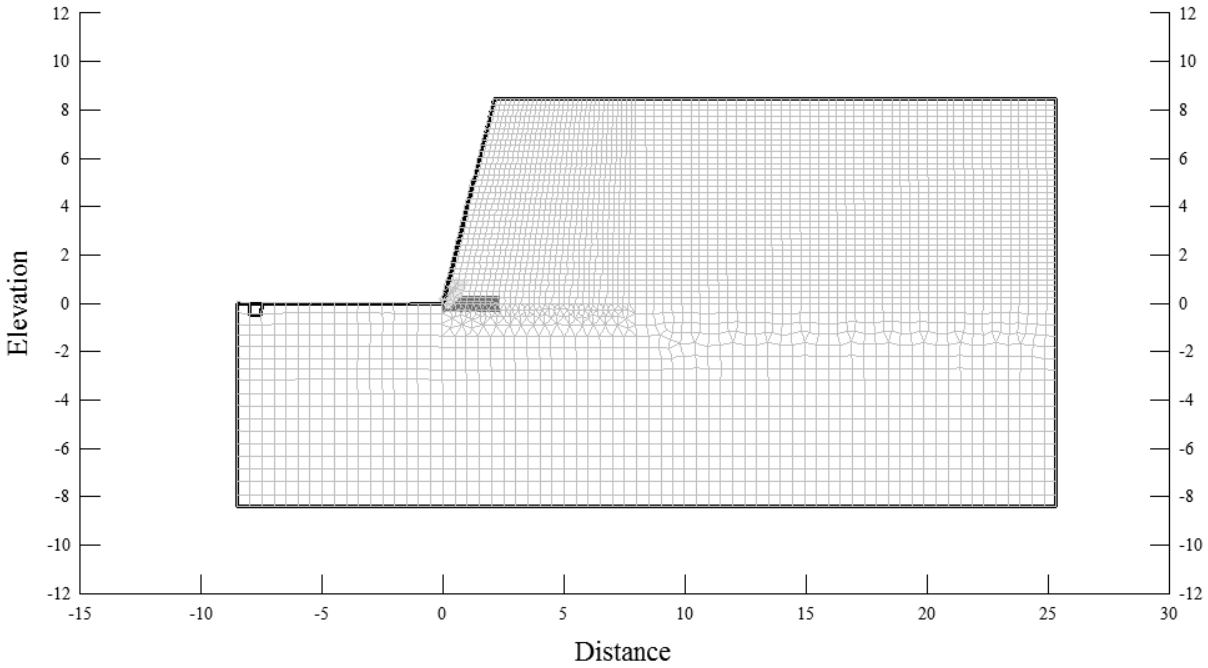

Figure D.39. FEM Model with Stabilization of Base and Inclined Cracking.

½H:1V Slope FEM Model for k_o = 3.0

Deformation Mesh Displayed at 10X Magnification

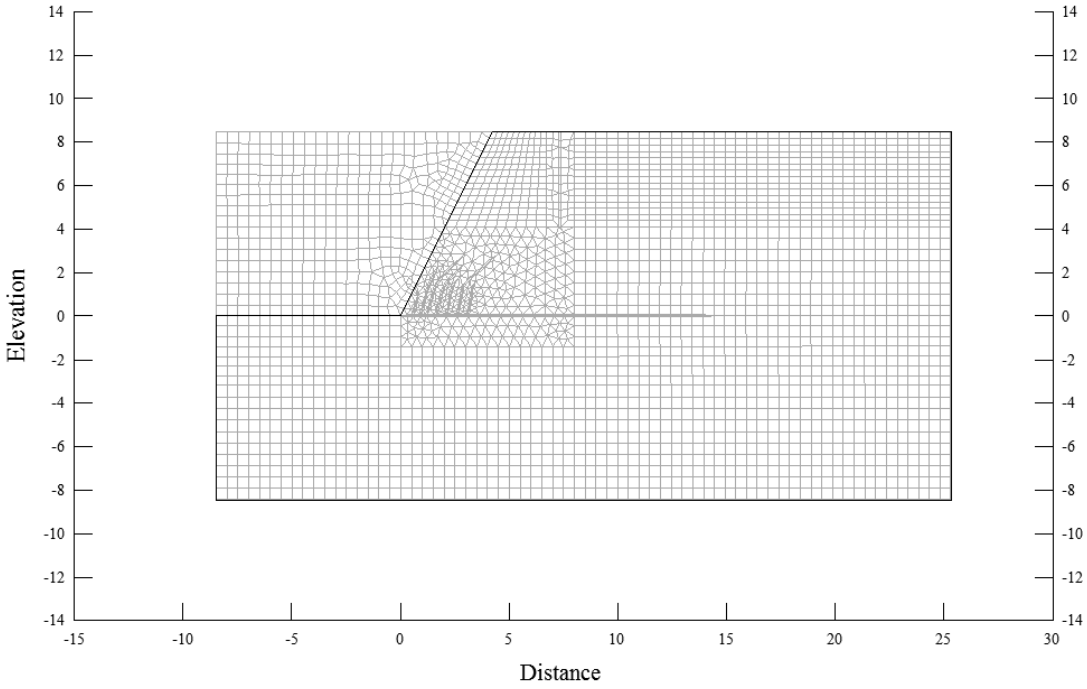

Figure D.40. Initial FEM Model for k_o = 3.0

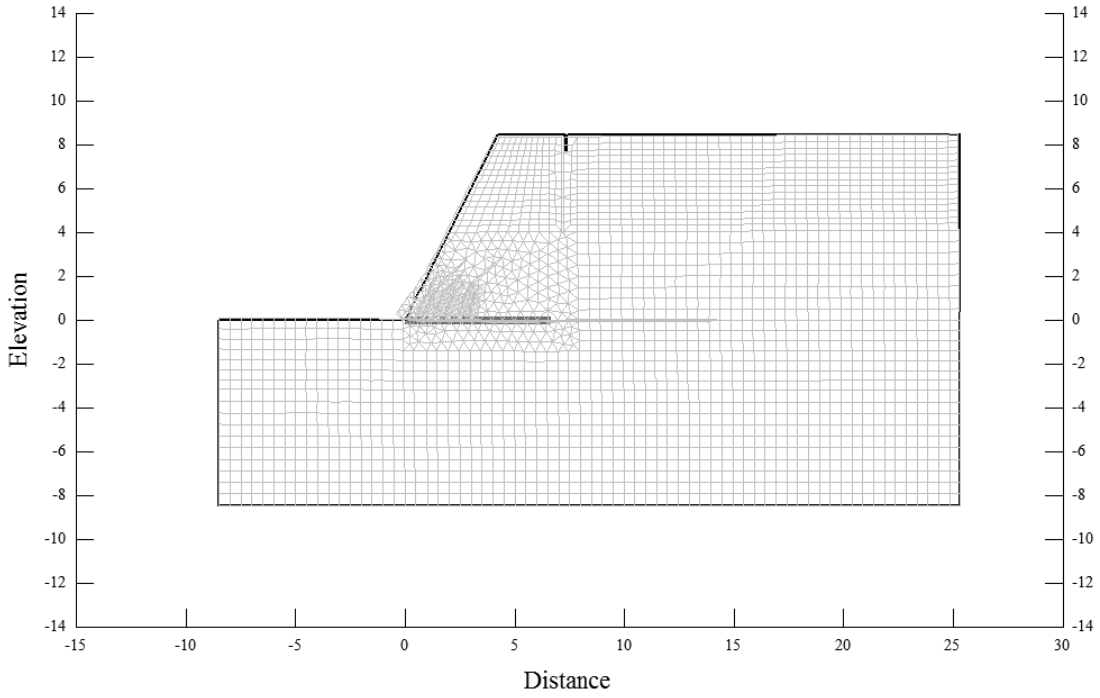

Figure D.41. FEM Model with Onset of Base, Inclined and Tension Cracking due to LSR.

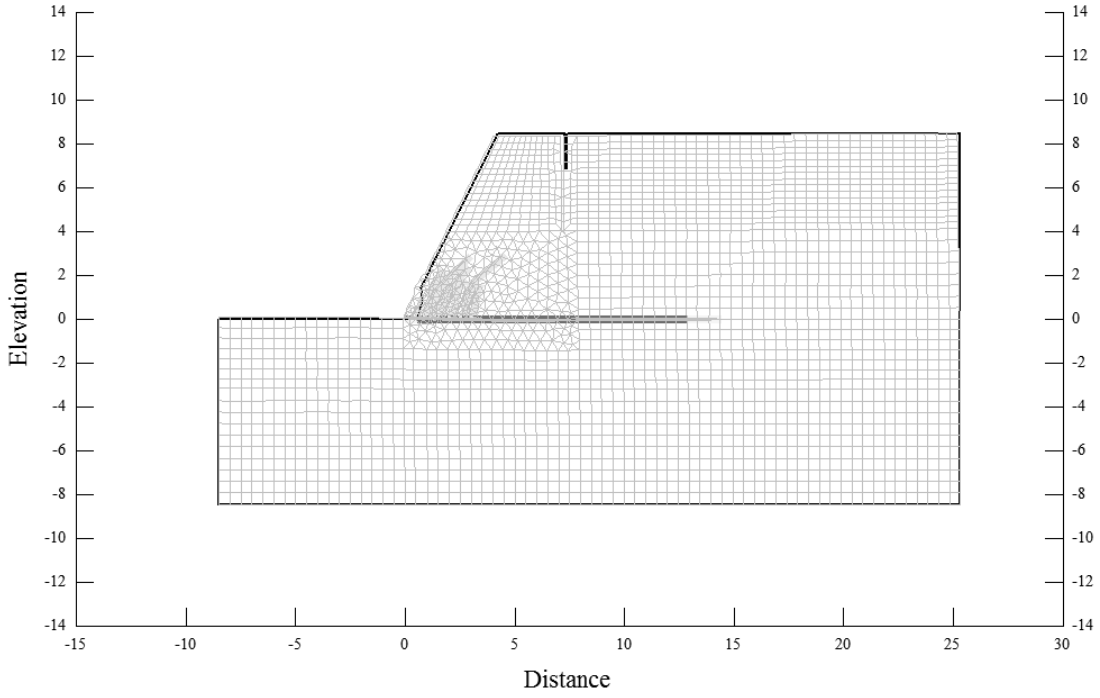

Figure D.42. FEM Model with Continued Propagation of Base, Inclined and Tension Cracking.

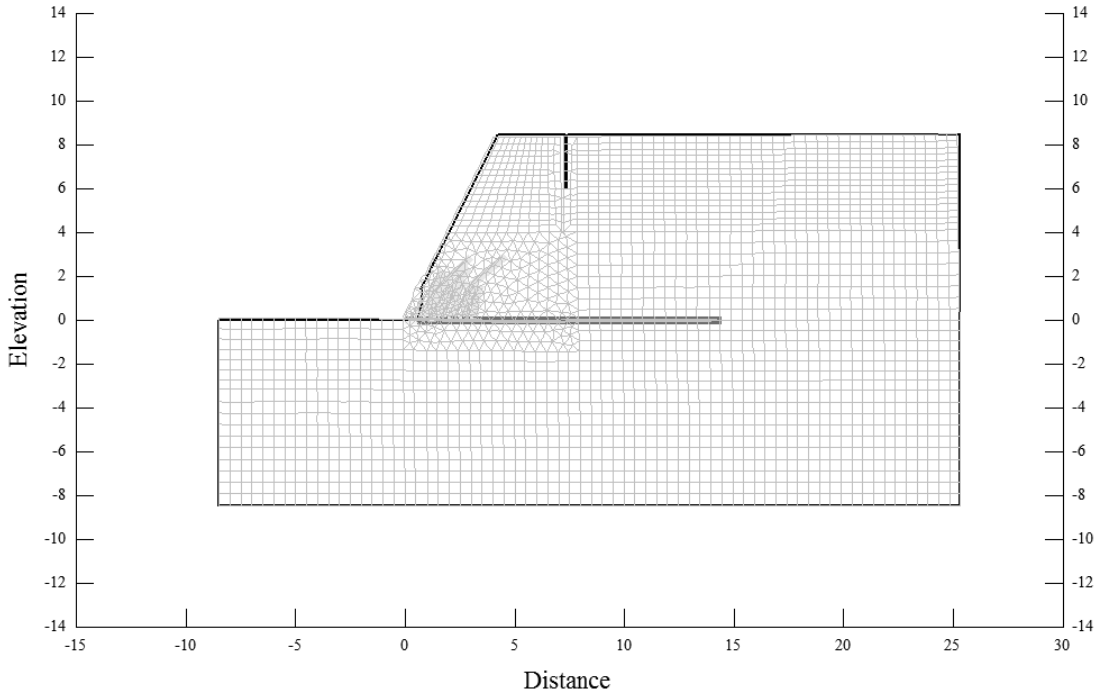

Figure D.43. FEM Model with Continued Propagation of Base and Tension Cracking.

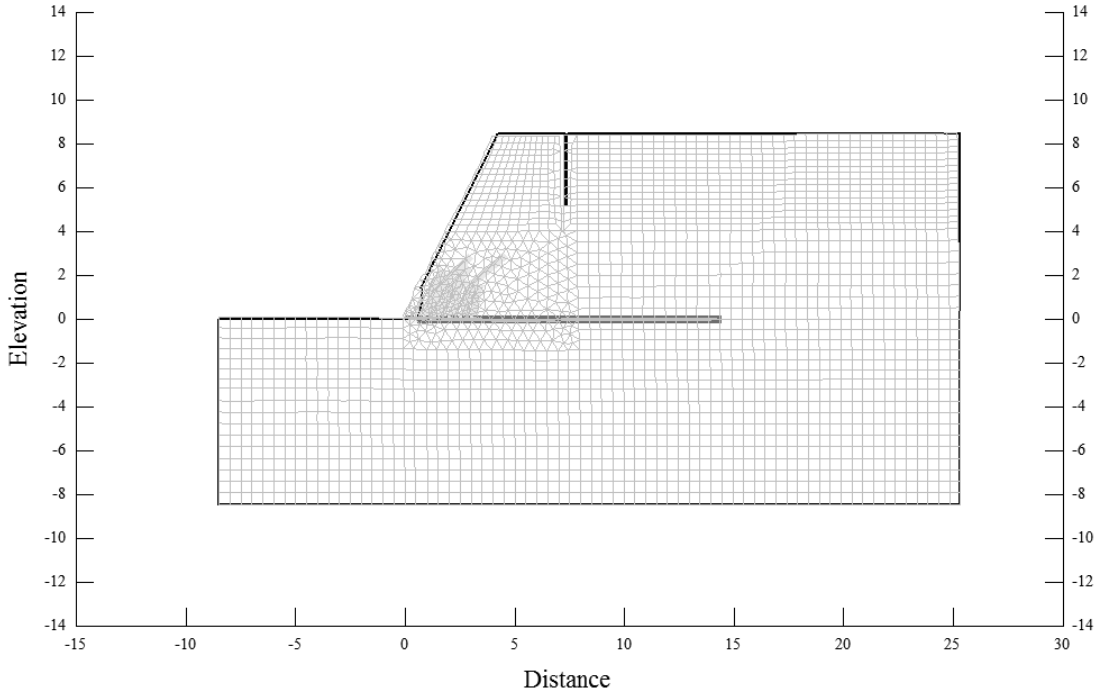

Figure D.44. FEM Model with Continued Propagation of Tension Cracking.

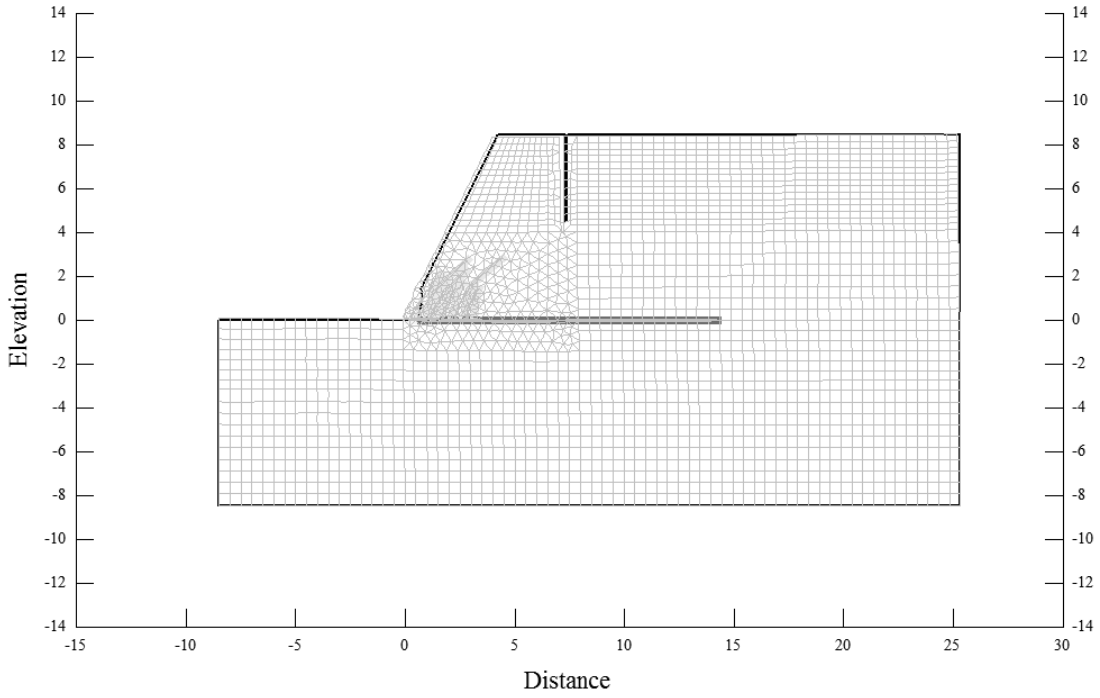

Figure D.45. FEM Model with Continued Propagation of Tension Cracking.

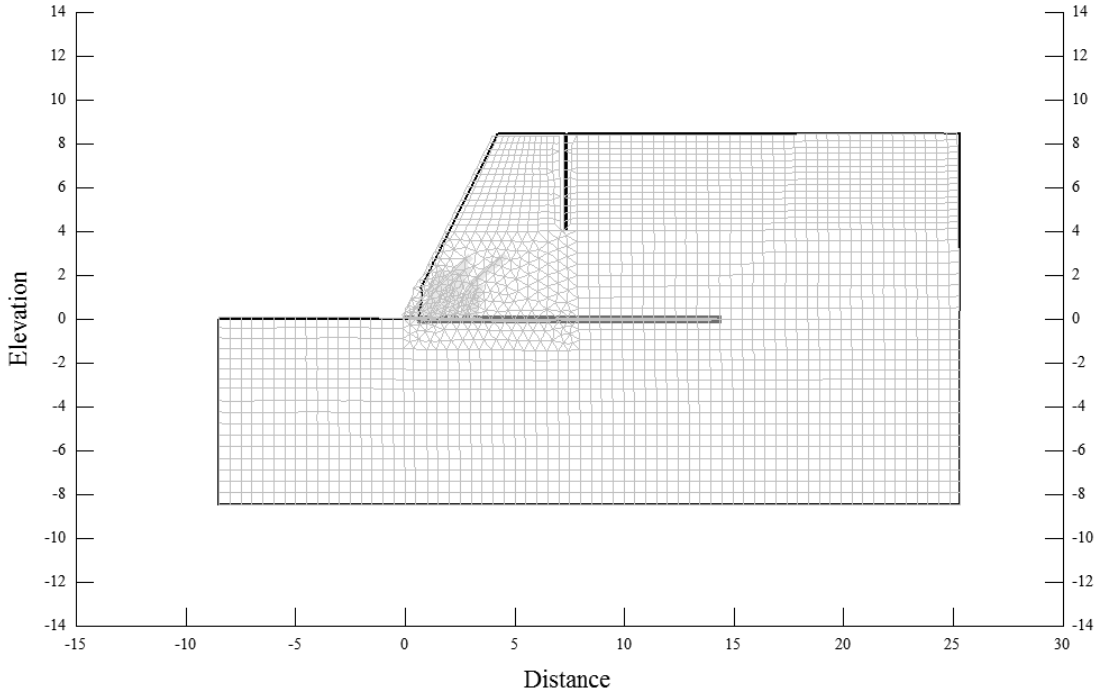

Figure D.46. FEM Model with Stabilization of Base, Inclined and Tension Cracking.

½H:1V Slope FEM Model for k_o = 2.0

Deformation Mesh Displayed at 20X Magnification

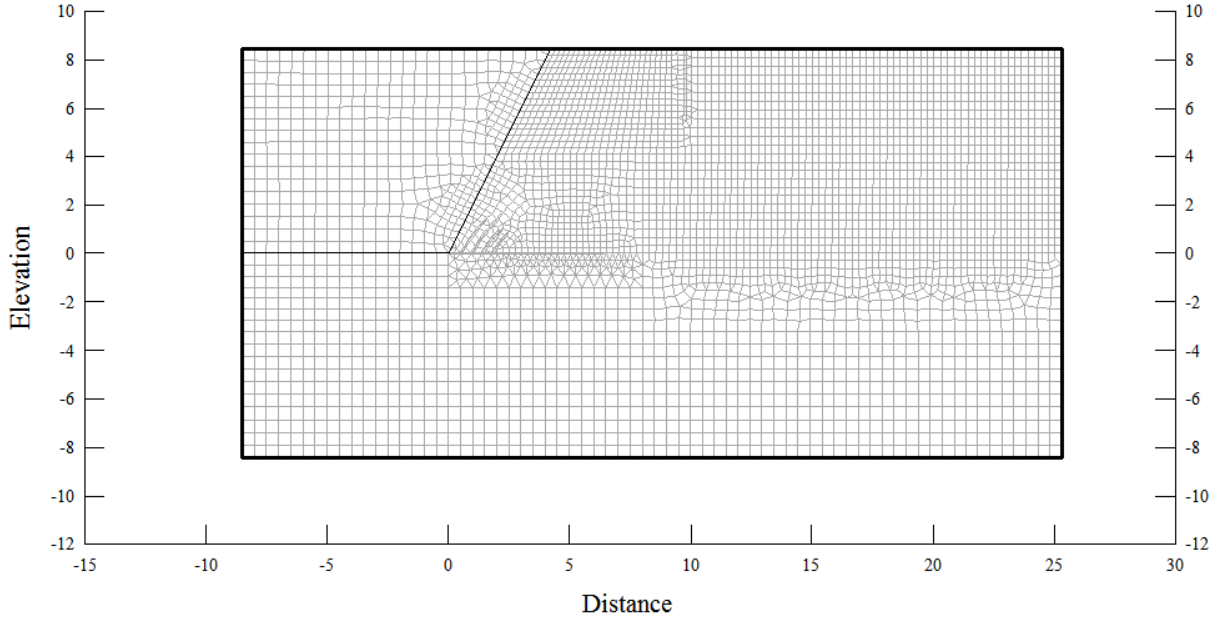

Figure D.47. Initial FEM Model for k_o = 2.0

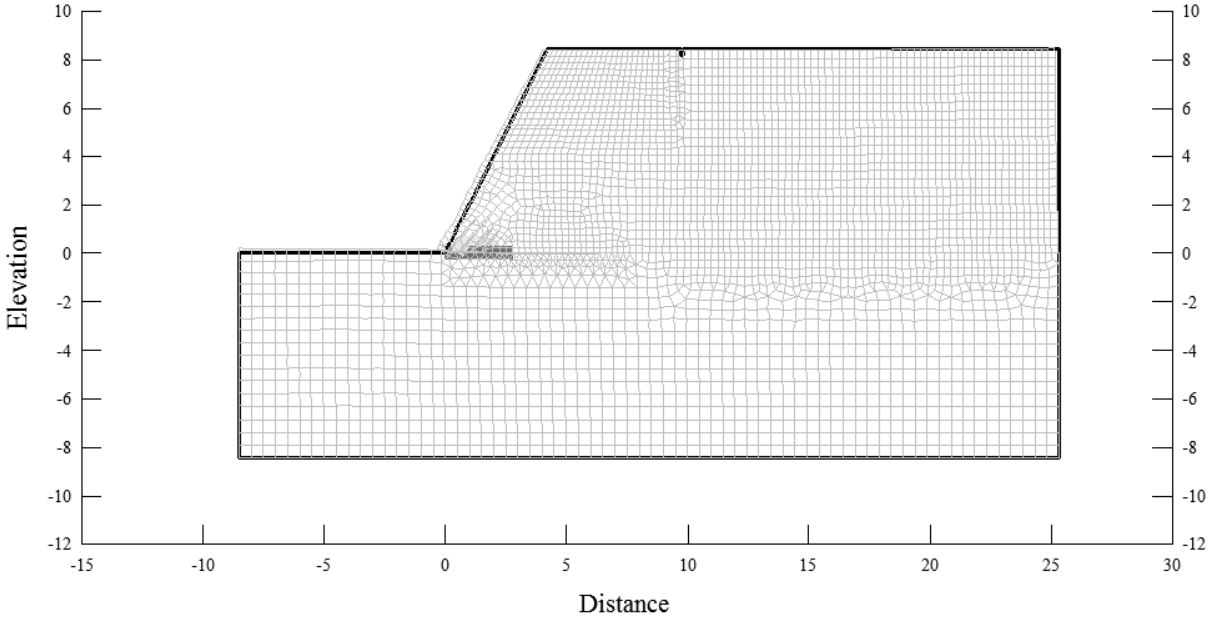

Figure D.48. FEM Model with Onset of Base, Inclined and Tension Cracking due to LSR.

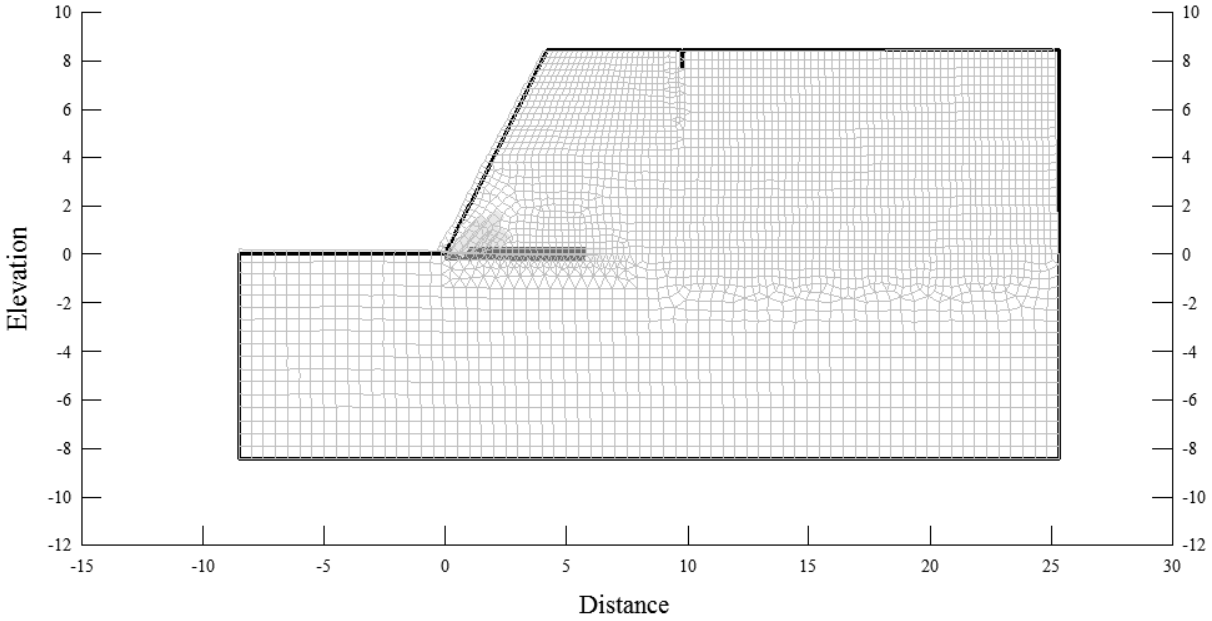

Figure D.49. FEM Model with Propagation of Base, Inclined and Tension Cracking.

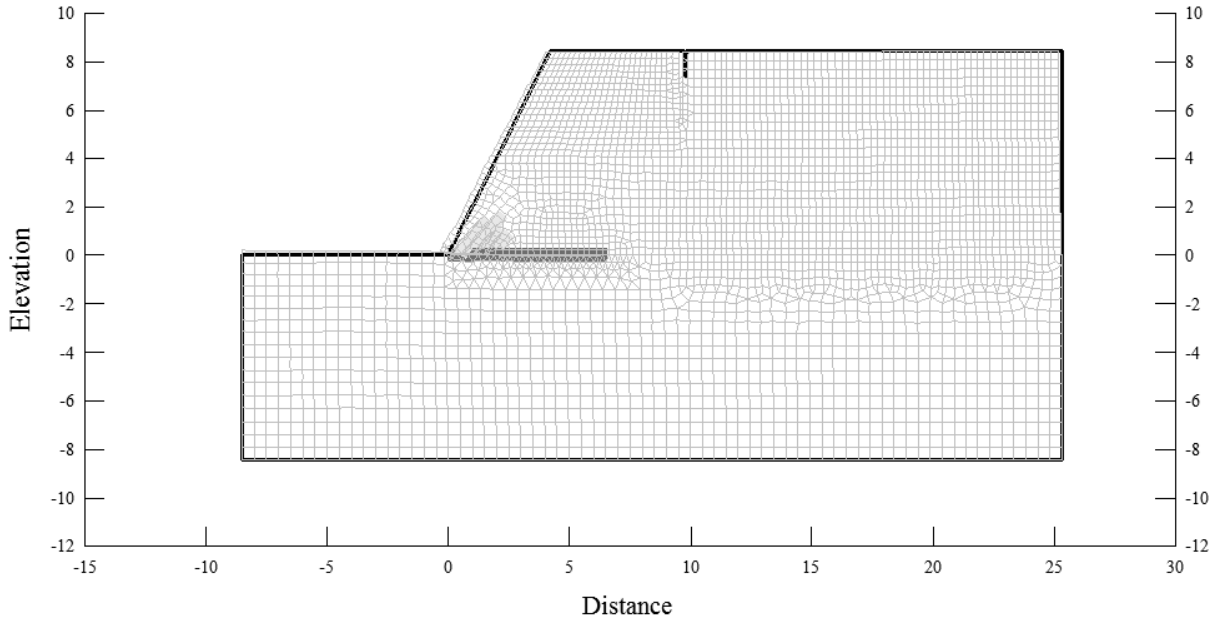

Figure D.50. FEM Model with Continued Propagation of Base and Tension Cracking.

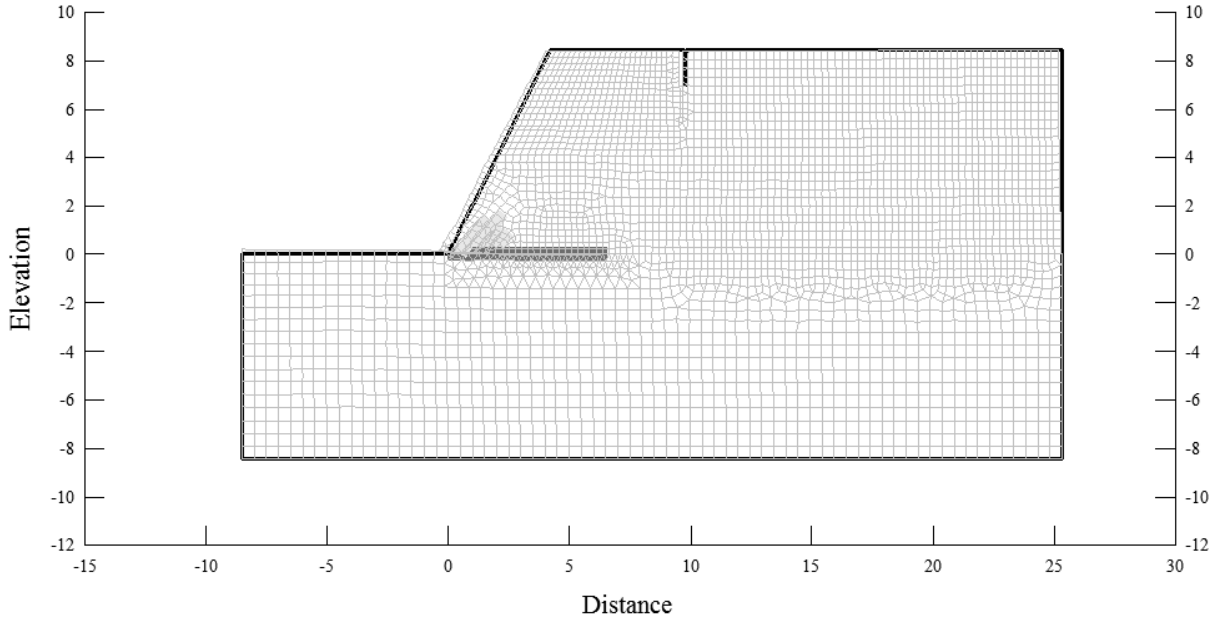

Figure D.51. FEM Model with Continued Propagation of Tension Cracking.

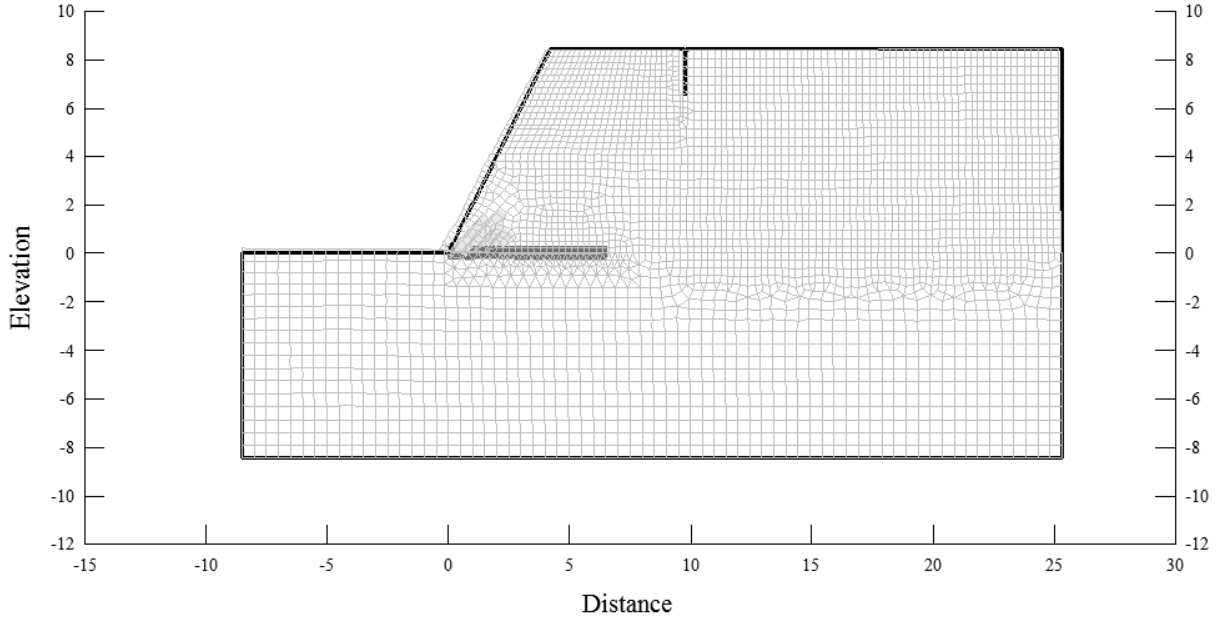

Figure D.52. FEM Model with Continued Propagation of Tension Cracking.

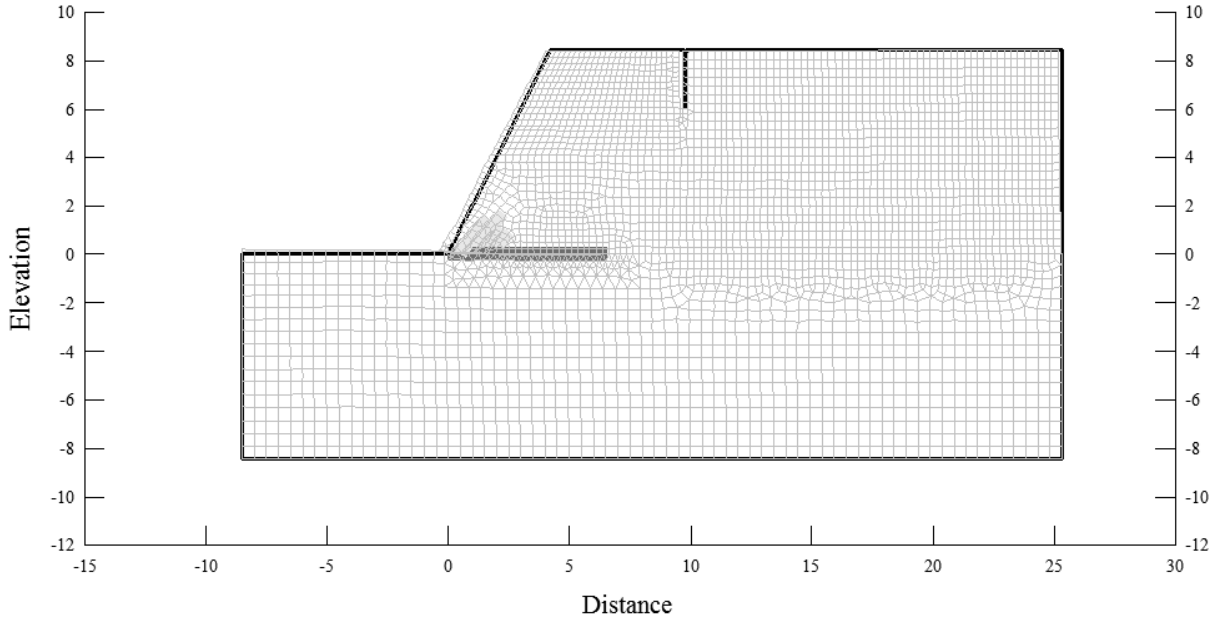

Figure D.53. Stabilization of Base, Inclined and Tension Cracking.

½H:1V Slope FEM Model for k_o = 1.0

Deformation Mesh Displayed at 20X Magnification

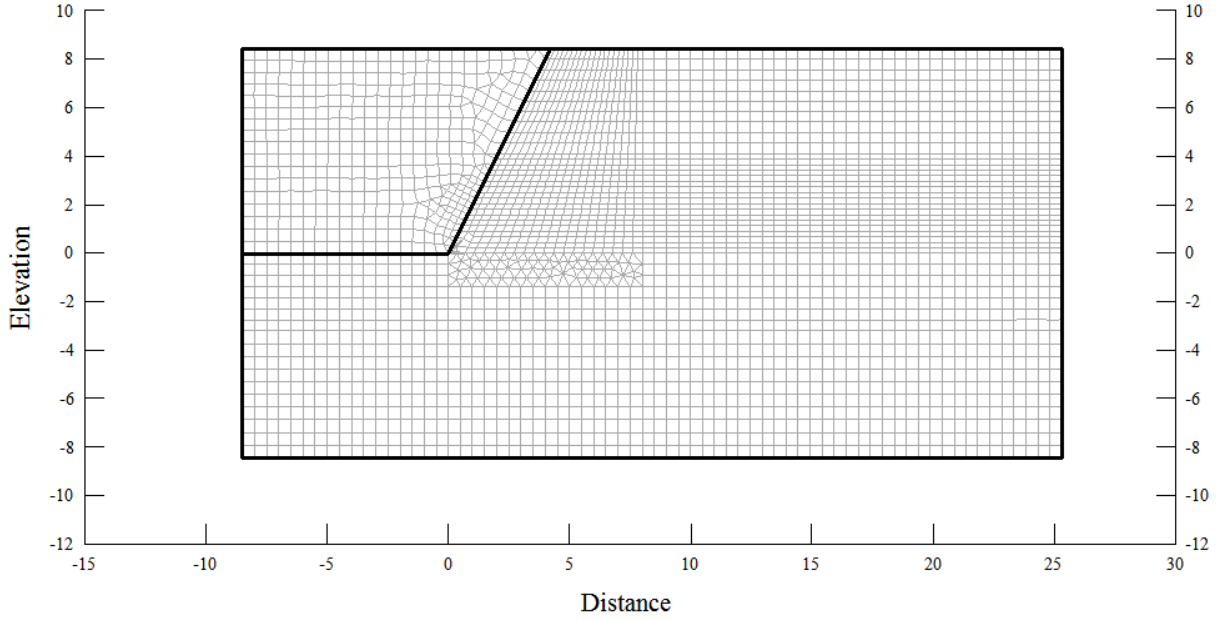

Figure D.54. Initial FEM Model for k_o = 1.0

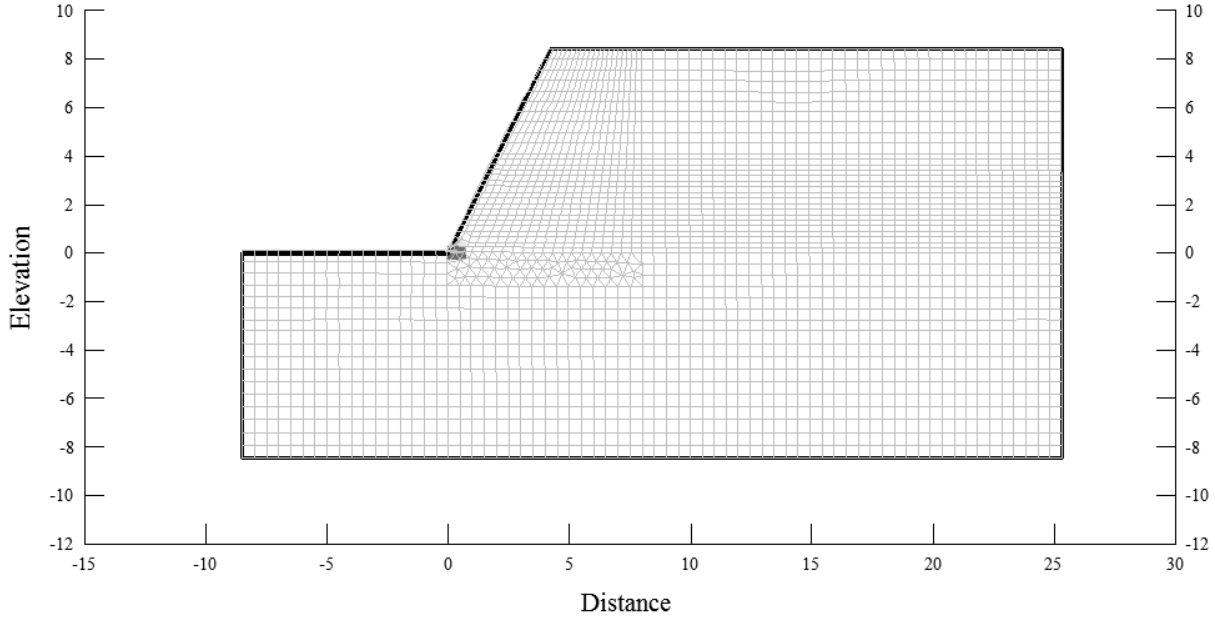

Figure D.55. FEM Model with Onset of Base and Inclined Cracking due to LSR. Lateral Stresses Were Not of Sufficient Magnitude to Produce Tensile Cracking.

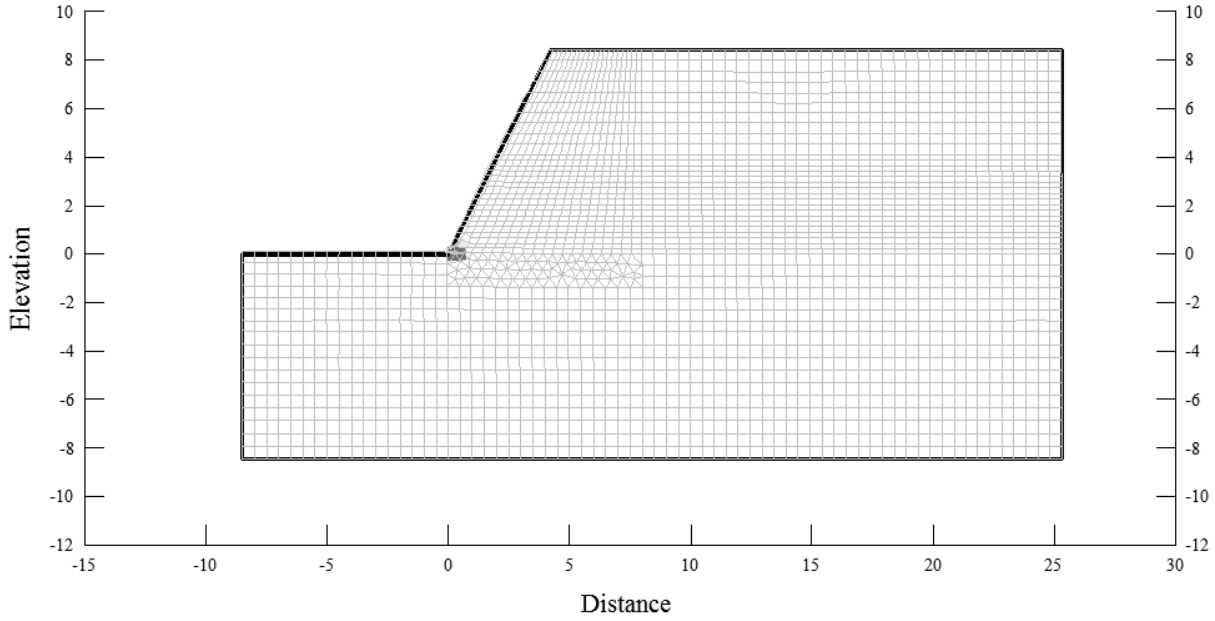

Figure D.56. FEM Model with Stabilization of Base and Inclined Cracking.

APPENDIX E

FEM MODELS FOR EVALUATION OF $\phi = 0°$ VERTICAL SLOPES WITH AN OPEN TOE CRACK

Vertical Slope FEM Model for k_o = 3.0, 2.0, and 1.0, with *Crack* = 0.5

Deformation Mesh Displayed at 30X Magnification

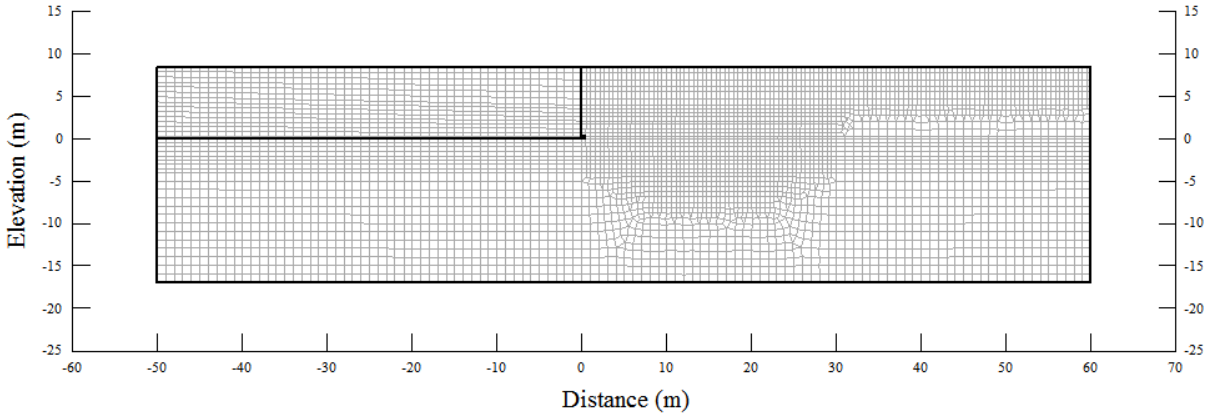

Figure E.1. Initial FEM Model for k_o = 3.0, 2.0, and 1.0, with *Crack* = 0.5.

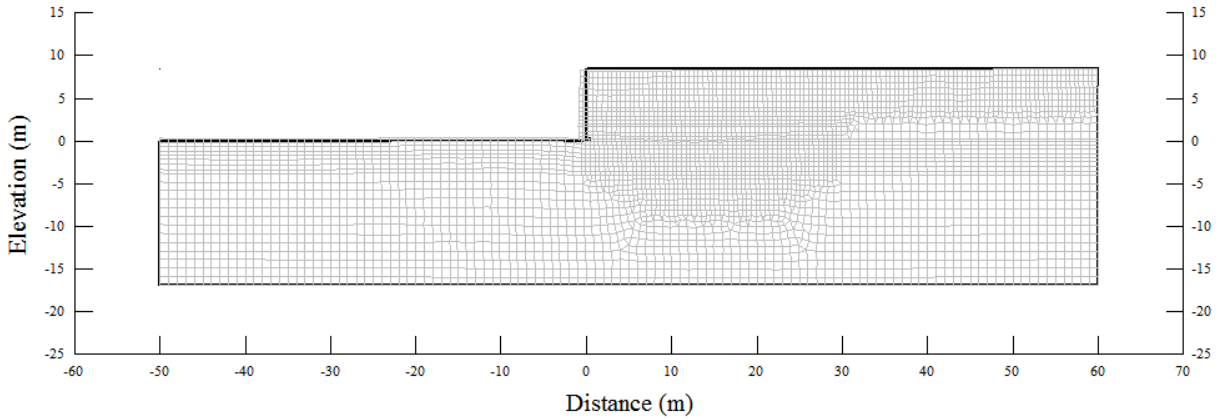

Figure E.2. Deformation mesh due to LSR for k_o = 3.0 and *Crack* = 0.5.

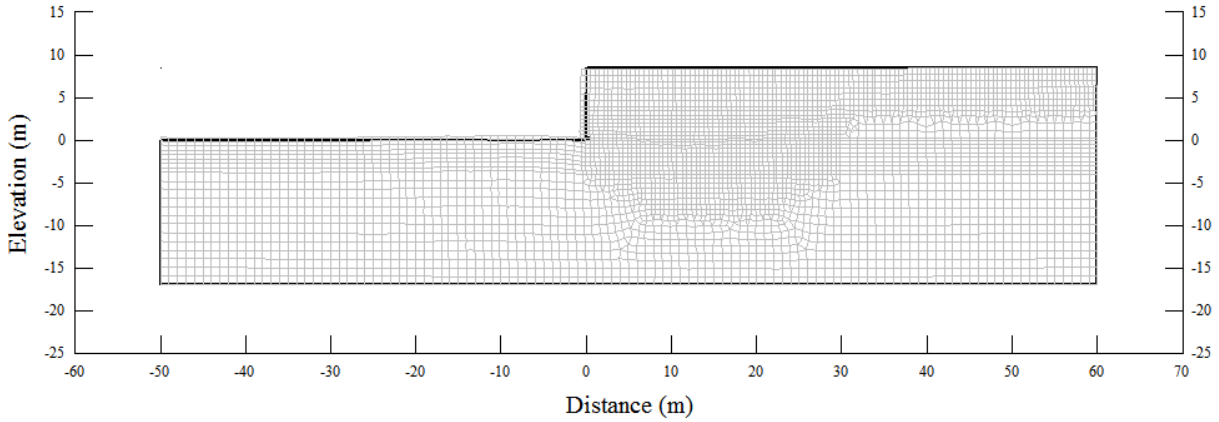

Figure E.3. Deformation mesh due to LSR for k_o = 2.0 and *Crack* = 0.5.

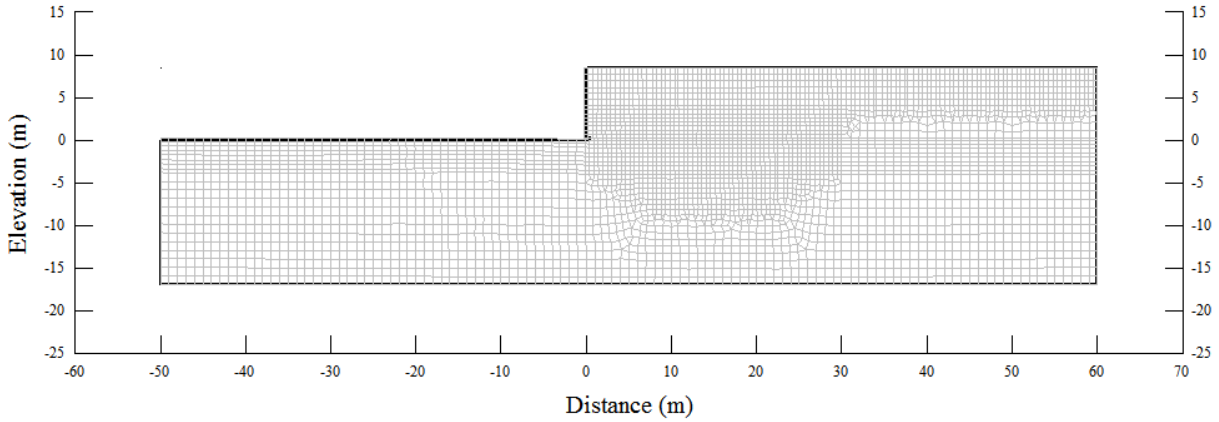

Figure E.4. Deformation mesh due to LSR for k_o = 1.0 and *Crack* = 0.5.

Vertical Slope FEM Model for k_o = 3.0, 2.0, and 1.0, with *Crack* = 0.33

Deformation Mesh Displayed at 30X Magnification

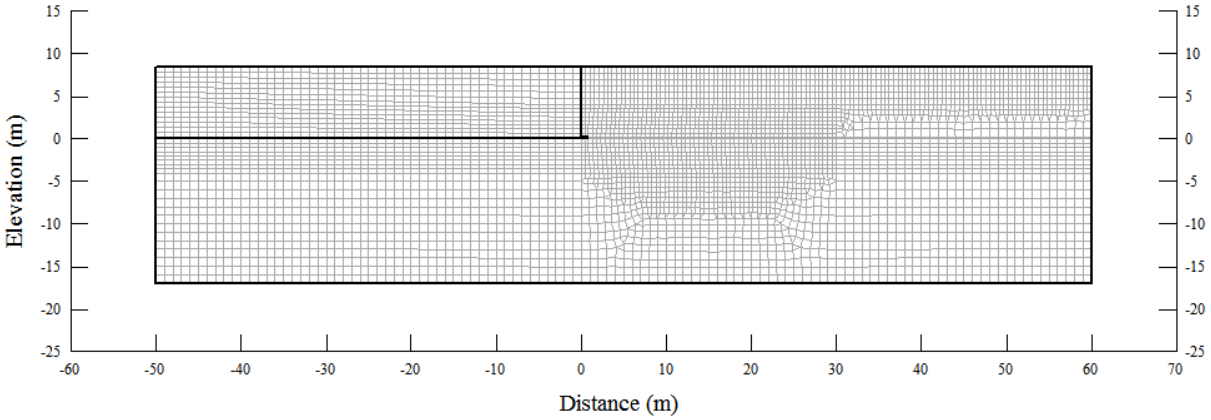

Figure E.5. Initial FEM Model for k_o = 3.0, 2.0, and 1.0, with *Crack* = 0.33.

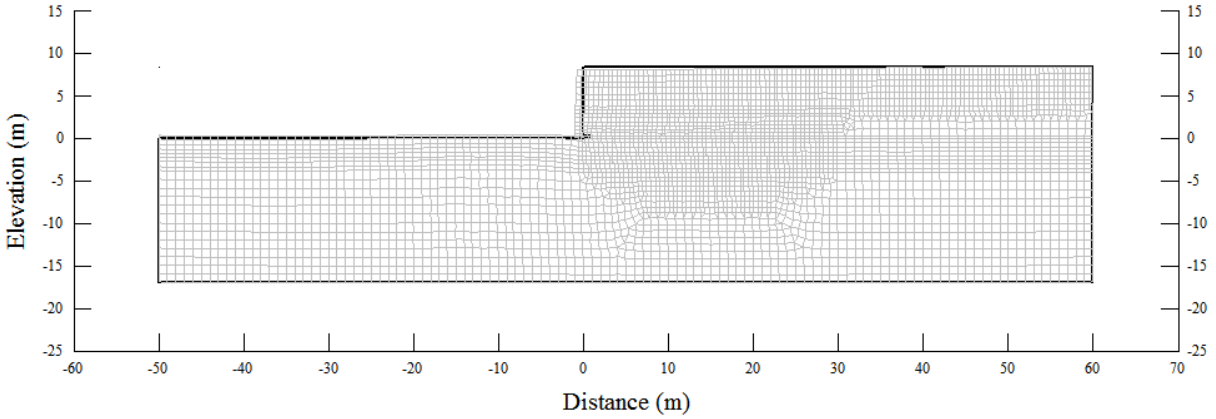

Figure E.6. Deformation mesh due to LSR for k_o = 3.0 and *Crack* = 0.33.

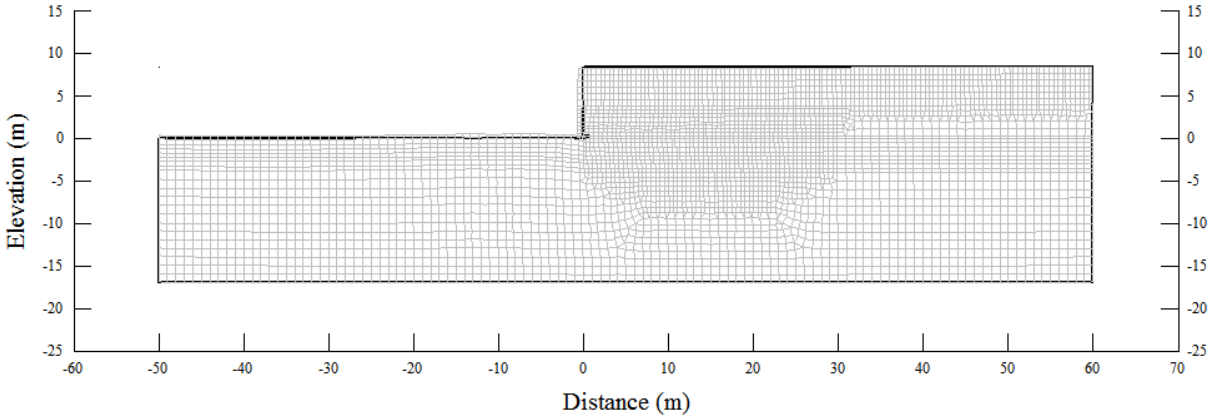

Figure E.7. Deformation mesh due to LSR for k_o = 2.0 and *Crack* = 0.33.

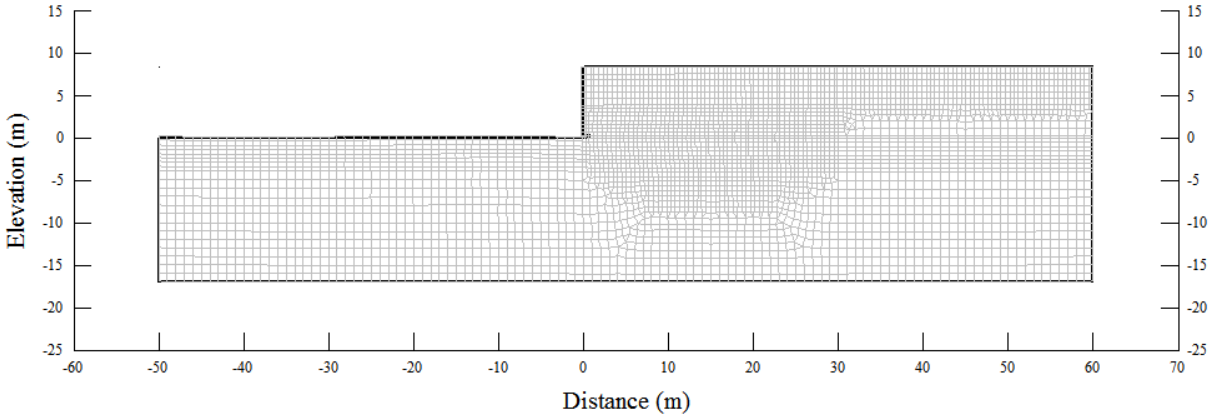

Figure E.8. Deformation mesh due to LSR for k_o = 1.0 and *Crack* = 0.33.

Vertical Slope FEM Model for k_o = 3.0, 2.0, and 1.0, with *Crack* = 0.25

Deformation Mesh Displayed at 30X Magnification

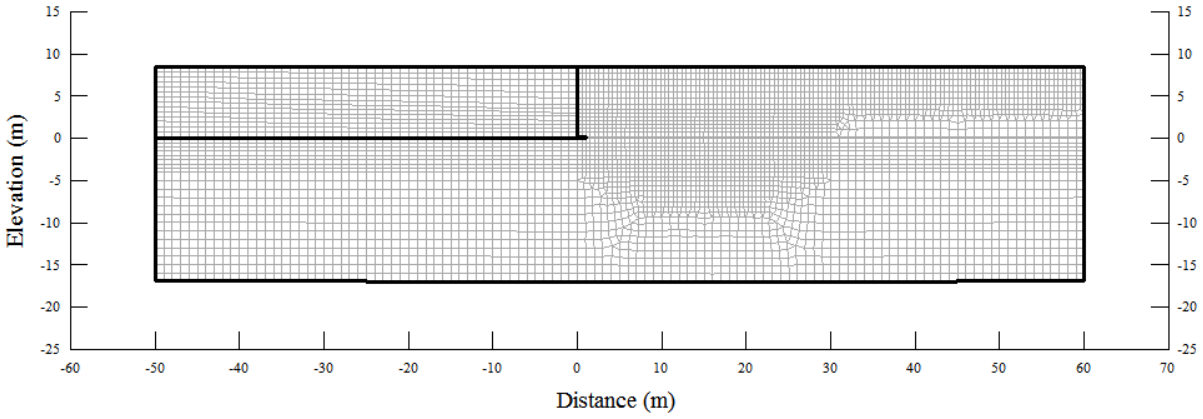

Figure E.9. Initial FEM Model for k_o = 3.0, 2.0, and 1.0, with *Crack* = 0.25.

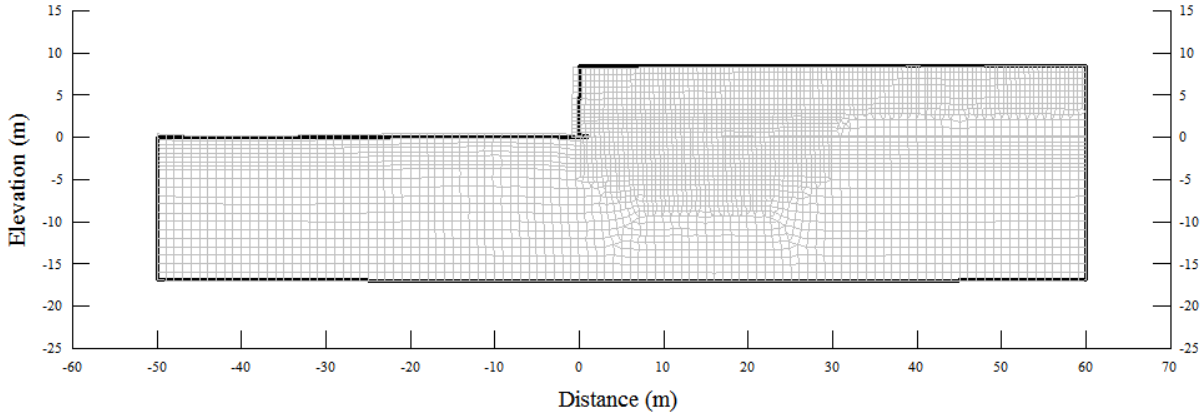

Figure E.10. Deformation mesh due to LSR for k_o = 3.0 and *Crack* = 0.25.

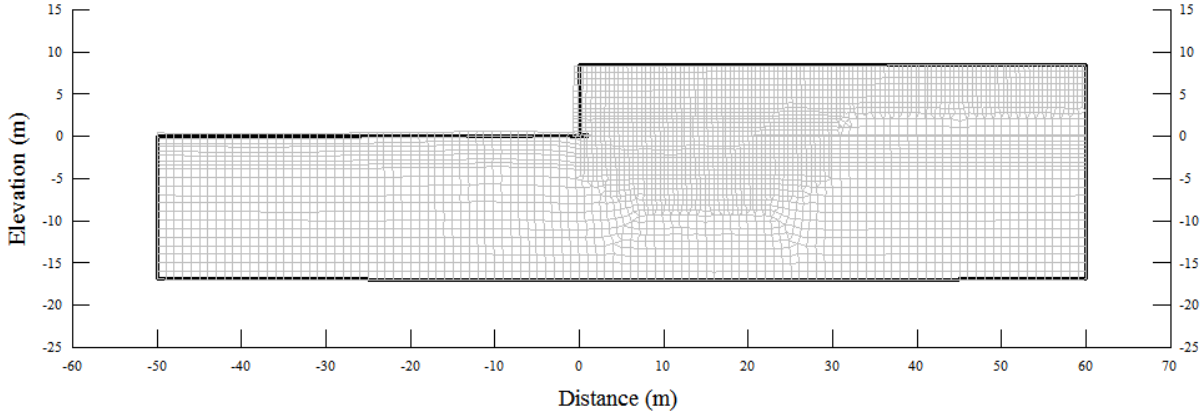

Figure E.11. Deformation mesh due to LSR for k_o = 2.0 and *Crack* = 0.25.

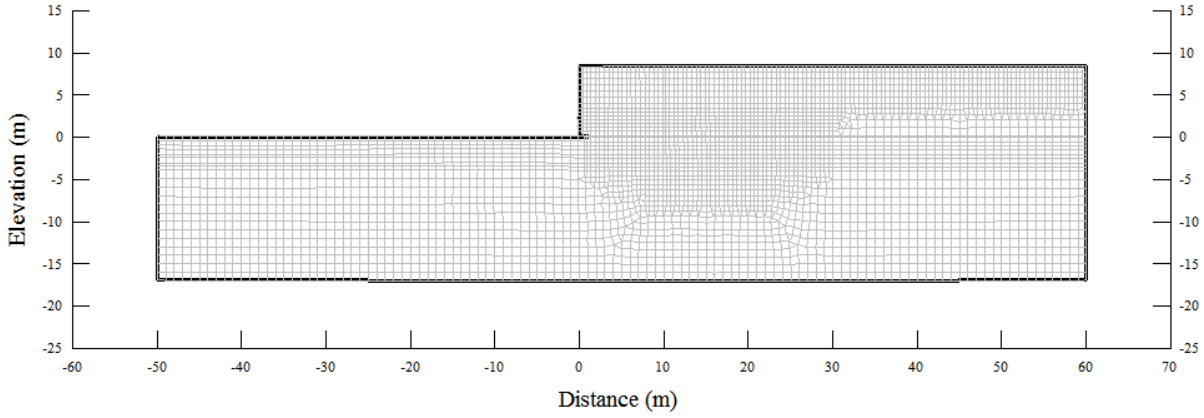

Figure E.12. Deformation mesh due to LSR for k_o = 1.0 and *Crack* = 0.25.

APPENDIX F

FEM MODELS FOR EVALUATION OF $\phi = 0°$ VERTICAL SLOPES ON A SAND BASE

Vertical Slope FEM Model for k_o = 3.0, 2.0, and 1.0

Deformation Mesh Displayed at 20X Magnification

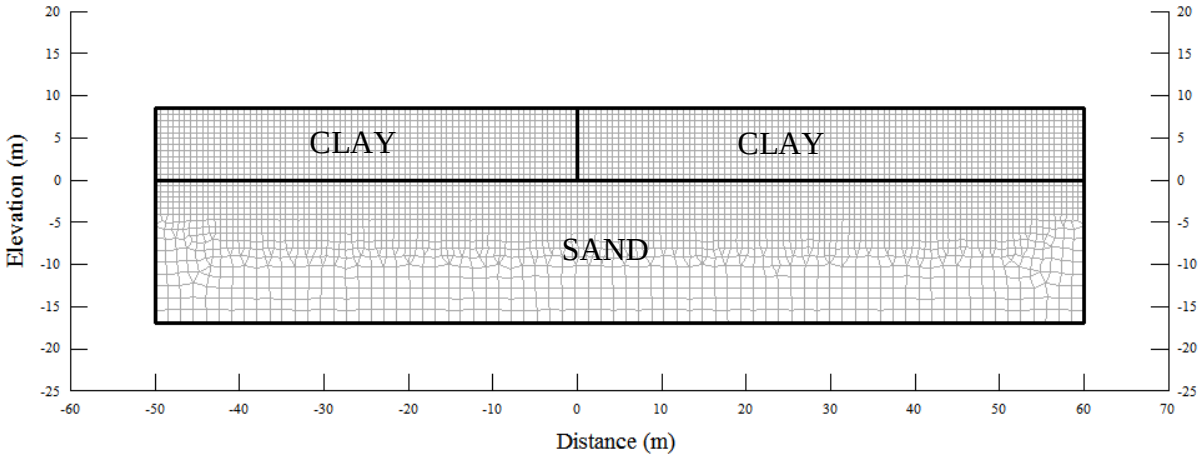

Figure F.1. Initial FEM Model for k_o = 3.0, 2.0, and 1.0.

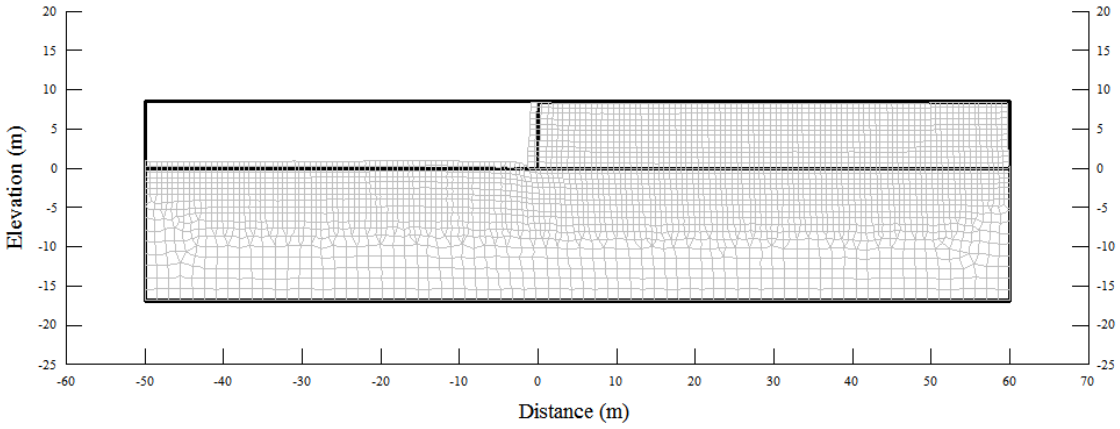

Figure F.2. Deformation mesh due to LSR for k_o = 3.0.

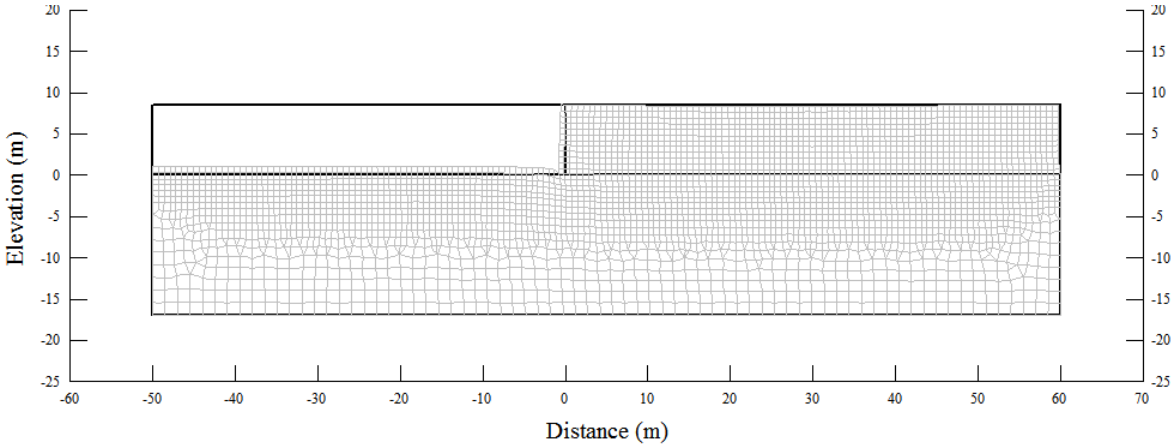

Figure F.3. Deformation mesh due to LSR for k_o = 2.0.

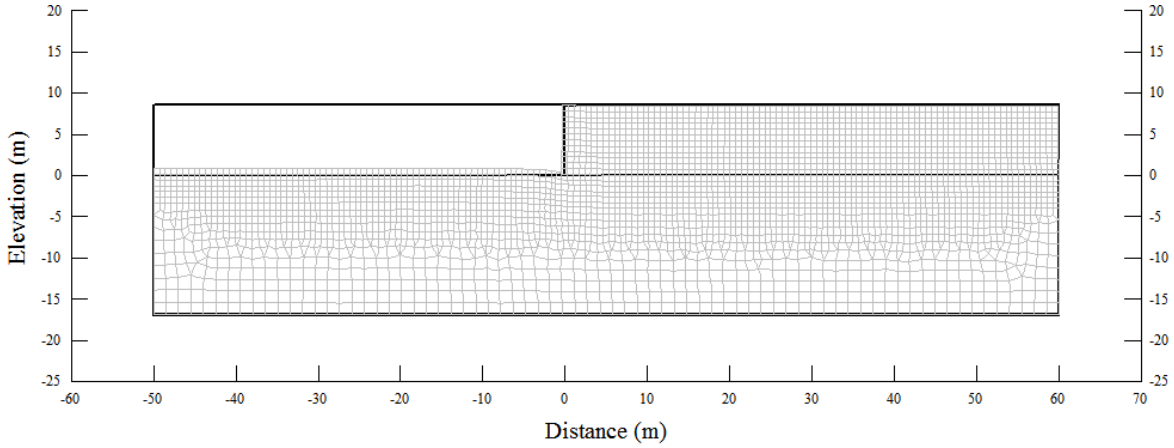

Figure F.4. Deformation mesh due to LSR for k_o = 1.0.

¼H:1V Slope FEM Model for k_o = 3.0, 2.0, and 1.0

Deformation Mesh Displayed at 20X Magnification

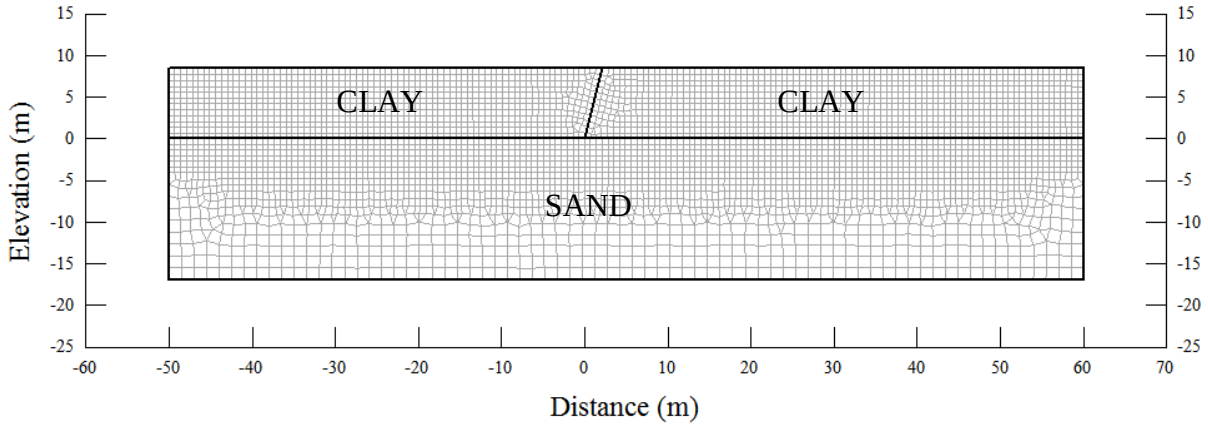

Figure F.5. Initial FEM Model for k_o = 3.0, 2.0, and 1.0.

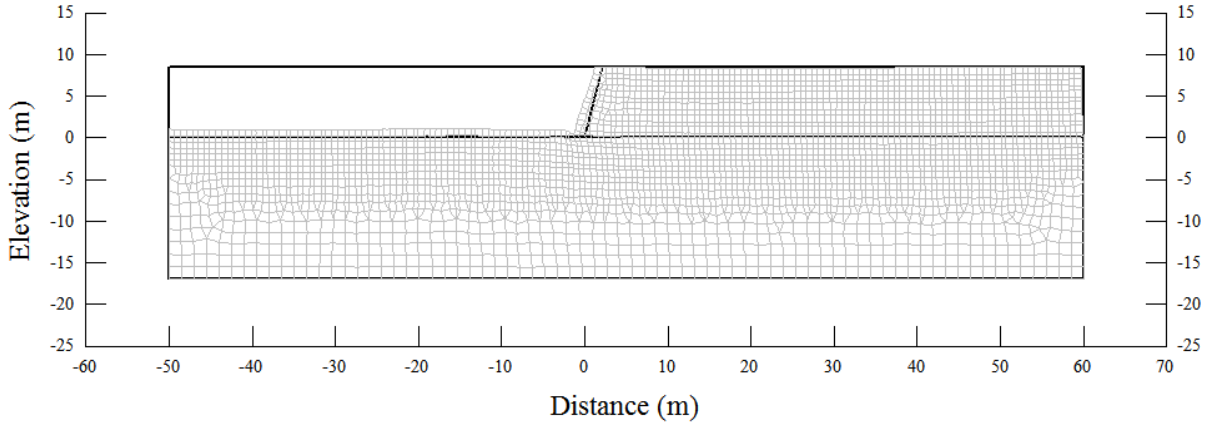

Figure F.6. Deformation mesh due to LSR for k_o = 3.0.

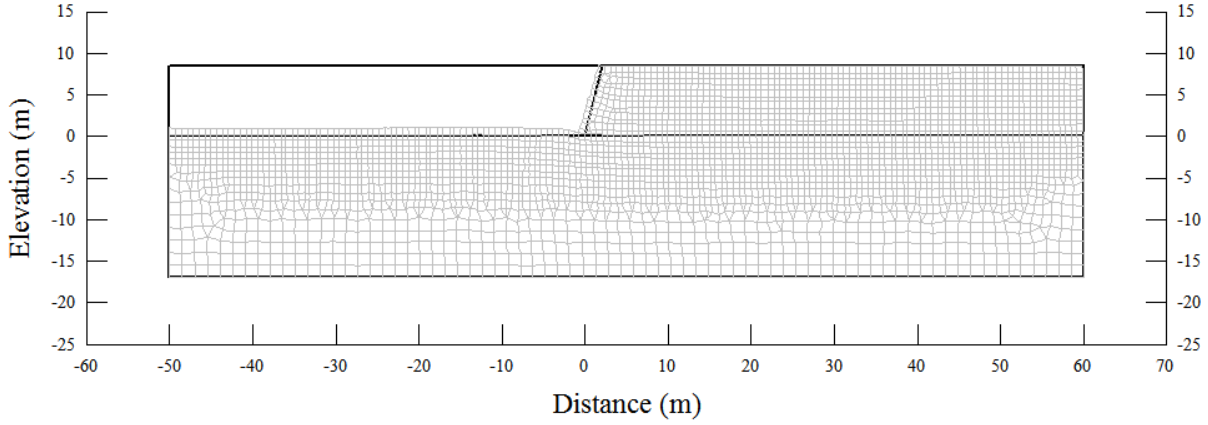

Figure F.7. Deformation mesh due to LSR for k_o = 2.0.

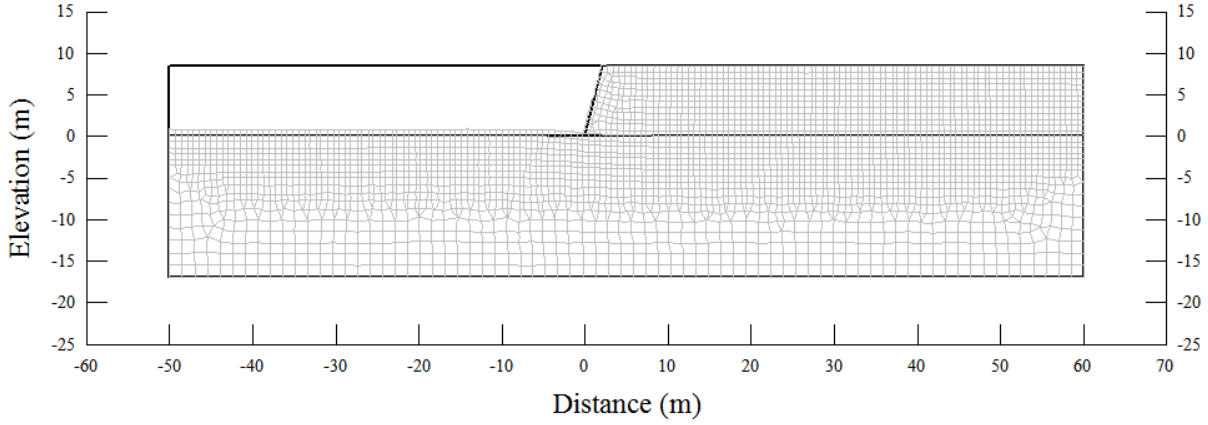

Figure F.8. Deformation mesh due to LSR for k_o = 1.0.

½H:1V Slope FEM Model for k_o = 3.0, 2.0, and 1.0

Deformation Mesh Displayed at 20X Magnification

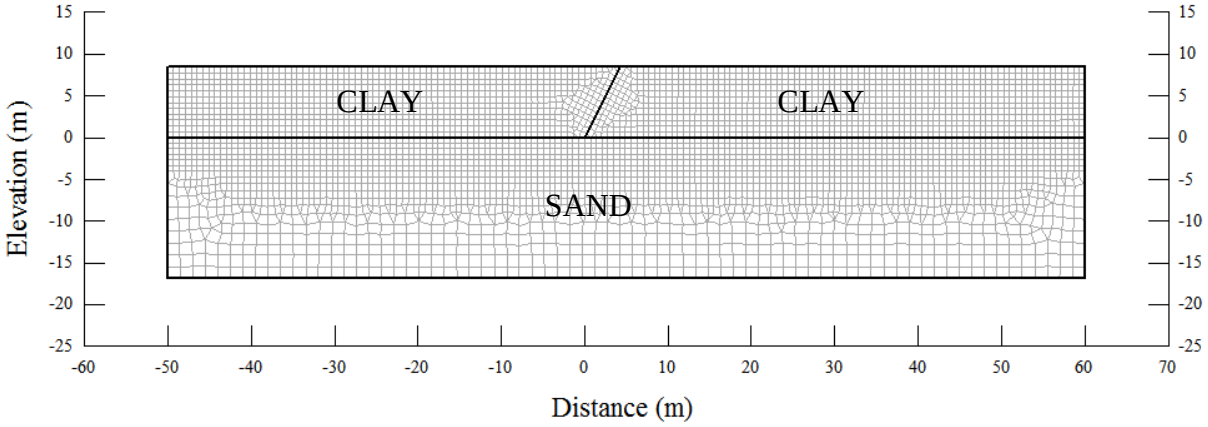

Figure F.9. Initial FEM Model for k_o = 3.0, 2.0, and 1.0.

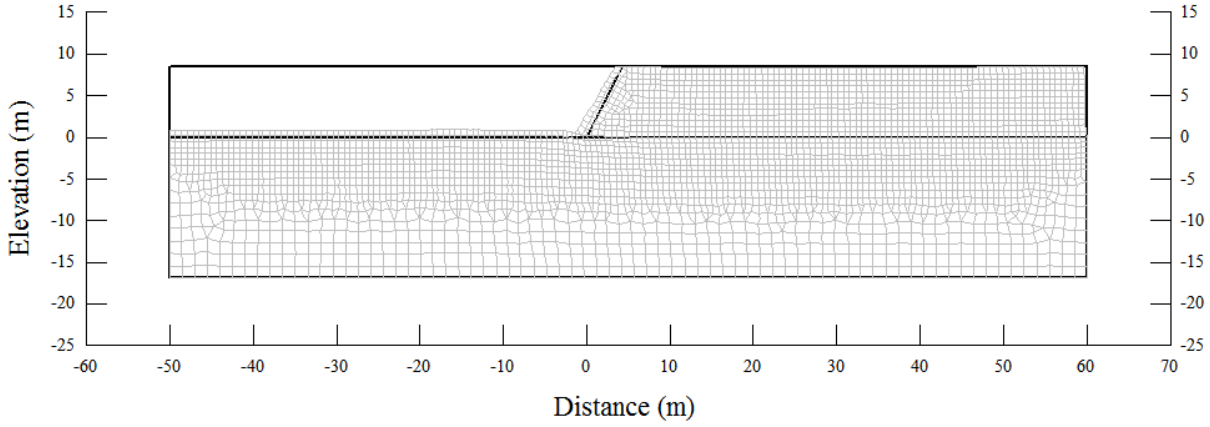

Figure F.10. Deformation mesh due to LSR for k_o = 3.0.

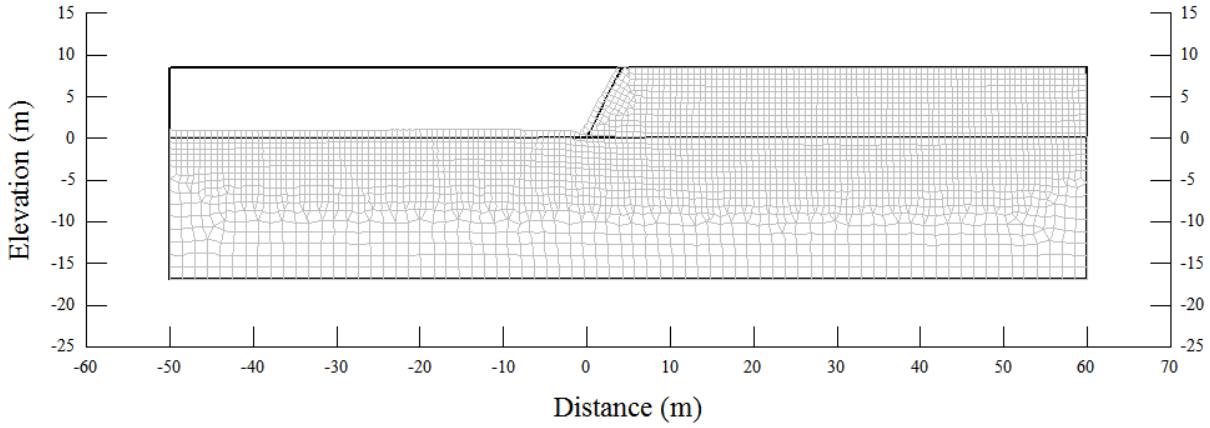

Figure F.11. Deformation mesh due to LSR for k_o = 2.0.

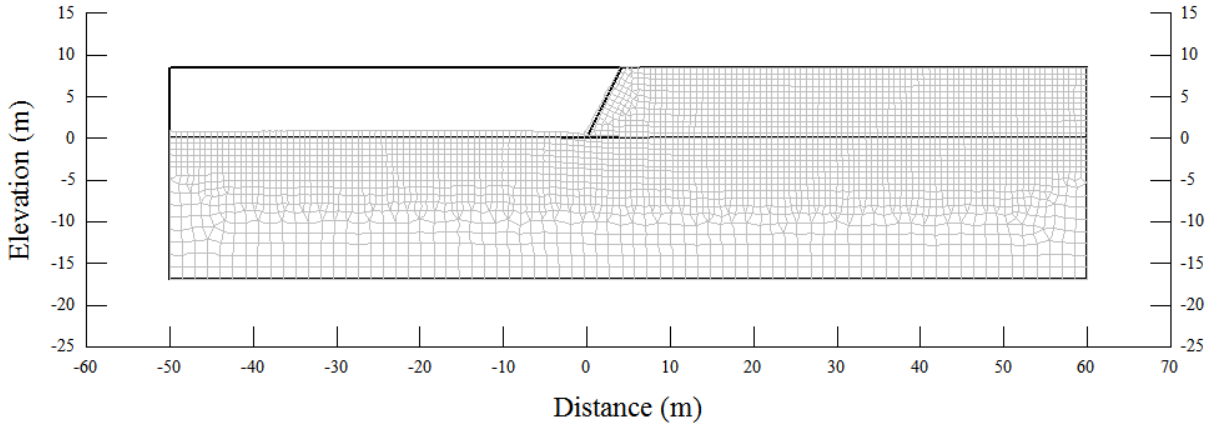

Figure F.12. Deformation mesh due to LSR for k_o = 1.0.

BIBLIOGRAPHY

AASHTO (1996). *Standard Specification for Highway Bridges*, American Association of State Highway and Transportation Officials, Washington, DC.

AASHTO, (2007). *AASHTO LRFD Bridge Design Specifications*, American Association of State Highway and Transportation Officials, Washington, DC.

AASHTO T236. "Standard Method of Test for Direct Shear Test of Soils Under Consolidated Drained Conditions", *Standard Specifications for Transportation Materials and Methods of Sampling and Testing*, American Association of State Highway and Transportation Officials, Washington, DC.

Ackenheil, A. C. (1954). *A Soil Mechanics and Engineering Geology Analysis of Landslides in the area of Pittsburgh*, Thesis presented to the University of Pittsburgh, Pittsburgh, PA, in partial fulfillment of the requirements for the degree of Doctor of Philosophy.

Aliabadi, M. H. (1999). *Fracture of Rock*, Edited by Aliabadi, M.H., WIT Press / Computational Mechanics Publications, Southampton, UK.

Alpan, I. (1967). "The Empirical Evaluation of the Coefficients k_o and k_{or}", *Soils and Foundations*, Vol. 7, No. 1.

Anderson, T. L. (1995). *Fracture Mechanics: Fundamentals and Applications, 2nd Edition*, CRC Press, Inc., Boca Raton, FL.

AREMA (2007). *Manual for Railway Engineering*, American Railway Engineering and Maintenance-of-Way Association, Lanham, Maryland.

ASTM D3080. *Standard Test Method for Direct Shear Test of Soils Under Consolidated Drained Conditions*, American Society for Testing and Materials, West Conshohocken, Pennsylvania.

Barsom, J. M. and Rolfe, S. T. (1987). *Fracture and Fatigue Control in Structures*, Prentice-Hall, Inc., Englewood Cliffs, NJ.

Bathe, K. J. (1982). *Finite Element Procedures in Engineering Analysis*, Prentice-Hall, Inc., Englewood Cliffs, NJ.

Bazett, D. J., Adams, J. I., and Matyas, E. L., (1961). "An Investigation of Slide in a Test Trench Excavated in Fissured Sensitive Marine Clay", *Proceedings of the 5th International Conference on Soil Mechanics*, Paris, Vol. 1, pp. 431-435.

Bieniawski, Z. T. (1974). "Estimating the Strength of Rock Materials", *Journal of the South African Institute of Mining and Metallurgy*, Vol 74, pp. 312-320.

Bishop, A. W. (1967). "Progressive Failure with Special Reference to the Mechanism Causing It", *Proceedings of Geotechnical Conference,* Oslo, Vol. 2, pp. 142-150.

Bishop, A. W., Kumapley, N. W., and El-Ruwagih, A. (1975). "The Influence of Pore Water Tension of on the Strength of Clay", *Transactions of the Royal Society of London*, Vol. 278, Series A, pp. 511-554.

Bjerrum, L. (1967). "Progressive Failure in Slopes of Overconsolidated Plastic Clay and Clay Shales", *Journal of Soil Mechanics and Foundation Division,* ASCE, Vol. 93, No. SM5, pp. 1-49.

Boresi, A. P., Schmidt, R. J., and Sidebottom, O. M. (1993). *Advanced Mechanics of Materials*, John Wiley & Sons, Inc., New York, NY.

Bowles, J. E. (1996). *Foundation Analysis and Design, Fifth Edition*, The McGraw-Hills Companies, Inc., New York, NY.

Broek, D. (1986). *Elementary Engineering Fracture Mechanics*, Kluwer Academic Publishers, Hingham, MA.

Broek D. (1989). *The Practical Use of Fracture Mechanics*, Kluwer Academics Publishers, Norwell, MA.

Brooker, E. W., and Peck, R. B., (1993). "Rational Design Treatment of Slides in Overconsolidated Clays and Clay Shales", *Canadian Geotechnical Journal*, Vol. 30, pp. 526-544.

Burland, J. B., Longworth, T. I. and Moore, J. F. A. (1977). "A Study of Ground Movement and Progressive Failure Caused by a Deep Excavation in Oxford Clay", *Geotechnique*, Vol. 27, No. 4, pp. 557-591.

Burland, J. B. and Hancock, R. J. (1977). "Underground Car Park at the House of Commons, London: Geotechnical Aspects", *Struc. Engineer*, Vol. 55, 87-100.

Burland, J. B. and Moore, J. F. A. (1973). "The Measurement of Ground Displacement around Deep Excavations", *Proceedings of the Symposium of Field Instrumentation*, British Geotechnical Society, London, pp. 70-84.

Chandler, R. J. (1972). "Lias Clay: Weathering Processes on their Effect on Shear Strength", *Geotechnique*, Vol. 22, No. 3, pp. 403-431.

Chandler, R. J. (1974). "Lias Clay: The Long-Term Stability of Cutting Slopes", *Geotechnique*, Vol. 24, No. 1, pp. 21-38.

Chao, Y. J, and Liu, S. (1997). "On the Failure of Cracks under Mixed-Mode Loads", *International Journal of Fracture*, Vol. 87, pp. 201-223.

Chudnovsky, A., Saada, A., and Lesser, A. J. (1988). "Micromechanisms of Deformation in Fracture of Overconsolidated Clays", *Canadian Geotechnical Journal*, Vol. 25, pp. 213-221.

Clough, R. W. (1960). "The Finite Element in Plane Stress Analysis", *Proceedings of the 2nd ASCE Conference on Electronic Computation*, Pittsburgh, PA.

Clough, R. W. and Woodward, R. J. (1967). "Analysis of Embankment Stresses and Deformations", *Journal of Soil Mechanics and Foundation Division*, ASCE, Vol. 93, No. 4, pp 529-549.

Clough, G.W., and O'Rourke, T.D. (1990). "Construction Induced Movements of In-Situ Walls", *ASCE Geotechnical Special Publication No. 25 – Design and Performance of Earth Retaining Structures*, 439-470.

Covarrubias, S. W. (1969). "Cracking of Earth and Rockfill Dams", Harvard Soil Mechanics Series, Vol. 82.

Craig, R. F. (1992). *Soil Mechanics; 5th Edition*, Chapman & Hall, New York, NY.

Culmann, K. (1866). Die Graphische Statik, Zurich.

Das, B. M., (1990). *Principles of Geotechnical Engineering, 2nd Edition*, PWS-Kent Publishing Company, Boston, MA.

Duncan, J. M. (1996). "State of the Art: Limit Equilibrium and Finite-Element Analyses of Slopes", *Journal of Geotechnical Engineering,* ASCE, Vol. 122, No. 7, pp. 577-596.

Duncan, J. M., and Chang, C. Y. (1970). "Nonlinear Analysis of Stress and Strain in Soils", *Journal of Soil Mechanics and Foundation Division*, ASCE, Vol. 96, No. SM5, pp. 1629-1653.

Duncan, J. M., and Dunlop, P. (1969). "Slopes in Stiff-Fissured Clays and Shales", *Journal of Soil Mechanics and Foundation Division*, ASCE, Vol. 95, No. SM2, pp. 467-492.

Dunlop, P., and Duncan, J. M. (1970). "Development of Failure around Excavated Slopes", *Journal of Soil Mechanics and Foundation Division*, ASCE, Vol. 96, No. SM2, pp. 471-493.

Dunnicliff, J. (1993). *Geotechnical Instrumentation for Monitoring Field Performance*, John Wiley & Sons, Inc. New York, New York.

Dyskin, A. V. and Germanovich, L. N. (1995). "A Model of Fault Propagation in Rocks Under Compression", *Proceedings of the 35th U.S. Symposium on Rock Mechanics*, Lake Tahoe, NV, pp. 731-738.

Erdogan, R. and Sih, G. C. (1963). "On the Crack Extension in Plates under Plain Loading and Transverse Shear", *Journal of Basic Engineering*, ASME, Vol. 85, pp. 519-527.

EM 1110-2-1913. *Design and Construction of Levees*, Engineer Manual of the US Army Corps of Engineers, Washington, DC.

Fang, H. Y. and Fernandez, J. (1981). "Determination of Tensile Strength of Soils by Unconfined-Penetration Test", *Laboratory Shear Strength of Soil, ASTM STP 740*, R. N. Yong and F. C. Townsend, Eds., pp 130-144.

Fang, H. G., Mikroudis, G. K., and Pamukcu, S. (1989). "Fracture Behavior of Compacted Fine-Grained Soils", *ASTM STP 1020 - Fracture Mechanics: Perspectives and Directions*, Edited by Wei, R. P. and Gangloff, R. P., ASTM International, West Conshohocken, PA, pp. 659-667.

Fellenius, W. (1927). *Erdstatische Berechnungen mit Reibung and Kohaesion*, Revised Edition, W. Ernst u. Sons, Berlin.

Fellenius, W. (1936). "Calculation of the Stability of Earth Dams", Trans. 2nd Congress on Large Dams, Washington, DC, Vol. 4, pp. 445-462.

Gibson, M. and Morgenstern, N. R. (1962). "A Note on the Stability of Cuttings in Normally Consolidated Clays", *Geotechnique*, Vol. 12, No. 3, pp. 212-216.

Goodman, R. E. (1989). *Introduction to Rock Mechanics, 2nd Edition*, John Wiley & Sons, New York, New York.

Gray, R. E., Ferguson, H. F., and Hamel, J. V. (1978). "Slope Stability in the Appalachian Plateau, Pennsylvania, and West Virginia, USA." *Rockslide and Avalanches*, B. Voight, Ed., 2, 447-471.

Griffith, A. A. (1921), "The phenomena of rupture and flow in solids", *Philosophical Transactions of the Royal Society of London*, A 221, pp. 163-198.

Griffiths, D. V. (1982). "Computation of Bearing Capacity Factors using Finite Elements", *Geotechnique*, Vol. 32, No. 3, pp. 195-202.

Griffiths, D. V. (2000). "Stability Analysis of Highly Variable Soils by Elasto-Plastic Finite Elements", *Course Notes: Advanced Numerical Applications and Plasticity GeoMechanics*, International Centre for Mechanical Sciences, Udine, Italy.

Griffiths, D. V. (2009). Personal communication via electronic mail dated 07 December 2009.

Griffiths, D. V. and Lane, P. A. (1999). "Slope Stability Analysis by Finite Elements", *Geotechnique*, Volume 49, No. 3, 387-403.

Hallam, A. (1975). *Jurassic Environments*, Cambridge University Press.

Hamel, J. V. (1998). "Mechanism of Pleistocene Rock Slides Near Pittsburgh, Pennsylvania", *International Journal of Rock Mechanics and Mineralogical Sciences*, Volume 35, No. 4/5.

Hamel, J. V. (2009). Personal communication via electronic mail dated 17 November 2009.

Hamel, J. V. and Adam, W. R. (1981). "Claystone Slides, Interstate 79, Pittsburgh, Pennsylvania", *Proceedings of the International Symposium on Weak Rock*, Tokyo, Japan.

Hamel, J. V. and Flint, N. K. (1972). "Failure of Colluvial Slope", *Journal of the Soil Mechanics and Foundations Division*, ASCE, Vol. 98, No. SM2.

Hellen, Trevor (2001). "How to Undertake Fracture Mechanics Analysis with Finite Elements", *The International Association for the Engineering Analysis Community: NAFEMS Report HT18*, Glasgow, United Kingdom.

Hoek, E. (1983). "Strength of Jointed Rock Masses", 23rd Rankine Lecture, *Geotechnique*, Vol. 33, No. 3, pp. 187-223.

Holtz, R. D. and Kovacs, W. D. (1981). *An Introduction to Geotechnical Engineering*, Prentice-Hall, Englewood Cliffs, NJ.

Horri, H. and Nemat-Nasser, S. (1985). "Compression-Induced Microcrack Growth in Brittle Solids: Axial Splitting and Shear Failure", *Journal Geophs. Res.*, Vol. 90, No. B34, pp. 3105-3215.

Huebner, K.H., Dewhirst, D. L., Smith, D. E. and Byrom, T. G. (2008). *The Finite Element Method for Engineers, 4th Edition*, John Wiley & Sons, Inc., Hoboken, NJ.

Hunter, J. H. and Schuster, R. L. (1968). "Stability of Simple Cuttings in Normally Consolidated Clays", *Geotechnique*, Vol. 18, No. 3, pp. 372-378.

Hussain, M. A., Pu, S. L., and Underwood, J. H. (1974). "Strain Energy Release Rate for a Crack Under Combined Mode I and Mode II", *ASTM STP 560 - Fracture Analysis*, ASTM International, West Conshohocken, PA, pp. 2-28.

Ingraffea, A. R. and Heuze, F. E. (1980). "Finite Element Models for Rock Fracture Mechanics", *International Journal for Numerical and Analytical Methods in Geomechanics*, Vol. 4, pp. 25-43.

Irwin, G. R. (1956). "Onset of Fast Crack Propagation in High Strength Steel and Aluminum Alloys", *Sagamore Research Conference Proceedings*, Vol. 2, pp. 289-305.

Irwin, G. R. (1957), "Analysis of Stresses and Strains Near the End of a Crack Traversing a Plate", *Journal of Applied Mechanics*, ASME, Vol. 24, pp. 361-364.

James, P. M. (1970). *Time Effects and Progressive Failure in Clay Slopes*, Ph.D. Thesis, London University.

Janbu, N. (1968). "Slope Stability Computations", *Soil Mechanics and Foundation Engineering Report*, The Technical University of Norway, Trondheim, Norway.

Kawai, T. (1979). "A New Approach to Soil Mechanics and Geotechnical Engineering", *3rd International Conference in Australia on Finite Element Methods*", Sydney, Australia.

Khatri, V. N. and Kumar, J. (2009). "Stability of an unsupported Vertical Circular Excavation in Clays under Undrained Condition", *Computers and Geotechnics*, Elsevier Science Publishers, Vol. 37, pp. 419-424.

Kulhawy, F. H., Trautmann, C. H., Beech, J. F., O'Rourke, T. d., McGuire, W., Wood, W. A., and Capano, C. (1983). *Transmission Line Structure Foundations for Uplift-Compression Loading*, Report No. EL-2870, Electric Power Research Institute, Palo Alto, CA.

Kutschke, W.G., Petersen, W.K, Zorn, E.V., and Meyers, J.R. (2007). "Geotechnical Challenges Posed by Weak Claystone in Deep Cuts", *Proceedings of the 58th Highway Geology Symposium*, Pocono Manor, Pennsylvania.

Kutschke, W. G., Petersen, W. K, and Meyers, J. R. (2007). "Rock Slope Protection System for Differential Weathering Materials", *Proceedings of Geo-Denver 2007, Embankments, Dams and Slopes: Lessons Learned from New Orleans Levee Failures and Other Current Issues, Geotechnical Special Publication No. 161* (CD-ROM), ASCE, Reston, VA.

Kutschke, W. G., Petersen, W. K, Meyers, J. R., and Zorn, E. V. (2007). "Rock Cut Slope Instrumentation within Variable and Potentially Unstable Sedimentary Rock Strata", *Proceedings of the 7th International Symposium on Field Measurements, Geotechnical Special Publication No. 175*, (CD-ROM), ASCE, Reston, VA.

Kutschke, W.G., Petersen, W.K, and Meyers, J.R. (2008). "Rock Slope Design for New Railroad Alignment in Indiana County, Pennsylvania", *Proceedings of 23rd ASCE Central PA Geotechnical Conference*, Hershey, PA.

Kutschke, W.G., and Vallejo, L.E. (2010). "Failure Analysis of an Instrumented Stiff Clay Slope", *Proceedings of Geo-Florida 2010, Advances in Analysis, Modeling and Design, Geotechnical Special Publication No. 199* (CD-ROM), ASCE, Reston, VA.

Lambe, T. W., Whitman, R. V. (1969). *Soil Mechanics*, John Wiley & Sons, Inc., New York, NY.

Lee, F. H., Lo, K. W., and Lee, S. L. (1988). "Tension Crack Development of Soils", *Journal of Geotechnical Engineering*, ASCE, Vol. 114, No. 8, pp. 915-929.

Li, H. S., Yang, H.T. and Liu, Z.l. (2000). "Experimental Investigation of Fracture Toughness K_{IIC} of Frozen Soil", *Canadian Geotechnical Journal*, Vol. 37, No. 1, pp. 253-258.

Liu, Y. and Mahadevan, S. (2006). "Threshold Stress Intensity Factor and Crack Growth Prediction under Mixed-Mode Loading", *Engineering Fracture Mechanics*, Elsevier Science Publishers, Vol. 74, pp. 332-324.

Marsland, A. (1972). "The shear strength of stiff fissured clays", *Stress Strain Behavior of Soils*, Edited by R.H. G. Parry, G. T. Foulis and Co., England, pp. 59-68.

Mayne, P. W. (1984). "K_o-c_u/σ'_{vo} Trends for Overconsolidated Clays", *Journal of Geotechnical Engineering*, ASCE, Vol. 110, No. 10, pp. 1511-1516.

Morris, P. H., Graham, J., and Williams, D. J. (1992). "Cracking in Drying Soils", *Canadian Geotechnical Journal*, Vol. 29, pp. 263-277.

Naylor, D. J. and Pande, G. N. (1981), *Finite Elements in Geotechnical Engineering*. Pineridge Press, Swansea, U.K., 1981.

Palmer, A. C. and Rice, J. R. (1973). "The Growth of Slip Surfaces in the Progressive Failure of Over-Consolidated Clay", *Proceedings of the Royal Society of London,* A. 332, pp. 527-548.

Pande, G. N., Beer, G., and Williams, J. R. (1990). *Numerical Methods in Rock Mechanics,* John Wiley and Sons, Inc., New York, NY.

PennDOT (1950). *L.R. 120, Section 23 – Allegheny County, Widening of Blvd. of the Allies, Bluff St. Sta. 673+63 to Sta. 689+37, Blvd. of Allies, Sta. 682+72 to Sta. 695+91,* Contract Drawings, Commonwealth of Pennsylvania, Department of Highways, Bridge Unit, Pittsburgh, PA.

Petersen, R., Iverson, N.L., and Rivard, P.J. (1957). "Studies on Several Dam Failures on Clay Foundations", *Proceedings of the Fourth International Conference on Soil Mechanics and Foundation Engineering,* London, Vol. 2, pp. 348-352.

Pomeroy, John, (1982). *Landslides in the Greater Pittsburgh Region, Pennsylvania,* Geological Survey Professional Paper 1229, USGS, Washington, DC.

Reches, Z. and Lockner, D. A. (1994). "Nucleation and Growth of Faults in Brittle Rocks", *Journal Geophys. Res.*, Vol. 99B, pp. 18159-18173.

Rice, J. R. (1968). "A Path Independent Integral and the Approximate Analysis of Strain Concentration by Notches and Cracks", *Journal of Applied Mechanics,* Vol. 35, pp. 379-386.

Rudnicki, J. W. and Rice, J. R. (1975). "Conditions for the Localization of Deformation in Pressure-Sensitive Dilatant Materials", *Journal of the Mechanics and Physics of Solids,* Vol. 23, pp. 371-394.

Saada, A.W., Chudnovsky, A., and Kennedy, M. (1985). "A Fracture Mechanics Study of Stiff Clays", *Proceedings of the 11th International Conference on Soil Mechanics and Foundation Engineering,* Vol. 2, pp. 637-640.

Serafim, J. L. and Pereira, J. P. (1983) "Considerations of the Geomechanics Classification of Bieniawski", *Proceedings of the International Symposium of Engineering Geology and Underground Constructio*n (L.N.E.C., Lisbon, Portugal) Volume 1, Section II, pp. 33-42.

Sih, G. C. (1973). *Handbook of Stress Intensity Factors for Researchers and Engineers,* Institute for Fracture and Solid Mechanics, LeHigh University, Bethlehem, PA.

Sih, G. C. (1974). "Strain Density Factor Applied to Mixed Mode Crack Problems", *Int. J. Fracture*, Vol. 10, pp. 305-321.

SIGMA/W (2007). *Stress-Deformation Modeling with SIGMA/W 2007: An Engineering Methodology*, GEO-SLOPE International, Ltd., Alberta, Canada.

Sills, G. C., Burland, J. B. and Czechowski, M. K. (1977). "Behaviour of an Anchored Diaphragm Wall in Stiff Clay", *Proc. 9th International Conference on Soil Mechanics and Foundation Engineering*, Tokyo, Volume 2, 147-154.

Skempton, A. W. (1964). "Long Term Stability of Clay Slopes", *Geotechnique*, Vol. 14, No. 2, pp. 77-101.Smith, I. H., and Hobbs, R. (1974). "Finite Element Analysis of Centrifuged and Built-Up Slopes", *Geotechnique*, Vol. 24, No. 4, pp. 531 – 599.

Skempton, A. W. (1966). "Some Observations on Tectonic Shear Zones", Proceedings of the First International Congress on Rock Mechanics, Vol. 1, pp. 329-335.

Skempton, A. W. (1977). "Slope Stability of Cuttings on Brown London Clay", *Proceedings of the Ninth International Conference on Soil Mechanics and Foundation Engineering*, Tokyo, Vol. 3, pp. 261-270.

Skempton, A. W. and Hutchinson, J. N. (1969). "Stability of Natural Slopes and Embankment Foundations", *7th International Conference on Soil Mechanics and Foundation Engineering, State-of-the-Art Volume*, Mexico City, Mexico, pp. 291-340.

Skempton, A. W. and LaRochelle, P. (1965). "The Bradwell Slip; A Short-Term Failure in London Clay", *Geotechnique*, Vol. 15, No. 3, pp. 221-242.

Skempton, A. W. and Sowa, V. A. (1963). "The Behavior of Saturated Clays during Sampling and Testing", *Geotechnique*, Vol. 13, pp. 269-290.

Smith, I. M. and Hobbs, R. (1974). "Finite Element Analysis of Centrifuged and Built-Up Slopes", *Geotechnique*, Vol. 24, No. 4, pp. 531-559.

SSC-345, (1990). "Elastic-Plastic Fracture Mechanics – A Critical Review", Ship Structure Committee, US Coast Guard, Washington, DC.

Stein, S. K. (1987). *Calculus and Analytic Geometry, 4th Edition*, McGraw-Hill Book Company, New York, NY.

Taylor, D. W. (1937). "Stability of Earth Slopes", *Journal of the Boston Society of Civil Engineers*, Vol. 24, pp. 197-246.

Taylor, D. W. (1948). *Fundamentals of Soil Mechanics*, John Wiley & Sons, Inc., New York, NY.

Terzaghi, K., (1925). *Erdbaumechanik*, Franz Deuticke, Vienna.

Terzaghi, K. (1943). *Theoretical Soil Mechanics*, John Wiley and Sons, New York, NY.

Terzaghi, K. (1950). "Mechanism of landslides", *Application of Geology to Engineering Practice* (Berkey Volume): New York, Geological Society of America, pp. 83-123.

Terzaghi, K., and Peck, R. B. (1967). *Soil Mechanics in Engineering Practice*, Wiley, New York, NY.

Terzaghi, K., Peck, R. B., and Mesri (1996). *Soil Mechanics in Engineering Practice, 3rd Edition*, John Wiley & Sons, Inc., New York, NY.

URS (2005) *Geotechnical Engineering Report – Keystone Buildout, Indiana County, PA*, Pittsburgh, PA.

USDA Technical Release 60, *Earth Dams and Reservoirs*, United States Department of Agriculture, Soil Conservation Service, Engineering Division, Washington, DC.

Vallejo, L. E. (1985), "Fissure Interaction and Progressive Failure of Slopes", *Proceedings of the 11th International Conference on Soil Mechanics and Foundation Engineering*, San Francisco, 4, pp. 2353-2356.

Vallejo, L. E. (1987). "The Influence of Fissures in a Stiff Clay Subjected to Direct Shear", *Geotechnique*, Vol. 37, No. 1, pp. 69-82.

Vallejo, L. E. (1988). "The Brittle and Ductile Behavior of Clay Samples Containing A Crack Under Mixed Mode Loading", *Theoretical and Applied Fracture Mechanics*, Elsevier Science Publishers, Vol. 10, pp. 73-78.

Vallejo, L. E. (1989). "Fissure Parameters in Stiff Clays Under Compression", *Journal of Geotechnical Engineering*, ASCE, Vol. 115, No. 9, pp. 1303-1317.

Vallejo, L.E. (1991). "A Plane Stress Direct Shear Apparatus for Testing Clays" *Geotechnical Engineering Congress 1991,* F.G. McLean, D.A. Campbell, and D.W. Harries (eds.), *Geotechnical Special Publication No. 27,* ASCE, Vol. II, pp. 851-862.

Vallejo, L. E. (1994). "Application of Fracture Mechanics to Soils: An Overview", *Geotechnical Special Publications No. 43,* ASCE, Reston, VA, pp. 1-20.

Vallejo, L. E., and Pramono, E. (1984). "Development of Fracture Regions in Brittle Materials", Proceedings of the 25th Symposium on Rock Mechanics", Northwestern University, Evanston, IL, pp. 47-54.

Wang, J., Zhu, J, and Chai, H. (2007). "Experimental Study on Fracture Behavior of a Silty Clay", *ASTM Geotechnical Testing Journal*, Vol. 30, No. 4.

Westergaard, H. M. (1939). "Bearing Pressures and Cracks", *Journal of Applied Mechanics*, Vol. 6, pp. 49-53.

Whittaker, B. N., Singh, R. N., and Sun, G. (1992). *Rock Fracture Mechanics: Principles, Design and Applications*, Elsevier Science Publishers, Amsterdam, The Netherlands.

Wu, T.H., Williams, R.L., Lynch, J.E. and Kulatilake, P.H. (1987). "Stability of Slopes in Red Conemaugh Shale of Ohio", *ASCE Journal of Geotechnical Engineer*, Volume 113, No. 3.

Wyllie, D.C. and Mah, C.W (2006), *Rock Slope Engineering, Civil and Mining, 4th Edition (based on the 3rd Edition by E. Hoek and J. Bray)*, Spon Press, New York, NY.

Xie, Heping (1993). *Fractals in Rock Mechanics*, A.A. Balkema Publishers, Brookfield, VT.

Zienkiewicz, O. C. and Taylor, R. L. (1989). *The Finite Element Method, 4th Edition*, McGraw Hill, New York, NY.

Zienkiewicz, O. C., Valliappan, S., and King, I. P. (1968). "Stress Analysis of Rock as a No-Tension Material", *Geotechnique*, Vol. 18, No. 1, pp. 56-66.0nn